

REPORT DOCUMENTATION PAGE

Form Approved
OMB No. 0704-0188

Public reporting burden for this collection of information is estimated to average 1 hour per response, including the time for reviewing instructions, searching existing data sources, gathering and maintaining the data needed, and completing and reviewing the collection of information. Send comments regarding this burden estimate or any other aspect of this collection of information, including suggestions for reducing this burden, to Washington Headquarters Services, Directorate for Information Operations and Reports, 1215 Jefferson Davis Highway, Suite 1204, Arlington, VA 22202-4302, and to the Office of Management and Budget, Paperwork Reduction Project (0704-0188), Washington, DC 20503.

1. AGENCY USE ONLY (Leave blank) 2. REPORT DATE JUNE 1996 3. REPORT TYPE AND DATES COVERED FINAL 1989 - 1995

4. TITLE AND SUBTITLE "MODELING FOR MICROSTRUCTURAL CONTROL IN SPRAY FORMING." 5. FUNDING NUMBERS N00014 - 89 - J - 1957 - P00001

6. AUTHOR(S) ROGER D. DOHERTY

7. PERFORMING ORGANIZATION NAME(S) AND ADDRESS(ES) DEPARTMENT OF MATERIALS ENGINEERING DREXEL UNIVERSITY 32ND & CHESTNUT STREET PHILADELPHIA, PA 19104 8. PERFORMING ORGANIZATION REPORT NUMBER

9. SPONSORING / MONITORING AGENCY NAME(S) AND ADDRESS(ES) OFFICE OF NAVAL RESEARCH ARLINGTON, VA 22214 10. SPONSORING / MONITORING AGENCY REPORT NUMBER

11. SUPPLEMENTARY NOTES DISTRIBUTION STATEMENT A Approved for public release Distribution Unlimited

19960708 048

12a. DISTRIBUTION / AVAILABILITY STATEMENT PUBLIC - WORK EITHER PUBLISHED OR TO BE PUBLISHED. 12b. DISTRIBUTION CODE

13. ABSTRACT (Maximum 200 words) The earlier "Drexel" model of Spray Forming was modified with improved measurements of the atomization process: particle size distribution, radial mass flux and gas velocity field as a function of process parameters. The model was also extended to predict, successfully, the droplet undercoolings, the deposit shapes and, in a two dimensional model, the temperatures in the deposit. (A three dimensional thermal model was started but not completed under this funding) Experiments, designed using the model, showed that the droplet sticking efficiency rose and the deposit porosity fell as the fraction liquid in the spray increased from 0.1 to 0.3 for billets and from 0.2 to 0.5 for tubes. Thermal models indicated that the fraction liquid in the deposit approached that in the spray for billets but fell below that in the spray for tubes. The results show that fraction liquid (ideally on the top surface of the deposit) is the best control parameter for spray forming. Grain sizes in the deposit closely tracked the solidification times but showed a slower coarsening rate (a smaller grain size) than expected from both experiments in pure materials and as modeled here. The discrepancy arose from inhibition of grain growth, in the solid- liquid state, by extrinsic impurity phases, often nitrides produced during gas atomization.

14. SUBJECT TERMS SPRAY FORMING, MODELING, SHAPE, GRAIN SIZE, POROSITY. 15. NUMBER OF PAGES 49 + 119 = 168 16. PRICE CODE

17. SECURITY CLASSIFICATION OF REPORT UNCLASSIFIED 18. SECURITY CLASSIFICATION OF THIS PAGE 19. SECURITY CLASSIFICATION OF ABSTRACT 20. LIMITATION OF ABSTRACT

Modeling for Microstructural Control in Spray Forming

N00014-89-J-1957-P00001

Department of Materials Engineering
Drexel University
Pa 19104

Professor Roger D. Doherty

With

Dr.P.Mathur
Dr. S. Annavarapu
Dr. Cheng Cai*

*Ph.D awarded for his contribution to this study

(215-895-2330, Fax 215-895-6760)
(dohertd@duvm.ocs.drexel.edu)

Final Report

Abstract / Executive summary

The earlier numerical "Drexel" model developed in the previous study by Mathur has been significantly extended to two ways. Firstly the needed experimentally measured input parameters for the model notably the Particle Size Distribution, PSD, (and its radial variation) the Radial Mass Flux, MFR, and the gas velocity field in the Osprey chamber were established for the alloys investigated (high strength low alloy steel, IN625 and Cu-Ti) and the range of Osprey facility operating conditions. A revised empirical equation, given as eq. 1 on page 2, fitted the PSD data well as well as earlier data supplied by Osprey Metals. The RMF was also fitted well by the empirical equation given here as eq.2 on p3. The more accurate parameters measured were incorporated into the Model.

The model itself was then significantly developed in several ways. First, a hypothesis for the determination of droplet undercooling in gas atomization of liquid metals in general, and thus in Spray Forming, was developed and incorporated into the spray model. The hypothesis was that the smallest droplets, which cool most quickly, should show *homogeneous nucleation* with undercoolings of about $0.3T_m$. These droplets are accelerated, by the gas stream, faster than are larger droplets and, as a result, will frequently impact the larger, slower-moving and less-cooled droplets. It is proposed that all impacts of partially (or fully) solidified droplets onto larger droplets would lead to nucleation of solidification of the larger droplets - if the larger droplets were supercooled. Numerical evaluation of this hypothesis, within the framework of the Drexel Spray Model, predicted that the magnitude of resulting undercooling would fall with increased droplet size. (The larger droplets which cool more slowly are thus likely to be struck by small solidified droplets after only falling just below the liquidus temperature). This prediction of the size dependence of droplet undercooling matched qualitatively and quantitatively the previous measurements of undercoolings reported by Mathur[27]. In addition, although there was a very high frequency of collisions, most of these involved the impact of very small droplets on larger ones - and assuming that all collisions (except those between two fully solid droplets) led to coalescence of the droplets to give one larger droplet, the model also predicted only a small change in the Particle Size Distribution - at least when measured in terms of *droplet mass*. These conclusions are likely to be applicable to all gas atomization experiments and processes - or at least those with high volume densities of droplets.

A second modification of the Spray Forming model was also developed. This predicted the three dimensional shape of spray formed deposits by combining the known Radial Mass Flux with the imposed motions of the substrate, and, where needed, motion of the spray cone. This shape model was developed into an operating software package "DU SHAPE" and transferred to NSWC and their equipment developers, MTS by the author of the software, Dr. Cheng Cai. This package predicts the final dimensions of deposits assuming an average sticking efficiency of droplets onto the deposit. By comparison with measured shapes the critically important parameter of sticking efficiency was measured for different deposit geometries (tubes and billets), different alloys (Cu-Ti and IN625) and different operating conditions, gas pressure, metal flow rate, superheat etc. The three dimensional shape model was able to be used to design substrate motion to produce a range of desired deposits such as variable thickness tubes, curved tubulars etc.

The shape model was then further developed into a means of predicting the temperature distributions in deposits as two and three dimensional thermal models. The two dimensional model is rather realistic for billet shapes and it could, apparently reliably, predict the temperature distribution and the evolution of the temperature distribution during

spray deposition of billets. It shows that the top surface of the deposits achieved, quite quickly, a similar fraction liquid to that in the depositing spray. The predicted time for solidification initially increases with height into the deposit, from the substrate, but at the top of the deposit that completed solidification in the absence of any continuing further flux of semi-solid material the time for complete solidification fell. The measured grain sizes correlated rather well with the spatial variation of the predicted freezing times. However the predicted grain sizes were significantly larger, at each position, than the grain sizes those predicted by standard solid liquid coarsening theory using the model predicted solidification times. (See below). For the spray formed tubes, the simple two dimensional thermal model is clearly inadequate and the full three dimensional model is needed for calculating the freezing behaviour and in particular the fraction liquid on the surface of the tube during deposition. The three dimensional thermal model was not completed under the funding of this award. For the tubes it appears likely, that as shown by the simple two dimensional model, that the cooling effect of rotating outside the spray and the chilling effect of the gas stream on deposited tube and on the rotating substrate keeps the surface region at a lower fraction liquid than the fraction liquid the spray.

The models were used to design experiments that were carried out at Drexel and at NSWC and to analyse other experiments previously carried out at NSWC. These experiments initially tested, and the results then confirmed, the idea that for a particular series of experiments, for example spray formed billets of Cu-Ti or spray formed tubes of IN 625, *a single parameter - the fraction liquid in the spray* - determined all the measured process and structural results of the deposition. These results included the Sticking Efficiency, the porosity and the solidification time. The last of these parameters, in turned, determined the as-cast grain size. The Sticking Efficiency of droplets to the tubes was also shown to be effected by the centrifugal effects of rotation speed. Within the conditions used, the sticking efficiency rose and the porosity fell with increased fraction liquid in the spray for the two systems studied. However the fraction liquid in the spray needed to give high yields and low porosities was significantly different in the two systems. This optimum fraction liquid in the spray was about 0.3 for *Cu-Ti Billets* but much higher, over 0.5, for *IN625 tubes*. Further experiments are being conducted to determine if the differences are alloy or geometry dependent. However, the thermal model results argue strongly for the dominant role of geometry. For billets, the fraction liquid on the deposit surface, under the spray quickly approaches the fraction liquid in the arriving spray. For tubes the fraction liquid on the deposit surface always falls below that of the arriving spray. If this early result can be confirmed experimentally and it can be confirmed by the numerical models, then the conclusion would be that either the only control parameter is *the fraction liquid on the deposit surface* or at least that this parameter is more important than the fraction liquid in the spray.

A major, separate, but related, investigation explored the reasons for the smaller than expected grain sizes in spray formed deposits. The initial prediction for the grain size came from modeled solidification times and the conventional dendrite arm spacing (grain size) / solidification time relationship for metallic alloys. The early work by Mathur et al. [2] giving predicted solidification times were largely confirmed by experimental measurements and subsequent studies by for example Grant et al.[4,5,22] showed similar results. In the present work a detailed experimental survey was carried out on the coarsening rate of solid - liquid mixtures under conditions similar to those in spray formed deposits. This is coarsening under the condition of high fraction solid and with commercial purity material. The results showed that, under these conditions, the rate of coarsening was significantly reduced below that reported for moderate fractions solid ($f_s \approx 0.5$) The result was found for, three spray cast alloys, aluminum alloy AA2014 (Al-Cu-Mg), Cu-Ti and IN625 and also for two conventionally cast aluminum alloys (chill cast Al-6%Cu and DC cast AA2024 (also Al-Cu-Mg). These alloys were all found to have a

second solid phase in addition to the primary solid phase and solute-rich liquid. Many earlier studies of high purity binary alloys (Fe-Cu, Co-Cu and Pb-Sn) had shown the opposite effect - an *acceleration* of coarsening at high fractions solid. Two new models for grain coarsening at high fractions solid were developed in this study which when applied to the data on high purity alloys matched, rather accurately, the observed acceleration of coarsening at high fraction solid. The acceleration essentially arises by reduced diffusion distances as $f_s \rightarrow 1$. The data on the spray formed and commercial purity alloys showed that the retardation of grain coarsening was therefor an *extrinsic* effect arising from grain boundary drag exerted by second phase particles. These particles may arise from impurities or trace alloy additions present in the alloy (Fe or TiB₂ in Al for example) or by nitrogen pick-up during nitrogen gas atomization leading to nitride formation for example TiN in Cu-Ti alloys. The observation of boundary pinning by particles provided a qualitative explanation for the fine grain sizes observed in spray formed deposits. However, in the one system studied so far in quantitative detail - Cu-Ti quantitative agreement was lacking. The observed coarsening rates were obtained in studies of spray formed samples cooled to room temperature before reheating into the solid liquid phase field. For Cu -Ti it appears that this lead to much larger reductions of coarsening rate, probably due to additional TiN precipitation in the solid state, than were seen in other systems. Quantitative testing is now being carried in the IN 625 system which does not appear to show the anomaly seen in the Cu-Ti system.

It seems to be confirmed that by use of numerical models of the process, Spray Forming can be rather well controlled. There is a continuing need for empirical data on PSD and RMF in different alloy systems and in different gas atomization systems. This will remain essential until a proper science base on gas atomization is eventually established. There is a need for final development and then critical evaluation of three dimensional thermal models of the deposits - particularly for non-billet geometries. Billet geometry is adequately characterised in the existing two dimensional thermal models. The non-billet geometries include the commercially important ones of tubes, coatings and thin sheets. With a good three dimensional thermal model, built on the successful three dimensional shape model, then numerical design studies should be readily performed to determine optimum deposition conditions for minimum porosity. Porosity results in regions of the deposit that are laid down too cold - that is with an insufficient fraction liquid. Finally, the current work on grain sizes in spray formed deposits needs to be completed to allow successful quantitative prediction of grain sizes based on observed coarsening rates in the spray formed microstructure. The need for grain size prediction comes not only from the intrinsic value in controlling the grain size, a length scale which in spray formed deposits is also the segregation scale, but from the potential to use the model to back-calculate from observed grain sizes in the deposit, the critical determinant of this parameter the fraction liquid in the spray - and in turn the determinant of the fraction liquid in the spray is the PSD. If this approach can be developed, and it seems reasonable that it could, then from the careful analysis of the grain size and its spatial variation in one or two spray deposition runs then the PSD should be capable of being back-calculated. Similarly from careful measurements of deposit shape, the MFR should also be calculable, by use of the existing three dimensional shape model. It would of course be necessary to confirm the validity of these back calculated parameters in carefully controlled evaluation studies.

If Spray Forming is to be applied in wider range of alloys and products then the modeling approach combined with carefully designed experiments as used here seems an important part of the technology base of the subject.

Contents

Introduction	p.1
I) Improved Model Inputs	p.2
Ia Particle Size Distributions	p.2
Ib Radial Variation of both the PSD and the Mass Flux	p.3
Ic Atomizing Gas Velocity Field	p.4
II) Modeling of Spray Forming	p.5
IIa. Droplet Collisions in Flight - A Model for Nucleation of Solidification in Gas Atomization.	p.6
IIb Three Dimensional Shape Modeling	p.13
IIc Thermal Modeling (Two and Three Dimensional)	p.16
III Experimental Investigations of Spray Forming	p.17
IIIa) Sticking Efficiency and the Nature of Material Failing to stick to the Deposit.	p.17
IIIb) Designed Experiments to test the Role of Fraction Liquid	p.20
IIIc) Spray Formed Shapes and the Sticking Efficiency E_s .	p.21
IIId) Temperatures in the Deposit - Use of the Thermal Models	p.22
IV Microstructural Development in Spray Forming	p.25
IVa) Grain Size in Spray Formed Deposits	p.25
IVa) Porosity. (Control by Fraction Liquid)	p.26
V. Inhibited Grain Coarsening at High Fractions Solid - Spray Forming and Commercial Alloys:	p.29
VI Current Investigations	p.32
VII Summary and Conclusions	p.33
References	p.35
Figure Captions	p.37
Tables	p.45
Figures	
Appendix A DU SHAPE	
Appendix B S. Annavarapu and R.D. Doherty: <i>Acta Mater. and Metall.</i> 43 (1995) 3207-3230.	

Introduction

The first ONR sponsored research investigation at Drexel University on Spray Forming under the direction of Professors Diran Apelian and Alan Lawley was reported to ONR by Mathur et al.[1] and the main research results were published by Mathur et al.[2] in the following year. This prior work established a basic numerical model for each of the successive stages of the spray forming process. These stages are:

- (i) Liquid atomization to give a liquid spray having a wide distribution of droplet sizes,
- (ii) Heat transfer to the gas stream and momentum transfer to the metal droplets,
- (iii) Consolidation of the partially solidified droplets on the substrate to form a deposit,
- (iv) Heat transfer to the gas from the deposit leading to its complete solidification.

The philosophy of the Drexel spray forming model was to use experimentally determined values for those needed parameters that could *not* be reliably modeled. An important example of a needed, experimentally-determined, parameter was the particle size distribution (PSD) in the spray. The model then used appropriate interpolated values of this and other empirical parameters to calculate numerically all other aspects of the process where reliable physics existed, for example the heat and momentum transfer between the gas stream and the droplets and the heat transfer from the deposit to the gas stream. The outputs of the model then characterised the thermal and physical properties of the material at each stage of the process. The output from the first stage in the process was used as the input for the second stage, and so on upto to the final stage of cooling and solidification of the deposit. The model was very successful in first establishing[1,2] what is now universally agreed to be the essential physical processes occurring in spray forming, see for example[3-5]. These essential processes are that successful spray forming requires that the *deposit surface remains partially molten during deposition* and that, as a result of this partially molten condition in the deposit, although solidification is very rapid in the spray during droplet flight, solidification goes to completion in the deposit *at much slower rates*, in some cases even approaching the final solidification rates seen in ingot solidification. Pravin et al.[2] also established a very important microstructural result that the grain size in the deposit was *significantly finer* (typically by a factor of about two) than would have been expected from use of the usual models of grain or segregate coarsening together with the theoretically predicted, and experimentally confirmed, times of solidification within the deposit.

There were two major objectives of the present study that followed from the initial study. First, the initial model and the empirical inputs to the model were to be revised and extended to generate *a more accurate model* for use in the operational control, and analysis, of spray forming processes. This aspect of the work was to be carried out in collaboration with the Spray Forming Group at David W. Taylor Naval Surface Warfare Center in Annapolis, which is under the direction of Dr. Ivan Caplan. The second objective was to investigate how the microstructure of the deposit, notably the amount and distribution of the small amount of porosity, found in all spray formed deposits, and the as-cast grain size of the deposit, could be initially scientifically understood and then subsequently predicted for the usual range of spray forming operating conditions.

The following report describes the work carried out and the results achieved under this project. The current principle investigator, Prof. Roger Doherty, who had not been previously involved with the first ONR project, was invited to join the current project at an early stage and he became the sole P.I. after the departure of Prof. Diran Apelian to become Provost of Worcester College in 1991.

I) Improved Model Inputs.

Ia Particle Size Distributions (PSD)

As initially reported at the First Spray Forming Conference, ICSF I in 1990[6] it was found early in the present study that the Particle Size Distributions (PSD) measured initially at Drexel University [1,2] were in error. The PSDs measured in a tall spray forming chamber, at Howmet Corporation in Michigan, in an early stage of this study, gave significantly finer mean particle sizes than had been previously measured in the small chamber at Drexel University under equivalent operating conditions. It seems likely that these differences arose from incomplete solidification of the larger sized droplets in the Drexel chamber before their impact on the chamber walls and floor. Such impact of large droplets on the chamber is likely to lead to fragmentation of the droplets and thus a decrease in the mean droplet size when measured using the solidified powder collected in the overspray chamber. Following this discovery, a series of spray forming runs were carried out at David Taylor Laboratory at NSWC, with the substrate removed, using an extended tower that increased, to 3m, the flight distance from atomiser to the floor of the chamber. Fig. 1 shows schematically the collection system used. Figs. 2-4 show the typical log-normal PSD found for the three alloys systems studied: IN 625, the alloy of current Navy interest for tube applications, the high strength low alloy steel (HSLA) then of interest to the Navy and Cu-6wt%Ti alloy, the Drexel model alloy used for fundamental studies of spray forming.

The mass median droplet diameter is plotted in fig. 5 as a function of the three major process variables: (i) The Superheat, which is the difference between pouring temperature, T_p , and the alloy liquidus temperature, T_m , (ii) The Gas / Metal Ratio, GMR, and (iii) The atomizing gas pressure, P. For comparison with the experimental results, also plotted are two of the earlier proposed empirical equations: those of Lubanska [9] and of Miller - Giles [10], together with the new correlation developed in the present study. This new correlation is given as eq.(1) and appears to match the data rather well. K_{NC} is an alloy and equipment dependent empirical parameter.

$$d_m = K_{NC} (1/P)^{0.5} (GMR)^{0.33} \exp (T_m / T_p) \quad (1)$$

Figs. 6-8 show the fitted values of the experimentally measured values of the PSDs for IN 625 and Cu-6wt%Ti. Fig.6 shows (a) the mass-median diameter, d_m , (in μm) and (b) the natural logarithm of the standard deviation in μm , $\ln \sigma$, as a function of atomizing gas pressure and the Gas/Metal Ratio for IN625 at a constant superheat of 120°C, for the usual log-normal distribution law, quoted subsequently as eq.6:

$$w(d) = \{ 1 / (\ln \sigma \sqrt{2\pi}) \} \exp \{ (\ln d - \ln d_m)^2 / 2 \ln^2 \sigma \}$$

In fig 7, the same results are given for Cu-6wt%Ti, while in fig.8 the same parameters are plotted against the superheat at a fixed Gas/Metal ratio of 0.89.

The results of these studies for the dependence on Pressure and GMR do appear to fit quite well with the current empirical data provided by Osprey Metals [11]. The empirical constant, K_{NC} , is expected to depend on the liquid metal density, the surface tension and the liquid metal viscosity at the pouring temperature but in the absence of reliable numbers for these variables no further analysis was attempted. Given the importance of the PSD for the spray forming process it would have been good to have continued these studies for a greater range of variables - for example to study the separate effects of the gas and metal flow rates and particularly to study a wider range of alloys. In the opinion of the

investigators at Drexel, establishing an extensive and reliable data base on the PSD of alloys of interest in Spray Forming will be of critical importance for reliable modeling of the process. It is also of importance for all forms of gas atomization for powder metallurgy. The acquisition of this data is hindered by the lack of the continued availability of the tall tower at NSWC used in the initial studies. Grant, in a recent review of spray forming[5], commented on the wide range of uncertainties of the current methods of attempting to *predict the mean particle size in gas atomization* and the lack of any prediction for the spread in size (the standard deviation) around the mean diameter in the critical first stage, gas atomization, of spray forming.

Ib Radial Variation of both the PSD and the Mass Flux (RMF)

The samples collected in separate rings of the collection system in fig.1 were used to determine the *radial variation* of the Particle Size Distribution and also the Radial variation of the Mass Flux (RMF) for the conditions used above to determine the average PSD. Fig.9 shows the PSD for Cu-6wt%Ti under conditions of total metal flow of 0.32kg/s, Gas / Metal ratio of 0.68 and metal superheat of 120°C. Log normal distributions gave reasonably good fit to the different radial collections and it can also be seen that the mass median particle diameter, d_m , falls at increasing radial distances. A similar result was found and reported [6] in the initial investigation carried out in collaboration with Howmet Corporation. It should be noted that the outer collection was for all droplets outside the third ring including the powders collected in the cyclone separator. The outer ring was arbitrarily assigned a mean radial distance of 60mm in figs. 10-12 which show the mass-median diameter, d_m , (in μm) and the natural logarithm of standard deviation, $\ln \sigma$, also in μm , for three of the runs. Cu-6wt%Ti and HSLA80 steel, figs. 10 and 11 show, as also seen in fig.9, a steady fall of the mean particle size with increasing radial distance. The standard deviation also falls steadily though showing a rise for the highest radius. For IN 625, in fig 12, the center of the spray, at zero radius, shows a smaller mass-median particle diameter than the next two rings but has the smallest standard deviation in the outer parts of the spray.

The Radial Mass Flux was determined by weighing the total powders collected in the inner three rings and the outer part (the chamber and the cyclone). The measured Mass flux was converted into a *deposition rate* in mm/s and then fitted to various empirical equations. The best equation was found to be[7,8]:

$$dD/dt = A \exp\{ -(r/B)^2 \} + C \quad (2)$$

A is a measure of the axial deposition rate, B determines the characteristic width of the distribution and C is a constant that appears to arise from powder recirculation and other effects. Fig. 13 (fig 3 of) [7] illustrates the influence of the main processing variables of atomizing gas pressure and metal flow rate on the three fitting parameters A, B and C for a superheat of 120°C and a spray height of 350mm. R_{\max} is the radial distance with the highest, area-weighted, deposition rate, D_A , eq.3.

$$D_A dR = (dD/dt) 2\pi R dR \quad (3)$$

The values presented are averages for the three alloys used, although there were minor variations between the alloys, Cu-6wt%Ti, HSLA80 and IN625. All three alloys have rather similar liquid densities. A back-propagation neural network regression was carried out on the experimental data [8] and the results shown in figs 14-16. Fig. 14 shows the fitted curves for the parameters A and B for IN 625 at a constant superheat of 120°C. Fig.

15 shows the fit for Cu-6wt% Ti at a constant metal flow rate of 0.24kg/s. Fig.16 shows the linear increase of the background deposition rate, the parameter C, with the metal flow rate for all three alloys. A, the axial deposition rate, rises rapidly with metal flow rate and more slowly with increasing gas pressure. B, however, falls with increasing gas pressure - that is a higher atomizing gas pressure keeps the particle distribution focussed towards the axis. B, a measure of the spreading is almost unaffected by changes in the *metal* flow rate.

Ic Atomizing Gas Velocity Field (in the absence of a metal stream)

The gas velocity and its variation with position in the chamber and with nitrogen atomizing gas pressure were carefully measured in the Osprey chamber at Drexel University using a pitot tube method[12-13]. These measurements were made for a single phase gas jet without any accelerating droplets in the gas stream. During a real atomization process there is a very significant momentum/ kinetic energy transfer from the atomizing gas to the stream of liquid metal. The gas kinetic energy atomizes the liquid stream to droplets and accelerates the resulting droplets. *So the gas velocities in a spray forming experiment will fall faster in a real spray forming run than the results reported here in the absence of liquid metal stream.* This effect is however computed in the spray model. The ends of the pitot-static tube were connected to a digital pressure indicator through a differential pressure transducer. A standard Pitot-tube (5/16" with a hemispherical tip) with a tip coefficient of 1.0 was used. In accordance with BS 1042[14] the pitot tube was fixed rigidly to the chamber side walls to minimized vibration errors. The vertical alignment of the stagnation tube was set by a plumb-line from the metal nozzle for each measurement. The sampling interval was about 20s. The low and mean high of the supply pressure and thus the pressure differential were each measured. The temperature during these studies was about 85°F (30°C) which was within the calibration range (10 - 50°C) of the transducer and indicator. A typical range of reading was 0.06psi (v of 70m/s) at the periphery of the jet to 9.0psi at the axis (v of 330m/s).

Measurements were carried out at the following *axial* distances from the atomizer, x = 70, 125, 200 300 and 400mm and at a range of *radial* distances, 0, 6, 12.5. 18.8 and 25mm from the axis of an atomizing ring diameter of 1.5" (39mm). These measurements were made in the absence of a substrate. In addition, the velocities of the gas stream parallel to a tilted substrate, used for billet solidification placed at the usual spray height of 350mm, were also measured. The gas velocities adjacent to the deposit on the substrate are of critical importance for estimation of the heat transfer from the solidifying deposits to the passing gas. All the gas velocities, (v) were determined from the differential pressure using eq. 4 for the compressible transonic gas flow over a Pitot-tube[15]:

$$v = [2\gamma / (\gamma - 1)]^{1/2} \{ (P_o / \rho_o) [(P_s/P_o)^{(\gamma-1)/\gamma} - 1] \}^{1/2} \quad (4)$$

Where: P_s is the stagnation point pressure
 P_o is the supply gas pressure
 ρ_o is the a density of the nitrogen gas at P_o
 γ is the specific heat ratio, $C_p / C_v = 1.4$, for the diatomic nitrogen gas.

Fig.17 shows the fall of the measured gas velocity along the axis of the gas jet with axial flight distance, x, for atomizing gas pressures of 4 to 9bar. For the choked flow conditions in the nozzle the exit velocity is close to to sonic velocity (mach1) of 354m/s for the pressures used. The highest velocities seen at 70mm were 287-337m/s for atomizing

gas pressures of 4 to 9 bar and by about 125mm the jet appears to be fully "mixed" after which the velocity falls almost linearly with distance reaching 155 to 180m/s at a flight distance of 400mm.

The radial variation in velocity is seen in figs. 18 and 19. In fig 18(a) to (e) the gas velocity normalized to the axial velocity is plotted as a function of the atomized normalised radius r / d_s (where d_s was the atomizing ring diameter of 39mm) at increasing axial distances. The radius of the jet, R_{jet} or $r_{0.5}$, defined as the radius where the velocity has fallen to 0.5 of the axial velocity is indicated on each plot. The radius of the jet expanded to about 25 mm at a flight distance of 400mm. The results for the range of atomizing gas pressures appear to superimpose indicating a lack of effect of atomizing gas pressure on the radial spreading of the jet. The data of fig.18 are replotted in fig. 19 using the jet normalized radius $r/r_{0.5}$ (R/R_{jet}) at the increasing axial distances of 70 to 400mm. The Osprey reported plot is also shown and it is seen that the Osprey result is approached at the longer flight distances but, at shorter flight distances, the radial gas velocity falls off more slowly at small radii, $r/r_{0.5} < 1$. At larger radii, however, especially at the shorter flight distances, (see series 1 at 70mm) the axial velocity falls faster than reported by Osprey.

The increase of the jet radius, R_{jet} , where the velocity has fallen to 50% of the axial velocity, is seen in fig 20 to increase slowly during the "jet mixing" region, out to a flight distance of 125 mm, but then the jet radius then expands almost linearly with further flight distance in the region, see fig. 17, where the axial velocity was falling almost linearly with distance. The radius of the gas nozzle ($d_s/2$ of 19.5 mm) is indicated as the jet radius at the nozzle - that is at the flight distance of zero.

Fig. 21 replots the data of fig 17 against the axial distance, here normalized against the nozzle diameter for comparison with other reported data including that provided by Osprey - the Osprey results were used in the earlier analysis [1,2]. The modification for the predicted cooling effect of the faster gas flow field, now measured, on the droplets in flight was, perhaps surprisingly, found not to be very significant. This lack of significant additional cooling appears to arise since the resulting higher rate of heat transfer was largely matched by the decreasing flight time, and thus cooling time, of the droplets. As a result, the thermal results previously reported [1,2] were not greatly modified by the more accurate data on the gas flow field now available. However the higher gas velocities at a tilted substrate measured in fig. 22 as 167 to 188m/s are significantly higher than previously assumed [1,2] As a result the calculated heat transfer coefficient at the deposit at the substrate distance are significantly increased from 700-1000 $W.m^{-2}.K^{-1}$, compared to the previously estimated values of 500 $W.m^{-2}.K^{-1}$. The velocities close to the tilted substrate at 350mm flight distance, 167 to 188m/s, are significantly smaller than the axial gas velocities of 177 to 208m/s at the same flight distance measured *in the absence of a substrate*, fig.17.

These new and revised experimental data were all incorporated into the existing Drexel Model of spray forming and used in subsequent pre-planing and post spray analysis of all experimental spray forming runs carried out. Further developments of this model are described in the next section.

II) Modeling of Spray Forming

As part of this study Cai [8] reviewed the models for this process starting from the original Drexel Model developed by Mathur et al. [2] and its later development, [6, 7, 17] together with the models of Lavernia et al. [18-21], Grant et al.[4,22] and others [23-26]. All of

these models, although having different levels of sophistication, are basically very similar and give rather, one is glad to note, very similar predictions.

As first recognized and modeled by Mathur et al.[2] the spray on reaching the deposit in successful spray forming has a distribution of droplet sizes. The different droplet sizes have *with very different enthalpy contents*. Small particles are cold and will be fully solid before impact. Many of these very small droplets however may not penetrate the boundary layer of high velocity gas passing the substrate and so will then be swept past the deposit and end up in the overspray powder (see Section IIIi - Experimental Investigations). The largest particles are much hotter and will be fully liquid, while medium sized particles, which make up the largest *weight fraction* of the spray, have an intermediate enthalpy and will be, at impact, partially liquid and partially solid. The solid will have the fragile fine dendritic morphology easily deformed by high velocity impact [3]. After deposition on the deposit, the high density of droplets found in the usually very high deposition rates of spray forming (kg/s) are expected to equilibrate rapidly and quickly achieve a weighted average of enthalpy [2]. The computed enthalpy is more easily visualized as a mean temperature or even more conceptually useful, as a mean *fraction liquid* of the spray.

Fig. 23 from Grant et al.[4] shows how the predicted solid fraction in a spray of Al-4wt% Cu rises with spray distance, with increasing axial gas velocity and thus gas pressure, with lower metal flow rates and with lower melt superheats. Fig. 24 shows that the computed temperature of the top surface of the deposit matches the experimentally measured values as the time of deposition increases upto and in one case beyond the end of the deposition. This agreement is similar to that initially found by Mathur et al. [1,2] using higher temperature alloys in actual Osprey Equipment. The results from Grant et al.[4] are quoted here since the Drexel equipment was not capable of measuring temperatures in the deposits of the form used in this study - rapidly rotating billets and tubes. In the current on going investigation (1995-6) a modified substrate is being used to measure temperatures in the deposits.

Given the success of the original Drexel model developed by Mathur et al [2], in the present study many parts of the existing Drexel Model developed previously have been maintained notably the models of heat and momentum transfer in the spray. However the improved input parameters, the measurement of which was described above, were incorporated into the model. Several significant extensions to the model have been produced, however, and these are described below:

IIa. Droplet Collisions in Flight - A Model for Nucleation of Solidification in Gas Atomization.

Introduction. The modeling results [2] have shown that the velocity and temperature of atomized droplets in flight are strongly dependent on their size, see for example fig.25. Small droplets are more rapidly accelerated by the gas jet and they cool faster than large droplets within the spray cone. Thus, at a given flight distance, droplets of different sizes exhibit different states of solidification, namely fully liquid, partially solid (mushy) or fully solid. The largest droplet size d^* that is fully solid at a given flight distance had been previously predicted [2] assuming two extreme conditions respectively: (i) No undercooling (i.e. perfectly efficient heterogeneous nucleation) and (ii) Complete or maximum undercooling (the undercooling predicted for homogeneous nucleation). Also, the variation of d^* with flight distance has been measured experimentally for three alloys (Ni-20wt%Cr, Fe-20wt%Mn and AISI 1026) using glass slides to intercept the droplets in flight [1,27], and from these results back calculating the degree of undercooling, f_u , for droplets of different sizes, from the model of droplet temperature in flight. f_u is defined as

the ratio of the actual undercooling, ΔT , to the critical undercooling, ΔT_c , required for homogeneous nucleation, i.e.

$$f_u = \Delta T / \Delta T_c \quad (5)$$

The experimental results had shown that f_u decreases exponentially with droplet volume and this trend does not appear to vary with the properties of the alloys investigated, Fig. 26. Thus, very small droplets ($<50 \mu\text{m}$) experience significant undercooling prior to nucleation while large droplets ($>150 \mu\text{m}$) experience very small undercooling.

Microscopic observations made in the present investigation, show the surface morphology of the powders collected after gas atomization, Fig. 27. It was found that most of particles have some satellites attached to their surface, and the bigger the particle the larger the number of satellites. Irregularities in shape were also observed in a few particularly large particles. Fig. 28 is a micrograph showing the cross-sections of particles. It can be seen that a small spherical particle is embedded in a large spherical particle with dendrites *radiating outwards from the small particle*. The scale of the dendritic structure of the small sphere is *somewhat finer* than that of the larger one. Thus, it can be concluded (i) that the small droplet had pre-solidified, early in flight before colliding with the large droplet, and (ii) that this collision event has apparently initiated heterogeneous nucleation of the larger droplet. The above results support the hypotheses: (i) that droplets do interact with each other through collisions in flight, particularly in the dense spray, (ii) that such collisions most likely occur between droplets of various sizes with different velocities, fig 25, and states of solidification, and (iii) That large undercooled liquid droplets should be heterogeneously nucleated by collision in flight with small, solid-containing, droplets. It is well established, see for example Feest et al. [28], that contact between an undercooled melt and a solid particle of the same, copper - nickel, alloy always lead to nucleation of the melt. It would be of great interest to see if this idea works equally for aluminum atomization despite the coherent thin oxide layer always expected on aluminum. The Drexel apparatus however lacks the necessary safety features for aluminum atomization.

Since nucleation in the droplets may also be caused by any pre-existing catalytic particles, there is a need to consider the controlling origin of nucleation. The classical experiments by Turnbull and coworkers [29] on homogeneous nucleation overcame this problem by dividing the liquid mass of pure metals into many small droplets with an emulsifying agent; only a few droplets contained impurities and the majority were not subjected to any catalytic effect. It was found that small liquid droplets can undercool significantly below their equilibrium melting temperature (by about $0.18T_m$) which is very large compared to what is possible in ingot casting. A careful analysis by Cantor and Doherty [30] on later experiments[31] has concluded that Turnbull's experiments did not show true homogeneous nucleation, presumably since the emulsifying agents were not completely inert, and a higher undercoolings ($0.3T_m$) have been reported later by others [32]. Similarly, inert gas atomization also produces a large number of small droplets, and any pre-existing catalytic particles will be isolated in a finite number of droplets, leaving the others free to cool to a lower temperature before solidification begins. Following the hypotheses proposed above, it was proposed that collision-induced heterogeneous nucleation might explain the above relationship between the degree of undercooling and the droplet size because the droplet collisions are phenomena essential to the Osprey process. Though the specific issue of the physics of droplet collisions has not yet received detailed attention, the hypotheses was tested numerically by extending the previous model to include droplet collisions.

The Model

Model Assumptions

The collision model was established based on the previous model of droplet/gas interactions[2]. The governing equations of momentum and heat transfer during the droplet/gas interactions remain unchanged. Here, specific attention was given to droplet/droplet interactions, i.e. the collisions in flight.

To simplify the calculation, several assumptions were made about the initial droplet conditions. In general, gas atomization involves a wave instability of the melt stream, ligament formation, ligament break-down into droplets and spheroidization of the droplets [33-37]. Although the disintegration process may continue to occur during flight in the spray, according to some observations [38] atomization in the Osprey process is complete essentially in a few microseconds, which is about the droplet spheroidization time [39]. Thus, droplets are expected to travel not more than a few millimeters before spheroidizing while solidification is expected to occur later in flight. Indeed, a majority of the solidified droplets collected are always found to be spherical (Fig. 27). In comparison to the time of flight and solidification of the droplets (1 to 100 milliseconds), the initial spheroidization stage can be neglected, and individual droplets are treated as spheres. The effects of gas turbulence and circulation are also ignored so that droplets were assumed to travel in linear trajectories within the spray cone. The initial droplet size and mass distributions are undetermined unless *in-situ* measuring techniques are used [40]. To overcome this problem, the final distribution of particles collected after solidification in flight was used for the input parameters of the initial PSD. The starting expectation had been that collisions would significantly modify the PSD and that a series of iterations would then be needed to establish the initial PSD that gave rise after collisions to the final measured PSD. As shown below this correction was found not to be necessary. Both the size and mass distributions of the droplets for the annular Osprey atomizers are approximated as Gaussian on a log-normal plot.

Given the random nature of gas atomization, the initial diameter, location and time of individual droplets to be introduced at the top of spray cone must be determined statistically in order to satisfy both the size and mass distributions. The mass probability density function of a droplet with diameter d is given by eq. 6:

$$w(d) = \{1/\ln \sigma \sqrt{2\pi}\} \exp \{ (\ln d - \ln d_m)^2 / (2\ln^2 \sigma) \} \quad (6)$$

where d_m is the mass-median diameter and σ is the standard deviation. In this study it was shown by Cai [8] that the number probability density function of a droplet with diameter d is given by a similar expression:

$$w(d) = \{1/\ln \sigma \sqrt{2\pi}\} \exp \{ (\ln d - \ln d_n)^2 / (2\ln^2 \sigma) \} \quad (7)$$

where d_n is the number-median diameter, which in turn is related to d_m by:

$$d_n = d_m \sigma (-3 \ln \sigma) \quad (8)$$

Knowing the droplet number distribution, the number flow rate of a droplet with diameter d can be calculated from the following equation:

$$\dot{n}(d) = \dot{N} n(d) \quad (9)$$

where \dot{N} is the total number of droplets formed by gas atomization per unit time. Also, \dot{N} is related to the melt mass flow rate \dot{M}_m by:

$$\dot{N} = 6 \dot{M}_m / \{ \pi \rho_m (d_m d_n)^{3/2} \} \quad (10)$$

where ρ_m is the melt density. Thus, when each droplet enters successively into the spray, its initial diameter can be determined statistically by solving the following equations:

$$d = J^{-1}(R) \quad (11)$$

$$\text{and} \quad J(d) = \int_0^{d_{\max}} n(d) d \ln d \quad (12)$$

where R is the uniform random function with a range from 0 to 1, and J^{-1} is the inverse function of J . Similarly, the initial radius of each droplet can be selected randomly using the equations:

$$r = K^{-1}(R) \quad (13)$$

and

$$K(r) = \{ 2\pi \int_0^{r_0} \dot{M}(r) r dr \} / \dot{M}_m \quad (14)$$

where r_0 is the radius of the spray cone and $\dot{M}(r)$ is the radial mass distribution function both at a given flight distance. Also, the circumferential coordinate ϕ of each droplet is calculated by:

$$\phi = 2\pi R \quad (15)$$

Finally, the time moment for each droplet to enter into the spray is assumed to be:

$$\tau = \dot{N} \Delta t R \quad (16)$$

where Δt is the time step size for updating calculations. Note that this approach meets only the requirement for overall size and mass distributions because data on their local distributions are not available.

Another assumption is related to the calculation of the critical undercooling for homogeneous nucleation ΔT_c . In the previous model [2], ΔT_c was given by the standard equation[41]:

$$\{\Delta T_c / T_m\}^2 = 16 \pi \gamma_{sl}^3 / \{3 \Delta H_f^2 k T \ln(N)\} \quad (12)$$

where γ_{sl} is the solid-liquid interfacial energy, ΔH_f the latent heat of fusion, k Boltzmann's constant, and N the number of atoms in the droplet and so a function of droplet diameter. In the absence of data on the solid-liquid interfacial energy, γ_{sl} can be estimated by assuming that the reported values of maximum undercooling in the material were obtained

under conditions at or near homogeneous nucleation [32]. For example, a $20\mu\text{m}$ droplet with an undercooling of $0.3 T_m$ was assumed as the base for calculation of ΔT_c .

2. Rules of Collision

In the collision model, the spray is represented by a large number of spherical droplets. Current implementation models approximately 0.5 to 1 million droplets due to the limitations on the involved computer time and physical details. The spatial location, velocity and temperature of each droplet were calculated and stored in the computer (IBM 9121 mainframe) after each time interval. Thus, the occurrence of an intersection between the trajectories of any two droplets was recorded for a possible collision. The droplet collisions were calculated as three-dimensional events in the spray cone, but the model also took advantage of symmetries in the spray to reduce the magnitude of the computation. The collision events are always unsteady in the beginning, but finally they reach a steady state.

One of the critical steps in the analysis was the establishment of rules for the outcome of a collision based on the size and extent of solidification of the two droplets which collide with each other. Rules for collision between droplets of different states are illustrated in Fig. 29 and described below:

- (i) Any pair of particles are considered to have collided within a time step in which the shortest distance between their linear trajectories for the step is smaller than the sum of their radii.
- (ii) Collision between two pre-solidified droplets is ignored.
- (iii) Impact of a small solid particle with a larger *undercooled* liquid droplet always nucleates solidification of the large particle.
- (iv) Impact of a smaller droplet, either solid or liquid, hitting a larger droplet which is liquid, always leads to coalescence of the two droplets.
- (v) If any capture occurs, irrespective of it causing nucleation or not, the pair of colliding particles coalesce instantly to form a new larger spherical droplet which continues to fly in the spray. The new size, velocity and temperature are calculated assuming mass, momentum and enthalpy conservation.

The problem of overcounting or undercounting collision events was taken care of by rule (i), properly choosing the size of the time step and droplet tracing algorithm. The algorithm recorded all collision events of the individual droplet to take into account ternary or multiple collisions in the dense spray. Clearly, these rules are simplistic because there is, at present, no physical model that can treat effectively the complex issues of droplet collisions at a macroscopic level, and it is still not affordable to simulate the microscale details of collision for all droplets in the spray. A collision between two liquid droplets might, in fact, cause break-up into several finer droplets; but this possibility was ignored, however, in the present model because of the lack of a proper physical understanding of what might cause this to occur. Rule (iv) which corresponds to a maximum "coarsening" was intended to study the possible maximum effect of collisions on the droplet size distribution.

Results and Conclusions of the Collision Model:

Analysis using Eq. (10) predicts that a large number of droplets are created per unit time during gas atomization, typically $10^8/\text{s}$, assuming a metal flow rate of 0.2kg/s , a droplet mean diameter of $150\mu\text{m}$, a standard deviation of 2.1 and a density of 8000kg/m^3 for the metal. Calculations show that most of the collisions take place within the first 50mm of flight where the spray is still narrow and retains a high droplet density. The average rate of collision events, absorption events through coalescence with nucleation and without

nucleation, and nucleation events attributed to the impact of a solid on an undercooled liquid in the spray is plotted against time in Figs.30-32. The rate curves become asymptotic after an initial transition period of about 150ms, indicating stability not withstanding random scattering. The number of droplets in the spray with time was found to vary around its average value about 5×10^5 by $\pm 10\%$.

The model found that about 38% of the droplets created during atomization resulted from absorption coalescence while the remaining, 62%, droplets were unchanged before reaching the substrate. For all the collisions, 57% occurred between solid particles leading to no absorption, 43% lead to absorption but only 18% of all the collisions caused nucleation following coalescence, using the rules assumed above. A scatter plot of the degree of undercooling is shown in fig. 33 as a function of droplet diameter. The large range of scatter comes from the statistical nature of the simulation which is likely to have some connection with the statistical nature of real gas atomization. Mean values of the scatter are plotted in fig.34 which also includes the previous experimental data [2]. In agreement with the previous experiment, the model shows that undercooling in droplets larger than about $50\mu\text{m}$ is reduced very significantly by heterogeneous nucleation via droplet collisions. Both the initially input distribution and that modified by collision are given in fig. 35. The model predicts only a slight skewing of the size distribution toward larger sizes. That is, the collisions do not significantly change the size distribution. The size distribution input into the model was that finally measured - and would have been modified by collisions. As noted above, it was initially assumed that the model would have to be rerun iteratively to correct for the collision-induced modification to the PSD but the small change in the particle size distribution (mass weighted) indicated that this modification would not significantly alter the undercooling conclusions of the collision model.

The model clearly shows that the collisions have almost no effect on the undercooling of very small droplets ($<20\mu\text{m}$). This is expected because of the fast cooling leading to near homogeneous nucleation. For very large droplets ($>250\mu\text{m}$), the degrees of undercooling are also not significantly dependent on the collisions because of their slow cooling and relatively large heat content that must be removed before they reach a undercooled state during flight. However, the predicted undercooling of medium droplets does vary significantly dependent on their sizes and collision history. Indeed, by comparing the particles of similar sizes collected on glass slides [2], it had been observed that only the medium diameter particles ($50\text{-}200\mu\text{m}$) exhibit a wide range of states indicating their experience of different nucleation conditions.

The results reveal that the majority of the collisions are caused by small particles with diameters around d_n hitting large particles with diameters around d_m . Note that d_n is $29\mu\text{m}$ if d_m is $150\mu\text{m}$ for a standard deviation, $\ln \sigma$, of 2.1 according to Eq. (8). This can be explained by the fact that the number of collision events is dependent mainly on the droplet population in the spray. The small particles with diameters close to d_n dominate the population and thus dominate the collisions. On the other hand, particles with diameters close to d_m dominate the mass. Thus, even when maximum coalescence occurs, the size distribution *by mass* is not affected significantly as shown by the model prediction in Fig. 35. This result suggests that downstream particle size measurements can be used in the spray solidification model with confidence because the mean droplet size in the Osprey process is typically $100\text{-}200\mu\text{m}$. However, gas atomization for making fine particles $<40\mu\text{m}$, coalescence or agglomeration via impact could become very significant. The results generated here for spray deposition of course apply equally to the gas atomization

used in general powder metallurgy. For gas atomization the results found here should have very great significance for the microstructure of gas atomized powders - powders nucleating with high undercooling will solidify very rapidly while those nucleating at smaller undercoolings, the majority of the mass of the material, will have much slower solidification rates. In spray forming the fine powders that impact the partially molten deposit will be partially remelted and their very fine microstructures will be lost. (For a consideration of this see section IV, Microstructural Development in Spray Forming below)

Conclusion of the Collision model

A computer model of random collisions between flying droplets formed by gas atomization in the spray deposition process accounts adequately for our previous experiments that small droplets become fully solid prior to substrate impact while large droplets remain partially liquid and that, critically, small pre-solidified particles can nucleate large undercooled liquid droplets by impact with each other during flight in the spray. Droplet collisions will terminate the undercooling of large droplets prior to homogeneous nucleation and induce heterogeneous nucleation. For medium-sized droplets, the degree of undercooling is reduced very significantly by early nucleation caused by the collisions. The degree of undercooling decreases exponentially with the droplet size, matching the previous observations. In addition, droplet collisions in the region of the spray beyond that of atomization (the region modeled here) have only a secondary effect on the final PSD.

IIb Three Dimensional Shape Modeling

i) Preform Geometry.

i.i) Representation of the Deposit.

The geometry of the solid preform was defined by two bounding surfaces - the inner surface that between the substrate and the deposit and the outer surface growing under the spray, the latter determined by the local growth velocity. It was necessary to develop a geometric representation of the substrate and preform surfaces and their movement in a 3-D coordinate system. Multiple coordinate systems were required to define uniquely all the moving elements - the sprays, the preform and the substrate.

For the numerical calculation all surfaces were discretized into a finite number of small elements, fig. 36. All elements were connected to each other at their edges and nodes. Any location or point \mathbf{p} of an element was expressed in terms of two parameters u, v as:

$$\mathbf{p} = \mathbf{p}(u, v) \quad (13)$$

It was necessary to distinguish surface *growth* from deposit *motion* by using both a local coordinate system and a reference coordinate system. Growth is given by the change in the coordinates of the point \mathbf{p} defined in the *local* coordinate system while motion is given by a change of the local coordinate system itself defined in the reference coordinate system.

i.ii) Local Normal Growth Rate (LNGR)

The growth rate of the deposit is determined by several process variables. These are:

a) The Mass Flux distribution - the mass sprayed per unit time in unit area at a given location. This was determined from the empirically measured RMF (section Ib) as \dot{D} in units of m/s.

b) The sticking efficiency (SE or E_s) which is the ratio of the mass added to the deposit to the mass in the spray that *actually hits* the deposit, or more precisely is on a linear path that extrapolates to the deposit. Some failure to stick may arise from very small particles being swept away by the gas stream deflected by the substrate. An overall value of SE was assumed to apply to the deposit depending on the conditions of the spray (deposit type, alloy and fraction liquid) and SE/E_s was determined *empirically* from the shape/size predictions of the model compared to the experimentally observed shape/size. The physical factors that determine SE are not at present known. The empirical determination of the SE using the shape model was a major objective of the present work. Once SE were established for a given alloy then the shape model should be able to predict rather reliably future shape effects under different conditions.

c) The substrate motion which determines the velocity of a point \mathbf{p} .

d) The shadow factor, f_{shadow} , accounts for the absence of deposition at locations in the shadow of the deposit, i.e. out of sight of the source of origin of the spray. f_{shadow} was determined from the geometry of the deposit and the mass flux direction. f_{shadow} is zero when the point \mathbf{p} is in the shadow otherwise f_{shadow} was one.

e) The incident angle between the mass flux direction and the surface normal \mathbf{n} at the point \mathbf{p} determines the normal component of the mass flux.

f) Account was also taken of the fact that more mass is captured if the deposit is moving towards the spray than away from the spray. This velocity effect was combined with the effect of the angle of impact by the total angle factor f_{angle} which is given, as a linear approximation, as:

$$f_{\text{angle}} = \{ (\mathbf{v} - \bar{\mathbf{v}}_{\text{spray}}) / |\bar{\mathbf{v}}_{\text{spray}}| \} \cdot \mathbf{n} \quad (14)$$

By combining all these factors the local normal growth rate \dot{G}_n at a point \mathbf{p} is given by:

$$\dot{G}_n = \dot{D} E_s f_{\text{shadow}} f_{\text{angle}} / E_c \quad (15)$$

E_c is the consolidation factor defined as the ratio of the apparent density ρ at a point \mathbf{p} to the theoretical density of the alloy ρ_{th} . E_c is also given in terms of the porosity ψ at the same point as:

$$E_c = 1 - \psi \quad (16)$$

From a knowledge of the local normal growth rate, \dot{G}_n , at each time step Δt , allows a determination of the displacement of the point \mathbf{p} due to growth as:

$$\Delta \mathbf{p} = (\dot{G}_n \cdot \mathbf{n}) \Delta t \quad (17)$$

Since all the variables used in Eq.17 are functions of time, numerical integration of this equation is obviously required.

iii) Deposition Yield and Target Efficiency

Deposition Yield, Y , is critically important to the commercial success of spray forming and is defined as the ratio of the mass of the deposit to the mass sprayed. Y is readily predicted using the approach of (ii) above.

$$Y = E_{ot} E_s \quad (18)$$

E_s is the sticking efficiency to be determined while E_{ot} is the *target* efficiency - the ratio of the mass of the spray that hits the substrate and the deposit to the total mass sprayed. Only droplets that actually hit the substrate and the deposit will have the possibility of becoming part of the spray formed object. E_{ot} can be predicted directly using the fully developed spray model.

iv) Multiple and moving sprays.

The effect of multiple sprays was easily handled by summation of the local growth rates from all the individual sprays:

$$\dot{G}_n = \sum \dot{G}_{ni} \quad (19)$$

The most common example of a moving spray is the scanning atomizer. The effect of this was included by making the coordinate system oscillate at the given frequency and amplitude. This method is an oversimplification since it ignores possible increased gas turbulence in the scanning gas stream.

v) Computational method.

The numerical approach used computed the deposit geometry at each node of the emeshed surface during the deposition. Values of the time step were calculated based on the required stability of the updated Lagrange scheme used and were typically 1-10 milli-seconds. As the geometry changes during deposition, the mesh used can become coarse and distorted. A remeshing technique was therefore employed to overcome this difficulty. The problem of the shadow effect was solved using a modified "hidden surface" computer algorithm [42]. In the algorithm, for each time step, if the normal displacement Δp for a point p was greater than zero then a search procedure for every suspect patch was activated to examine if the point p was in the shadow of the suspect patch. This was done by locating the intersection between the suspect patch and the incident line from the spray origin to p . If this intersection lay inside the deposit then the point P was in the shadow of the suspect patch and f_{shadow} was set at 0.

An operating software package based on this three dimensional shape model - "DU SHAPE" was developed and provided to the Naval Surface Warfare Center, Caderock Division for their evaluation and use. A copy of the operating notes of this package is provided as Appendix A of this report.

vi) Results of the Shape Model.

The major results of the Shape model will be described and discussed in section IV of this report "Experimental Investigations of Spray Forming", in which a major result of the analysis of the experiments in the light of the model was the determination of the sticking efficiency for a range of experimental situations. However one set of results based on the shape model, that so far, is without experimental comparison can be given here to illustrate the power of the model. In addition a *motion planner module* was developed by Dr Cheng Cai as part of this project in collaboration with NSWC and MTS Systems Inc to compute the time dependent motions of the MTS designed robot manipulator used at NSWC with its five axes of motion. The shape model was implemented to follow the instructions of the motion planner using the assumption of rigid body motion. The simulation was accomplished by decomposing any complex motion into two simple components: rotation and translation.

Some Results from the Shape Model

The first example is rather simple. Fig. 38 shows a calculated thickness profile formed in a sheet with a linear atomizer with an assumed mass distribution with a maximum deposition rate of 4mm/s and characteristic widths of 30 and 90mm in the x and y directions and a substrate withdrawal rate of 3mm/s in the x direction for a total deposition time of 80 seconds. The predicted uniformity of the sheet is of course merely a result of the *assumed uniformity* of the mass distribution along the linear atomizer.

A much more meaningful example of the power of the Drexel Shape model is shown in the following three figures. Fig. 39 shows the prediction for a spray formed tube, deposited onto a substrate with segments of varying diameter. Deposition required continuous adjustment of the withdrawal rate in order to try to produce desired wall thicknesses in the tube. This example nicely illustrates the use of the model for planning

the motion of a run to produce a desired result, since a nearly uniform wall thickness n only be produced in such a tube by correct control of the withdrawal rate. A more complex problem was the attempt to design a process for spraying *a curved tube*, that is an elbow, by means of the rotation about the longitudinal axis of the elbow, fig. 40, the direction normal to the diagram. It can be seen that this motion plan produced a tube of non constant wall thickness despite the constant spray height. The variation of the wall thickness arose from the difference of *scan length on the inside and outside* of the elbow. As a result of this prediction an alternative scheme was designed and studied, fig. 41, in which simultaneous axial and perpendicular to axial translations were used to replace the rotation about the longitudinal axis of the elbow. This strategy gave a uniform wall thickness but with tube ends that were not perpendicular to the *tube* axis and would need to be cropped. To make a 45° bend a 50° angle would have to be sprayed.

IIc Thermal Modeling (Two and Three Dimensional)

i) Thermal Model of the Spray.

The thermal model of heat and momentum transfer in the spray developed by Mathur et al.[1,2] was maintained essentially unchanged except for modification of the input parameters as described in section I. The measured nucleation behavior was unchanged by the collision model other than allowing predicted rather than empirical undercoolings for the systems studied. The spray model, predicts the enthalpy of droplets of different sizes and then, using the mass based particle size distribution, averages the enthalpy of the whole spray at the moment of impact, fig.42. From this enthalpy value, the fraction liquid in the spray is determined assuming thermal equilibration between the droplets in the spray. If the deposit is continuously under the spray then the spray enthalpy will also be the enthalpy and fraction liquid of the deposit surface - at least in the steady state after the chilling effect of the initial substrate becomes insignificant. The deposit surface will have a lower enthalpy than the spray enthalpy at the start of the deposition before the substrate has been heated by the arriving partially molten spray. In addition, if the substrate is rotated or oscillated under the spray such that the surface moves into and out of the spray path - for example in the spraying of tubes - then even after the near steady state is achieved in the average enthalpy and fraction liquid of the surface, this enthalpy and fraction liquid will oscillate as the surface moves under and out of the spray and *the surface fraction liquid will be less than that of the spray.*

ii) Thermal model of the deposit.

The initial one-Dimensional analysis developed by Mathur et al.[1,2] was modified in this project (by Mathur himself) to a two dimensional model and the further extension to a true three dimensional thermal model is being developed by Dr. Cai both in the project being reported and in the continuation of the project in 1995-6. The early one and two dimensional thermal models were based on a simple finite difference scheme with a cylindrical billet growing under the spray and a simple thermal model of conductivity within the deposit and heat transfer to the high velocity gas at the top and side surfaces of the deposit and heat transfer to the substrate. For billets deposited onto insulating substrates the heat loss to the substrate was, apart from the initial stage of deposition, found to be negligible. As reported [7] at the Second International Conference on Spray forming in 1993 there was a significant increase of the predicted cooling rate on going to a two dimensional model since there was significant heat loss to the sides of the deposit - an effect not modeled in the early work [1,2]. The faster cooling rate predicted in the two dimensional model was largely offset in the predictions of total solidification time quoted by Mathur et al. [2] by the influence in the present study of a PSD with a larger mean size

than had been initially measured and modeled [1,2]. The balancing of two effects, or rather two errors, is a significant reminder that the successful prediction of a result by a model need not mean that the models is correct !

Improved Thermal Modelling of the Deposit (Two and Three Dimensions)

As described in detail by Cai[8], the evolving three dimensional shape modeled by the shape model will allow the potential of coupling of the shape model to a full three dimensional *thermal model of the deposit and the substrate*. As the deposit grows, metal with the enthalpy of the spray is added to the deposit bringing with it its enthalpy. Enthalpy is removed from the surface by three dimensional heat flow into the deposit and out of the deposit into the turbulent high velocity gas stream whose velocity has been measured albeit in the absence of the metal stream, section Ic. The spray model predicts how the gas momentum has been decreased and its enthalpy increased by transfer between the gas stream and the metal. These values allow an estimation of the heat transfer from the deposit to the gas stream. Enthalpy is also lost by radiation from the deposit surface and this can also be predicted assuming knowledge of the emissivity of the deposit surface. There is also a loss of enthalpy to the substrate - whose prediction requires a knowledge of the heat transfer coefficient. This enthalpy loss rapidly become insignificant in the spray forming of billets but for spraying of tubes - where fresh contact with a rotating substrate occurs continuously - this loss is more significant and was not satisfactorily solved in the present program (1989-94) see 8] but is being actively studied in the present program (1995-6). Finally there is enthalpy generation in the deposit by the release of the latent heat of solidification. To model solidification, two assumptions were made - firstly that the arriving spray rapidly achieved thermal equilibrium with the deposit and given the very fine scale of the dendritic microstructure (see section IV) solute equilibrium was assumed - that is the fraction liquid is determined by the total enthalpy together with near equilibrium (Lever Rule) values of the solid and liquid compositions. During the much slower and solidification of the deposits the solidification behavior was assumed to follow a non equilibrium lever rule (Schiel Equation) form, see [43], based on complete solute mixing in the liquid but no solute diffusion in the solid. These microstructural assumptions allow a definite relationship between the enthalpy and the local temperature in the partially solid parts of the deposit. Such a relationship must be established for thermal modeling in solidifying two phase structures.

The major results of the established thermal models for billets but not yet for tubes will be described in section III Experimental Investigations of Spray Forming. This is needed since the two and three dimensional thermal models require measured sticking efficiencies to give the required evolving deposit shapes needed for modeling. The current results for the two dimensional thermal model apply only to billets - the evolving shape of tubes cannot be matched in any satisfactory way to evolving tubes. A three dimensional thermal analysis is essential for the thermal model of tubes as they are currently produced either commercially or in the experimental facilities at NSWC, Caderock and at Drexel University.

III Experimental Investigations of Spray Forming

a) Sticking Efficiency and the Nature of Material Failing to stick to the Deposit.

In an early experiment to gain insight into this problem a simple experiment was carried out in collaboration with R. McCormick and R. Dalal of Howmet Corporation in Whitehall Michigan and reported in the first International Conference on Spray Forming in 1990 [6]. In this experiment, Cu-6wt% Ti was sprayed in a tall chamber using a series of concentric

collection rings - similar to the method used subsequently at DTRC as shown in fig.1. A major distinction of this first experiment was that it was carried out three times. In the first run there was no substrate and material was collected in all the rings at a flight distance of 1.8m. In the second and third runs a flat substrate, at a flight distance of 500mm, intercepted material that would have gone into the inner three rings and a deposit was formed on the substrate. The material in the outer ring was collected weighed and subjected to a sieve analysis to determine how the PSD of material was changed by the presence of the deposit. In the first of the two substrate experiments, the substrate was stationary while in the final experiment the substrate was rotated. The runs were carried out with a super heat of 150°C, at an atomizing gas pressure of 10 bar and at a metal to gas ratio of 1.7. The PSD seen in these experiments was similar to that found in the later experiments at DTRC, figs. 4 and 10.

In the first run, without the substrate, the material collected in the outer ring was about 30% of the total mass sprayed - giving, if the substrate had been there, a measured "target" efficiency of 70%. In the next run, a stationary substrate was inserted and there was then a negligible amount of material in the inner rings, but the outer ring collected about 16% *more material* than in the first run with no substrate. This extra material was that that would have been intercepted by the substrate but *which did not stick to the deposit*. This experiment gave a direct estimation of the overall sticking efficiency to the deposit of 89%. That is 11% by mass of the material that had been on the correct trajectory to hit the substrate was not captured by the growing deposit. The liquid fraction predicted by the spray model, at the flight distance of the deposit for the known PSD in this experiment, was 0.39 [6].

Even more striking was the observation of a change in the PSD of the material collected in the outer ring in the presence of a substrate, see fig. 43. There was a dramatic increase in the amount of small droplets - those significantly less than 100 μm in diameter - in the presence of the substrate. This increase clearly distorted the PSD from its usual log-normal form. The proportion of fine droplets found in the outer ring increased even more when the substrate was rotated, see fig. 44.

There are several possible causes of the sticking efficiency, E_s , being less than 100%. First the presence of the substrate will distort the gas flow field, fig.22, and this may sweep many of the droplets, especially the small ones that will be fully solidified, away from ever hitting the deposit. Second, these small solid droplets, if they manage to hit the deposit, may still "bounce off" the surface especially if the deposit is largely solid. Then impact of droplets may "splash off" liquid from the surface and finally the high velocity impact of the larger droplets, especially those that are fully liquid, may break-up and also splash off the substrate - carrying liquid that is likely to be in the form of small diameter droplets after impact induced fragmentation. These small liquid droplets will then solidify in flight, beyond the deposit, *but at a slower solidification rate* than for droplets of the same size directly atomized by the gas at the atomizer. The reason for this difference in solidification rate is the lower velocity of the gas at the deposit flight distance - compared to the very high gas velocity close to the point of initial atomization where the high velocity, and cold, gas hits the metal stream - see figs. 17, 21 and 22.

State of Material Failing to Adhere - Capture in Wax Traps

Measurement of the significant amount of material failing to adhere to the deposit, indicates two problems for modeling the process including the solidification of the deposit: What is the yield and what is the fraction liquid of the material that fails to adhere to the deposit? In the experiment reported above about 11 % of the material failed to adhere to the deposit when the fraction liquid was 0.39. This fraction is expected to vary with spray deposition

conditions and an investigation of this effect formed a major feature in subsequent experiments, described in section III-iii below. The second problem concerns the thermal-physical state of the material that fails to stick. If this was either all solid, or all liquid, then the estimate of the fraction liquid on the surface of the deposit would be considerably in error. If all the the material failing to stick was liquid then the fraction liquid in the material on the surface of the deposit would fall from 0.39 to $(0.39-0.11) / 0.89$, that is 0.31. If the material failing to adhere were all solid then the fraction liquid in the deposit would rise to $1 - (0.61-0.11) / 0.89$, that is 0.44. These changes in the fraction liquid would greatly modify both the physical state of the deposit interface and the enthalpy of the deposit. Changes in the deposit surface could change the sticking process while the change in deposit enthalpy will change the deposit solidification time and the coarsening of the grain size, see sections IV and V.

In order to gain some insight into the state of material that fails to adhere to the deposit, experiments with a series of wax-containing, aluminum traps were placed in the Spray Chamber in the Osprey Apparatus at Drexel. The aluminum traps were designed so that the entrance to the traps was accessible by direct line of sight from the top surface of the deposited billet but was inaccessible to material coming directly from the spray. Material entering the trap is embedded in the wax - the gas escaped from the side of the traps. Billet spray forming runs with Cu-6wt%Ti were performed in the presence of these wax collection traps. Captured droplets were subsequently removed from these traps, by melting the wax. The captured droplets were mounted in plastic and prepared for metallographic examination by the usual processes of grinding, polishing and etching. The results of this study confirmed first the previous result that most of the material that came from the deposit had small droplet diameters - typically only 20 μm . This is of course much smaller than the mass-mean droplet size of 120 μm but comparable to the number-mean droplet size. However measurements were made of the relative numbers of small droplets with either fine or coarse dendrite cell sizes, indicating either very fast or slower solidification. The results showed that a high proportion of the droplets, upto 50% in some cases, were liquid when leaving the substrate. Comparison was made with the scale of the dendritic solidification structures seen in similar sized particles captured in tall chamber experiments in which the small particles were expected to solidify rapidly soon after atomization. In those studies about 10% of the small particles had coarser dendrite cell sizes. Although these observations were only semi-quantitative, due to poor statistics and the uncertainties that the trapping was non selective, they lend support to the following simple hypothesis. This hypothesis is that since the material that failed to adhere to the deposit and was collected as small spherical droplets appeared to be partially solid and partially liquid at the moment of leaving the deposit, *it was reasonable to assume that the material that failed to adhere to the deposit was representative in enthalpy, and thus fraction liquid, of the spray before impact.* This is, of course, only a first approximation, but it appears more reliable for estimating the enthalpy of the deposit than assuming either that only fully solid droplets, or only fully liquid droplets, failed to adhere. As in other areas of this report, the current results are apparently the first observations of an important aspect of the spray forming process. The results are restricted to one alloy and one spray forming mode, Cu-Ti billet deposition, and need to be supplemented by a wider range of studies to determine there genral applicability.

These simple experiments, described in the first two parts of section III, are amongst the only ones reported in which attempts have been made to study *directly* the processes occuring at the critical step of spray forming - the impact of the high velocity droplets on the partially solid surface of a spray formed deposit. All other experiments, such as those described in the following sections, attempt to gain insight into the mechanisms of spray forming by *indirect means* - such as the measurement of process yield, sticking efficiency,

and the deposit microstructure as a function of (i) process variables or (ii) more usefully, the model predicted fraction liquid.

b) Designed Experiments to test the Role of Fraction Liquid

The two *major* sets of experiments carried out to gain quantitative insight into the essential features of spray forming were performed as follows. It was assumed that if the Drexel model of Spray forming [1,2, 6,7,17] and similar models developed by other groups, for example that of Grant et al. [4], were valid then it is likely that an important control parameter of the process could be *the fraction liquid in the spray*. This parameter is modeled rather well from a knowledge of the PSD and Gas Flow field. It is likely to be only *one* of at least two control parameters - the other being *the fraction liquid on the deposit interface*. This second parameter is derived from the first but is at present, in the absence of a completed and verified three dimensional thermal model of the deposit, not readily calculable. It can safely be assumed however, that the deposit surface fraction liquid *will not be higher* than the fraction liquid in the spray.

On the basis of this assumption, the following two sets of experiments were designed and carried out:

Billets of Cu - 6wt% Ti Spayed Formed at the Osprey Facility at Drexel University

Here a range of runs were actually *designed* using the Spray Model to produce a wide range of liquid fractions (from 0.1 to 0.47) in order to measure the influence of this parameter on (i) the sticking efficiency of droplets to the deposit, and (ii) two aspects of the deposit microstructure: the *porosity in the deposit* and the *as-cast grain size*. The details of the experiments are listed in Table 1 under the "Experimental Settings" which were selected to yield the parameters given in Table 1 as "Model Predictions". The design parameter was the fraction liquid in the spray which was varied within the range shown. These limits were close to the operating limits of the facility supplied by Osprey - notably a fixed distance between the atomizer and the substrate position for the billet of 350mm. The Osprey facility used was an industrial design - based on several years of experience of Osprey Metals - so is likely to cover the empirically determined range for successful spray forming.

Tubes of IN625 Sprayed at NSWC.

Table 2 list the conditions used in the set of runs carried out at NSWC. In this part of the study the runs were largely those already carried out by NSWC for their own research purposes. These runs were however then analysed using the Drexel Spray model to determine the listed "Model Predictions" most significantly the fraction liquid in the spray, at the spray height of the substrate. In a few cases, additional runs were designed using the Drexel spray model to complete the range of fractions liquid explored and performed at NSWC.

The results of both of these two sets of runs were analysed with respect to the fully developed three dimensional *shape* model. The major output of this was the determination of the overall sticking efficiencies, E_s , of the two sets of data for the two shapes. These sticking efficiencies were correlated with the first of the two proposed control parameters the fraction liquid in the spray at the moment of deposition.

The three dimensional *thermal* model being developed in the last stages of the study (1994) was not available for full comparison with the experiments so the experiments were compared with the earlier developed (1992) two dimensional thermal model for the Cu-

6wt%Ti billets. A simple two-dimensional thermal model for a tube deposited from one end was also written but the analysis was rejected as being too artificial for meaningful use. However one run of the spray forming of IN625 tubes at NSWC (run #241) was compared with the predictions of an early version of the three-dimensional model and is described below.

Finally both sets of microstructures of the experimental studies were investigated to determine the average *porosity* of the different spray formed billets and tubes. These measured porosities were then correlated, as with the sticking efficiencies above, with the fraction liquid in the spray.

c) Spray Formed Shapes and the Sticking Efficiency E_s .

Fig.45 illustrates the use of the shape model for a given set of experimental conditions. Initially a sticking efficiency, E_s , of one was assumed and the model run to determine the overall target efficiency, E_{ot} . A value of E_{ot} of 0.95 was found. A linear relationship between yield and sticking efficiency was then used as a first approximation from which the measured experimental yield of 0.73 gave a *first estimate* of the sticking efficiency of 0.77. The model was then rerun using this first estimate of the sticking efficiency (the linear curve) as input to give, after a couple of iterations, the accurate prediction, the non-linear curve, which yielded, for the experimental conditions used, a value of E_s of 0.79 from the measured yield of 0.73 in this particular experiment

The actual three dimensional shape predicted for the run, previously seen in Fig.45, is shown in Fig.46. This was a Cu-6wt%Ti billet sprayed deposited for 48s at a metal flow rate of 0.18kg/s, an atomizing gas pressure of 10bar, a superheat of 110°C giving a spray with 20% liquid. The tilted substrate, rotating at 180rpm, was withdrawn at 1 mm/s. Model predicted cross-sections of the billet are seen in Fig. 47 at 4s time intervals - this shows how the shape evolves during deposition only beginning to approach a steady growth regime after about 16-20s. Two alternative predicted shapes for the billet are shown in Fig. 47 together with the experimentally measured cross section. The sticking efficiency, (SE) E_s , of 0.8 is seen not only to match the measured yield of 0.79 from Fig. 45 but also the cross-sectional shape. This agreement suggests that the details of the shape model for example the role of angle of deposition appears to have been captured quite accurately in the model. The role of different withdrawal rates is seen in Fig. 48, this was modeled using the conditions of Figs 45-47 but at the withdrawal rates shown. Using the measured sticking efficiency for the withdrawal rate of 1 mm/s, the model shows that the yields are seen to vary with withdrawal speed - this is determined by the shape of the billet giving different *target* efficiencies. Other examples of the predicted and measured shapes in the Cu-Ti Billets are seen in Fig.49. The markedly different shape of the billet in Fig.49a was due to the significantly faster withdrawal rate set experimentally by mistake. The Shape model was clearly able to match the experimental result produced by the faster withdrawal rate - see Fig.48. These examples further illustrate the power of the three dimensional Drexel Shape Model developed in the later stages of this project by Dr Cheng Cai.

Analysis of the IN625 tubes sprayed at NSWC using the three dimensional shape model is shown in Figs. 50-53. Fig.50 shows a stereoscopic view of the predicted shape for a tube produced after 107s of deposition under the conditions shown in Fig.51. The Spray model gave a predicted fraction liquid in the spray of 0.50 and the value of the sticking efficiency needed to match the experimental shape was 0.53. The time evolution of the tube shape assuming a constant SE is seen in Fig. 52. The start and finish transients are seen arising since the ends of the tube only receive metal from the trailing or leading edge of the spray, as shown for the Radial Mass Distribution, eq.2. The effect of this is also seen in the low

deposition rate for the inner and outer surface of the tube - only the mid-wall region of the tube receives metal at the maximum, local normal growth rate, LNGR. One of the important results of this is that the enthalpy deposition rate, which is directly proportional to the LNRG, is *very low at the start of deposition* on the inner surface giving rise to cold deposition. This is of great significance for the high porosity seen at the inner surface - that adjacent to the substrate - see section IV-?. The comparison between the predicted and experimental shapes shown for four tubes in Fig.53 is satisfactory except for one case where the process parameters were varying during the run. As for the Cu-Ti billets, this agreement is achieved by use of the fitted value of the sticking efficiencies - the determination of the sticking efficiencies was one of the two major objectives of the experimental analysis.

The major results of this section are reanalysed in Figs. 54 and 55. In Fig.54 the data for the final sets of runs carried out at Drexel are shown. Early data reported to ONR in the annual progress report in April 93 [44] were not included - notably the results shown in Fig.53 for the billet withdrawn at the faster rate where an anomalously high SE of 0.87 was found. It appears for billets rotating at 185 rpm that provided the spray is sufficiently hot, so the fraction liquid is higher than 0.1, a reasonably constant SE of 0.8 ± 0.05 is found. As the fraction liquid approaches 0.5 the sticking efficiency falls - due it was found to parts of the deposit breaking off. In one example, an experiment run at a fraction liquid of 0.49, part of the deposit was found to have broken off and an irregular billet shape was produced, see Fig. 49, compared to the predicted regular shape.

In Fig.55 the data for tubes spray formed at NSWC are seen and the results appear remarkably different. For the spray formed tubes it is clear that the sticking efficiency at fraction liquids in the spray of less than about 0.5 to 0.52 are significantly reduced compared to those for the billets. The higher critical fraction liquid for IN625 *tubes* should be compared to the need for a fraction liquid of only about 0.2 for high sticking efficiencies in the Cu-Ti *billets*. This discrepancy is striking but is likely to arise from the greater cooling expected in the tube-forming geometry - that is there should be a much greater reduction in fraction liquid on the surface of the deposit compared to that in the spray for tubes which rotate out of sight of the spray and where the mandrel and predeposited tube are heavily chilled by exposure to the high velocity gas outside of the hot metal spray. This is discussed in more detail in the following Sections on Thermal Models and on Porosity. Also noticeable is the improved sticking efficiency as *the rotation rate was reduced* - indicating a considerable role for centrifugal effects in throwing off material at higher rotation rates - especially at higher fractions liquid. It is striking that the operating condition used by Sandvik for tube spraying of IN 625, Fig. 55, correspond to a much lower rotation rates and an even higher enthalpy in the spray but which give a high sticking efficiency.

The major conclusions from the experimental studies on sticking efficiency are as follows:

- i) That with rotating billets and tubes that there is a significant failure of material that is directed at the deposit to fail to stick - this is usually 20% or more, $(1 - SE) \times 100\%$.
- ii) That the sticking efficiency falls when *operating outside medium levels of enthalpy in the spray*. With a spray that is too cold the almost fully solid material fails to adhere - and in the extreme limit of 100% solid, found in gas atomization in tall chambers for powder production, no deposit will form at all. At too high a fraction liquid the rotating deposit start to centrifuge off material - a problem made worse for higher rotation rates. In some cases of high liquid fraction and high rotation rates, mechanical rupture of the deposit occurred.
- iii) Material that fails to adhere to the deposit shows a much finer particle size than the mass weight average diameter. The material that fails to stick to the deposit appears to be

made up of small presolidified particles that "bounce-off" the deposit together with small fully liquid droplets that are likely to come from the fragmentation of initially large fully liquid droplets that "splash-off" the deposit.

iv) The total yield of the process is significantly reduced if the target efficiency is not made as high as possible.

d) Temperatures in the Deposit - Use of the Thermal Models

The two dimensional axisymmetric thermal models developed early in the program have been used to predict the thermal profiles in spray formed billets using the fraction liquid predicted by the Spray model and the Sticking efficiencies determined above from the comparison of the experimental shapes and the three dimensional Shape model. The model predicted top surfaces temperatures of the billets are plotted as a function of deposition time in Fig. 56. The end of deposition is clearly seen as the time at which rapid cooling occurs. Only for the two billets with the lowest liquid fractions (17 and 20%) does the system approach steady state during the deposition. Comparison can be made with the ingot shapes predicted at increasing time shown for the billet with 20% liquid in Fig. 46. After about 20s both the top surface shape and top surface temperature are only changing slowly. A more detailed view of the temperatures in the billet sprayed at a fraction liquid of 0.191 (20%) is seen in Fig. 57. A shallow pool of semi-solid material to a depth of 3mm is predicted after 5s when the billet is 10mm high. The maximum temperature after 5 s, Fig. 56, is only just above the eutectic temperature giving a fraction liquid of only about 15%. After 15s, when the billet has grown to 30mm, the top surface temperature has increased to 893°C, giving a fraction liquid of 0.187, and the depth of the semi-solid region has grown to over 20mm. There is clearly a steady reduction in the temperature gradients vertically in the deposit. These changes continue up to the temperature profiles seen after 40s - the top surface temperature has increased to 894°C and the fraction liquid to 0.1905, which is very nearly that of the spray, 0.191. The depth of the pool is now almost 30mm and the major heat temperature gradients are to the *sides of the billet* which are exposed to the high velocity gas stream. The difference in billet shape seen for the billet in Fig. 46, using the three dimensional Model, and that in Fig. 57 for the axisymmetric two dimensional Thermal model are clearly visible. For the disc-like billet shape the use of the simple model though not fully correct appears to be likely to be not greatly in error. This is certainly not the case for the tubes discussed later.

From results such as those shown in Fig. 57, the local solidification time, t_s , can be determined - this is the time from a position in space first being occupied by semi-solid material deposited by the spray to the time when the local temperature drops below the eutectic temperature - here of 880°C. These solidification times are plotted in Fig. 58 for two positions: the billet side surface ("preform edge") and the billet (preform) center as a function of height of the deposit. These times are shown for two very different liquid fractions 0.19 (Fig. 57) and 0.49. For the colder spray, the center of the billet remains below the eutectic temperature giving a cold "dry" surface with fraction liquids of 0 for a height of about 2-3mm. The edge remains dry, $t_s < 0$, for nearly 10mm. The solidification time at the center then rises quickly to nearly 20s at a height of 10 to 20 mm, before falling slowly to a height of 60 mm and then falling quickly at the top of the deposit. With the higher fraction liquid in the spray, the model predicts a very much shorter distance to produce a semi-solid surface (this occurs at heights too small to show in the scale of Fig. 58b). The solidification times are much longer, ≈ 200 s, with the more liquid spray but they fall steadily with deposit height. The fall in solidification time arises since at short heights there is a large heat flux from the material arriving later (higher in the deposit), see Fig. 57. Only when deposition ends does this heating effect disappear, so causing material higher in the deposit to cool faster after deposition ends. These regions, high in the billet, have *shorter times after deposition* before the heat flux is removed.

This picture captured for the simpler problem of billet casting is significantly more complicated for tube deposition. The process studied is that used by NSWC and will be that for any industrial spray forming production. That is the tube is deposited from one end with a continuous movement of the mandrel and deposit in one direction under the spray, see Fig. 52. (Recent tube deposition studies have been carried out at Drexel under reciprocation, back and forth along the full length of the tube. This while scientifically interesting, such full reciprocation of little relevance to any process likely to be used industrially for making long tubes and will not be considered further here).

An early two dimensional axisymmetric, thermal model was constructed and briefly used for modelling the cooling in tubes. The output of one of these runs is shown in Fig. 59 and it can be seen that here, the two dimensional nature of the model is highly unrealistic. The two-dimensional axisymmetric geometry requires that the deposit is formed to a full height instantaneously as each position along the tube passes under the spray. That is, the spray is assumed to have negligible width in the direction along the tube - this is clearly very different from the shape evolution shown by the three-dimensional Shape model of Fig. 52. Certain thermal features of the process are successfully captured, at least semi-quantitatively, however. First it can be seen that due to the chilling effect of the mandrell, the bottom surface of the deposit remains partially molten for only a negligible short distance/time. This occurs not only at the start of the deposition as found for billets, see Fig. 58, but *continuously during tube deposition*, at the interface of the deposit with the substrate. Second there is a strong chilling effect on the top surface due to the gas stream that is only partially offset by the metal deposition rate. That is, as soon as the tube emerges from the spray, the top surface becomes highly chilled. As a result of this chilling effect the length of the semi-solid region, in the axial direction, become *shorter* as the run progresses, indicating that the top surface becomes colder and less liquid as the run progresses. Near steady state conditions are only being approached as the run ends at 64s.

An early version of the three dimensional thermal model applied to tube deposition is shown in Figs. 60 and 61. Fig.60 shows the predicted variation of top surface temperature, under the spray, for a NSWC tube deposition experiment for IN625, with a liquid fraction in the spray of 0.50, as a function of run time. The pyrometer measurement of the temperature is also shown as are the liquidus and solidus temperatures of the alloy. The model clearly captures the initial transient of about 5s to achieve the solidus temperature and the nearly constant surface temperature during the run. The pyrometer clearly overestimates the actual temperature - since this is indicated to be significantly above the liquidus temperature. The error is almost certain to arise from an incorrect value for the emissivity of the surface under the spray. Given this uncertainty the experiment can be said to do little more than confirm the qualitative predictions of the model.

Fig. 61 plots the solidification time for different positions along the deposited tube at four different heights (radial distance from the substrate interface). At greater heights there is metal for shorter distances, corresponding to the modeled shape - which is qualitatively similar to those seen in fig. 53. There is a surface layer for distances of nearly 400mm but at a radial distance of 31.5 mm there is metal only for about 50 mm. Metal close to the surface was above the solidus temperature for times of less than 1-2s, at a height of 10.5 mm the solidification times rose to about 25s. At a greater height, 21mm the solidification times increased to over 60s but then fell again due to the greater cooling effects as more of the deposited tube was exposed to the cooling gas as discussed above with regard to the simpler two dimensional model, fig.59. The origin of the final rise in temperature arose from the ending transient of the process. The outermost region of the tube had faster cooling rate for the reasons discussed in billet solidification. It should be recognized that

the results from the three dimensional thermal model are only preliminary as they have not been tested against experimental results so important tuning factors - notably heat transfer coefficients especially that between the deposit and the substrate. In order to control and understand the process of spray forming and the development of microstructure in spray formed deposits it is clearly essential to have a reliable model of the shape and temperature distributions in the deposit. The models described above appear to be approaching that goal - but more validation of the thermal model is clearly essential.

IV Microstructural Development in Spray Forming

One of the most striking and important features of spray forming is the microstructure produced by successful processing. Two features of this were examined in detail the grain size and the porosity.

a) Grain Size in Spray Formed Deposits.

Fig. 62 shows the equiaxed grain structure with finely distributed porosity typically seen in successful spray formed deposits. Apart from the fine scale porosity the microstructure is that typically found in wrought alloys and is much superior to the typical cored dendritic microstructures seen in cast metals, as discussed for example by [43, 45] in which large grain sizes are usually seen with the segregate spacing that of the dendrite cell size that is typically 100 μm or more. The segregate spacing in spray formed materials is found to be that of the grain size and the measured segregation, measured as the deviation of the composition from the alloy composition is also found to be greatly reduced in spray forming [5]. In contrast the fully solidified powders seen in conventional gas atomization have very fine dendrite (cell or segregate) spacings, but often with grain sizes that are that of the droplet itself, fig 63. In spray forming, the mass mean particle sizes are usually 100 - 200 μm so the grain sizes in the rapidly frozen droplets are much larger than those seen in the spray formed deposits [2,3,5]. The ability of spray forming to give the controlled shapes, especially that of tubes, as in casting but with the microstructures approaching that of wrought material is of course the commercial attraction of this process. Improved understanding of the development of microstructure in spray casting has been a major objective of the present project and the results of the early part of this have been presented in a paper published in 1993 [3] and discussed in [45,46].

The need to explain the change in microstructure between the large grain size, but fine cell size that seen in the overspray droplets, fig.63, and the equiaxed grain structure of spray formed deposit was considered in the initial study [1,2]. The fine dendrite cell sizes in the rapidly solidified powders is easily understood in terms of the very short solidification times giving only very limited time for dendrite arm coarsening [43]. The refinement of grain size in material spray formed into a deposit was explained as a dendrite fragmentation process [2]. This explanation is now widely accepted [3, 5, 47] since the impact of partially liquid fine dendritic droplets travelling at velocities of the order of 50 - 100 m/s onto a deposit is very likely to deform the dendritic skeleton [45]. Earlier studies of stir casting [49] have established a model of plasticity induced dendrite fragmentation based on dendrite arm bending, followed by the formation of grain boundaries by recrystallization and the break up of this polycrystalline dendrite by liquid wetting of the grain boundaries. Grain boundary wetting or melting occurs since the grain boundary can be replaced by two solid-liquid interfaces since, as confirmed by Gundoz and Hunt [50]:

$$2 \gamma_{sl} \leq \gamma_{gb} \quad (19)$$

γ_{sl} is the solid liquid energy and γ_{gb} is the energy of a high angle grain boundary. There are to date no detailed microstructural studies of the actual fragmentation process and it is not yet known to what size the dendrites are broken up by impact. Fig. 63 shows evidence for dendrite fragmentation in a droplet fitting the edge of a deposit and solidifying rapidly after impact. The dendrite has here broken up into individual solid particles on the scale of a few dendrite arms $\approx 5\mu\text{m}$.

The dendrite fragments will coarsen from the $1\text{-}5\mu\text{m}$ size scale to a much larger *grain* size during the extended solidification times of $10\text{-}200\text{s}$ in the deposit. The $1\mu\text{m}$ length scale corresponds to the droplet dendrite arm spacing arising from coarsening times of a few ms in flight, the larger values suggested from the fragmentation process seen in fig.63. The grain coarsening during deposit solidification is clearly seen in fig. 62. With a short solidification time of less than 20s the grain size is $19\mu\text{m}$ while for the same alloy with a deposit solidification time of 200s , due to the higher enthalpy in the spray, the grain size has coarsened to $50\mu\text{m}$. Fig. 64 shows the full set of results for the Cu-Ti Billets as (a) the measured grain size at an axial location 25mm above the substrate for a series of spray formed billets of Cu-6wt%Ti as a function of increased fraction liquid in the spray and (b) the corresponding longer model-predicted solidification times with higher liquid fraction in the spray. The detailed modeling of the grain coarsening shown in Fig 64a is described in section V. However a critical result is to be noted here - the grain size is consistently smaller by about a factor of two, from that predicted using the conventional dendrite coarsening model, see for example [43]. This result was first reported by Mathur et al.[1,2]

The grain size variation with position inside billets and tubes follows the prediction of the current thermal models very well - in all cases tracking with the predicted solidification times shown in figs. 58 and 61. Examples of the variation of grain size with height and radial position in Cu-6wt% Ti billets are shown in fig.65.

b) Porosity:

An even more important parameter of the deposit structure is the porosity. As discussed in a publication based on the present study, Annavarapu and Doherty[3] suggested that there are at least three different types of porosity. These are:

- i) High levels of often interconnected porosity found at cold regions of the deposit - most notably near the substrate interface. Examples are seen in figs. 66 and 67.
- ii) Fine spherical pores, believed to arise from trapped atomizing gas - found mainly at grain boundaries. Low magnification views of this ubiquitous porosity in spray forming is seen in fig. 62 and higher magnification views of the same feature are seen in fig. 68.
- iii) Coarse spherical pores, that are believed to arise from coalescence of trapped atomizing gas in deposits spray formed at very high liquid fractions. An example is seen in fig.69.

As briefly discussed in [3] atomizing gas entrapment is believed to be the dominant cause of each of these three types of porosity and the differences appear to arise from the thermal condition in the spray. Detailed analysis of the experimental runs was carried out to characterise the porosity and its correlation with thermal conditions. This is described below.

Correlation between Porosity and Fraction Liquid.

Porosity data were obtained from the many runs at NSWC on IN 625 tubes and from the Cu-Ti billets spray formed at Drexel University. In both cases the porosity was determined as a volume percentage of pores from density measurements using air and water weighing of each sample.

IN625 Tubes

15 Spray formed tubes of IN625 from runs #220-222, 241-250, 256-7 at NSWC were measured for porosity. Fig. 70 shows the variation of porosity along the length of three IN626 tubes, spray formed at different liquid fractions. It can be seen that the mean porosity falls as the tubes are spray formed hotter, that is with higher liquid fractions. It is also clear that there is a much higher porosity at the ends of the tubes. The origin of this second effect is easily understood from the influence of type (i) porosity - that at the substrate regions of the deposit. Regions close to the deposit surface that are spray formed under cold conditions, due to the chilling effect of the steel substrate, are much more porous than the bulk of the deposit. As a consequence density profiles made using vertical sections, fig. 70, can be misleading since porosity will rise at portions of the deposit, close to the end when only regions close to the deposit, with high porosity, have been formed. A more informative sectioning method is that shown in fig. 71 where the end effect has been eliminated by a more appropriate technique that allows the full thickness to be sampled at each position along the tube. Fig. 71 confirms that once the distorting effect of different tube thickness has been eliminated there is a much reduced increase of porosity along the tube. Fig. 72 shows the variation of porosity along the tube in more detail. Very high initial and final porosities are seen due to the thickness effect of fig. 70. There is however still a residual increase in porosity with deposition length - this may arise from the chilling effect of the gas stream on the as-deposited tube. The cooling effect reduces the solidification time, the effect shown in the simplified thermal model used in fig. 59, and so should also *on the deposit surface* under the spray.

The most important result of this part of the study, and possibly the whole investigation is shown in fig. 73. This shows how the average porosity in the IN 625 tubes varies with fraction liquid in the spray. The average values did not include the start and finish transient regions where the tube is very thin and has the high porosity of just the near substrate regions. It does include the substrate regions in the porosities given for the tubes with near full thickness. It is usually the case that the inner surface is removed by machining so the values reported in fig. 73 are significantly higher than the porosities found, in the as-cast state, in the bulk of the deposit. The critical result is the dramatic fall in porosity as the fraction liquid in the spray falls from 0.45 to 0.65. It is pleasing that, as described above and shown in fig. 55, there was also a rise in sticking efficiency as the fraction liquid rose from 0.45 to 0.55 at high rotation speeds and to 0.70 as the rotation speed was further reduced. So there is no conflict between the values of liquid fraction (enthalpy) needed to produce high yields and the values needed to give low porosity. Both the sticking efficiency and the porosity are improved by going to quite high fractions of liquid in the spray for the IN 625 tubes.

Cu-Ti Billets.

Fig. 62 showed a clear increase in general porosity as the fraction liquid in the spray fell. The pores were both smaller and more widely spaced with the higher enthalpy condition - even though there was more grain growth. The role of grain growth in causing gas pore coalescence is discussed in Section V. Fig. 74 shows for two of the Cu-6wt% Ti billets the measured density as a percentage of theoretical density, (100 - %porosity), for different positions in two billets at different liquid fractions. The highest densities are seen in the

center of the deposit - corresponding to material with the longest solidification times. In the billets spray formed against an oxide substrate there is only a thin layer of material with cold porosity at the substrate interface so there is only a small effect of the cold substrate porosity on the values of porosity plotted in fig. 74. The lowest densities, highest porosity is however seen on the outside of the billet against the substrate where the combination of cold substrate and gas cooling give a dry surface, seen for several seconds in the low fraction liquid billet in fig. 58. It may be noted that the use of the simpler two dimensional thermal model in contrast to the three dimensional shape model may have underestimated the chilling effect in this position. The three dimensional shape model captures the extended region at the substrate - this is of course not seen in the two dimensional thermal model with it enforced cylindrical symmetry.

The variation of average porosity with fraction liquid in the Cu-Ti billets is shown in fig. 75. A very similar trend to that found with the IN625 tubes is seen - a steady decrease in porosity with fraction liquid reaching 2% porosity at the highest liquid fraction shown. The enhanced porosity at very high fraction liquid, qualitatively seen in fig. 69 is to be noted. Recent studies at Alcoa have found a trend of increasing porosity with large pores of gas at very high fractions liquid - this indicates that the trend seen in fig. 75 should not be extrapolated to very high liquid fractions. As with the IN625 tubes, it is striking that there is again with the Cu-Ti billets a near optimum fraction liquid in the spray needed to give low porosity, fig. 75, and high sticking efficiency, fig. 54. There is, however, a very significant difference between the two sets of experiments - the optimum fraction liquid in the spray is *much higher* in the IN625 tubes of about 0.60 to 0.65, (figs. 55 and 75) than for the Cu-Ti billets where the optimum fraction liquid was from about 0.25 to 0.35. The origin of this difference *could* arise from the difference between the two alloys but it seems much more likely to arise from the difference in the thermal behavior of billets and tubes. The Billets were formed under a nearly continuous deposition on the top surface in which the model predicted a fraction liquid on the top surface of the deposit that approached that in the spray. For tubes where the tube rotated into and out of the spray, with cooling gas passing the surface of the tube at a position at right angles to the spray plume, where there was no heat input from the metal stream. In addition as the tube was deposited there was a growing region of exposed tube surface that was outside of the spray - leading to the higher billet cooling rates at the later regions of the tube, shown in fig. 59. It is striking that there is an parallel increase in porosity along the IN625 tubes that appears to correlate with this effect, see fig. 72. It appears likely that the discrepancy between the two sets of results arises from the need to consider two related control parameters. These are (a) the fraction liquid (enthalpy) of the spray and also (b) the fraction liquid on the deposit surface during deposition. For the billets it appears that the two parameters are similar and quickly become identical while for tubes the fraction liquid on the deposit surface is significantly less than that in the spray and that the difference increases as the tube deposition condition approaches steady state. In support of this idea is the result clearly seen in these sets of experiments for the high porosity almost always seen on the inner diameter of the tubes, fig. 67. Lower substrate porosity was much less of a problem in the billets, see fig. 74, except at the edge. The billets, as noted above, quickly showed an approach of the fraction liquid on the deposit towards that in the spray, fig. 57.

Current investigation of spray formed IN 625 billets and Cu-Ti tubes at Drexel is supporting the idea that the differences between the results seen in Figs 73 and 75 arise from the deposit geometry (tubes or billets) than from the alloy differences. High porosity is being seen in the Cu-Ti tubes and low porosity in the IN625 billets sprayed under similar thermal conditions. This work will be reported when completed.

V. Inhibited Grain Coarsening at High Fractions Solid - Spray Forming and Commercial Alloys:

Fig.64 illustrates an effect first described by Mathur et al. [1,2] and also subsequently by other investigators as noted by Grant[5]. This is, the grain size measured in the as-spray formed deposits is *significantly finer* than the values expected from conventional solid-liquid coarsening [43]. The assumption made by Mathur et al. [1,2], and followed in this investigation, is that dendrites in the atomized droplets are fragmented by high velocity impact to a small size on the top surface of the deposit. The fragmented dendrites will quickly reduce the curvature of their convoluted solid-liquid interface to form small spherical grains. The kinetics of this change, as of the subsequent growth of the spherical grains, are driven by the Gibbs-Thomson modification of the solute concentration in the two phases, see for example [51] followed by liquid diffusion of the solute. The effect is that regions with high curvature, such as tips of dendrites, melt and resolidify on surfaces with less positive curvature, the gaps between dendrites. Once the grains have become spherical there is then a net coarsening reaction in which small grains, with high curvature, shrink and vanish and larger ones grow - so yielding the standard equation for interfacial energy driven coarsening or "Ostwald Ripening" [51].

The equation for this is given by:

$$\bar{r}_t^3 = \bar{r}_0^3 + K_p t \quad (20)$$

\bar{r}_t and \bar{r}_0 are the mean grain radius after a time t and when t is zero and K_p is a constant determined by the alloys system. The terms are rather similar to the equivalent equation determined, usually empirically, for the dendrite arm spacing, λ :

$$\bar{\lambda}_t^3 = \bar{\lambda}_0^3 = K_D t \quad (21)$$

K_D is the constant for dendrite coarsening. The plot labelled "K from conventional das(dendrite arm spacing) tf (time of freezing) correlation" in fig.64 is derived from experimental measurements in the Cu-Ti alloy solidified in small ingots containing thermocouples to measure the freezing times. It is clear from fig.64 and as previously reported[1-3,5,6,18] that the conventional plot based on eq.21, *significantly overestimates the grain sizes actually measured in the spray formed deposits*. The magnitude of this discrepancy is typically a factor of 2-3. In the initial work at Drexel [1,2,52] the solidification times in the spray formed deposits were actual measured values from non-rotating substrates from which accurate thermocouple measurements could be made. In the work reported here, for example fig.64, the substrate rotation made this impossible so the freezing times are those calculated using the model. Grant et al. [4] have shown from infrared measurements in their studies that model predictions of the deposit temperatures are accurate, see for example fig.24. Other thermocouple studies, for example [53,54], have confirmed that a partially liquid state develops but remains for quite short times within spray formed sheets that were not rotated.

This discrepancy between the fine grain sizes measured in spray formed deposits and the coarser sizes predicted is a major challenge and one that a considerable effort was devoted in this study to resolving. The results of this investigation have been published by Annavarapu and Doherty [55] and this publication has been included as Appendix B of this report. The main results of the study were as follows:

i) The coarsening of solid in a spray formed deposit occurs for small spherical grains at a high fraction solid, $f_s > 0.6$ and usually $f_s > 0.8$.

ii) Experimental studies were carried out with chill cast Al-6.7%Cu, DC cast high Al 2024 (Al4.5%Cu 1.5%Mg) both grain refined and non-grain refined, Spray formed, commercial purity Al 2014 supplied by Osprey Metals, Spray formed Cu 4wt% Ti produced at Drexel and Spray Formed IN625, produced by NSWC in Annapolis. In each case fine grain samples were rapidly reheated to above the solvus temperatures to give different values of fraction solids, $0.5 < f_s < 1$, held at temperature for different times and then quenched. The coarsened grain sizes were then measured and plotted in the form of eq.21 as the solid spacing to the power three against total time in the solid liquid phase field. The last parameter was the sum of (i) the initial time of freezing determined either directly from thermocouple measurements, Al-Cu, Al 2024 or from the model predicted solidification time in the spray formed materials and (ii) the imposed supersolidus coarsening time. Typical plots are given in Appendix B as Figs B7, B10, B14, and B19 of Appendix B. In each case the observed coarsening rates while fitting well to the power law of eq.21 were in all cases significantly less than the rate constants found for dendrite arm coarsening in conventional solidification. In addition the rate constant fell as the fraction solid, f_s , increased towards unity. The largest reductions were with spray formed Cu-Ti and with grain refined 2024. Grant et al.[56]

iii) The fall in coarsening rate at high f_s was in marked contrast to a range of independent studies performed on high purity fine grain sized materials as shown in fig. B1. For the high purity materials, rapid acceleration of the coarsening rate with increased f_s was found particularly as $f_s \rightarrow 1$. This result is that expected for standard coarsening theory [51, 55, 57-58] since as the volume fraction of solid spherical particles increases but, at a given mean radius of the particles, the diffusion distance from small shrinking grains to larger growing ones decreases so accelerating the diffusion limited coarsening. In many of the experiments on the high purity alloys, see for example Hardy and Voorhees [56], the coarsening was carried out at a constant temperature with the volume fraction varied by altering the alloy composition. In the work on coarsening on spray formed alloys [55], f_s was increased by lowering the temperature which alters the solute content, X_l , in the liquid. As described by for example [55] the increased solute content reduces the predicted coarsening rate for spherical grains:

$$K_p = (8 D_l \gamma V / 9RT) \{ 1 / (X_l [1-k]^2) \} \quad (\text{for } k < 1) \quad (22)$$

This is eq.(B3g) where D_l is the diffusion coefficient in the liquid, γ is the solid-liquid interfacial energy, V the molar volume, R the gas constant, T the temperature and k the partition coefficient. As the temperature falls, with higher f_s , X_l rises reducing the coarsening rate as shown in convention arm coarsening experiments, see fig B3 and discussed for example in [45]. However this temperature/solute effect is much too small to account for the opposite effects reported here for coarsening in spray forming compared to the effects reported for high purity materials, fig. B1.

iv) The usual model for coarsening giving eq.21-23, is for independent dissolution of small particles and growth of large ones[45,51,58] this is a reasonable model for low volume fraction mixtures where the spherical particles are not in contact. However as the volume fraction of solid, f_s , approaches 1 the microstructure changes to one of a regular grain structure with liquid films at the grain boundaries. Coarsening in this structure becomes that of grain growth but with the grain boundary mobility determined by solute diffusion across the thin liquid films at the grain boundaries[59] or across the liquid regions at grain boundary edges (triple points) or grain corners. As part of this research, and fully

described by Annavarapu and Doherty [55] see appendix B, a series of theoretical models for grain coarsening at very high volume fractions was developed:

The model was based on an earlier suggestion of Higgins et al. [60,61] for coarsening at rates controlled by the grain boundary induced drag of solid particles at grain corners. It leads to the following prediction for coarsening at high volume fractions solid at rates determined by triple point drag:

$$\bar{\lambda}_t^3 = \bar{\lambda}_0^3 = K_{TPG} t \quad (23)$$

$$K_{TPG} = (6 D_l \gamma V / RT) \{ 1 / (X_l [1-k]^2) \} \{ 1 / [1-f_s]^{2/3} \} \quad (23a)$$

As the fraction solid, $f_s \rightarrow 1$ the predicted coarsening rate accelerates as seen qualitatively in fig.B1. As shown in Table 2 of [55] see appendix B, this equibinary alloys indicating that the model is capturing the experimental behavior rather well despite the simplification used in the model of Annavarapu and Doherty [55]. When applied to the experimental results of coarsening in spray forming for the two binary alloys, Al-Cu and Cu-Ti for which it could be directly applied, table B2, the model failed dramatically. As the temperature fell 625 to 575°C in Al-Cu and 1015 to 950°C in Cu-Ti the predicted coarsening rates rose from 799 to 802 (Al-Cu) and 732 to 851 (Cu-Ti) while the experimental values fell from 144 to 6 and 91 to 5 respectively. That is the observed rates went in the opposite direction with fraction solid and were wrong by over two orders of magnitude !

If the model were to apply then very much faster grain coarsening would occur and one of the characteristic advantages of spray forming - a fine grain structure and a corresponding fine segregate spacing, would be lost. (The grain boundaries in spray formed microstructures are the sites of the last liquid to freeze and this last liquid is solute and impurity enriched giving solute segregation on the grain boundaries in the as-solidified material - see fig.B8, B12 and B15.)

The present study, as described by Annavarapu and Doherty [3,55] has not given a quantitative answer to the origin of the inhibited coarsening at high volume fractions in spray formed deposits. However the qualitative origin of the effect seems to be well characterised. The microstructures in all the spray formed samples, and in the other cast structures also showing inhibited coarsening, figs. B9a and b, B12b, B13b and c, B15, B16 and B26, reveal irregularly shaped boundaries indicating pinning by second phase particles and in some cases, see for example fig. B26, the pinning particles can be seen. In support of this hypothesis, are the observations of Voorhees [62] from his current study of coarsening of high volume fraction solid-liquid mixtures in Sn-Pb. The observations come from preparatory experiments for a future micro-gravity space shuttle experiment, the accelerated coarsening seen in the high purity samples at high volume fraction solid as in the earlier study [57]. Voorhees reported that the accelerated coarsening seen in high purity alloys was replaced by inhibited coarsening in the presence of second solid phase impurity particles - predominantly oxides.

It appears therefore that the fine grain sizes characteristic of the spray formed microstructures are not *intrinsic to the process*. The fine grain sizes appear to arise from the presence of impurity second phase particles that form in many spray formed structures especially those based on commercial purity alloys. Almost all aluminum alloys contain small amounts of iron (0.15 to 0.4wt%) that produce aluminum iron eutectic particles, Al_3Fe , $Al_{12}Fe_3Si$ etc, during solidification - such particles are visible in fig.B9b. During atomization with nitrogen gas in spray forming a small - 100-200ppm - pick-up of nitrogen occurs giving the likelihood of fine nitrogen gas pores or in the presence of strong nitride

forming elements, Ti, Cr, Zr etc their replacement by fine nitride precipitates as for example Benz et al.[63]. In this work it was reported that argon atomized superalloys always had fine residual argon gas porosity but nitrogen atomized alloys showed fine nitride particles containing Ti and Nb - both at grain interiors and at grain boundaries. Ashok [64] has reported from his studies of spray formed copper that in the absence of nitride formers the copper always showed fine scale porosity at grain boundaries - this porosity only disappeared by spraying copper alloys containing small amounts of strong nitride formers particularly Zr. The grain size in the spray formed copper alloy plates was reported to be significantly finer in the presence of the nitride formers - indicating that grain growth inhibition was significantly more effective with solid nitride particles than with gas filled voids.

For the model alloy used in this study, Cu-Ti, the retardation of grain growth at high fraction solid was found to be much more marked than for the other two spray formed microstructures, see fig. 76. It is clear that there is a much more marked reduction in coarsening rate for Cu-Ti than for In625 or AA 2014. This data is for material spray formed at Drexel (Cu-Ti), NSWC (IN625) or at Osprey Metals (A2014), which after full solidification was reheated back into the two phase solid plus liquid region for the coarsening experiments. The dramatic fall in coarsening rate was not matched by a much finer grain size in the as cast Cu-Ti spray formed billets, see fig.64 which in common with other spray formed structures showed a similar 2-3 fold reduction in grain size compared to the K_D predicted values, based on the modeled freezing times. When the retarded values of K_{exp} were used to predict the expected grain size, assuming a starting grain size of $5\mu m$, then the grain sizes were underpredicted as seen also in fig.64. This prediction was made by numerical integration of coarsening rates as the temperature in the deposit fell and the local fraction solid increased, see figs.57 and 58. The failure of this prediction was not improved by assuming different initial grain sizes since the inhibited coarsening rates were so small. The only current explanation of the underprediction of coarsening rates using the experimental data is that the process of solidification and cooling to room temperature in Cu-Ti has generated more TiN precipitates impeding grain growth than were present during the initial solidification during spray forming - which produced the points shown in fig.64. This possibility is being actively investigated at present in several ways - as described below.

The investigation of grain coarsening in the spray formed alloys has confirmed that there is indeed significant inhibition of grain growth in the spray formed deposits - especially at high solid fractions. This inhibition is not intrinsic to the coarsening of spherical grains in a liquid matrix which in high purity alloys is greatly accelerated by high solid fractions - which give short diffusion distances. The inhibition appears extrinsic - appears to arise from impurity effects - either metallic impurities such as iron aluminides in commercial purity aluminum alloys, or to gas pick up in the atomization process that give weak inhibition in the presence of insoluble gas pores or strong inhibition in the presence of transition metal nitrides. Although a successful model was developed in this study for uninhibited grain growth at high solid fractions, no appropriate model is yet available for the inhibition of coarsening by the impurity phases.

VI Current Investigations:

IN the continuing work beyond the funding period reported here work is continuing in several directions.

- i) The full three dimensional thermal model is being completed and will be tested against a range of experimental runs. These include previous runs of billets and tubes and also special runs designed to test the model directly.

forming elements, Ti, Cr, Zr etc their replacement by fine nitride precipitates as for example Benz et al.[63]. In this work it was reported that argon atomized superalloys always had fine residual argon gas porosity but nitrogen atomized alloys showed fine nitride particles containing Ti and Nb - both at grain interiors and at grain boundaries. Ashok [64] has reported from his studies of spray formed copper that in the absence of nitride formers the copper always showed fine scale porosity at grain boundaries - this porosity only disappeared by spraying copper alloys containing small amounts of strong nitride formers particularly Zr. The grain size in the spray formed copper alloy plates was reported to be significantly finer in the presence of the nitride formers - indicating that grain growth inhibition was significantly more effective with solid nitride particles than with gas filled voids.

For the model alloy used in this study, Cu-Ti, the retardation of grain growth at high fraction solid was found to be much more marked than for the other two spray formed microstructures, see fig. 76. It is clear that there is a much more marked reduction in coarsening rate for Cu-Ti than for In625 or AA 2014. This data is for material spray formed at Drexel (Cu-Ti), NSWC (In625) or at Osprey Metals (A2014), which after full solidification was reheated back into the two phase solid plus liquid region for the coarsening experiments. The dramatic fall in coarsening rate was not matched by a much finer grain size in the as cast Cu-Ti spray formed billets, see fig.64 which in common with other spray formed structures showed a similar 2-3 fold reduction in grain size compared to the K_D predicted values, based on the modeled freezing times. When the retarded values of K_{exp} were used to predict the expected grain size, assuming a starting grain size of $5\mu m$, then the grain sizes were underpredicted as seen also in fig.64. This prediction was made by numerical integration of coarsening rates as the temperature in the deposit fell and the local fraction solid increased, see figs.57 and 58. The failure of this prediction was not improved by assuming different initial grain sizes since the inhibited coarsening rates were so small. The only current explanation of the underprediction of coarsening rates using the experimental data is that the process of solidification and cooling to room temperature in Cu-Ti has generated more TiN precipitates impeding grain growth than were present during the initial solidification during spray forming - which produced the points shown in fig.64. This possibility is being actively investigated at present in several ways - as described below.

The investigation of grain coarsening in the spray formed alloys has confirmed that there is indeed significant inhibition of grain growth in the spray formed deposits - especially at high solid fractions. This inhibition is not intrinsic to the coarsening of spherical grains in a liquid matrix which in high purity alloys is greatly accelerated by high solid fractions - which give short diffusion distances. The inhibition appears extrinsic - appears to arise from impurity effects - either metallic impurities such as iron aluminides in commercial purity aluminum alloys, or to gas pick up in the atomization process that give weak inhibition in the presence of insoluble gas pores or strong inhibition in the presence of transition metal nitrides. Although a successful model was developed in this study for uninhibited grain growth at high solid fractions, no appropriate model is yet available for the inhibition of coarsening by the impurity phases.

VI Current Investigations:

IN the continuing work beyond the funding period reported here work is continuing in several directions.

- i) The full three dimensional thermal model is being completed and will be tested against a range of experimental runs. These include previous runs of billets and tubes and also special runs designed to test the model directly.

ii) Experimental runs in which Cu-Ti and IN625 was deposited under non rotating unidirectional displaced substrate containing embedded thermocouples. The temperature time plots at different heights are being measured. Grain sizes at the corresponding positions are being measured and will be correlated with the predicted grain sizes derived from the previous coarsening studies described above.

iii) Runs are being carried out for Billets of IN625 deposited under a range of predicted fractions solid in the spray and for small tubes of Cu-Ti spray formed at Drexel. The objective here is to determine if the differences seen in the optimum fractions solid in the spray for Cu-Ti Billets and IN625 tubes reported above arise from alloy differences or the differences in deposition geometry. It is expected that deposition geometry is the dominant effect and this will be explored using the three dimensional thermal model.

iv. The grain size - freezing time studies carried out for Cu-Ti are being extended to IN 625 which shows a more moderate reduction in coarsening rate with fraction solid.

v. The proposed increased precipitation of TiN after reheating the spray formed deposits is being investigated.

VII Summary and Conclusions

The earlier numerical "Drexel" model developed in the previous study by Mathur has been significantly extended to two ways. Firstly the needed experimentally measured input parameters for the model notably the Particle Size Distribution (PSD) and its radial variation, the Radial Mass Flux (MFR) and the gas velocity field in the Osprey chamber were established for the alloys investigated (high strength low alloy steel, IN625 and Cu-Ti) and the range of Osprey facility operating conditions. The more accurate parameters measured were incorporated into the Model.

The model itself was then significantly developed in several ways. First, a hypothesis for the determination of droplet undercooling Gas Atomization in general, and thus in Spray Forming, was developed and incorporated into the spray model. The hypothesis was that the smallest droplets that cool most quickly should usually show homogeneous nucleation with undercoolings of about $0.3T_m$. These droplets are accelerated faster than larger droplets and will frequently impact larger slower moving and less cooled droplets. It was proposed that all impacts of partially or fully solidified droplets onto larger droplets would lead to nucleation of solidification of the larger droplets if these were supercooled. The numerical model of this hypothesis showed that it predicted that the magnitude of resulting undercooling would fall with increased droplet size. This prediction of the size dependence of droplet undercooling matched quantitatively the previous measurements of undercooling reported by Mathur. In addition although there was a very high frequency of collisions most of these involved the impact of small droplets on larger ones - and if it was assumed that all such collisions (except those between two fully solid droplets) led to coalescence, the model predicted only a small change in the Particle Size Distribution when measured in terms of *droplet mass*. These conclusions are likely to be applicable to small gas atomization experiments.

A second modification of the Spray Forming model was developed. This predicted the three dimensional shapes of spray formed deposits by combining the known Radial Mass Flux with the imposed motions of the substrate, and were needed the spray cone. This model was put into an operating software package "DU SHAPE" and transferred to NSWCC and their Equipment Developers MTS. This package predicts the final dimensions of deposits assuming a known average sticking efficiency of droplets onto the deposit. By

comparison with measured shapes the needed parameter of sticking efficiency was measured for different geometries, different alloys and different operating conditions. The three dimensional shape model was also used to design possible deposition runs to produce desired shapes - such as curved tubulars.

The shape model was then developed into a means of predicting the temperature distributions in deposits as two and three dimensional thermal models. The two dimensional model is rather realistic for Billet shapes and it can predict the temperature distributions and its evolution during spray deposition. It shows that the top surface of the deposits achieves quite quickly a similar fraction liquid to that in the spray. The time for solidification initially increases with height into the deposit but at the top of the deposit that completes solidification in the absence of any further flux of semi-solid material the solidification time falls. The measured grain sizes clearly correlate with the predicted freezing times but with grain sizes significantly below those predicted by standard solid liquid coarsening theory. For the Tubes the simple two dimensional thermal model is clearly inadequate and the full three dimensional model is needed for calculating the freezing behaviour and in particular the fraction liquid on the surface of the tube during deposition.

References

1. P.C.Mathur, D.Apelian and A.Lawley, "Spray Deposition: A Fundamental Study of Droplet Impingement, Spreading and Consolidation" Final Report to ONR Contract # N00014-84-K-0472) (1988),
2. P.C.Mathur, D.Apelian and A.Lawley, " Analysis of Spray Deposition" *Acta Metall.*, **37** (1989) p429.
3. S.Annavarapu and R.D.Doherty, "Evolution of Microstructure in Spray Forming" *Intern J. of Powder Metall.*, **29**, (1993) 331.
4. P.S.Grant, B.Cantor and L.Katgerman, "Modelling of Droplet Dynamic and Thermal Histories during Spray Forming" *Acta Metall. and Mater.*, **41** (1993) 3097, 3109.
5. P.S.Grant, "Spray Forming" *Prog. in Mater. Sci.*, **39** (1995) 497.
6. S.Annavarapu, R.D.Doherty, D.Apelian, A.Lawley and P.C.Mathur, "Fundamental Aspects of Consolidation and Microstructure Development during Spray Casting" *ICSF I - First International Conferenece on Spray Forming* (Sept 1990) Ed J.V.Wood., Osprey Metals, Red Jacket Works, Neath U.K. (Paper32).
7. C. Cheng, S. Annavarapu and R.D.Doherty, "Modeling - Based Microstructure Control in Spray Forming" *ICSF II - Second International Conferenece on Spray Forming* (Sept 1993) Ed J.V.Wood, Woodhead Publishing Ltd., Abington Hall, Abinton Cambridge CB1 6AH, UK. p.67.
8. Cheng Cai, "A modeling Study for Design and Control of Spray Forming" *Ph.D. Thesis*, Drexel University, June 1995.
9. H.Lubanska, *J. Metals*, **22**, (1970) 45.
10. R.K. Upadhyaya and H.S. Spacil, *Surf. Coat. Tech.*, **37**, (1989) 379.
11. J.Coombs, Osprey Metals Ltd, Neath U.K. *Private Comminication* (1991)
12. S.Connelly, T.S.Coombs and J.O.Medwell: " Flow characteristics of metal powders in atomized sprays" *Metal Powder Reports*, **41** (1986) 653.
13. A.R.Anderson and F.R.Johns, "Characteristics of free jets exhausting into quiescent air" *Jet Propulsion*, **21**, (1955) 13.
14. BS 1042 "Flow measurement" *British Standards Institution* (1946)
15. *Handbook of Fluid Dynamics*.
16. S.Elghobashi, T.Abou-Arab, M.Rizek and A.Mostafa: "Prediction of the particle-laden jet with a two equation turbulence model" *Intern. J. of Multi-phase Flow*, **10** (1984) 697.
17. P.C.Mathur, S.Annavarapu, D.Apelian and A.Lawley, "Spray Casting: An Integral Model for Process Understanding and Control", *Mater. Sci and Engr.*, **A142**, (1991) 261.
18. E.J.Lavernia, E.M.Gutierrez, J.Szekely and N.J.Grant, *Intern. J. of Rapid Solid.*, **4**, (1988) 89.
19. E.M.Gutierrez, E.J.Lavernia, G.M.Trapaga, J.Szekely and N.J.Grant, *Metall. Trans.*, **20A**, (1989) 71.
20. G.M.Trapaga, E.F. Matthys, J.J. Valencia and J.Szekely *Metall. Trans.*, **23B**, (1992) 701.
21. C.Y.A.Tsao and N.J.Grant, *Intern. J. of Powder Metal.*, **30**, (1992) 323
22. P.S.Grant, P.P.Maher and B.Cantor, *Mater. Sci and Engr.*, **A179**, (1994) 72.
23. D.T.Gethin, J.O.Medwell and N.Muhamad, "A comparison of lumped parameter numerical techniques for liquid metal sprays" *ICSF I - First International Conferenece on Spray Forming* (Sept 1990) Ed J.V.Wood., Osprey Metals, Red Jacket Works, Neath U.K. (Paper37).
24. U.Fritschung, H.Zhang and K.Bauckhage, " Modelling of thermal histories and solidification in the spray cone and deposit of atomized and compacted materials"

- ICSF II - Second International Conference on Spray Forming (Sept 1993) Ed J.V.Wood, Woodhead Publishing Ltd., Abington Hall, Abington Cambridge CB1 6AH, UK. p.35.
25. J.Forrest, S.Lile and J.S.Combs, "Numerical Modelling of the Osprey Process" *ibid.* p.117.
 26. E.S.Lee and S. Ahn, *Acta Metall. Mater.*, **42**, (1994) 3231.
 27. P. Mathur, "Analysis of the Spray Deposition Process", *Ph.D. Thesis*, Drexel University, Philadelphia (1988).
 28. E.A.Feest, R.D.Doherty and K. Holm, *Metal Trans.*, **4**, (1974) 115.
 29. D. Turnbull, *J. Appl. Phys.*, **21**, (1950) 1022 and D. Turnbull and R.E. Cech, *J. Appl. Phys.*, **21**, (1952) 804.
 30. B. Cantor and R.D. Doherty, *Acta metall.*, **27**, (1979) 33.
 31. R.T. Southin and G.A. Chadwick, *Acta metall.*, **26**, (1978) 223.
 32. J.H. Perepezko, *Mater. Sci. Eng.*, **65**, (1984) 125.
 33. M. Burger, E. Berg, S.H. Cho and A. Schatz, *Powder Metall. Int.*, **24**, (1992) 32.
 34. G. Jiang, H. Henein and M.W. Seigel, *Int. J. Powder Metall.*, **26**, (1990) 253.
 35. J.B. See and G. Johnston, *Powder Technol.*, **21**, (1978) 119.
 36. J.B. See, J.C. Runkle and T.B. King, *Metall. Trans.*, **4**, (1973) 2669.
 37. C. Seaton, H. Henein and M. Glatz, *Powder Metall.*, **30**, (1987) 37.
 38. A. Ünal, *Metall. Trans.*, **20B**, (1989) 2.
 39. O.S. Nichiporenko, et al., *Sov. Powder Metall. Met. Ceram.*, **7**, (1968) 1.
 40. V. Uhlenwinkel and K. Bauckhage, "Mass flux profile and local particle size in the spray cone during spray-forming of steel, copper and tin" ICSF II - Second International Conference on Spray Forming. (Sept 1993) Ed J.V.Wood, Woodhead Publishing Ltd., Abington Hall, Abington Cambridge CB1 6AH, UK.p.25.
 41. P. Haasen, *Physical Metallurgy*, Cambridge University Press, (1978).
 42. J.Clark, *Comm.ACM.*, **19** (1976) 547.
 43. M.C.Flemings, *Solidification Processing*, John Wiley (1974)
 44. R.D.Doherty and S. Annavarapu, *Annual Progress Report to ONR* Dr A.K. Vasudevan Program Manager Mechanics of Materials (contract # N 00014-89-J-1957-P0001 April 1993).
 45. R.D.Doherty, Chapter on Dendritic Growth, in *Crystal Growth*, ed B.Pamplin, Pergamon Press, Oxford U.K (1980) p. 485.
 46. S. Ashok, *Int. J. Powder Metall.*, **30**, (1994) 143.
 47. S. Annavarapu and R.D.Doherty, *Int. J. Powder Metall.*, **30**, (1994) 143.
 48. X.Liang and E. Lavernia, *Metal. Mater. Trans.*, **25A**, (1994) 2341.
 49. R.D.Doherty, E.A.Feest and Ho-In Lee, *Mater.Sci. and Eng.*, **65** (1984) 181.
 50. M. Gunduz and J.D. Hunt, *Acta Metall.*, **33** (1985) 1651.
 51. J.W.Martin and R.D.Doherty, *Stability of Microstructure in Metallic Systems*. Cambridge University Press, Cambridge U.K. (1976). Also 2nd Ed (1966) in Press
 52. S. Annavarapu, D.Apelian and A.Lawley, *Metall.Trans.*, **21A**, (1990) 3237.
 53. ICSF I - First International Conference on Spray Forming" (Sept 1990) Ed J.V.Wood., Osprey Metals, Red Jacket Works, Neath U.K. (Paper37).
 54. R. Kozarek, Private communications from Alcoa Technical Center (1994-6).
 55. S. Annavarapu and R.D.Doherty, *Acta Metall. and Mater*, **43** (1995) 3207.
 56. P.S.Grant, R.P.Underhill, W.T.Kim, K.P.Mingard and B.Cantor, "Grain Growth in Spray Formed Al.Alloys" ICSF II - Second International Conference on Spray Forming. (Sept 1993) Ed J.V.Wood, Woodhead Publishing Ltd., Abington Hall, Abington Cambridge CB1 6AH, UK.p.45.
 57. S.C.Hardy and P.W.Voorhees, *Metall.Trans.*, **19A**, (1988) 231.
 58. R.D.Doherty, "Diffusional Phase Transformations" in "Physical Metallurgy" Ed. R.W.Chan and P.Haasen, Elsevier Science B.V. Amsterdam (1966) p1633.

59. S. Annavarapu, J. Liu and R.D. Doherty, *Materials Science Forum*, **94-96**, (1991) p649.
60. G.T. Higgins, S. Wiryolukito and P. Nash, *ibid*, p671.
61. S.C. Yang, G.T. Higgins and P. Nash, *Mater. Sci. Technol.*, **8**, (1992) 10.
62. P.W. Voorhees, Private Communication (1996)
63. M.G. Benz, T.F. Sawyer, W.t. Carter R.J. Zaballa and P.L. Dupree, "Nitrogen in Spray Formed Superalloys" *ICSF II - Second International Conference on Spray Forming*. (Sept 1993) Ed J.V. Wood, Woodhead Publishing Ltd., Abington Hall, Abington Cambridge CB1 6AH, UK. p.171.
64. S. Ashok, Private Communication (1991).

Figure Captions

- Fig.1 Schematic of the experimental collection system used at NSWC for measurement of the radial variation of the particle size distribution (PSD) and mass distribution in a tall chamber with no substrate. The height was sufficient for all droplets to be fully solidified at the collector.
- Fig.2 PSD, in mass, for IN625 fully solidified droplets collected in all four rings. (Metal flow rate, MFR, of 0.30kg/s, gas metal ratio, GMR, of 0.75 kg/kg and a superheat ΔT_s of 120K. The mass-median diameter, d_m , was 172 μ m and the standard deviation was 2.17.
- Fig.3 PSD, in mass, for HSLA fully solidified droplets collected in all four rings. (MFR of 0.25kg/s, GMR of 0.84 kg/kg and a superheat ΔT_s of 60K. The mass median diameter, d_m , was 197 μ m and the standard deviation was 2.30.
- Fig.4 PSD, in mass, for Cu-6wt%Ti fully solidified droplets collected in all four rings. (MFR of 0.32kg/s, GMR of 0.68kg/kg and a superheat ΔT_s of 120K. The mass median diameter, d_m , was 106 μ m and the standard deviation was 2.68.
- Fig.5 The experimentally determined variation of the mass median diameter, d_m , with the process parameters in the atomization studies carried out in collaboration with David Taylor. Three empirical coorelations are shown, Lubanska, Miller - Giles and the new correlation developed in this study, given in the text as eq.1.
- Fig.6 The fitted experimental data for (a) the mass-median diameter, d_m , (in μ m) and (b) the log- normal standard deviation, ($\ln \sigma$ in μ m) as a function of atomizing gas pressure and the Gas:Metal Ratio for IN625 at a constant superheat of 120°C.
- Fig.7 The fitted experimental data for (a) the mass-median diameter, d_m , (in μ m) and (b) the log- normal standard deviation, ($\ln \sigma$ in μ m) as a function of atomizing gas pressure and the Gas:Metal Ratio for Cu-6wt%Ti at a constant superheat of 120°C.
- Fig.8 The fitted experimental data for (a) the mass-median diameter, d_m , (in μ m) and (b) the log- normal standard deviation, ($\ln \sigma$ in μ m) as a function of atomizing gas pressure and superheat for Cu-6wt%Ti at a constant Gas:Metal Ratio of 0.89.
- Fig.9 The particle size distributions for Cu-6wt%Ti at a constant Gas:Metal Ratio of 0.68 a metal flow rate of 0.32kg/s and a superheat of 120°C for the collection system seen in fig 1.
- Fig.10 The radial variation of the mass-median particle diameter and the log normal standard deviation for Cu-6wt%Ti at a constant Gas:Metal Ratio of 0.68 a metal flow rate of 0.32kg/s and a superheat of 120°C.

- Fig. 11 The radial variation of the mass-medium particle diameter and the log normal standard deviation for HSLA80 at a constant Gas:Metal Ratio of 0.84 a metal flow rate of 0.25kg/s and a superheat of 60°C.
- Fig. 12 The radial variation of the mass-medium particle diameter and the log normal standard deviation for IN 625 at a constant Gas:Metal Ratio of 0.75 a metal flow rate of 0.3kg/s and a superheat of 120°C.
- Fig. 13 Empirical fit of the experimental data for the radial mass distribution with the parameters A, B and C of eq. 2 with the process parameters. R_{max} is the radial distance with the highest area weighted deposition rate.
- Fig. 14 The effect of atomizing gas pressure and metal flow rate on the parameters A, axial deposition rate, and B, radial spread, of eq.2 for IN 625 at a constant superheat of 120°C.
- Fig. 15 The effect of atomizing gas pressure and melt superheat on the parameters A, axial deposition rate, and B, radial spread, of eq.2 for Cu-6wt% Ti at a constant metal flow rate of 0.24kg/s.
- Fig. 16 The effect of metal flow rate on the background deposition rate, the C parameter of eq.2, for all three alloys.
- Fig. 17 The variation of axial velocity of the Osprey Gas jet of Nitrogen with atomization pressure and flight distance, no liquid metal and no substrate.
- Fig. 18 The radial variation of nitrogen gas velocity normalized to the axial gas velocity as a function of the atomizer diameter (d_s is 39mm); At flight distances of (a) 70mm (b) 125 mm (c) 200 (d) 300 and (e) 400mm. The atomization gas pressure of 4 to 9 bar has a negligible influence on the normalized axial variation of velocity. The radius of the jet, R_{jet} , taken where the axial normalized velocity has fallen to 0.5 is indicated.
- Fig. 19 The normalized velocity, v/v_m , where v_m is the axial velocity against the normalized radius, $r/r_{0.5}$, where $r_{0.5}$ is R_{jet} , at increasing axial distances x , 70 to 400mm.
- Fig. 20 The radius of the jet, R_{jet} taken where the axial normalized velocity has fallen to 0.5, as a function of flight distance.
- Fig. 21 Variation of axial velocity with flight distance, normalized to mach 1 (354m/s), compared to previous reported variations.
- Fig. 22 Near substrate gas velocity at a tilted substrate at a flight distance, used for billet, production of 350mm.
- Fig. 23 Equilibrated Al-4wt%Cu solid fraction at axial spray heights of 0.2, 0.3 and 0.4m as a function of (a) Initial axial gas velocity at a metal flow rate of 0.025kg/s and a melt superheat of 150°C. (b) Metal flow rate in kg/s at an initial axial gas velocity of 150m/s and a melt super heat of 150°C and (c) Melt superheat (in °C) at an initial axial gas velocity of 150m/s and a metal flow rate of 0.025kg/s. (After Grant et al.[4])

- Fig.24 Numerically computed and experimentally measured, using infrared imaging, deposit temperatures as a function of time during spray forming of Al-4wt%Cu at two axial spray heights. (After Grant [5])
- Fig.25 Predicted variation of droplet velocity for Ni-20wt% Cr droplets of different diameters with flight distance along the spray axis. From Mathur et al.[2].
- Fig.26 Dependence of the degree of undercooling on droplet volume for these alloys measured from droplet impacts on glass slides passed through the spray at different flight distances. After Mathur [27].
- Fig.27 Surface morphologies showing evidence of droplet collisions (a) in Cu-6wt% Ti and (b) IN625.
- Fig.28 Sectioned droplets showing an apparent nucleation event in the larger droplet by impact of the, captured, small pre-solidified droplet while the larger droplet was undercooled.
- Fig.29 Schematic showing the modeling rules assumed for the collision of two droplets.
- Fig 30. Average number of droplet collisions occurring in each millisecond as a function of time.
- Fig 31. Average number of absorption events through coalescence occurring in each millisecond as a function of time.
- Fig 32. Average number of nucleation events occurring by impact of a solid droplet on an undercooled liquid droplet occurring in each millisecond as a function of time.
- Fig. 33 Scatter plot of the dimensionless degree of undercooling ($\Delta T/\Delta T_c$) as a function of droplet diameter.
- Fig.34 The mean dimensionless degree of undercooling ($\Delta T/\Delta T_c$) as a function of droplet diameter as modeled compared to the experimental data of Mathur [27].
- Fig.35 Predicted change of the particle size distribution due to droplet collisions during flight of 0.4m assuming the maximum possible absorption of droplets by capture according to the rules of fig. 29.
- Fig.36 : Finite element representatirion of a preform surface with two parameters u and v .
- Fig.37 Schematic showing how the local normal growth rate, \dot{G}_n , determines the incremental displacement, Δp , along the normal direction \mathbf{n} at a location \mathbf{p} on the surface during a time step Δt .
- Fig. 38 Predicted thickness profile of a spray deposited sheet formed by a linear atomiser (aligned in the y direction) while the substrate was moving with a linear displacement in the x direction.

- Fig.39 Example of a 3-D shape predicted using the shape model for a tube with multiple segments of varying diameters. The substrate shape was defined directly in CAD software and then interfaced with the model using the motion planner.
- Fig. 40 Elbow making strategy using rotation, longitudinal to the curve of the elbow, to maintain a constant spray height. (a) Schematic of the substrate motions. (b) Predicted shapes and cross sections.
- Fig.41 Elbow making strategy using translations axial to the elbow and perpendicular to axial of the elbow to maintain a constant spray height and to give a more constant wall thickness. (a) Schematic of the substrate motions. (b) Predicted shapes and cross sections.
- Fig.42 Flow chart of the Drexel model of the spray forming process showing the preset input parameters, the empirically determined parameters and the predicted outputs of the model.
- Fig.43 The PSD found for Cu-6wt%Ti sprayed into the outer ring of a collector system with and without a substrate that intercepted material in flight towards the inner collector rings.
- Fig.44 The data of fig.43 replotted to show the deviation from the log-normal distribution in the presence of a substrate. Additional data from a further run with the substrate rotating is also shown.
- Fig.45 Use of the three dimensional shape model for studies of the spray forming of a billet of Cu-6wt%Ti. The deposition lasted 48 seconds at a metal flow rate of 0.18kg/s an atomizing gas pressure of 10 bar a superheat of 110°C and a substrate withdrawal rate of 1mm/s.
- Fig.46 The shape predicted by the three dimensional shape model for a Cu-6wt% Ti billet deposited for 48 seconds at a metal flow rate of 0.18kg/s an atomizing gas pressure of 10 bar a superheat of 110°C, a substrate withdrawal rate of 1mm/s and a rotation of 185 rpm. The Spray model predicted a fraction liquid in the spray of 0.20.
- Fig.46 The predicted cross-section profiles of the billet shown in fig.46 at 4s time intervals of deposition.
- Fig. 47 Comparison of the predicted shape for two different assumed values of the sticking efficiency, 0.7 and 0.8, with the measured shape of the experimental billet of fig. 46.
- Fig.48 Effect of variation of the withdrawal rate on the predicted shapes of the billets produced under the other operating conditions of fig. 46.
- Fig. 49 Comparison of the predictions of the Shape Model with experimental results for Cu-6wt%Ti billets sprayed under a range of experimental conditions designed to yield a range of liquid fractions in the spray. Different assumed sticking efficiencies (SE) are illustrated. The elongated experimental shape of the billet at a fraction liquid of 0.16 (16%) arose from the accidental use of a significantly higher substrate withdrawal rate, see Fig.48. The Shape model has had no difficulty in matching this.

- Fig.50 The Three Dimensional Model predicted shape for an IN 625 tube produced after 107s of deposition time.
- Fig. 51 The recorded variation of four of the major process variables for the IN 625 tube shown in Figs 50.
- Fig. 52 The predicted cross sections of the IN625 tube seen in Fig.50 after 8s time intervals from the start of deposition.
- Fig. 53. Comparison of the predictions of the Shape Model for four IN625 Tubes sprayed at NSWCC for the conditions shown. The overall sticking efficiencies (SE) required to achieve the match with the experimental shapes is also shown.
- Fig.54 Variation of the sticking efficiency, measured from experimental runs in comparison to the prediction of the Shape Model with the designed Fraction Liquid (as %) in the spray as predicted by the Spray Model. Cu-6wt% Billets spray formed at the Osprey facility at Drexel University.
- Fig.55 Variation of the sticking efficiency, measured from experimental runs in comparison to the prediction of the Shape Model with the Fraction Liquid in the spray as predicted by the Spray Model. Data for IN625 spray formed at NSWCC at two different madre/substrate rotation rates together with one data point determined from data supplied by Sandvik at the lowest rotation speed.
- Fig.56 Billet temperatures at the top surface as predicted by the two dimensional thermal model for five of the Cu-Ti experiments at different liquid fractions in the spray.
- Fig 57 Predicted temperature contours after 5, 15 and 20s deposition of Cu-6wt%Ti at a fraction liquid in the spray of 0.19 (20% in Fig.56) showing the depth of the semi-solid region at the top of the ingot.
- Fig.58 Predicted local solidification times for two Cu-6wt%Ti billets sprayed at two different liquid fractions (a) 0.19 and (b) 0.49.
- Fig.59 Computed isotherms for an IN 625 tube deposited at NSWCC at a fraction liquid, in the spray, of 0.46. The geometry is indicated in the cartoon. The solid line in the deposit makes the predicted solidus isotherm where the fraction liquid reaches zero.
- Fig.60 Comparison of the model predictions and pyrometer measurements of the surface temperature, under the spray, for IN625 deposited at NSWCC at a fraction liquid, in the spray, of 0.5. The alloy liquidus and solidus temperatures are indicated.
- Fig.61 Predicted solidification times along the axial distance of the IN625 tube spray formed as shown in Fig.60. The axial distance of zero is the starting position of the center of the spray. The short curve from about 95 to 145mm is that at a radial distance of 31.5mm from the inner surface of the tube and is close to the outer surface. (The shape of the tube is similar to that at run #247 in Fig.53)

- Fig.62 Microstructure produced in spray formed billets of Cu-6wt%Ti billets at heights of 25mm from the substrate in the center of the billets at two different fractions liquid in the spray. (a) f_l of 0.19 with a solidification time of 18s giving a grain size of $19\mu\text{m}$ and (b) f_l of 0.49 with a solidification time of 206s giving a grain size of $46\mu\text{m}$. The reduced fine scale porosity at the higher fraction liquid is also clearly visible (measured at 5% and 1%). The positions observed are those indicated in fig. 58, describing the thermal model.
- Fig.63 Dendrite fragmentation of a Cobalt alloy, MP35N, during spray forming. From independent work by R.P. Singh at Drexel University.
- Fig.64 (a) The variation of grain size and (b) the variation of solidification time at an axial location in Cu-6wt%Ti billets 25 mm from the substrate both plotted against the fraction liquid in the spray. Two different attempts to model the change of grain size are also shown.
- Fig. 65 Variation of grain size (in μm) with position in Cu-6wt%Ti billets formed with different liquid fractions in the spray
- Fig. 66 Interconnected non spherical pores found here between subsequent layers in a Cu-6%Ti billet arising from enhanced gas cooling due here to incorrect substrate motion - the fraction liquid in the spray was 0.2.
- Fig. 67 High levels of porosity seen close to the substrate surfaces in a tube of In 625. The positions shown are described in fig.70.
- Fig. 68 Fine scale pores seen mainly but not universally at grain boundaries in the spray formed deposit. Cu-6wt%Ti billet sprayed at a fraction liquid of 0.26.
- Fig. 69 Large spherical pores seen mainly in deposits formed at at very high liquid fractions. Cu-6wt%Ti billet sprayed at a fraction liquid of 0.6.
- Fig. 70 Variation in porosity along the length of three IN626 tubes. The microstructures at positions Q and R in run 222 were previously shown in fig.67.
- Fig. 71 Variation in porosity along the length of the three IN625 tubes seen in Fig.70 - but measured on slant samples to give for each position a full sampling of the different radial positions in the tube.
- Fig. 72 Variation in porosity along a further IN 625 tube - the tube previously shown in figs. 50-52, with a fraction liquid of 0.50.
- Fig. 73 Variation of average porosity for IN 625 tubes, avoiding the transient regions at start and end of the tube, as a function of fraction liquid *in the spray*.
- Fig.74 Density distribution in spray form billets of Cu-6wt5 Ti at different liquid fractions.
- Fig. 75 Variation of average porosity for Cu-6wt%Ti billets as a function of fraction liquid in the spray.

Fig. 76 Normalized coarsening rate constant, K_{exp}/K_d , as a function of fraction solid, f_s , for three spray formed alloys AA 2014, Cu-4%Ti and IN625.

Table 1

The range of Osprey run conditions for Cu-6wt% Ti billets sprayed at Drexel University

Table 2

The range of Osprey run conditions for IN625 Tubes sprayed at NSWC.

EXPERIMENTAL SETTINGS

Metal Flow Rate:	0.08~0.37 kg/s
Atomizing Gas Pressure:	6~10.5 bar (87~152 psi)
Gas:Metal Ratio:	0.5~3.5 kg/kg
Melt Superheat:	100~170°C
Spray Height:	350 mm
Substrate Diameter:	120 mm
Rotation Speed:	180~185 rpm
Withdrawal Rate:	0.75~2 mm/s
Deposition Time:	20~80 s
Deposition Yield:	50-77 %

MODEL PREDICTIONS

Spray Liquid Fraction:	10~47 %
Droplet Mean Diameter:	55~155 μm
Maximum Deposition Rate:	4~32 mm/s
Target Efficiency:	65~95 %
Sticking Efficiency:	65~89 %

Table 1

The range of Osprey run conditions for Cu-6wt% Ti billets sprayed at Drexel University

EXPERIMENTAL SETTINGS

Metal Flow Rate:	0.28~0.89 kg/s
Atomizing Gas Pressure:	6~10 bar (87~145 psi)
Gas:Metal Ratio:	0.24~0.7 kg/kg
Melt Superheat:	100~120°C
Spray Height:	450~700 mm
Substrate Diameter:	120~191 mm
Rotation Speed:	180~240 rpm
Withdrawal Rate:	1.8~7.8 mm/s
Deposition Time:	24~144 s
Deposition Yield:	31-78 %

MODEL PREDICTIONS

Spray Liquid Fraction:	43~72 %
Droplet Mean Diameter:	160~280 μ m
Maximum Deposition Rate:	13~45 mm/s
Target Efficiency:	65~99 %
Sticking Efficiency:	45~78 %

Table 2

The range of Osprey run conditions for IN625 Tubes sprayed at NSW.

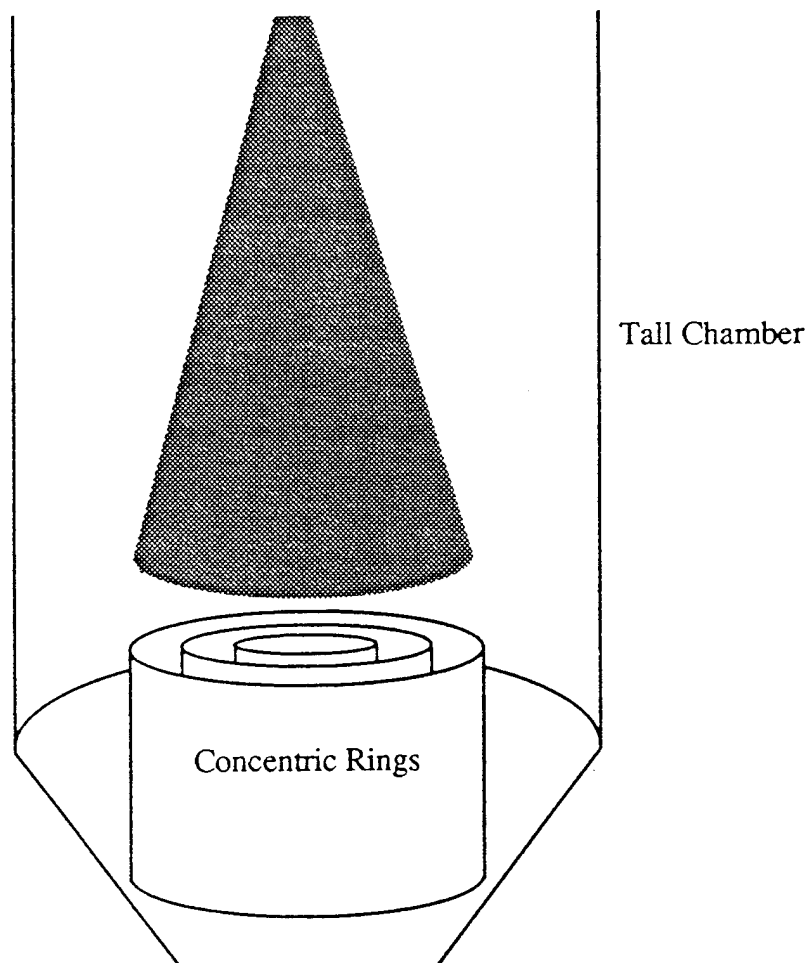


Fig.1 Schematic of the experimental collection system used at NSWC for measurement of the radial variation of the particle size distribution (PSD) and mass distribution in a tall chamber with no substrate. The height was sufficient for all droplets to be fully solidified at the collector.

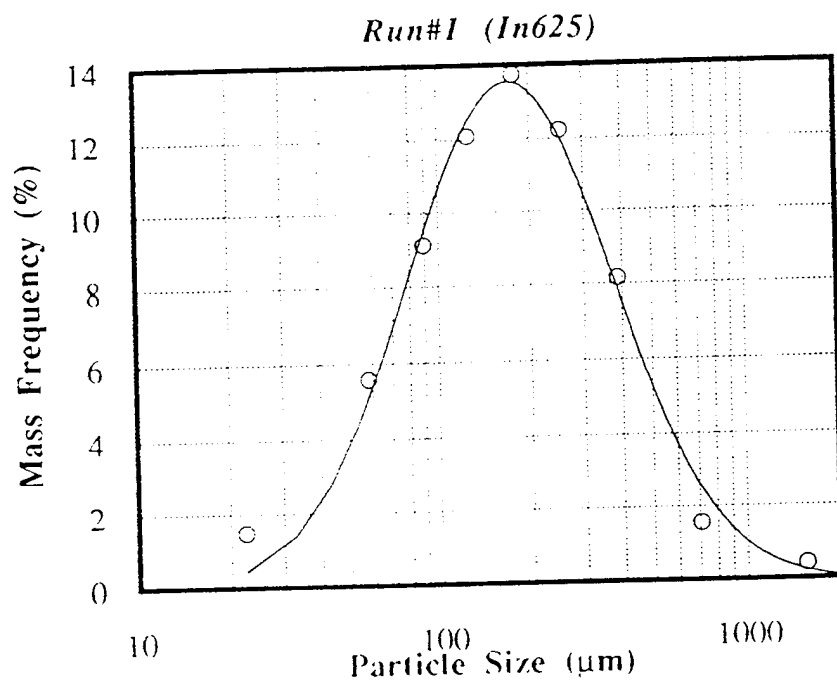


Fig.2 PSD, in mass, for IN625 fully solidified droplets collected in all four rings. Metal flow rate, MFR, of 0.30kg/s, gas metal ratio, GMR, of 0.75 kg/kg and a superheat ΔT_s of 120K. The mass-median diameter, d_m , was 172 μm and the standard deviation was 2.17.

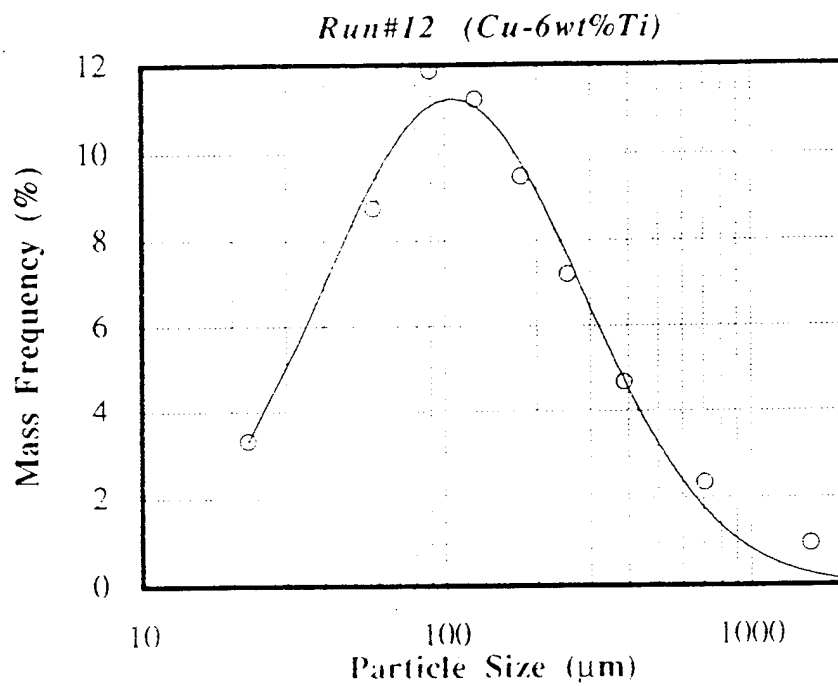


Fig.3 PSD, in mass, for HSLA fully solidified droplets collected in all four rings. MFR of 0.25kg/s, GMR of 0.84 kg/kg and a superheat ΔT_s of 60K. The mass median diameter, d_m , was 197 μm and the standard deviation was 2.30.

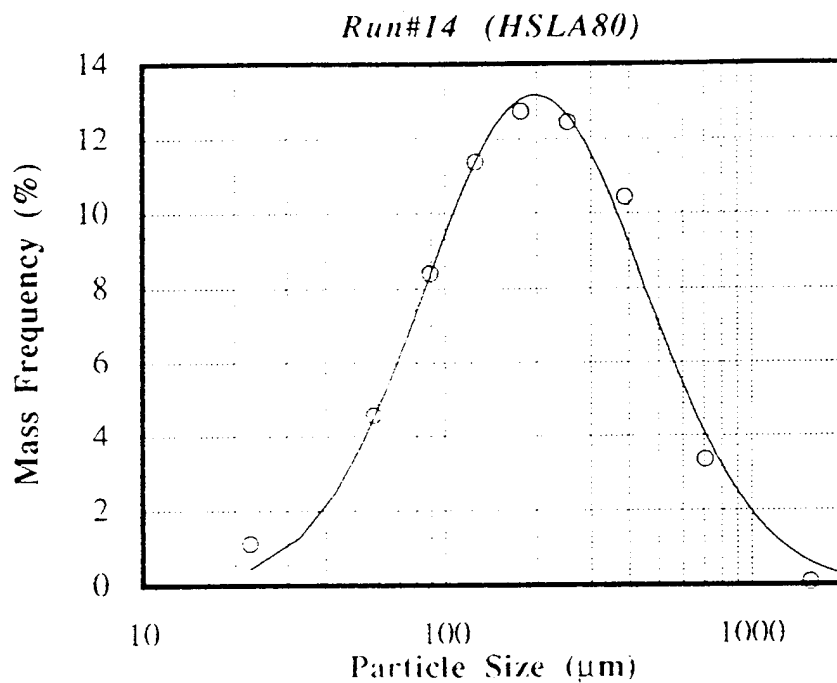


Fig.4 PSD, in mass, for Cu-6wt%Ti fully solidified droplets collected in all four rings. (MFR of 0.32kg/s, GMR of 0.68kg/kg and a superheat ΔT_s of 120K. The mass median diameter, d_m , was 106 μm and the standard deviation was 2.68.

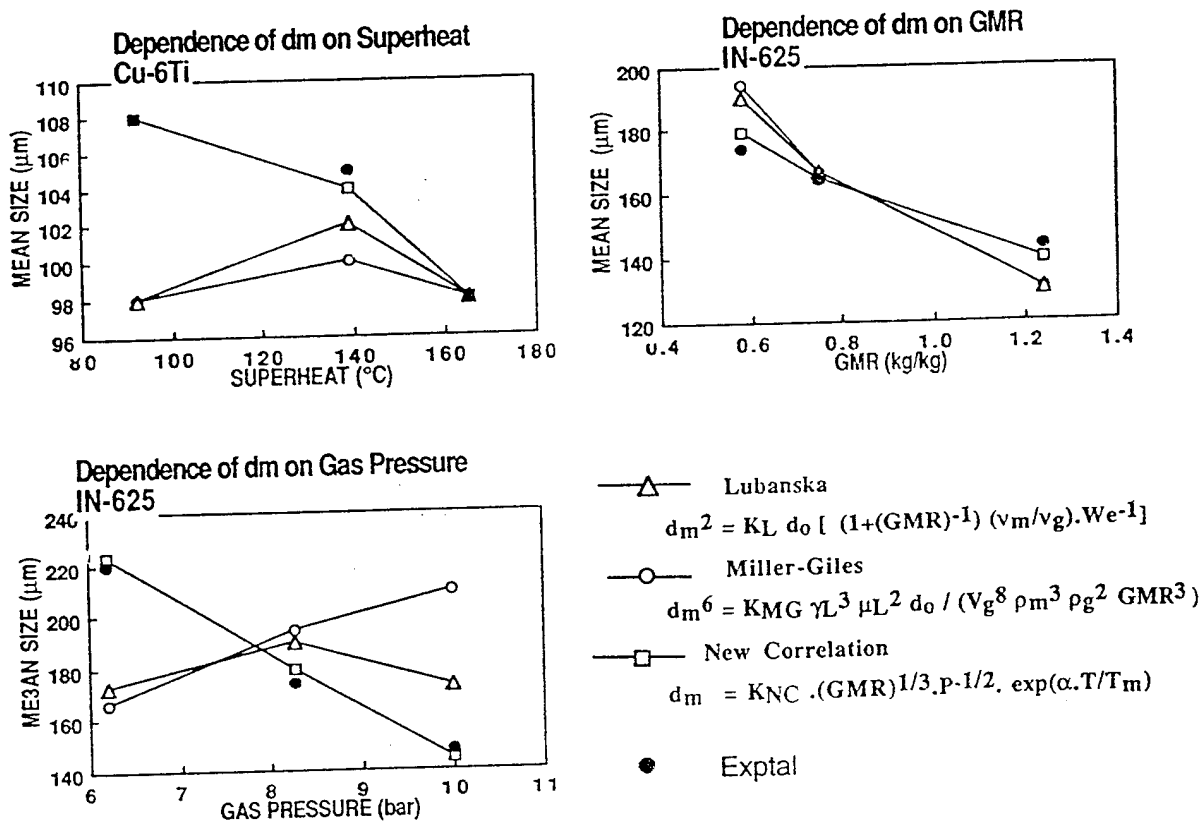
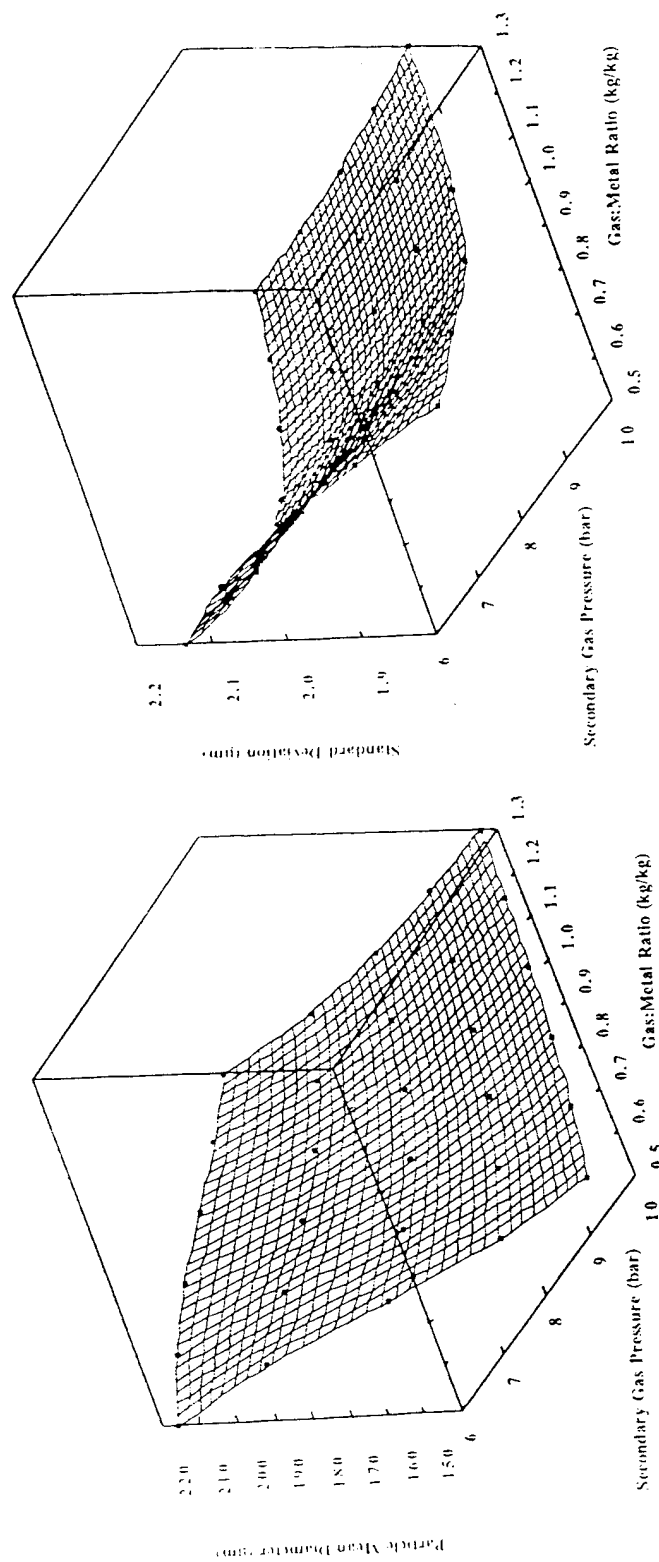


Fig.5

The experimentally determined variation of the mass median diameter, d_m , with the process parameters in the atomization studies carried out in collaboration with David Taylor. Three empirical correlations are shown, Lubanska, Miller - Giles and the new correlation developed in this study, given in the text as eq.1.

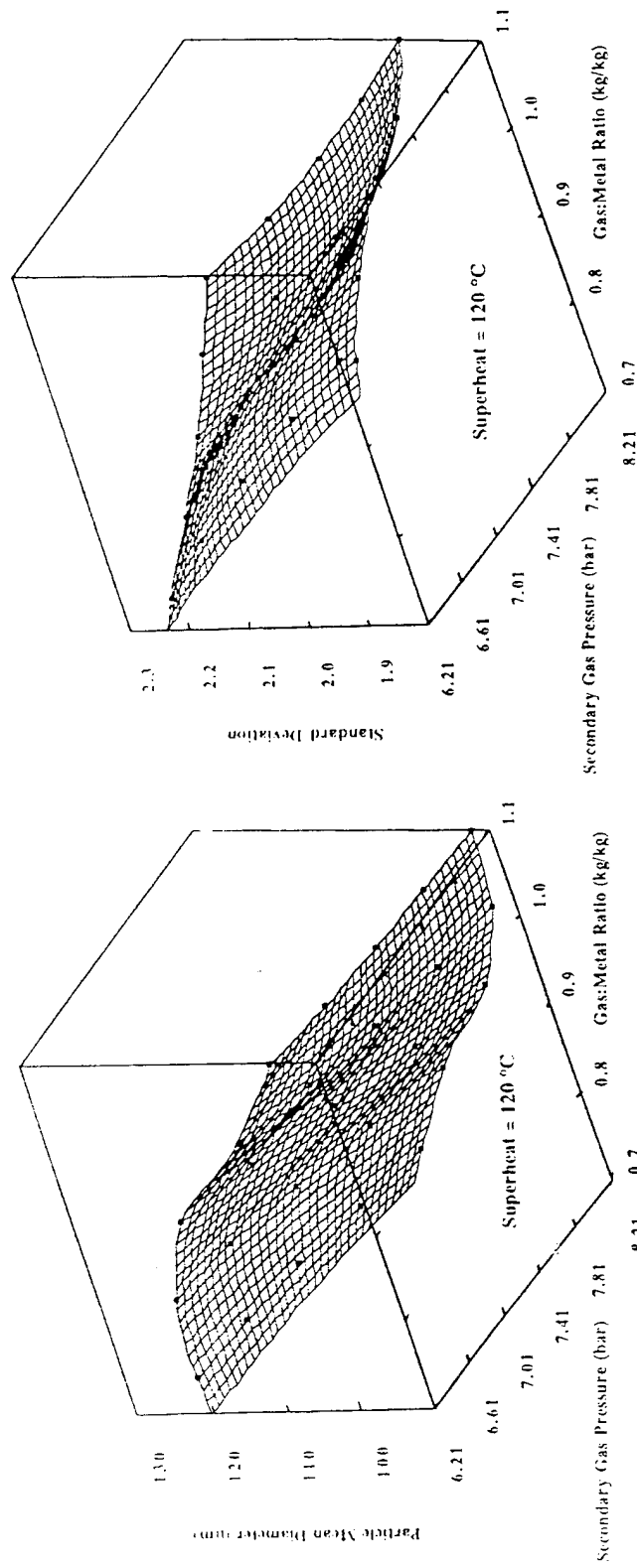


(a)

(b)

Fig.6

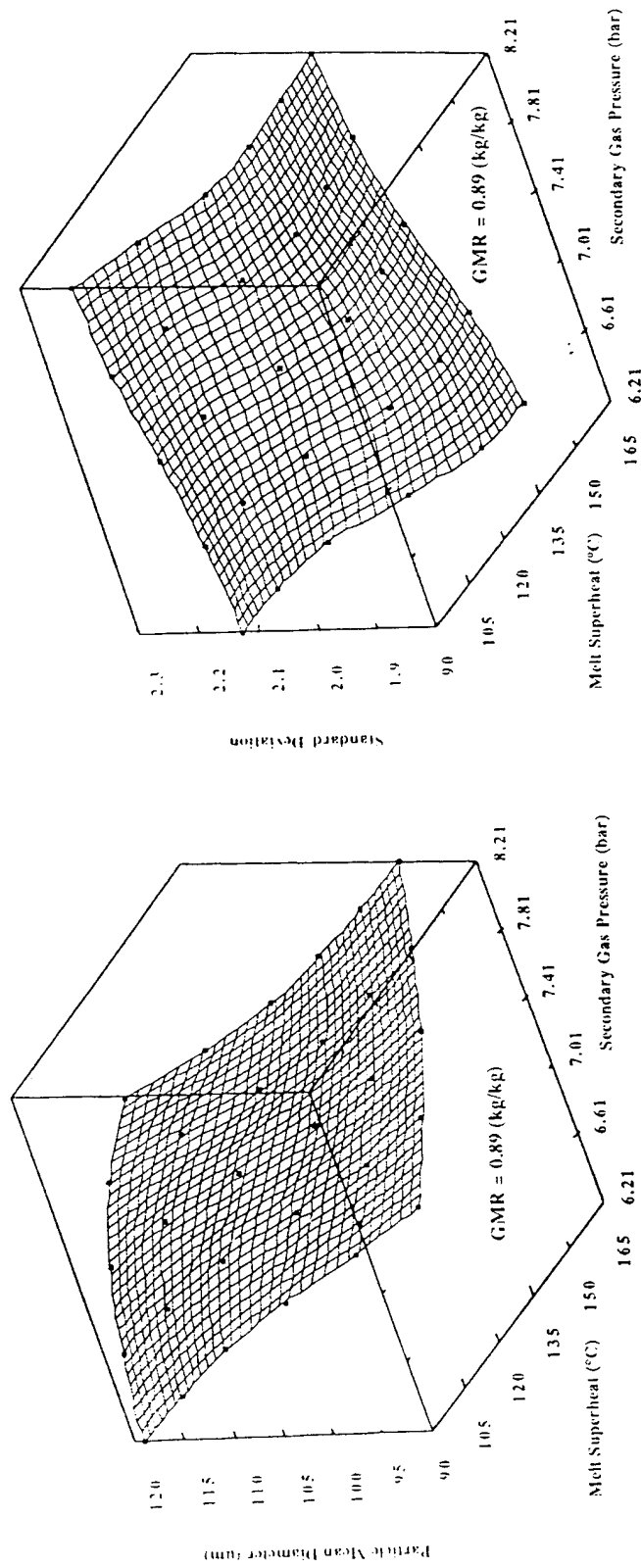
The fitted experimental data for (a) the mass-median diameter, d_m , (in μm) and (b) the log-normal standard deviation, ($\ln \sigma$ in μm) as a function of atomizing gas pressure and the Gas: Metal Ratio for IN625 at a constant superheat of 120°C.



(a)

(b)

Fig.7 The fitted experimental data for (a) the mass-median diameter, d_m , (in μm) and (b) the log- normal standard deviation, ($\ln \sigma$ in μm) as a function of atomizing gas pressure and the Gas: Metal Ratio for Cu-6wt%Ti at a constant superheat of 120°C.



(a)

(b)

Fig.8 The fitted experimental data for (a) the mass-median diameter, d_m , (in μm) and (b) the log-normal standard deviation, ($\ln \sigma$ in μm) as a function of atomizing gas pressure and superheat for Cu-6wt%Ti at a constant Gas: Metal Ratio of 0.89.

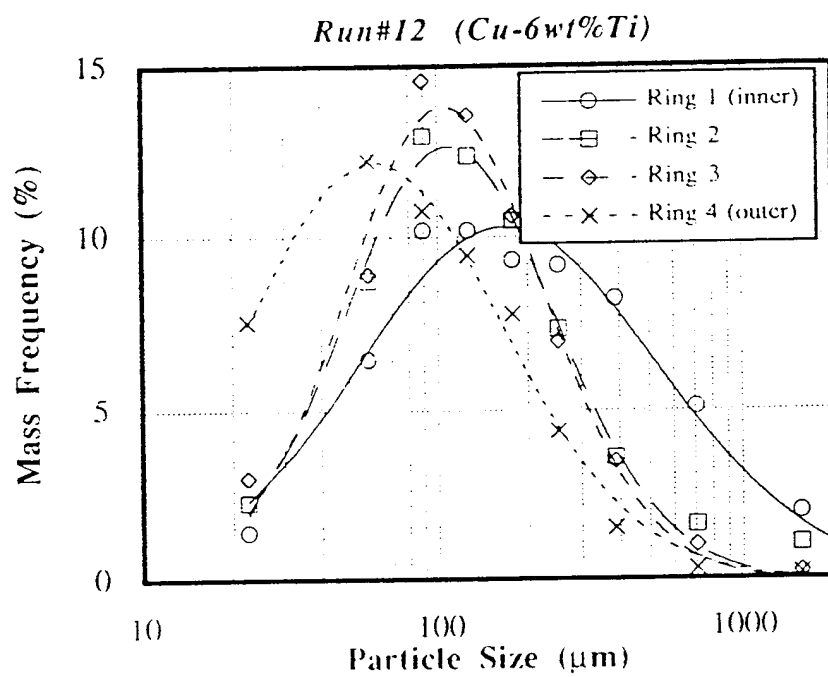


Fig.9 The particle size distributions for Cu-6wt%Ti at a constant Gas:Metal Ratio of 0.68 a metal flow rate of 0.32kg/s and a superheat of 120°C for the collection system seen in fig 1.

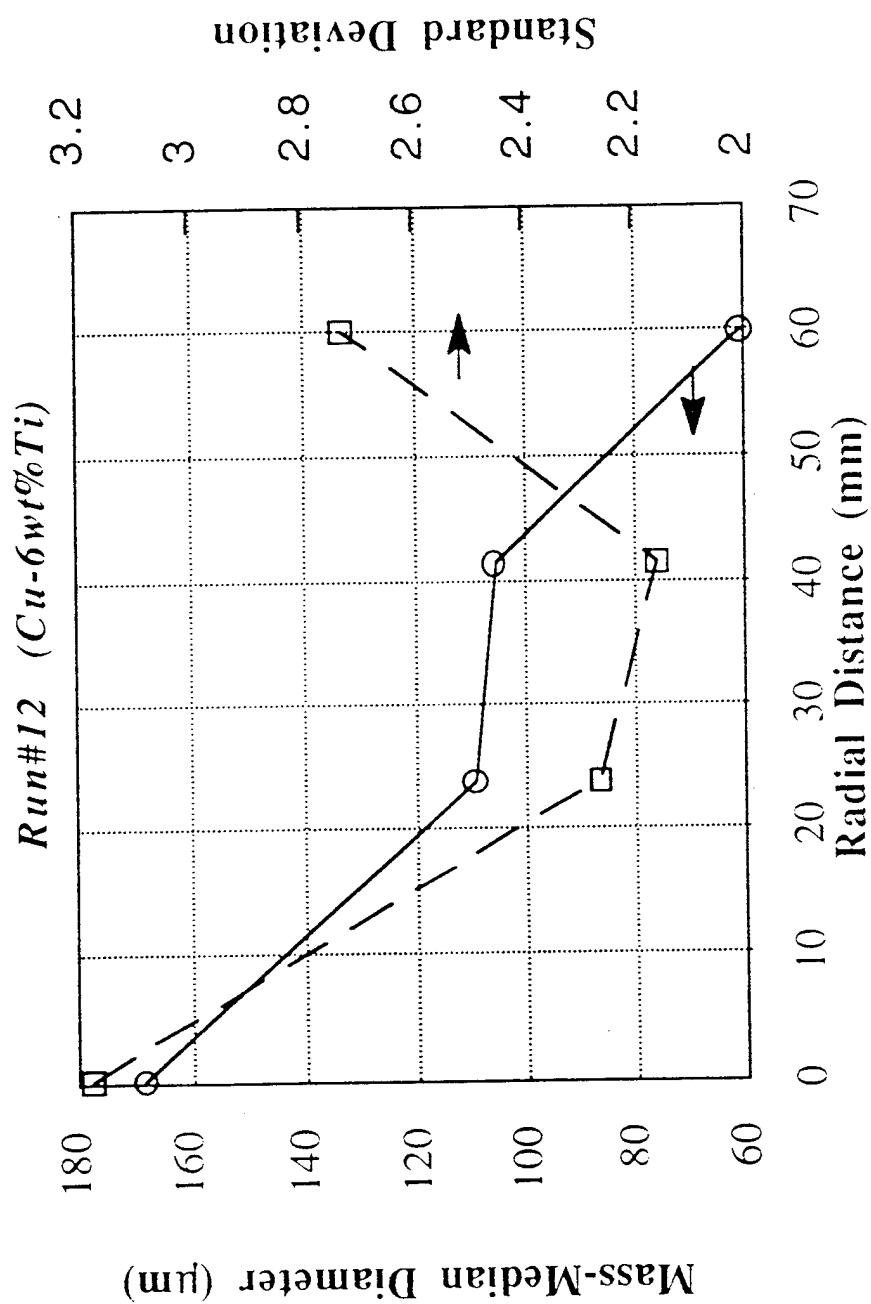


Fig.10 The radial variation of the mass-medium particle diameter and the log normal standard deviation for Cu-6wt%Ti at a constant Gas: Metal Ratio of 0.68 a metal flow rate of 0.32kg/s and a superheat of 120°C.

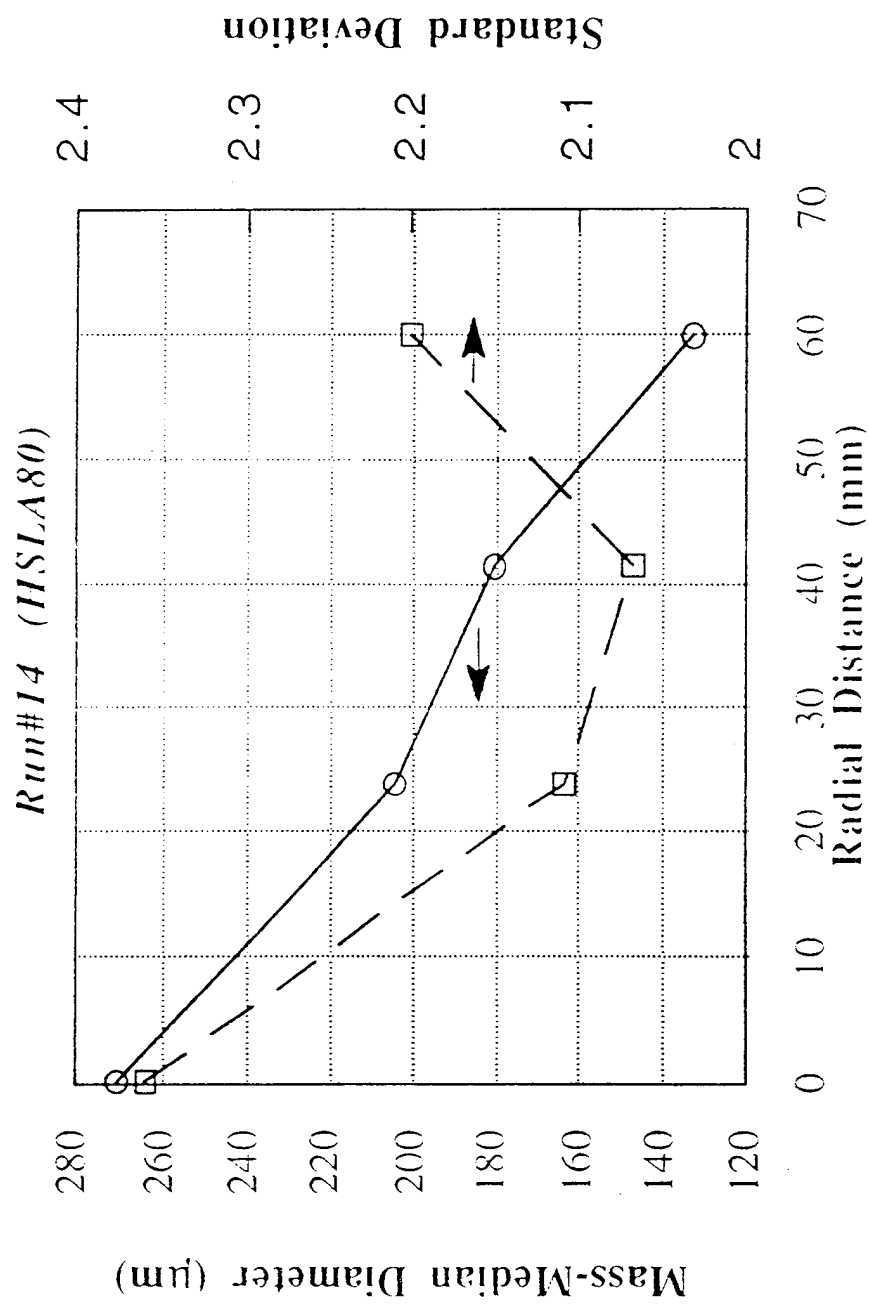


Fig. 11 The radial variation of the mass-medium particle diameter and the log normal standard deviation for HSLA80 at a constant Gas: Metal Ratio of 0.84 a metal flow rate of 0.25kg/s and a superheat of 60°C.

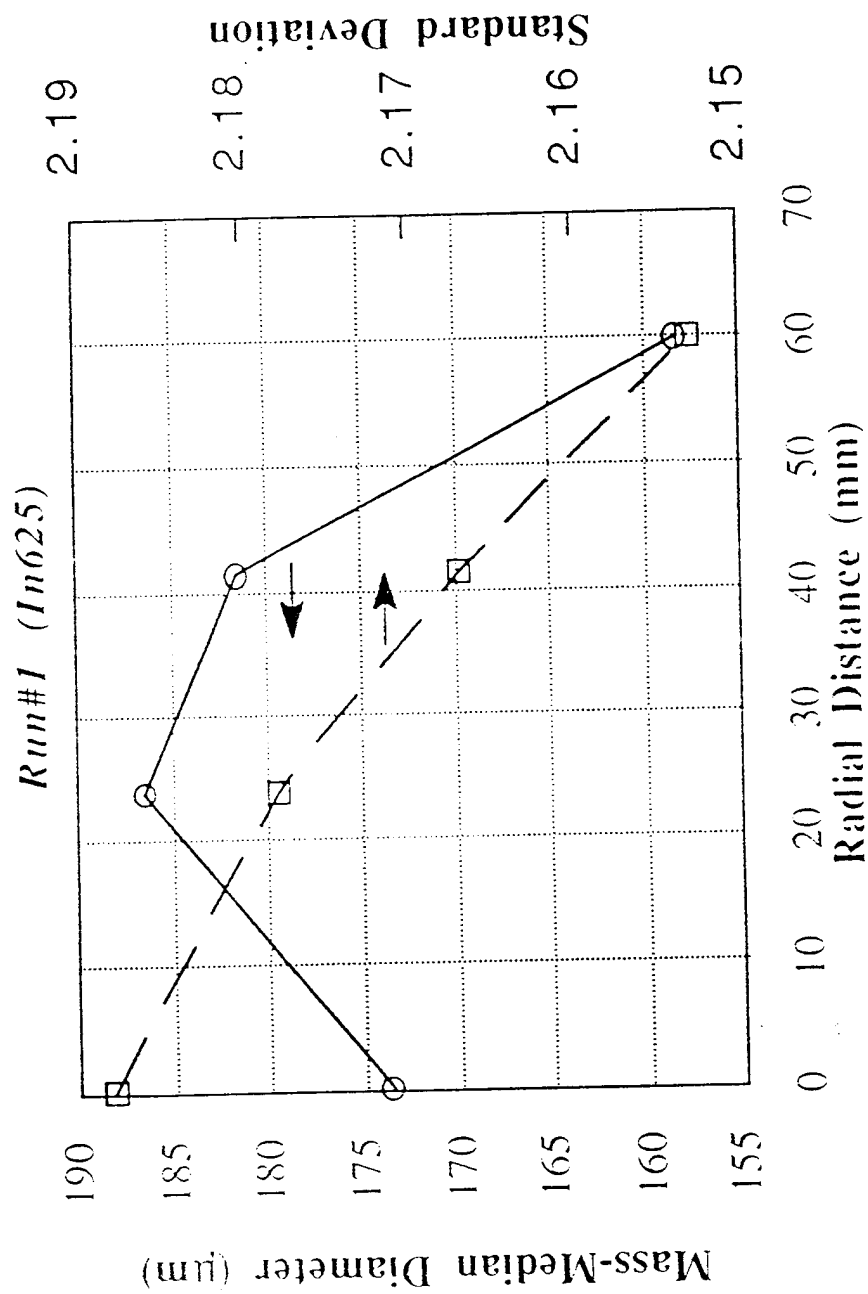


Fig.12 The radial variation of the mass-medium particle diameter and the log normal standard deviation for IN 625 at a constant Gas:Metal Ratio of 0.75 a metal flow rate of 0.3kg/s and a superheat of 120°C.

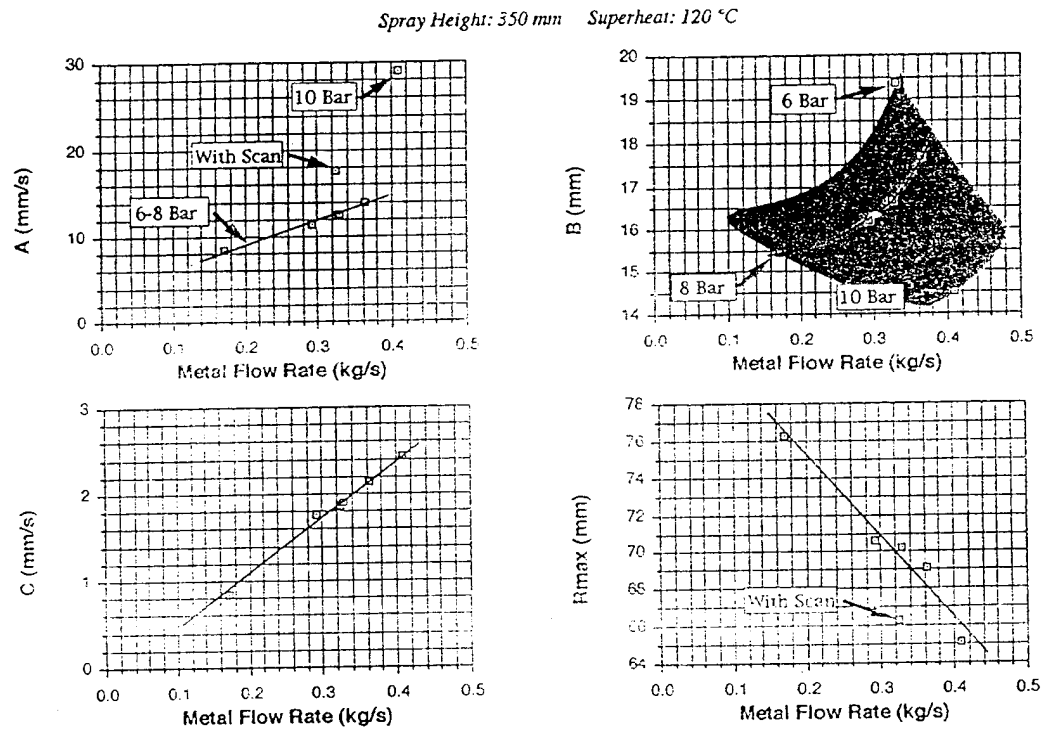
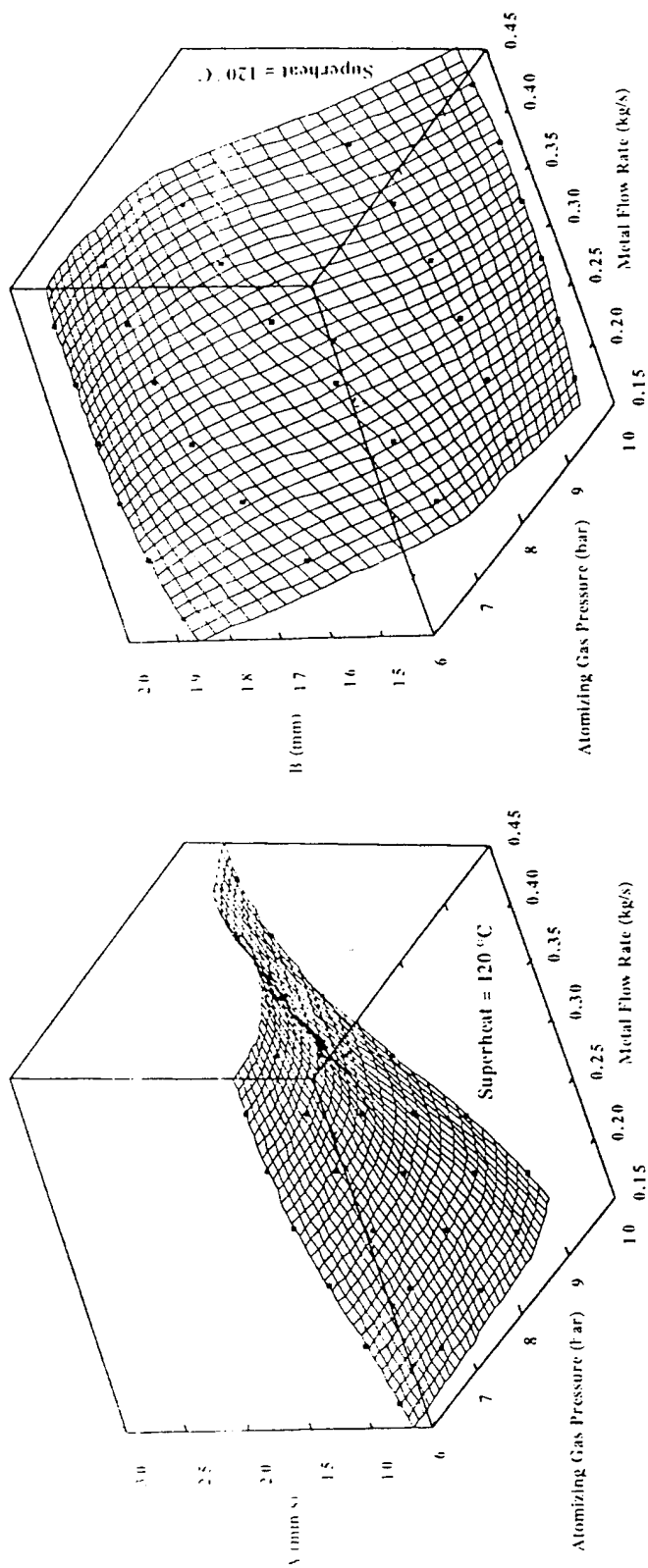


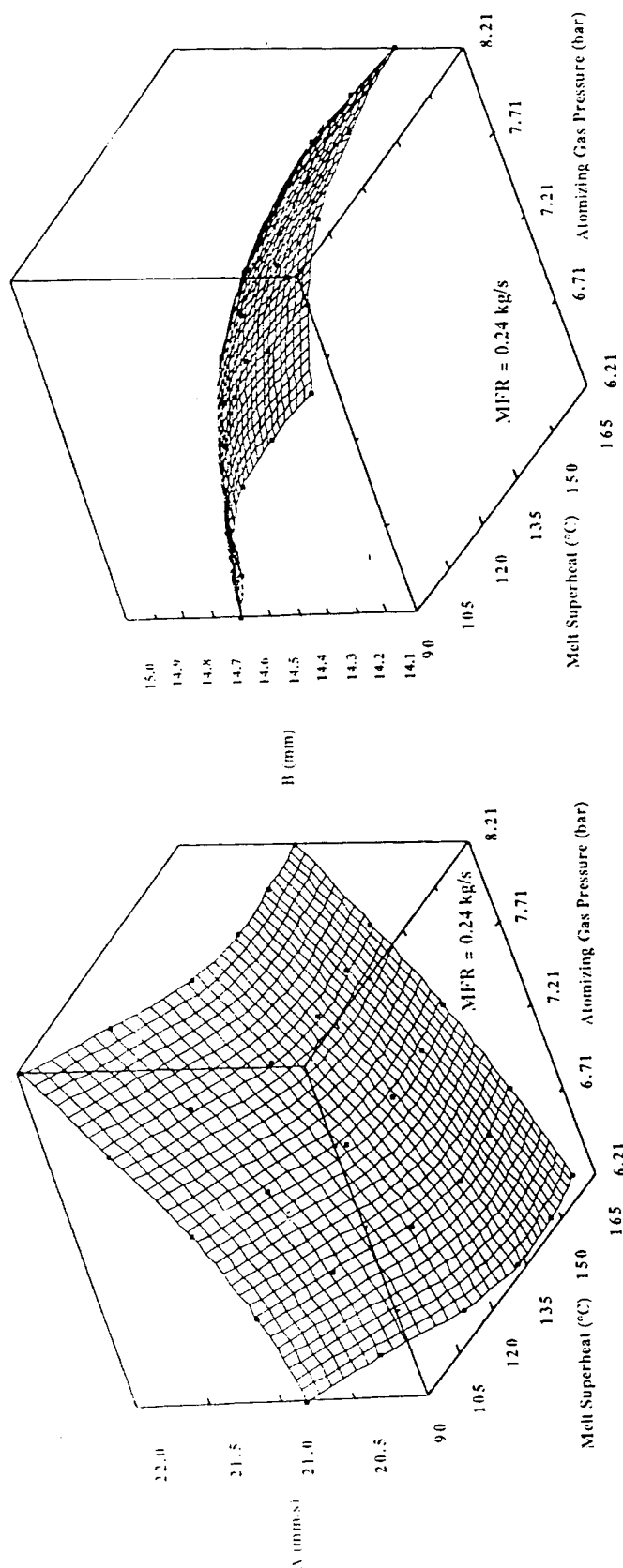
Fig. 13 Empirical fit of the experimental data for the radial mass distribution with the parameters A, B and C of eq. 2 with the process parameters. R_{\max} is the radial distance with the highest area weighted deposition rate.



(a)

(b)

Fig. 14 The effect of atomizing gas pressure and metal flow rate on the parameters A, axial deposition rate, and B, radial spread, of eq.2 for IN 625 at a constant superheat of 120°C.



(a)

(b)

Fig. 15 The effect of atomizing gas pressure and melt superheat on the parameters A, axial deposition rate, and B, radial spread, of eq.2 for Cu-6wt% Ti at a constant metal flow rate of 0.24kg/s.

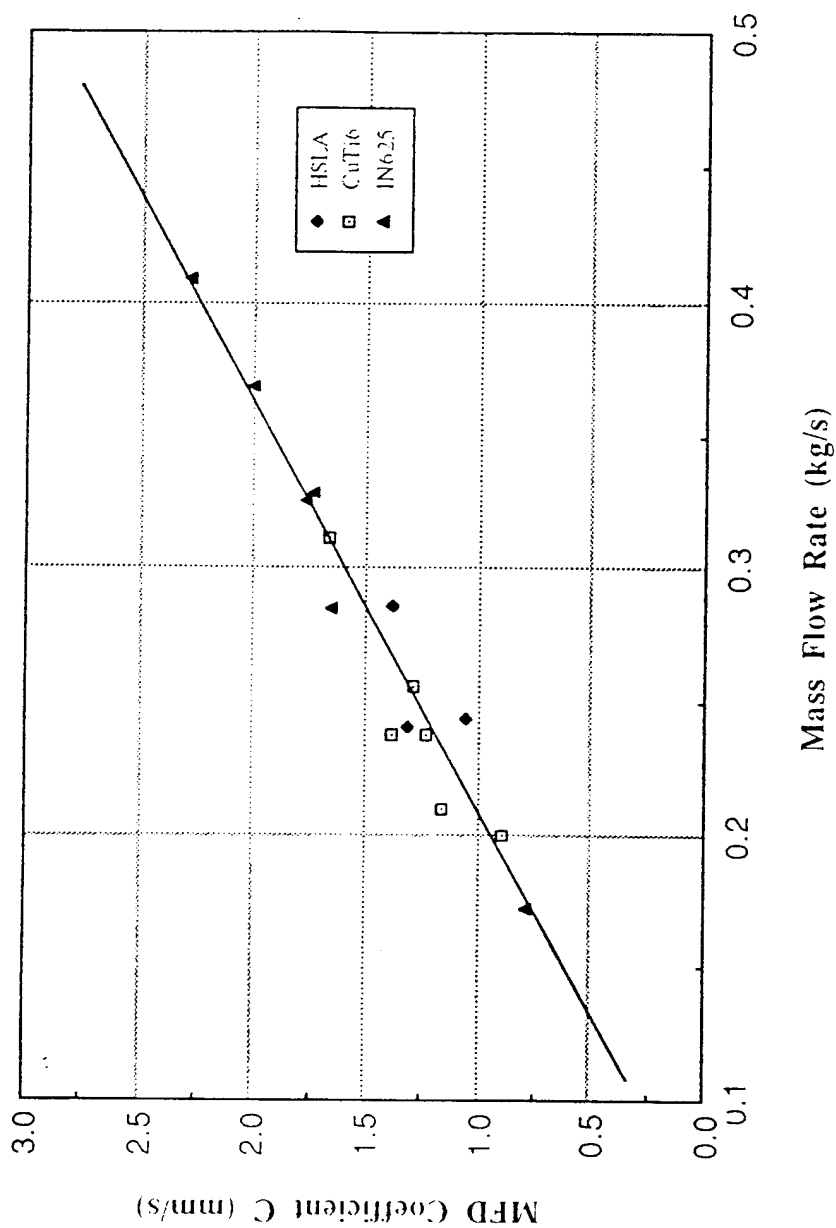


Fig. 16 The effect of metal flow rate on the background deposition rate, the C parameter of eq.2, for all three alloys.

Dependence of the Axial Velocity of Gas-Jet on Atomization Pressure and Flight Distance

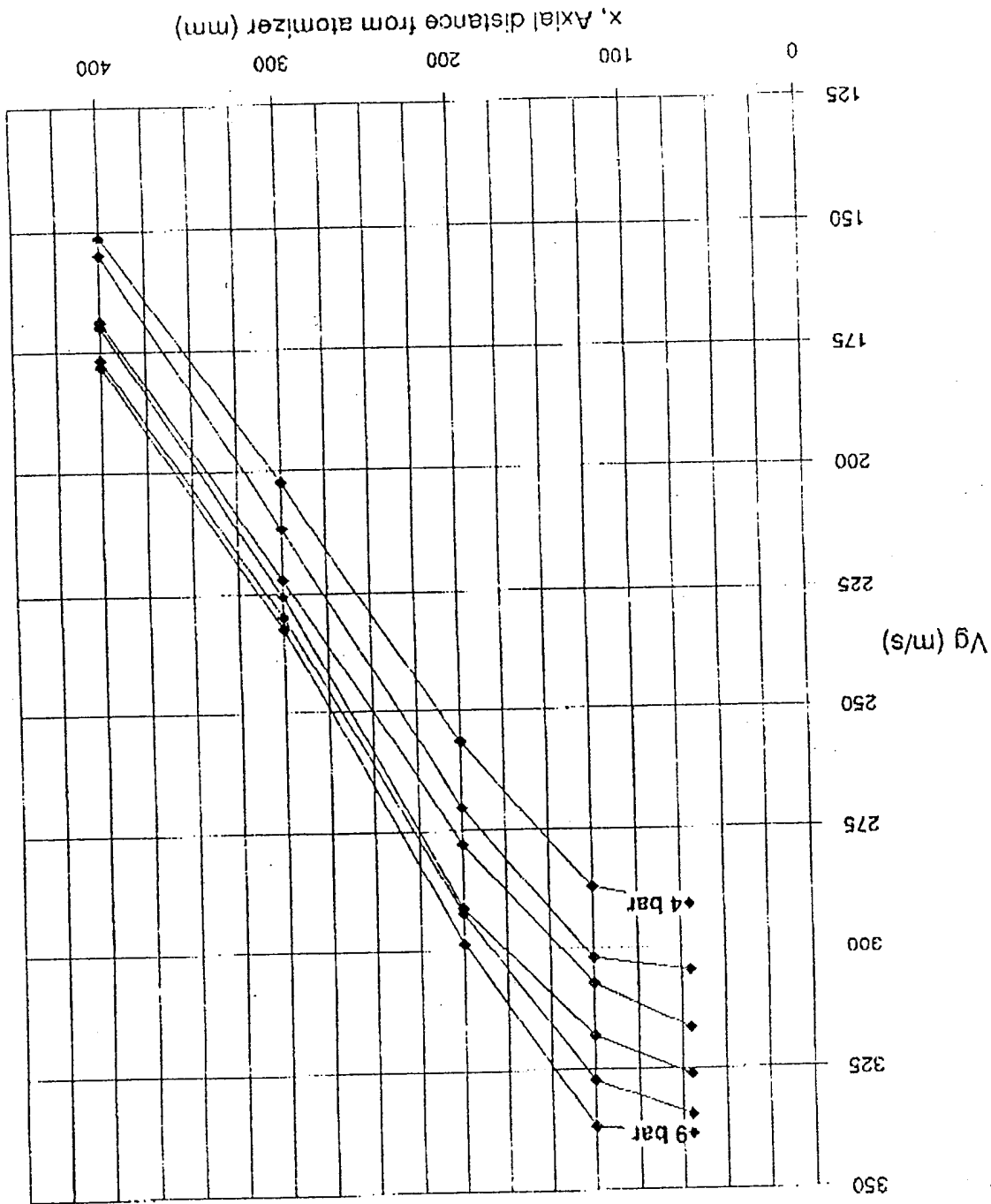


Fig. 17 The variation of axial velocity of the Osprey Gas jet of Nitrogen with atomization pressure and flight distance, no liquid metal and no substrate.

$$V/V_m - r/d_s @ 70\text{mm}$$

N-D Radial Velocity Distribution of Gas-Jet

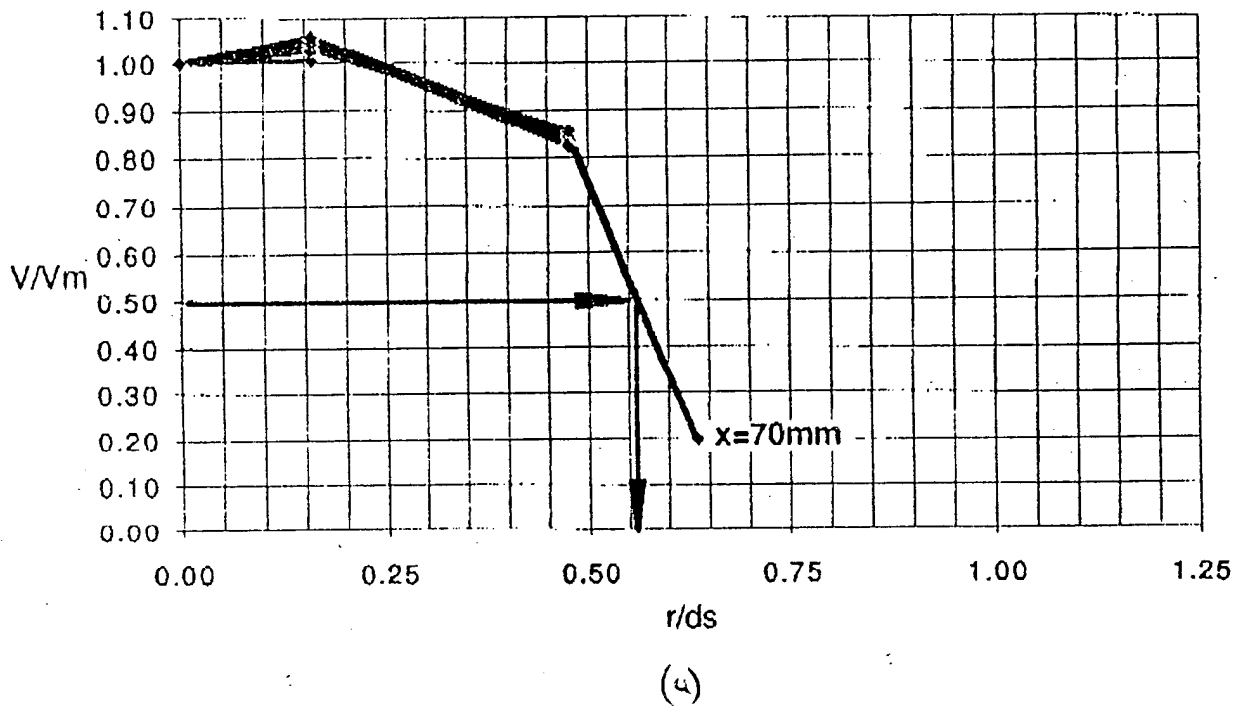
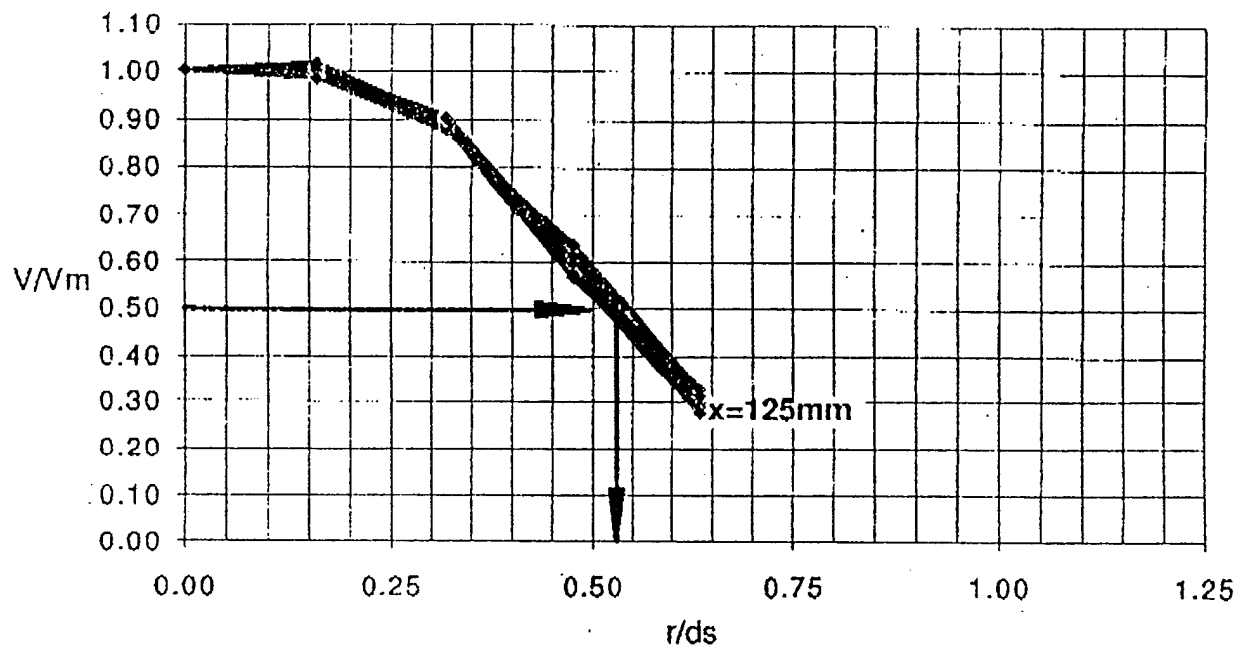


Fig. 18 The radial variation of nitrogen gas velocity normalized to the axial gas velocity as a function of the atomizer diameter (d_s is 39mm); At flight distances of (a) 70mm (b) 125 mm (c) 200 (d) 300 and (e) 400mm. The atomization gas pressure of 4 to 9 bar has a negligible influence on the normalized axial variation of velocity. The radius of the jet, R_{jet} , taken where the axial normalized velocity has fallen to 0.5 is indicated.

$V/V_m - r/d_s$ @ 125mm

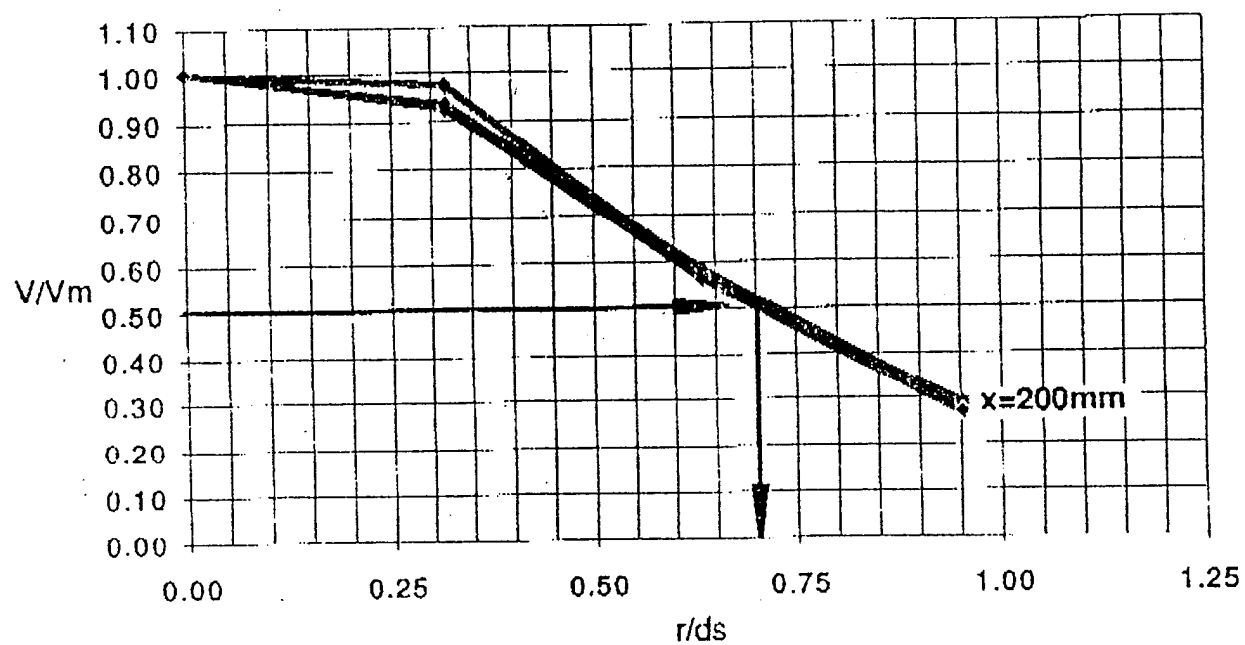
N-D Radial Velocity Distribution of Gas-Jet



(b)

$V/V_m - r/d_s$ @200m

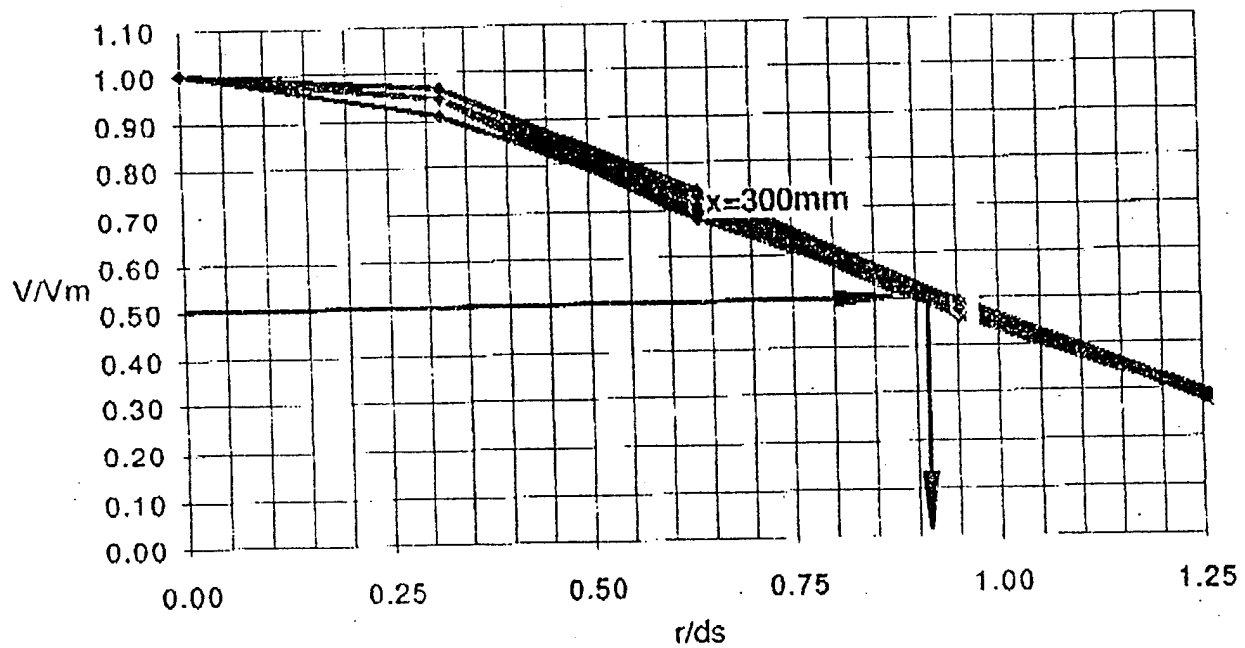
N-D Radial Velocity Distribution of Gas-Jet



(c)

$V/V_m - r/d_s$ @300mm

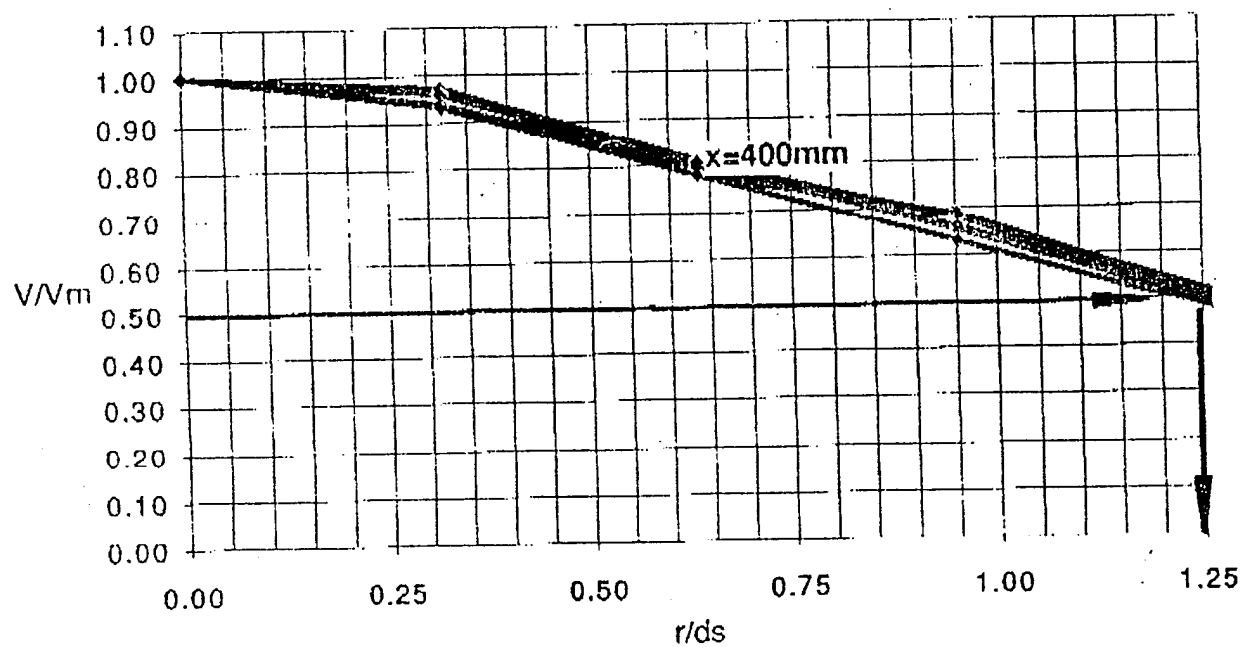
N-D Radial Velocity Distribution of Gas-Jet



(d)

$V/V_m - r/d_s$ @ 400mm

N-D Radial Velocity Distribution of Gas-Jet



(0)

Variation of Radial Jet Decay with Flight Distance

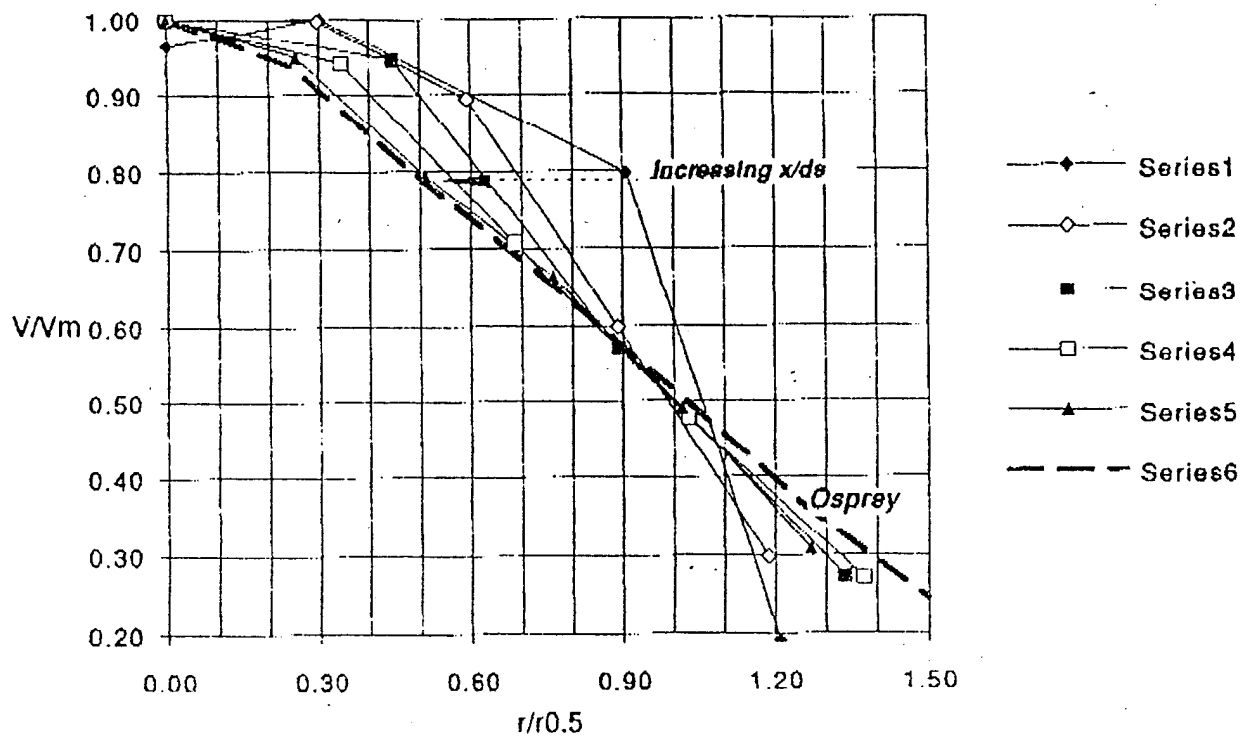


Fig. 19 The normalized velocity, v/v_m , where v_m is the axial velocity against the normalized radius, $r/r_{0.5}$, where $r_{0.5}$ is R_{jet} , at increasing axial distances x , 70 to 400mm.

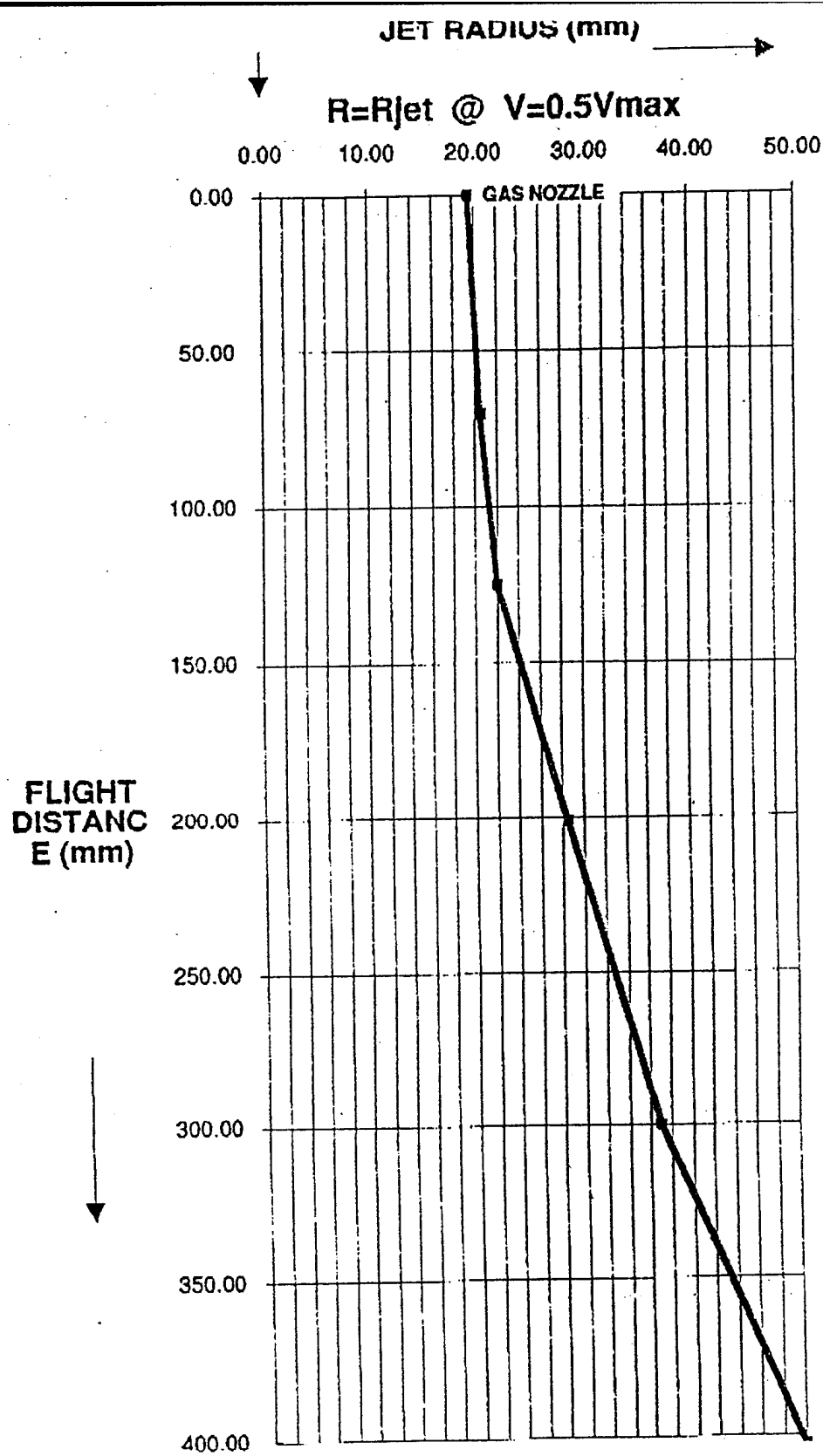


Fig. 20 The radius of the jet, R_{jet} taken where the axial normalized velocity has fallen to 0.5, as a function of flight distance.

Variation of Axial Jet Decay with Atomization Pressure $V_{max} = 354\text{m/s}$; $d_s = 39\text{mm}$

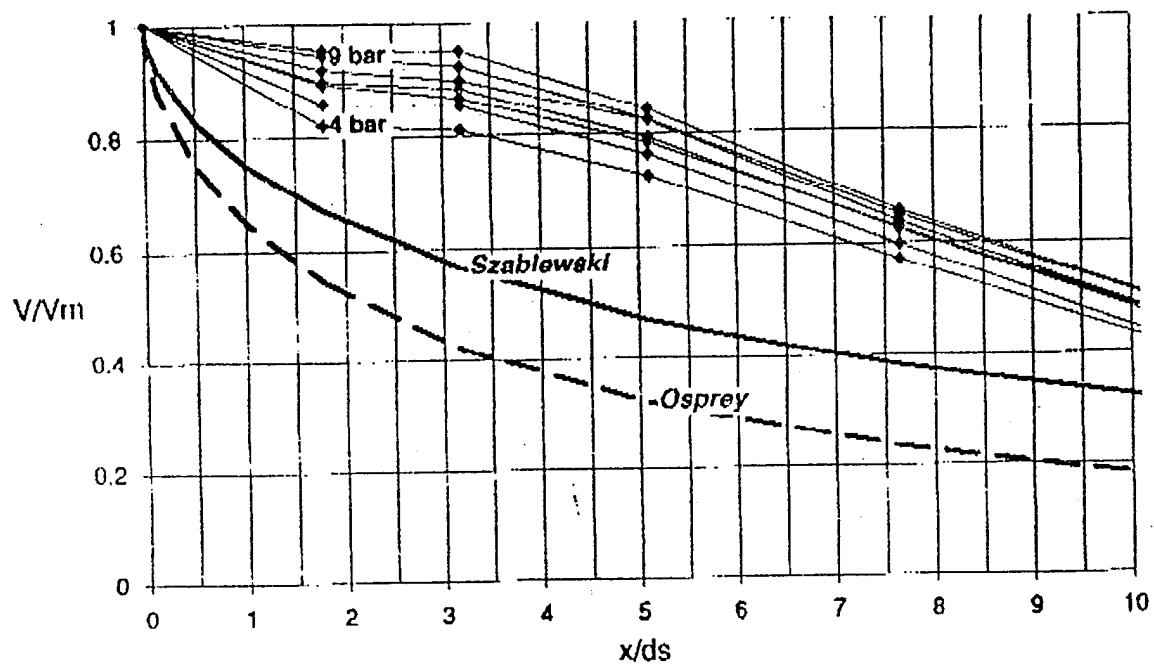


Fig. 21 Variation of axial velocity with flight distance, normalized to mach 1 (354m/s), compared to previous reported variations.

Boundary-Layer Gas Velocity at edge of Surface of Tilted Substrate @ $x=350\text{mm}$

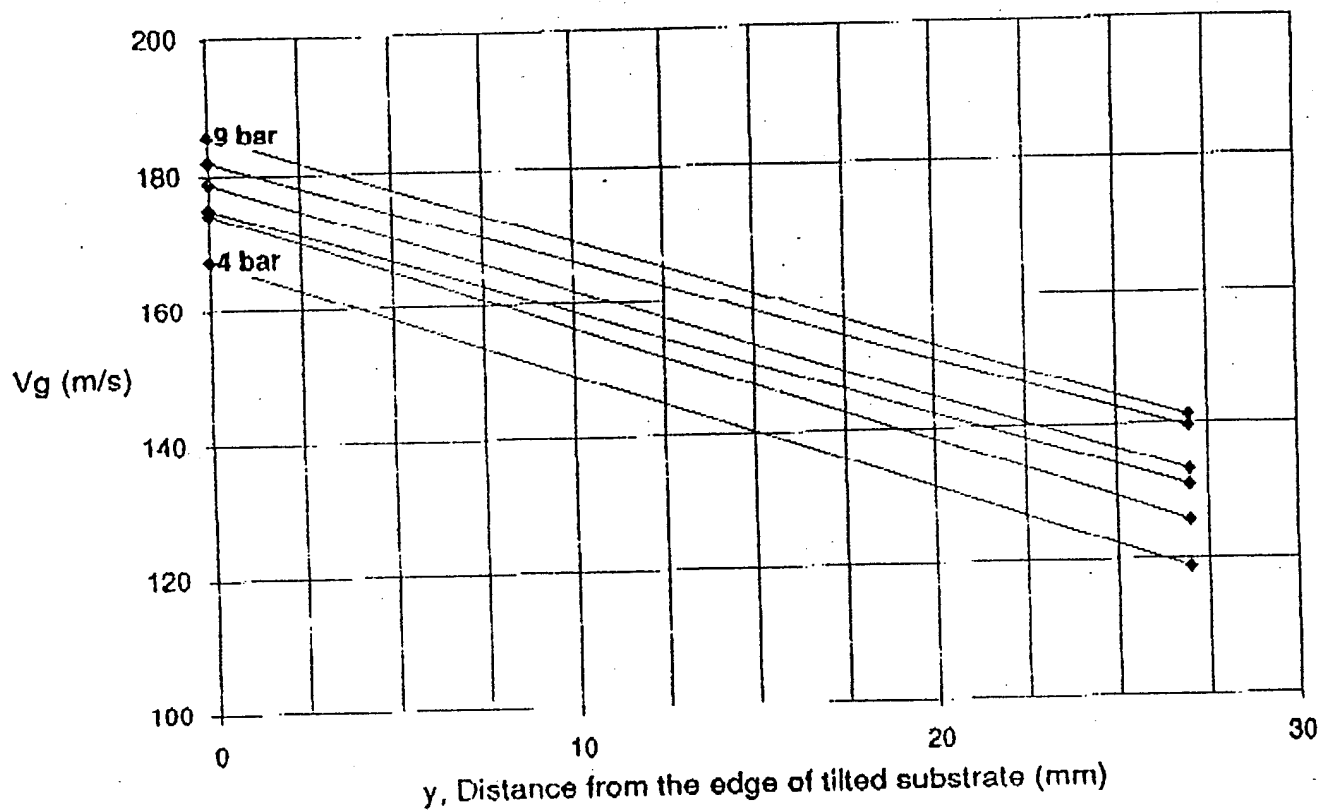


Fig. 22 Near substrate gas velocity at a tilted substrate at a flight distance, used for billet, production of 350mm.

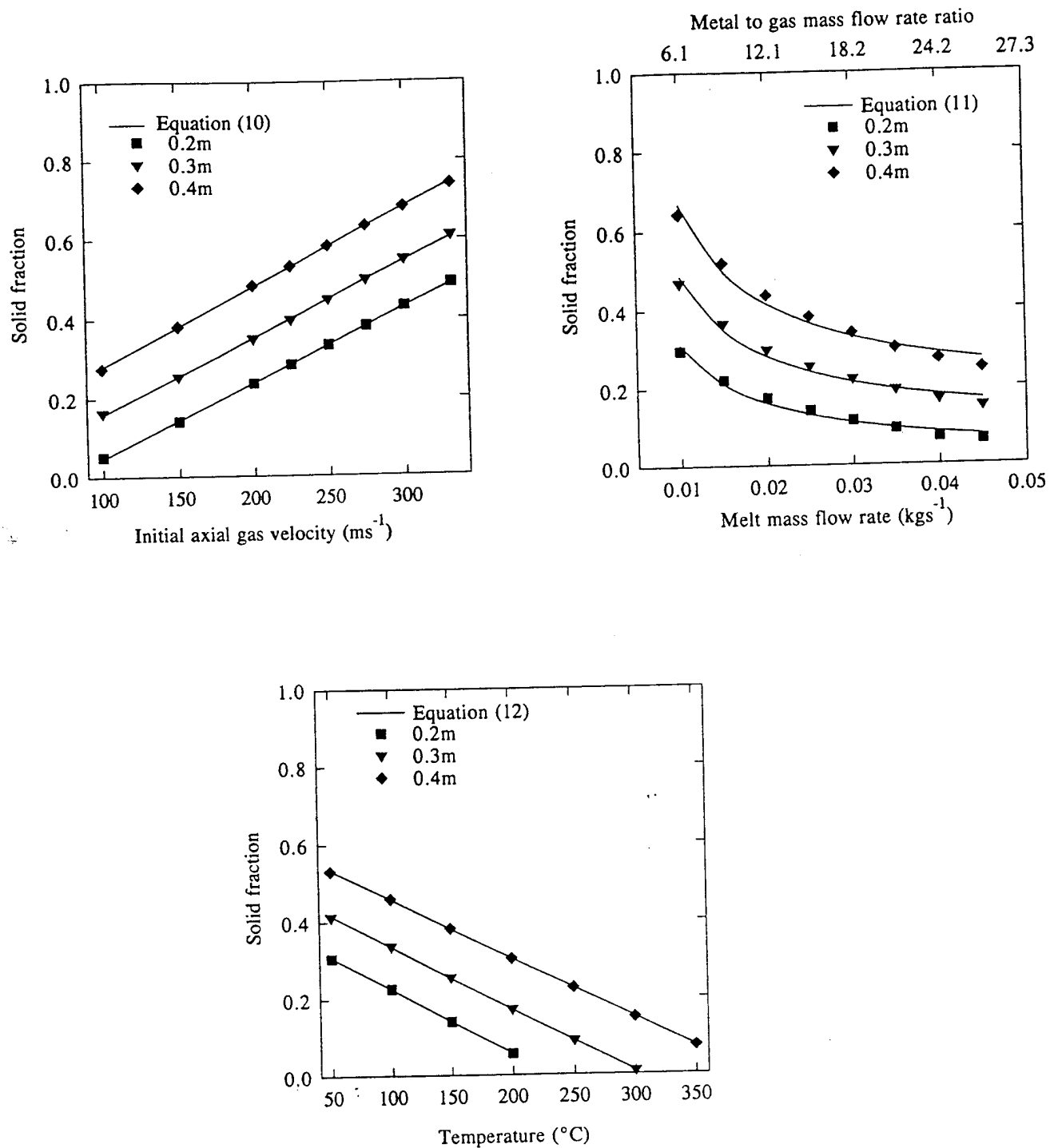


Fig. 23 Equilibrated Al-4wt%Cu solid fraction at axial spray heights of 0.2, 0.3 and 0.4m as a function of (a) Initial axial gas velocity at a metal flow rate of 0.025kg/s and a melt superheat of 150°C. (b) Metal flow rate in kg/s at an initial axial gas velocity of 150m/s and a melt super heat of 150°C and (c) Melt superheat (in °C) at an initial axial gas velocity of 150m/s and a metal flow rate of 0.025kg/s. (After Grant et al.[4])

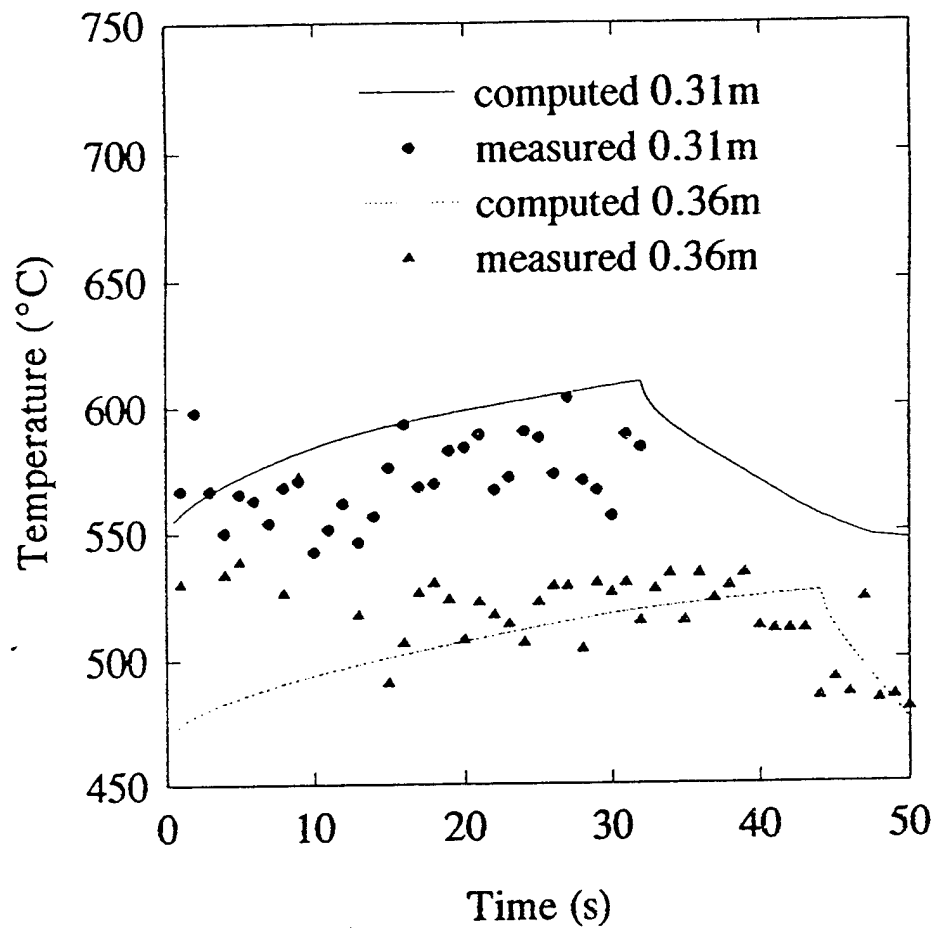


Fig.24 Numerically computed and experimentally measured, using infrared imaging, deposit temperatures as a function of time during spray forming of Al-4wt%Cu at two axial spray heights. (After Grant [5])

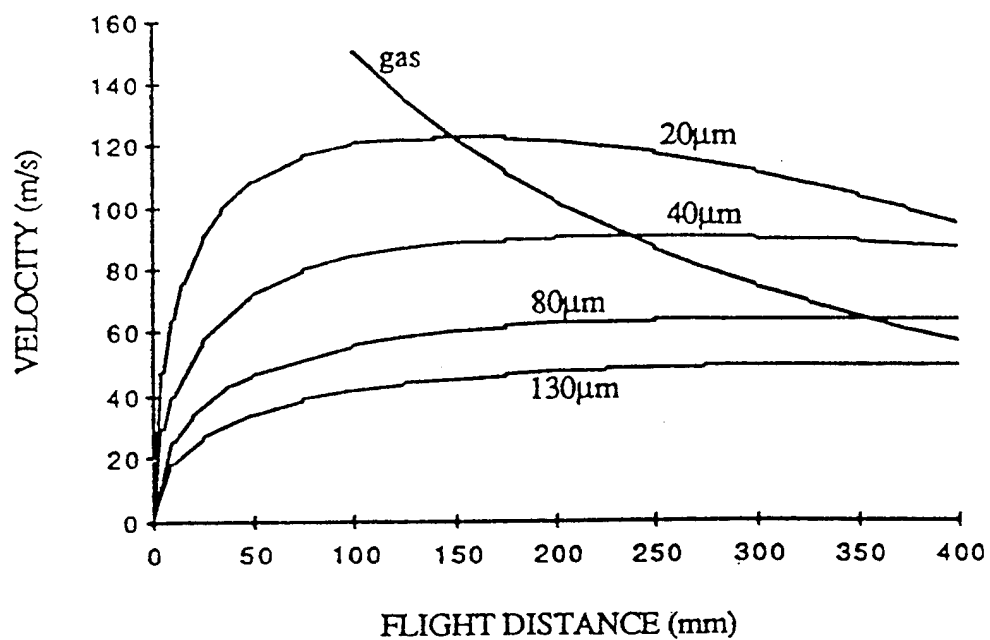


Fig.25 Predicted variation of droplet velocity for Ni-20wt% Cr droplets of different diameters with flight distance along the spray axis. From Mathur et al.[5].

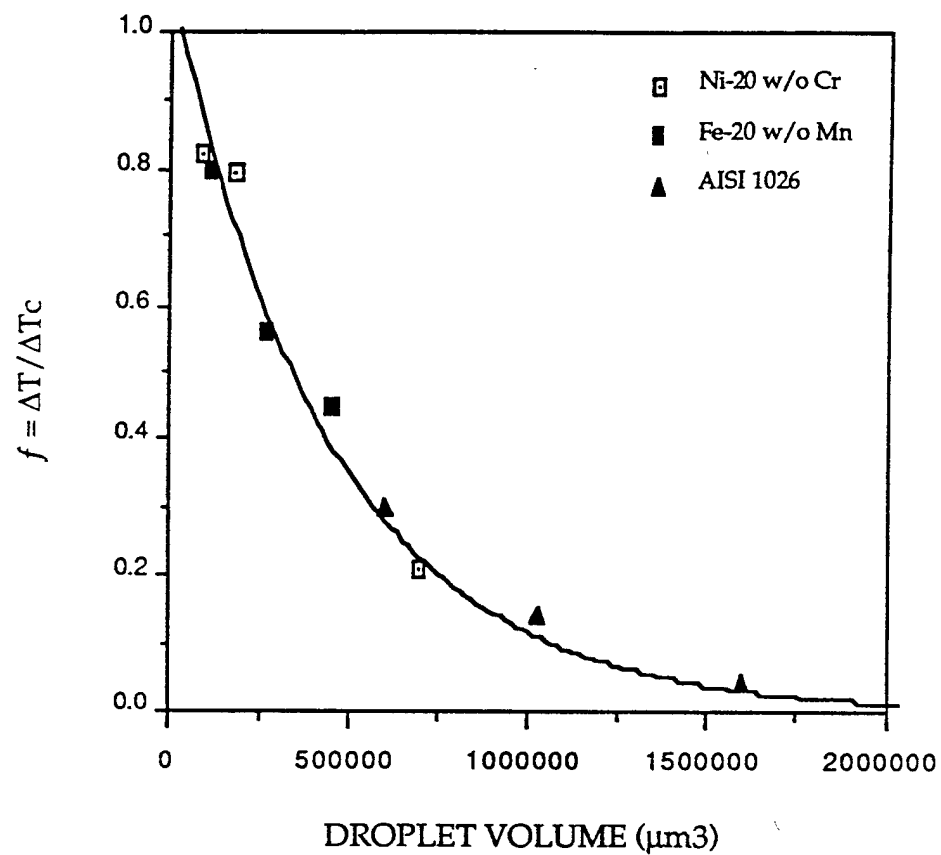


Fig.26 Dependence of the degree of undercooling on droplet volume for these alloys measured from droplet impacts on glass slides passed through the spray at different flight distances. After Mathur [27].



(a)



(b)

Fig.27 Surface morphologies showing evidence of droplet collisions (a) in Cu-6wt%_e Ti and (b) IN625.

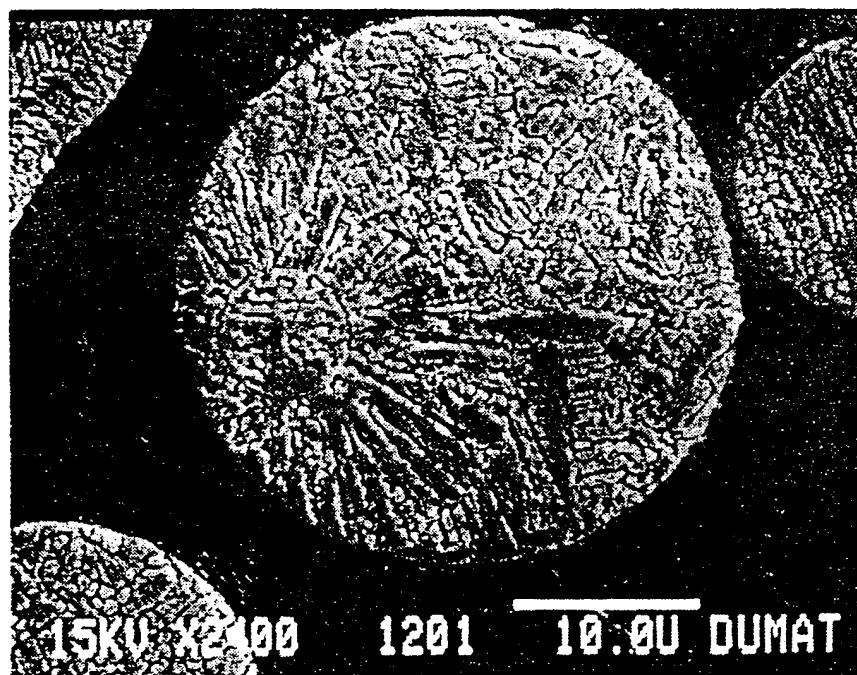


Fig.28 Sectioned droplets showing an apparent nucleation event in the larger droplet by impact of the, captured, small pre-solidified droplet while the larger droplet was undercooled.

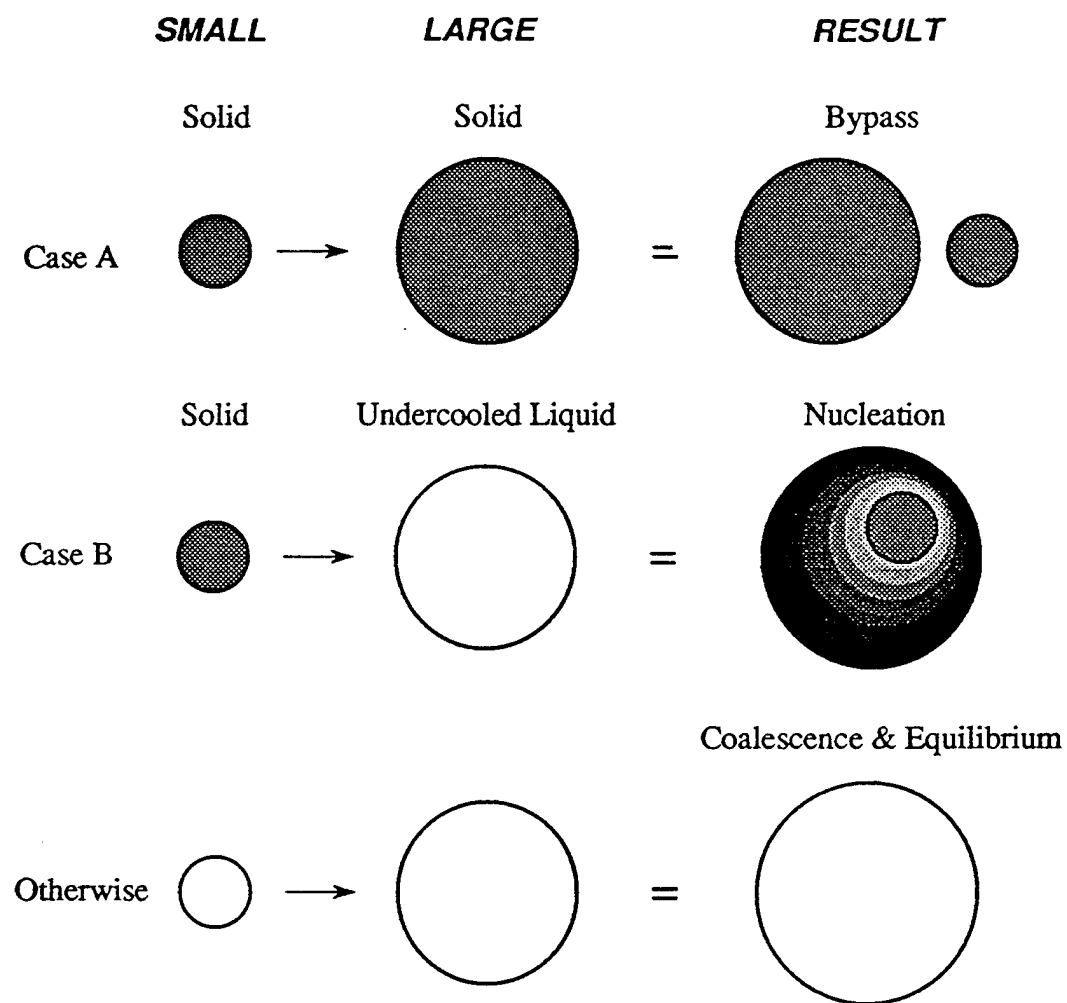


Fig.29 Schematic showing the modeling rules assumed for the collision of two droplets.

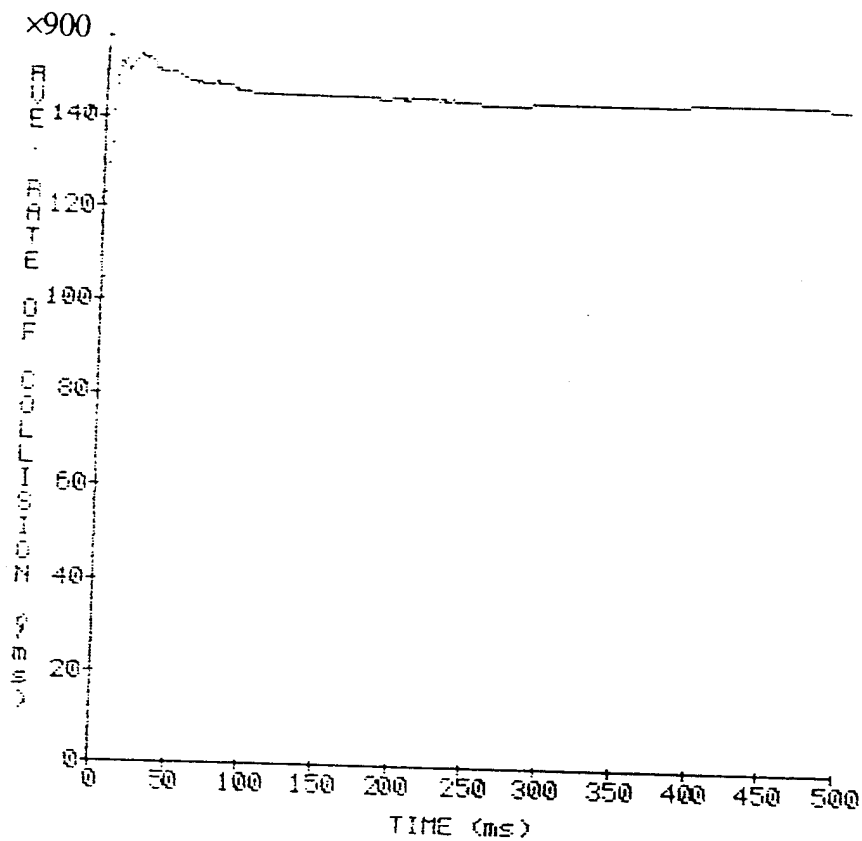


Fig 30. Average number of droplet collisions occurring in each millisecond as a function of time.

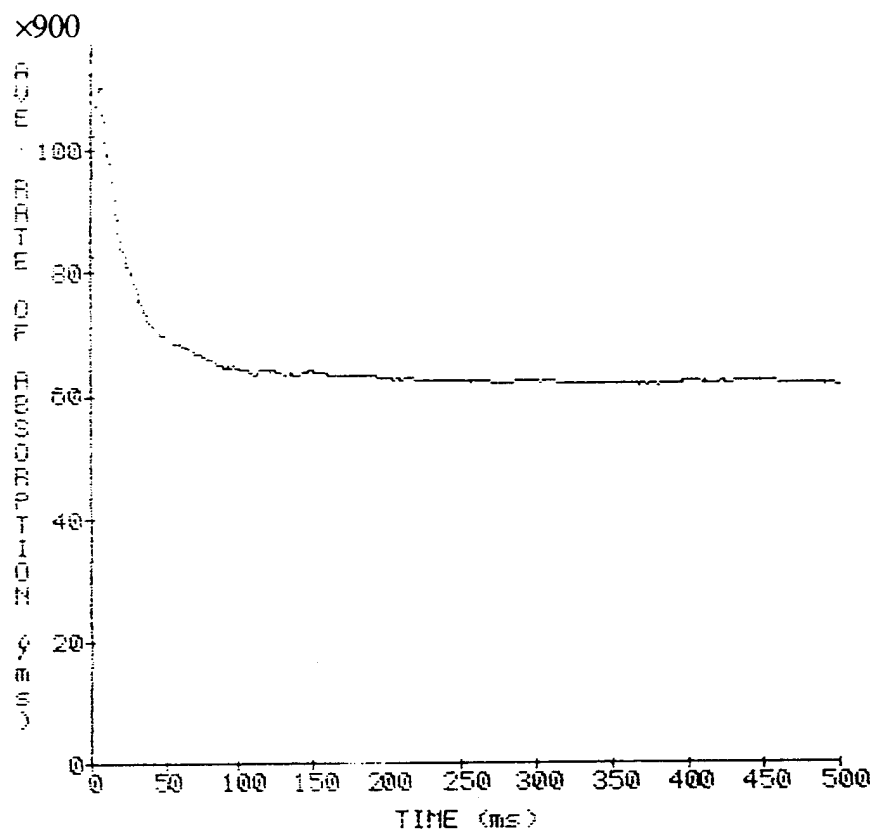


Fig 31. Average number of absorption events through coalescence occurring in each millisecond as a function of time.

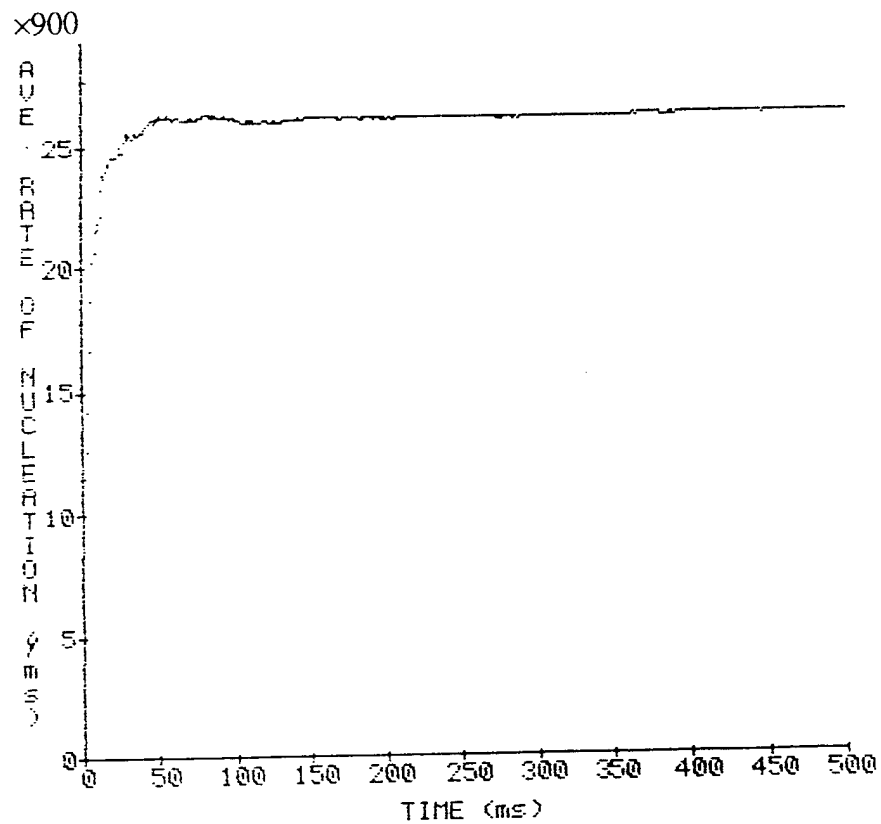


Fig 32. Average number of nucleation events occurring by impact of a solid droplet on an undercooled liquid droplet occurring in each millisecond as a function of time.

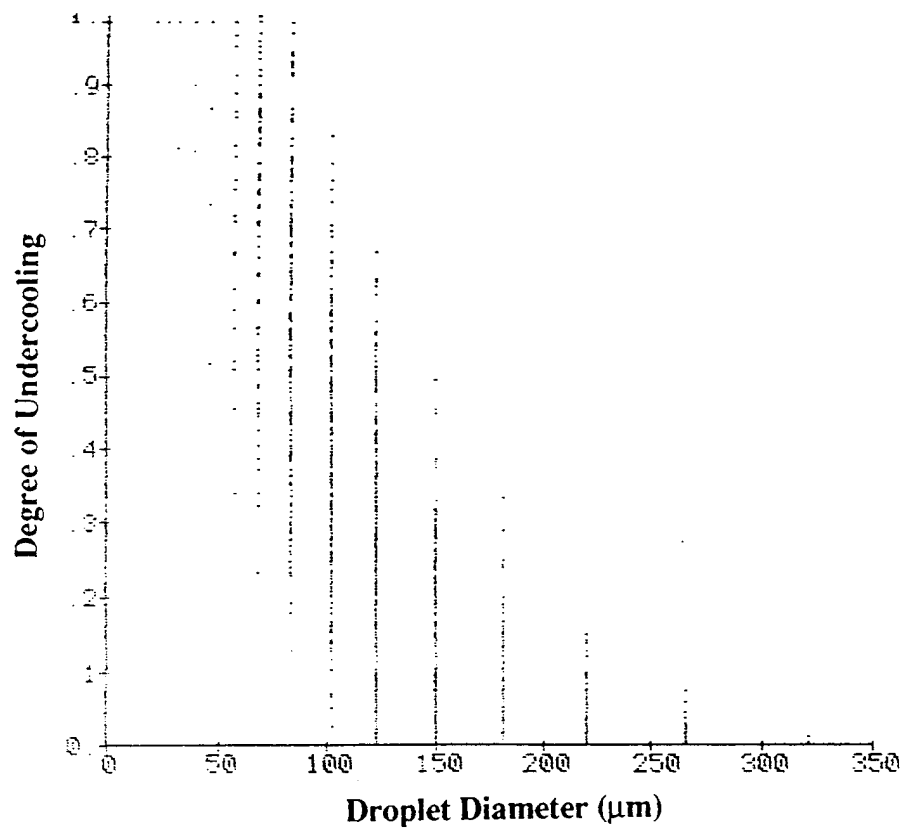


Fig. 33 Scatter plot of the dimensionless degree of undercooling ($\Delta T/\Delta T_c$) as a function of droplet diameter.

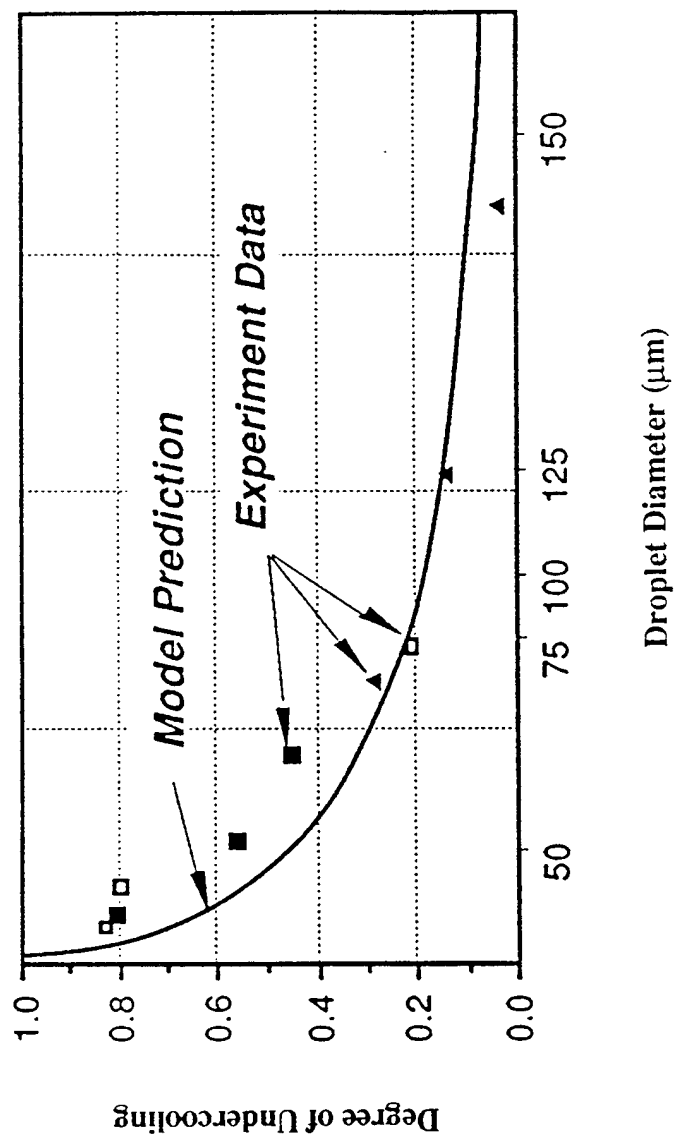


Fig.34 The mean dimensionless degree of undercooling ($\Delta T / \Delta T_c$) as a function of droplet diameter as modeled compared to the experimental data of Mathur [27].

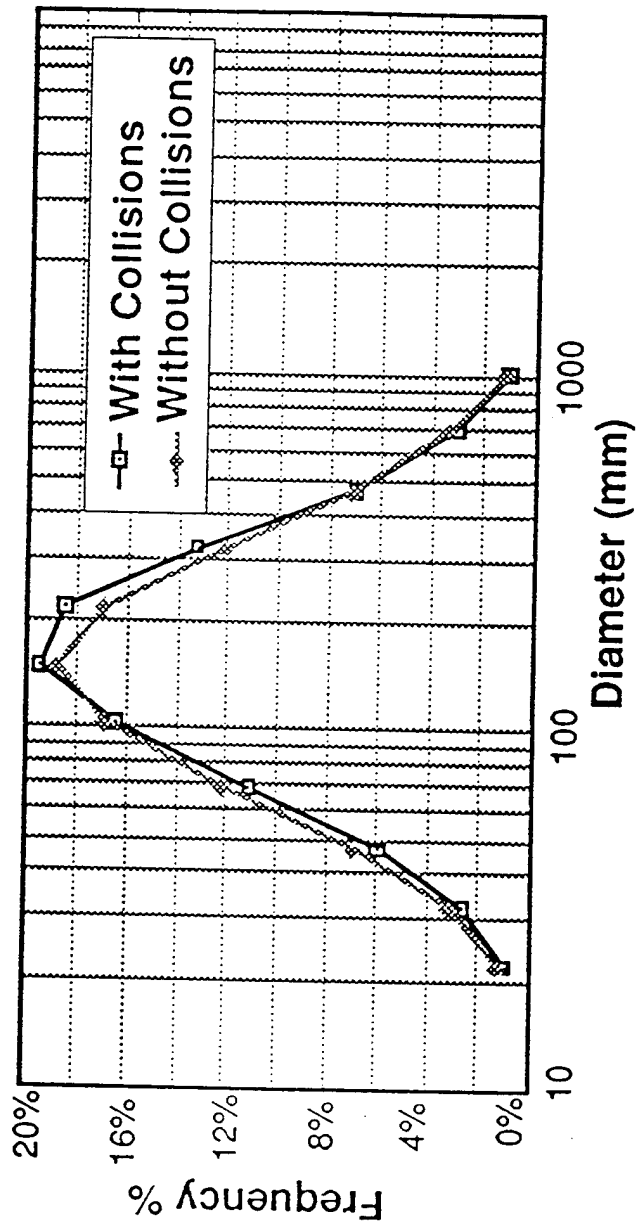


Fig.35 Predicted change of the particle size distribution due to droplet collisions during flight of 0.4m assuming the maximum possible absorption of droplets by capture according to the rules of fig. 29.

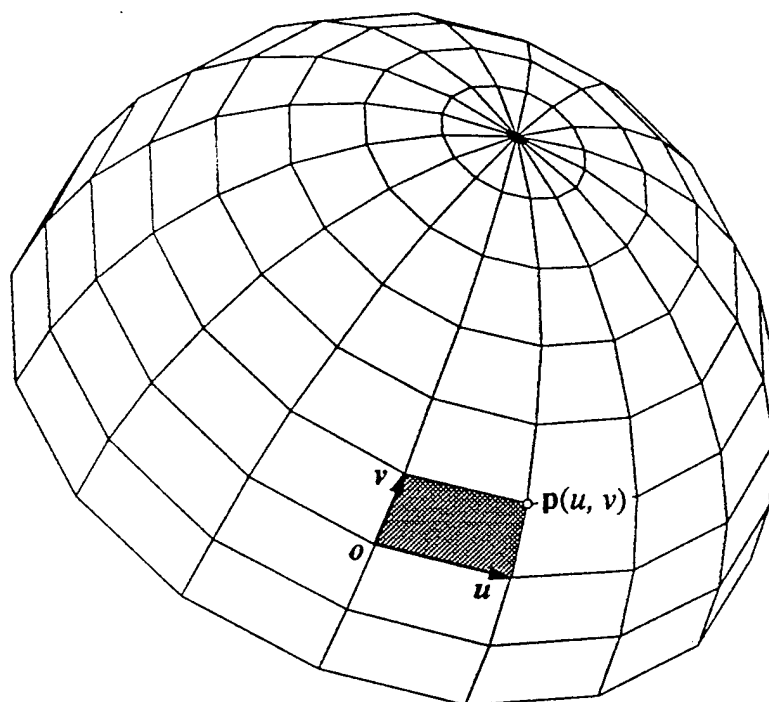


Fig.36 Finite element representation of a preform surface with two parameters u and v .

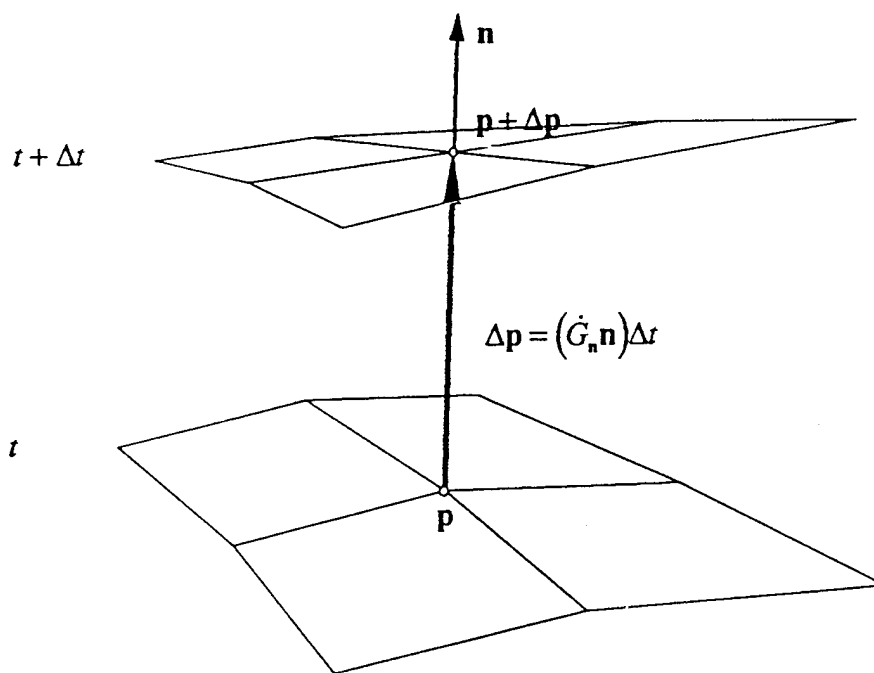


Fig.37 Schematic showing how the local normal growth rate, \dot{G}_n , determines the incremental displacement, Δp , along the normal direction n at a location p on the surface during a time step Δt .

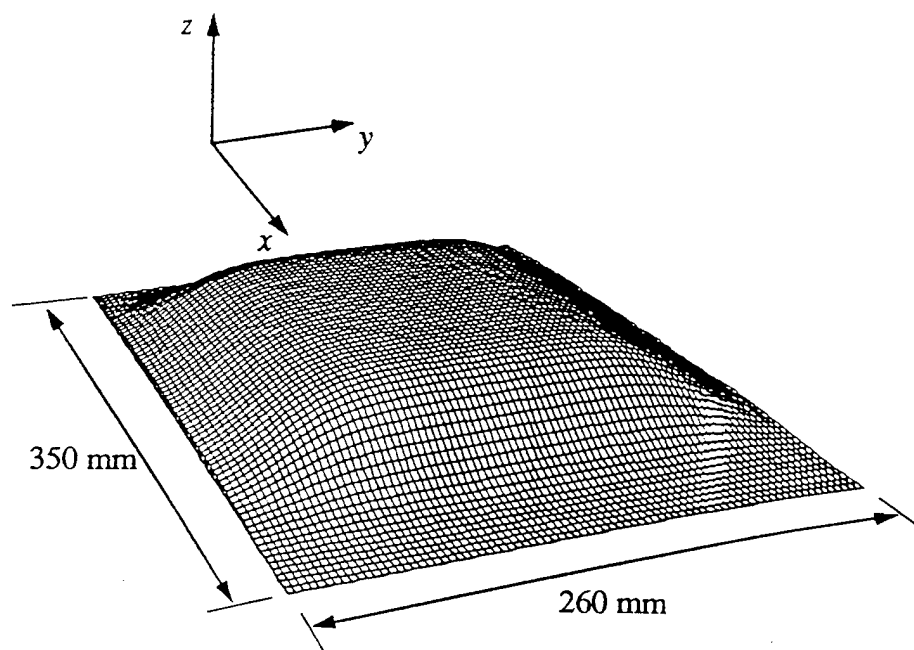
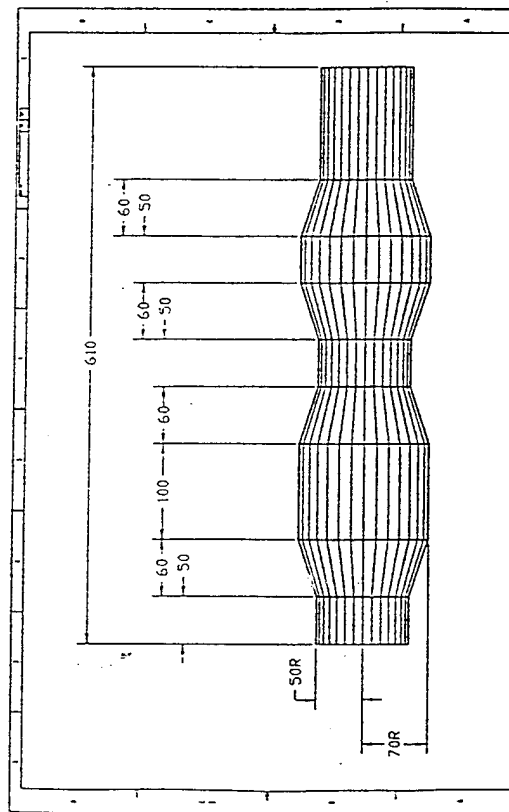
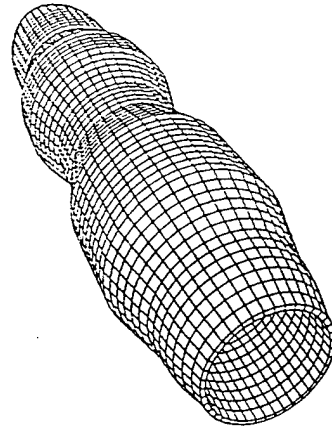


Fig. 38 Predicted thickness profile of a spray deposited sheet formed by a linear atomiser (aligned in the y direction) while the substrate was moving with a linear displacement in the x direction.

SUBSTRATE SHAPE
PROTOTYPE



PERSPECTIVE VIEW OF
PREDICTED TUBULAR REFORM



THICKNESS PROFILE

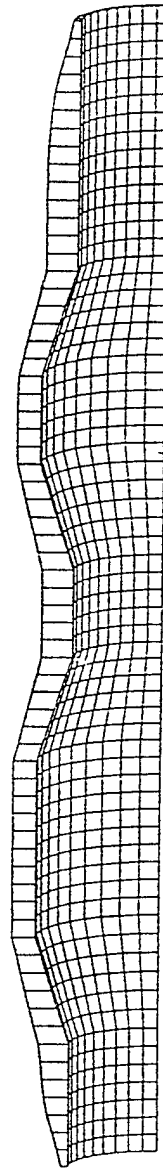


Fig.39 Example of a 3-D shape predicted using the shape model for a tube with multiple segments of varying diameters. The substrate shape was defined directly in CAD software and then interfaced with the model using the motion planner.

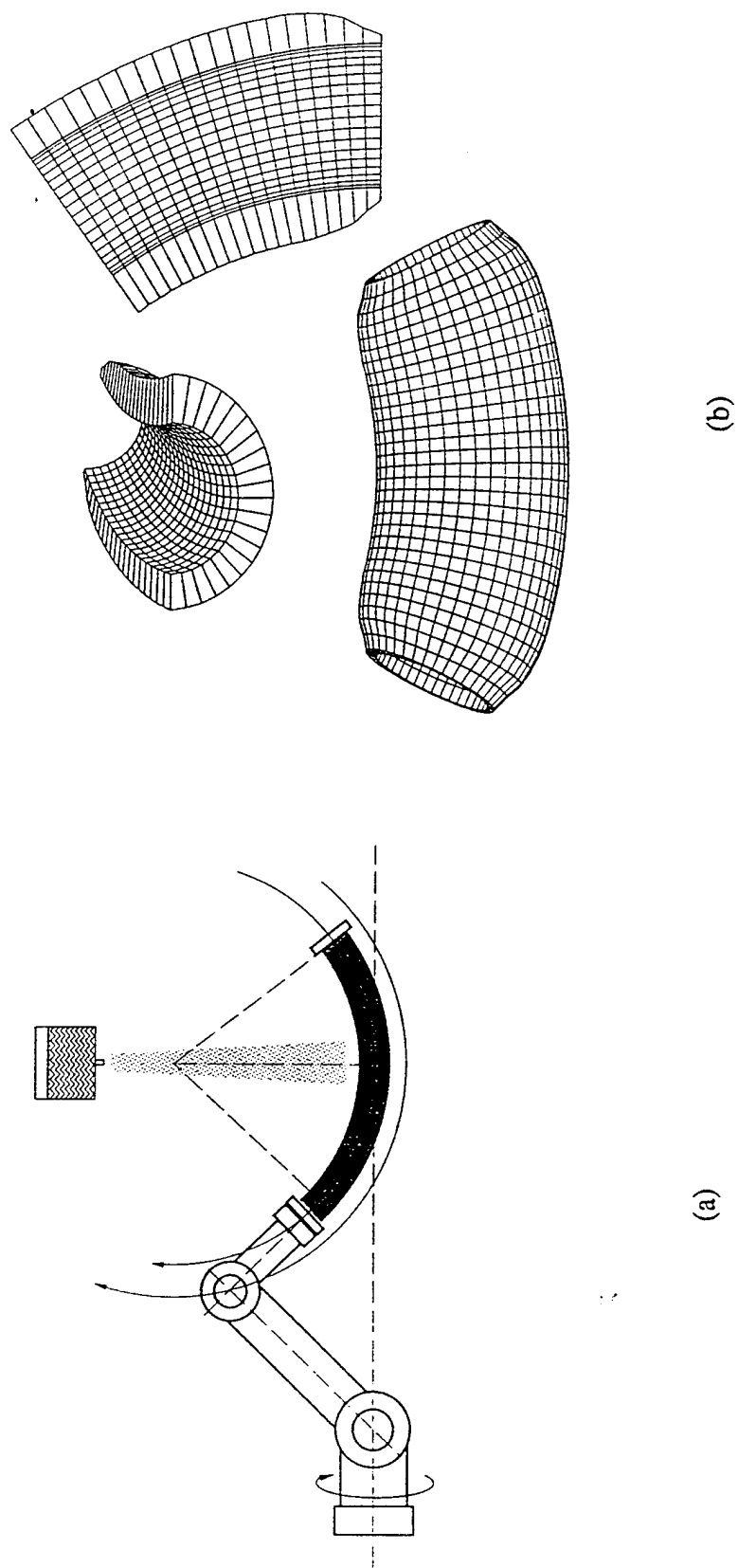


Fig. 40 Elbow making strategy using rotation, longitudinal to the curve of the elbow, to maintain a constant spray height. (a) Schematic of the substrate motions. (b) Predicted shapes and cross sections.

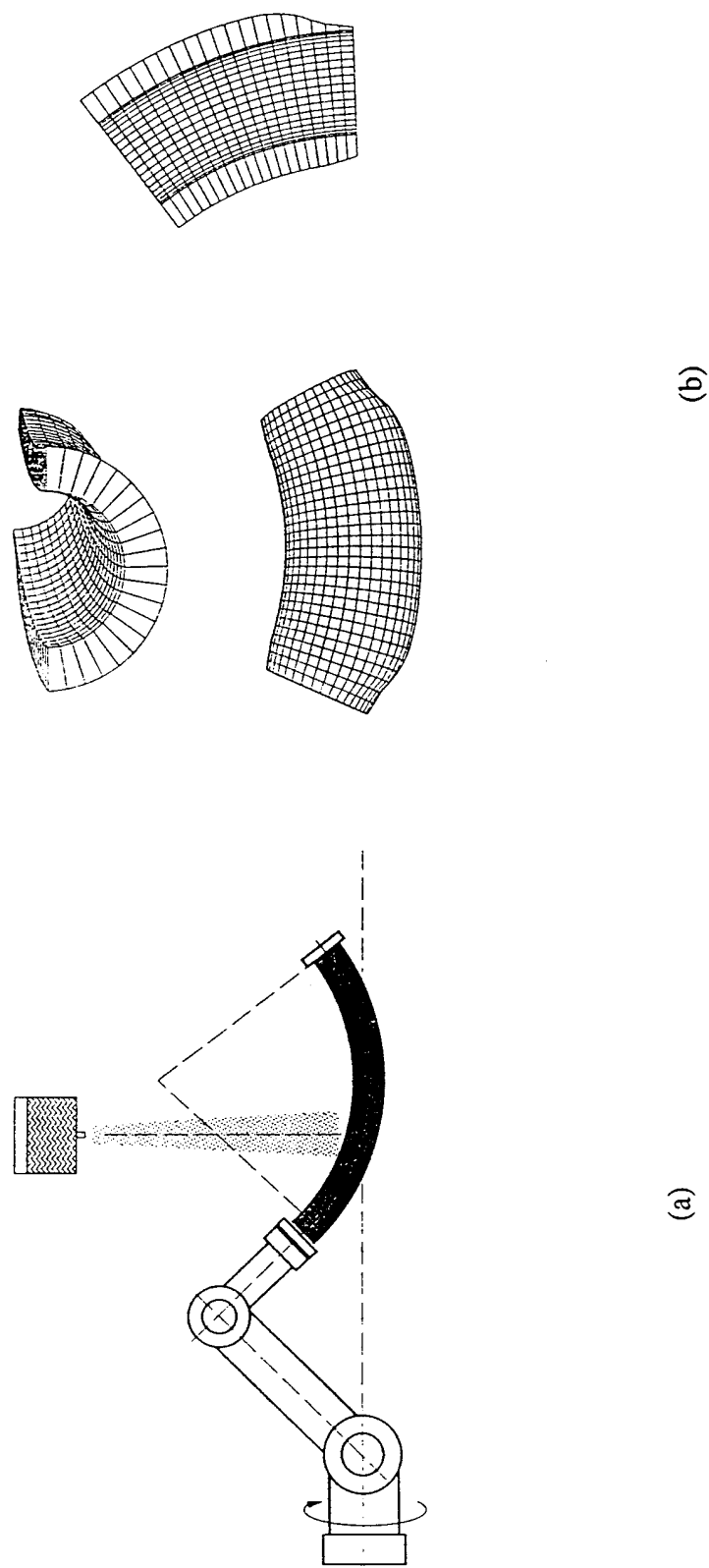


Fig.41 Elbow making strategy using translations axial to the elbow and perpendicular to axial of the elbow to maintain a constant spray height and to give a more constant wall thickness. (a) Schematic of the substrate motions. (b) Predicted shapes and cross sections.

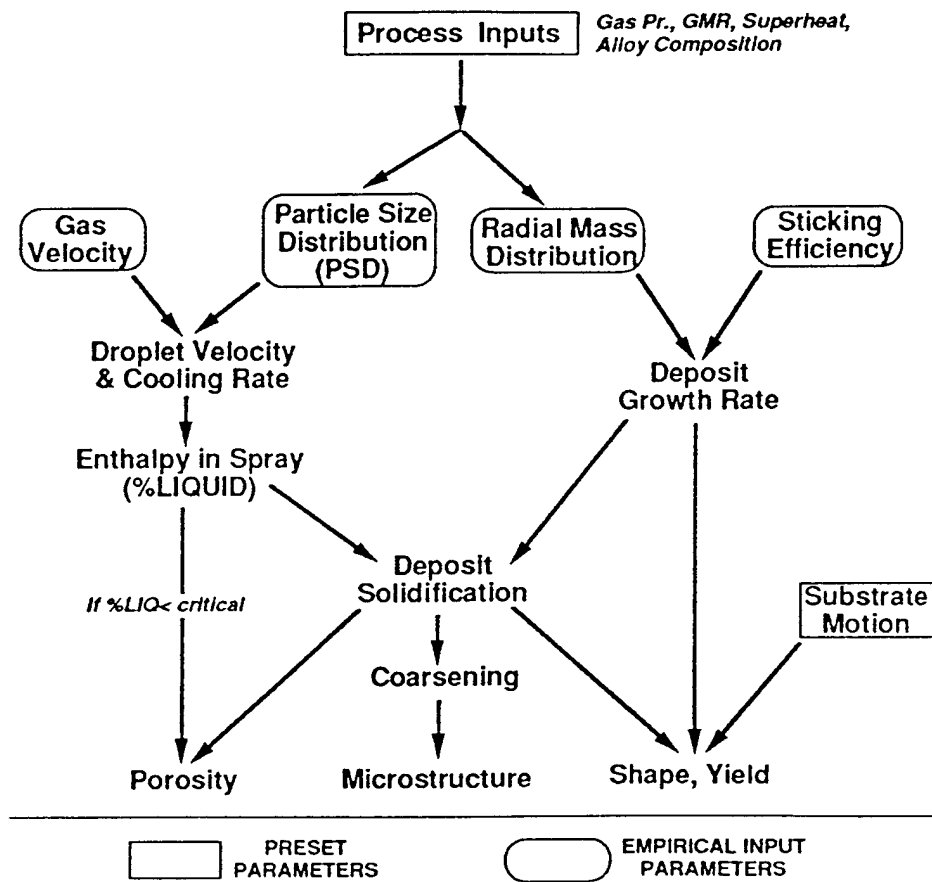


Fig.42 Flow chart of the Drexel model of the spray forming process showing the preset input parameters, the empirically determined parameters and the predicted outputs of the model.

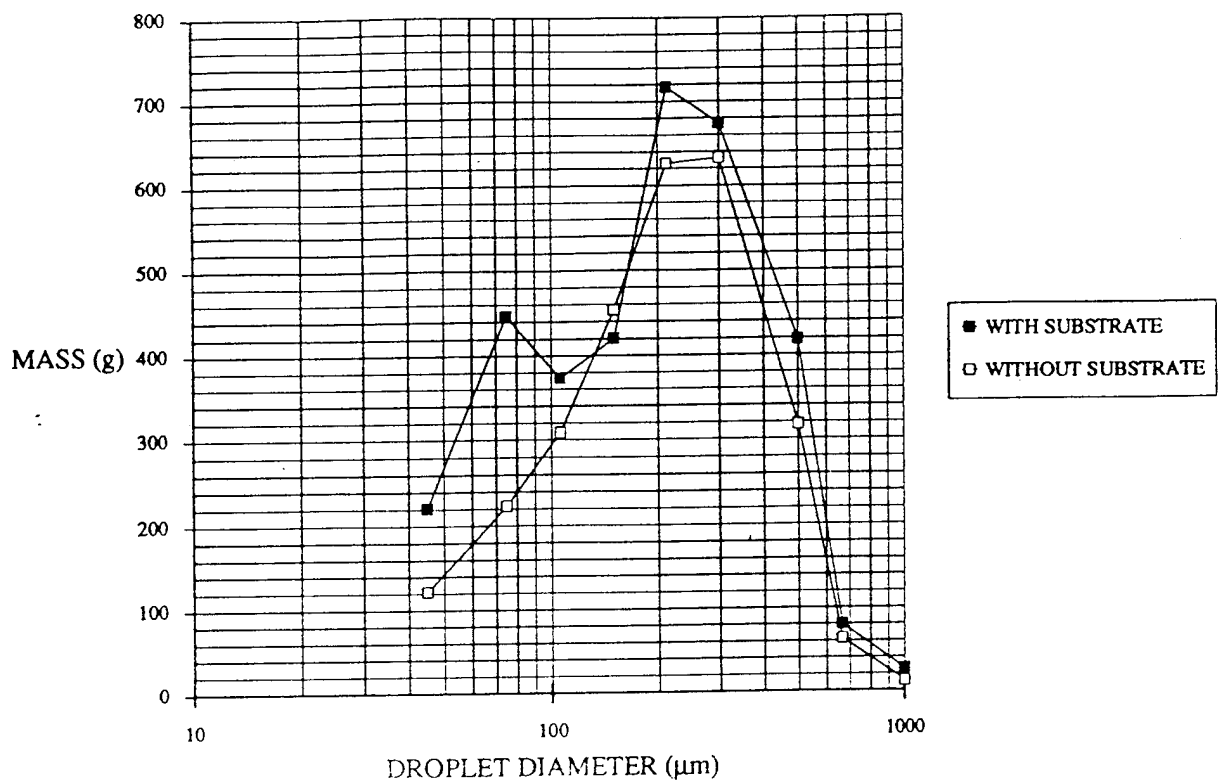


Fig.43 The PSD found for Cu-6wt%Ti sprayed into the outer ring of a collector system with and without a substrate that intercepted material in flight towards the inner collector rings.

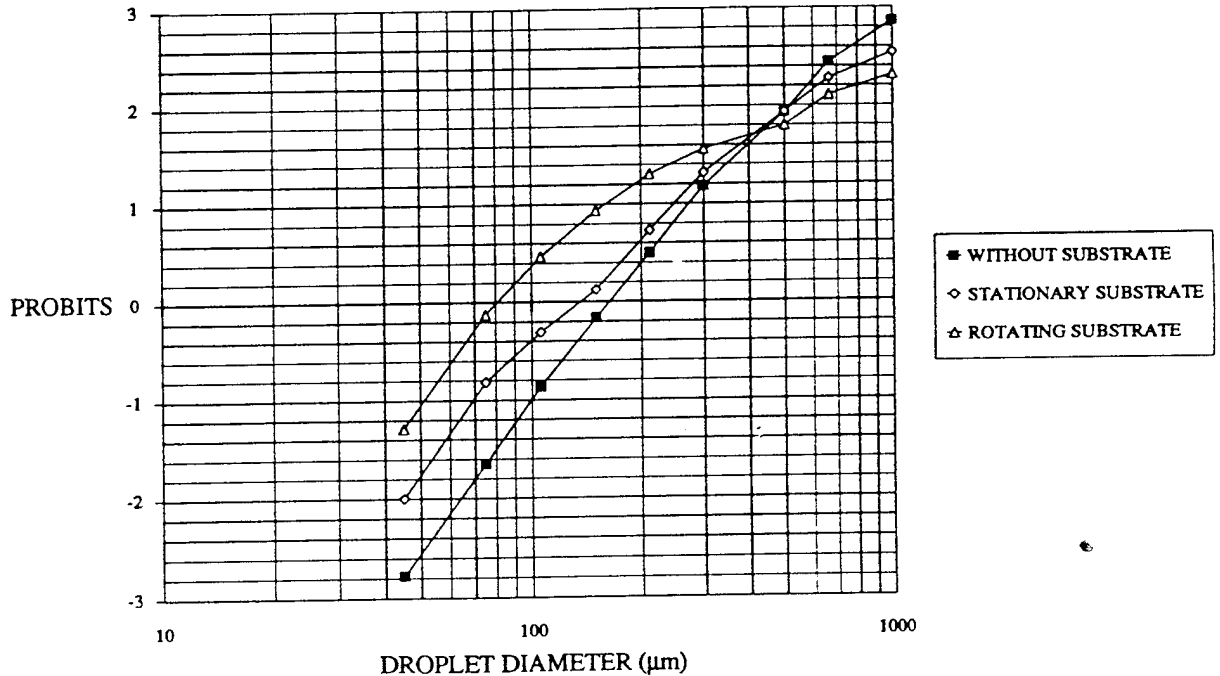


Fig.44 The data of fig.43 replotted to show the deviation from the log-normal distribution in the presence of a substrate. Additional data from a further run with the substrate rotating is also shown.

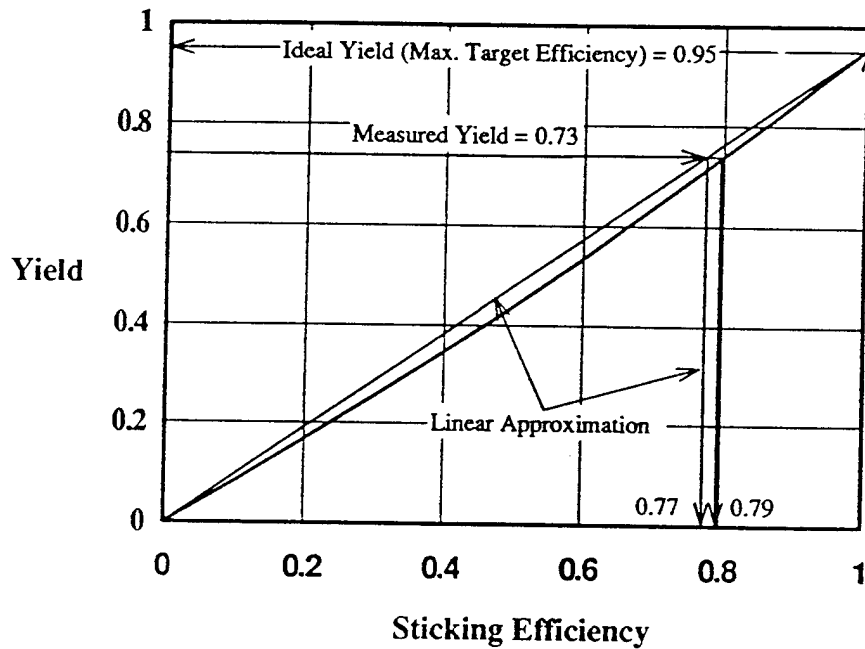


Fig.45 Use of the three dimensional shape model for studies of the spray forming of a billet of Cu-6wt%Ti. The deposition lasted 48 seconds at a metal flow rate of 0.18kg/s an atomizing gas pressure of 10 bar a superheat of 110°C and a substrate withdrawal rate of 1mm/s.

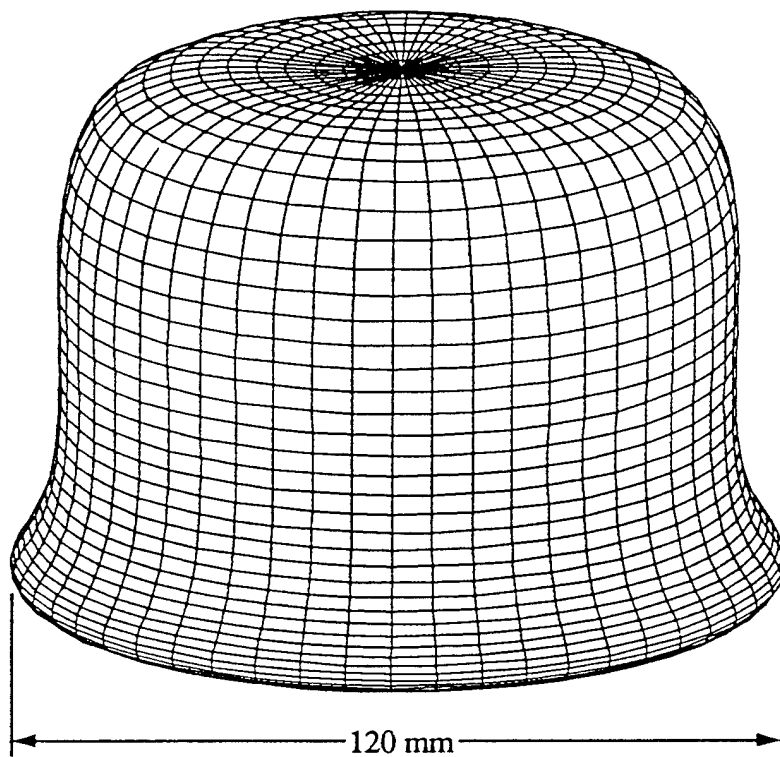


Fig.46

The shape predicted by the three dimensional shape model for a Cu-6wt% Ti billet deposited for 48 seconds at a metal flow rate of 0.18kg/s an atomizing gas pressure of 10 bar a superheat of 110°C, a substrate withdrawal rate of 1mm/s and a rotation of 185 rpm. The Spray model predicted a fraction liquid in the spray of 0.20.

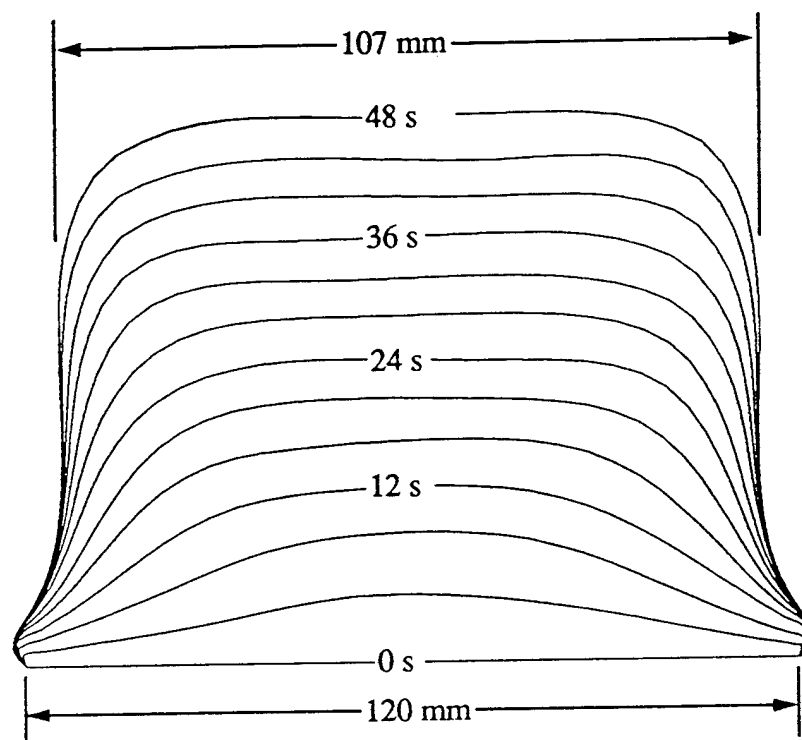


Fig.46 The predicted cross-section profiles of the billet shown in fig.46 at 4s time intervals of deposition.

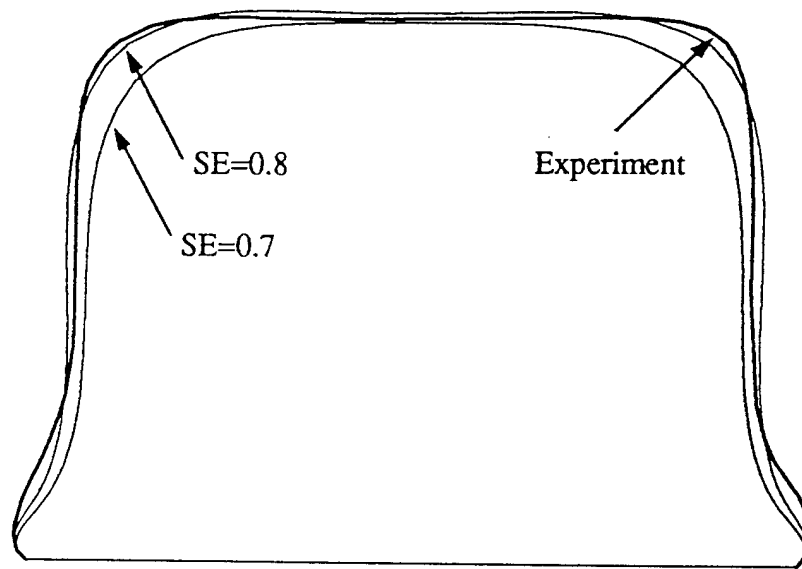


Fig. 47 Comparison of the predicted shape for two different assumed values of the sticking efficiency, 0.7 and 0.8, with the measured shape of the experimental billet of fig. 46.

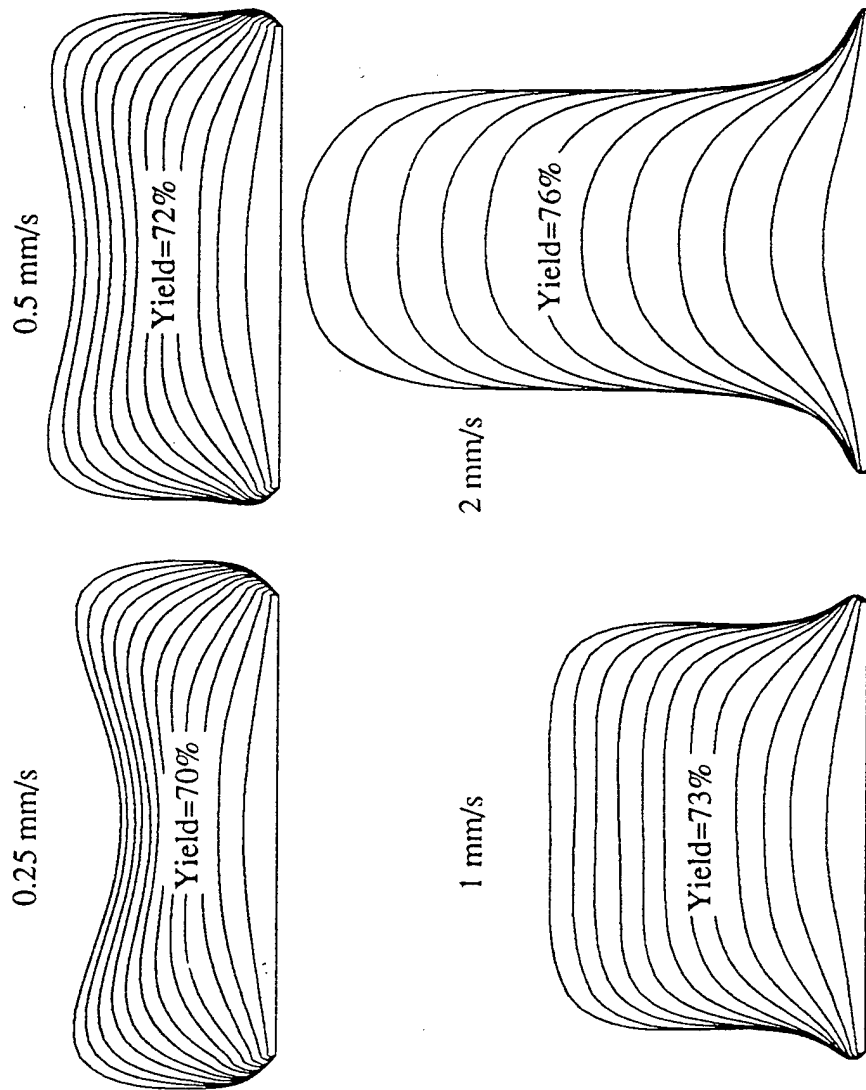


Fig.48 Effect of variation of the withdrawal rate on the predicted shapes of the billets produced under the other operating conditions of fig. 46.

rpm=185; scan freq=1.1 Metal flow rate=0.1kg/s deposition time= 97s %liquid=16%	rpm=185; scan freq=1.1 Metal flow rate= 0.17kg/s deposition time= 50s %liquid = 19%	rpm=185; scan freq=1.1 Metal flow rate=0.24kg/s deposition time= 40s %liquid=26%	rpm=185; scan freq=1.1 Metal flow rate=0.31kg/s deposition time= 30s %liquid=30%	rpm=185; scan freq=1.1 Metal flow rate=0.41kg/s deposition time= 20s %liquid =49%
--	--	---	---	--

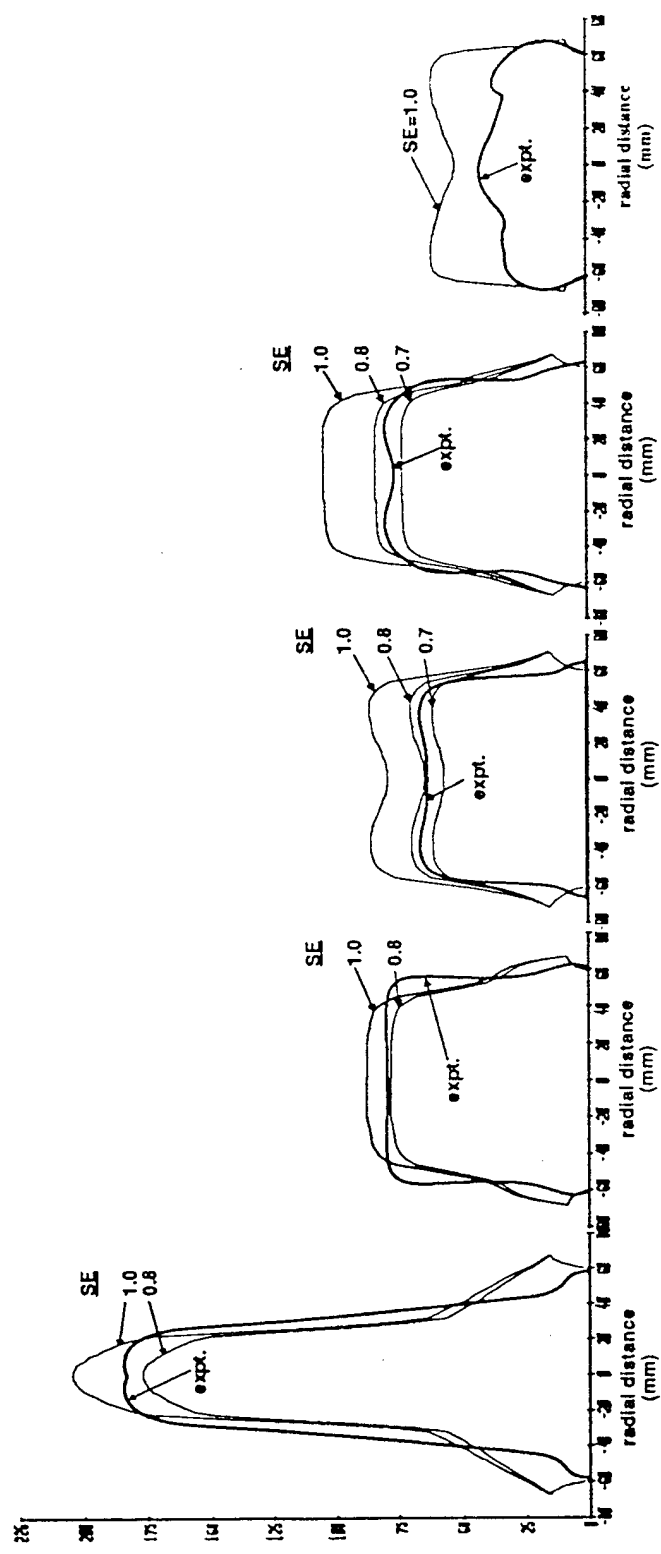


Fig. 49 Comparison of the predictions of the Shape Model with experimental results for Cu-6wt%Ti billets sprayed under a range of experimental conditions designed to yield a range of liquid fractions in the spray. Different assumed sticking efficiencies (SE) are illustrated. The elongated experimental shape of the billet at a fraction liquid of 0.16 (16%) arose from the accidental use of a significantly higher substrate withdrawal rate, see Fig.48. The Shape model has had no difficulty in matching this.

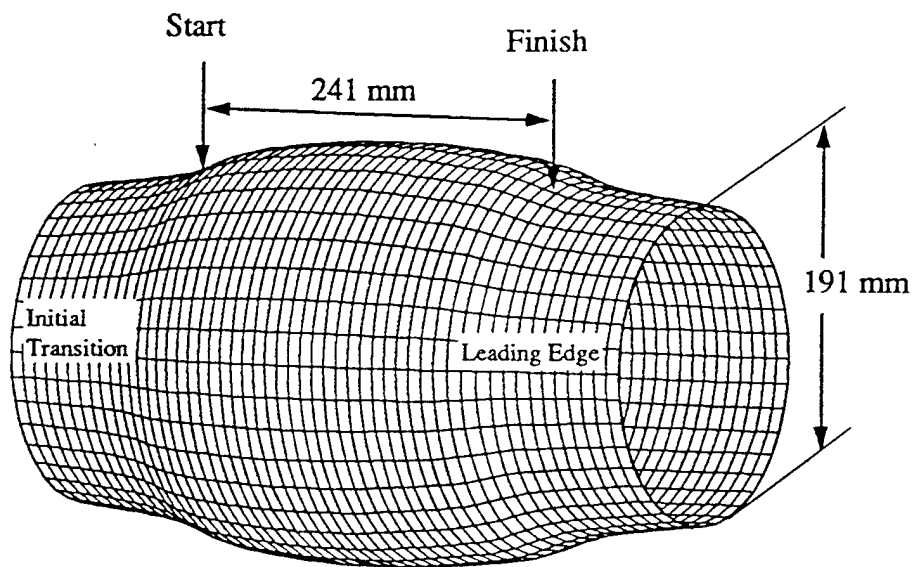


Fig.50 The Three Dimensional Model predicted shape for an IN 625 tube produced after 107s of deposition time.

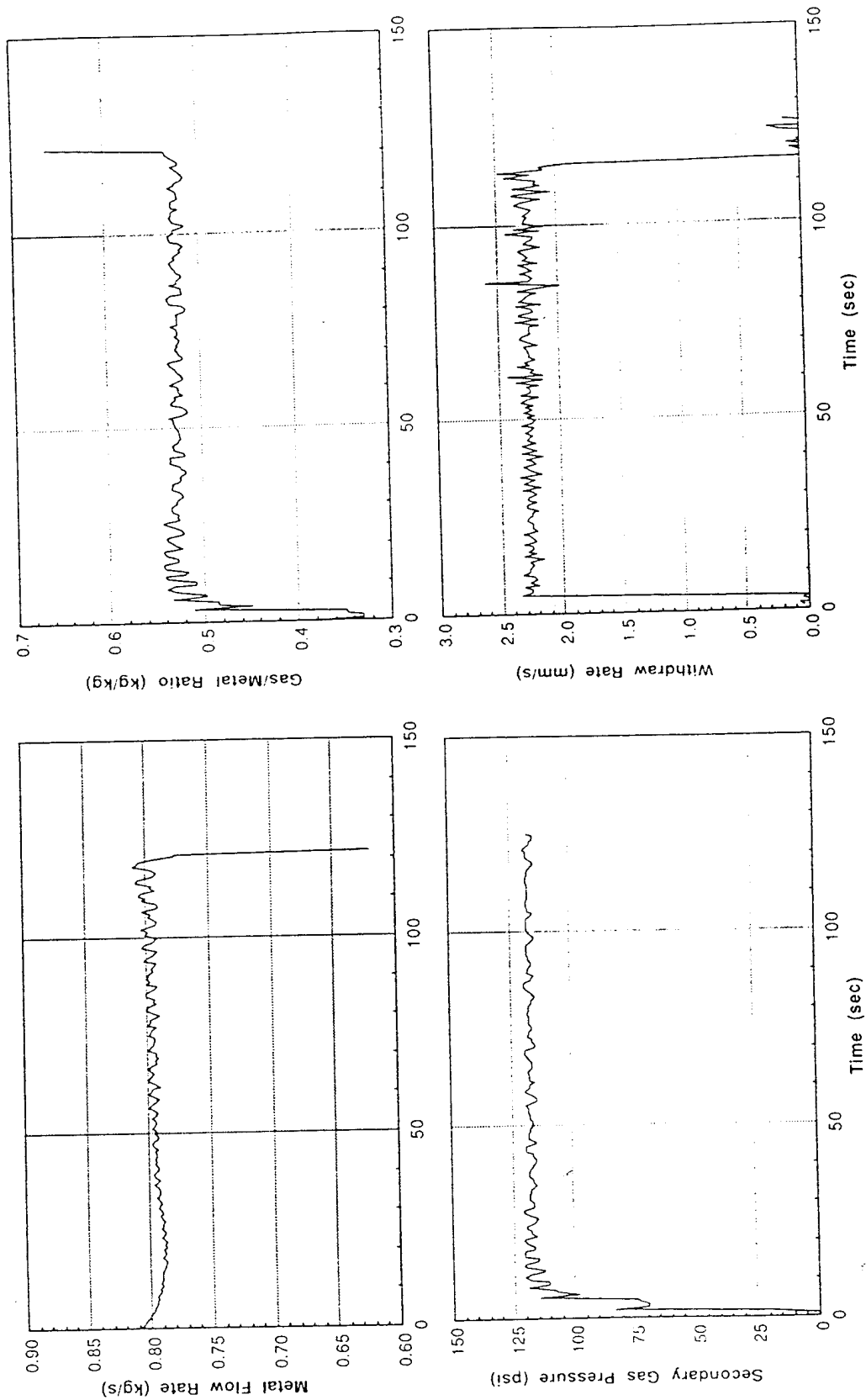


Fig. 51 The recorded variation of four of the major process variables for the IN 625 tube shown in Figs 50.

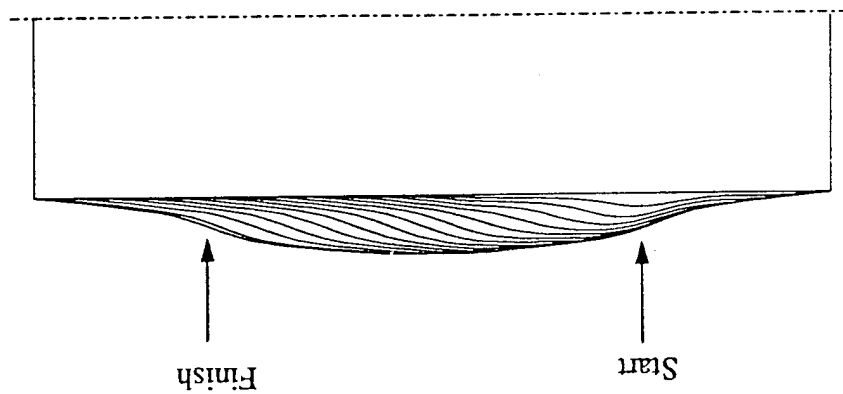


Fig. 52 The predicted cross sections of the IN625 tube seen in Fig.50 after 8s time intervals from the start of deposition.

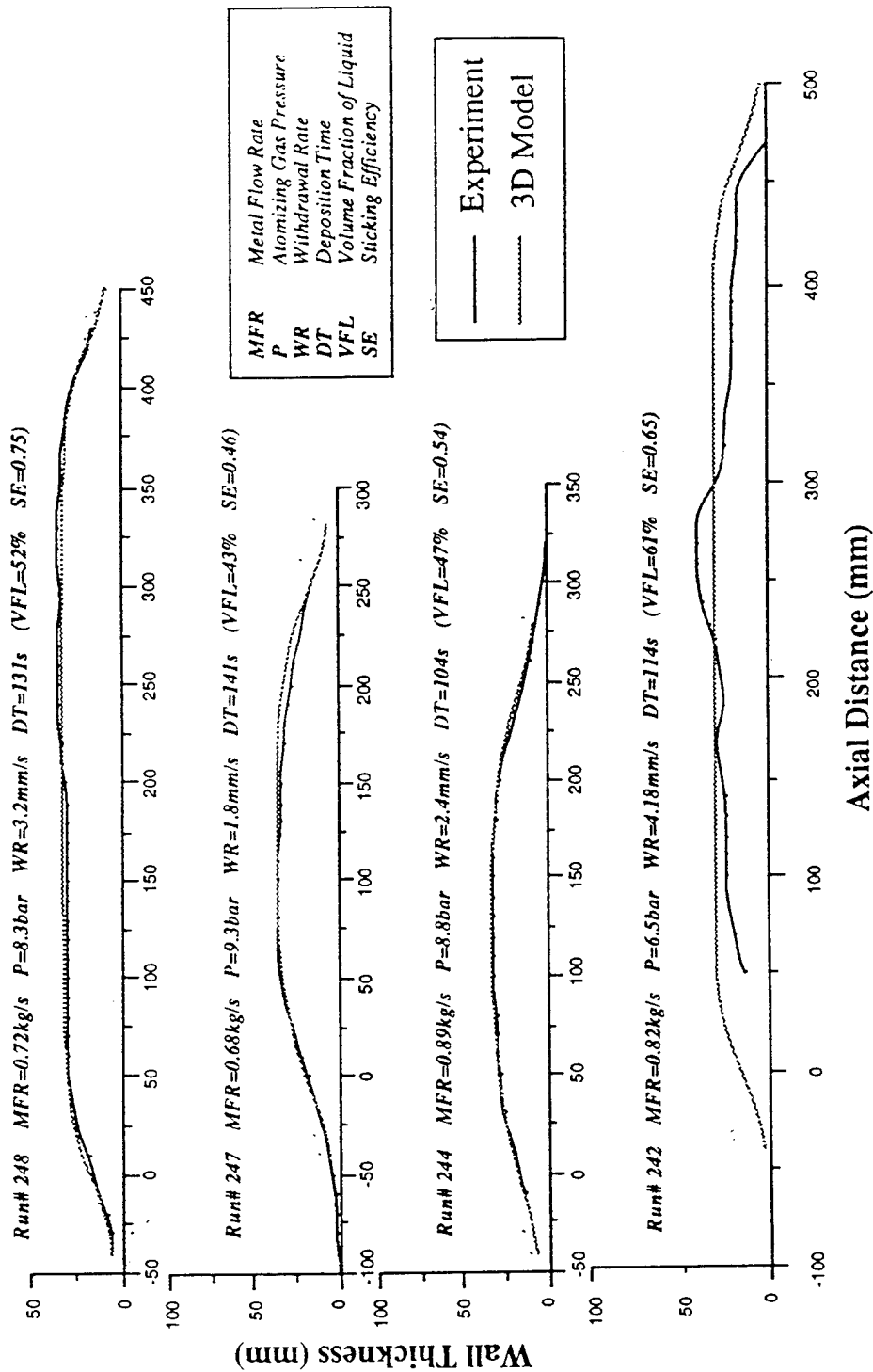


Fig. 53. Comparison of the predictions of the Shape Model for four IN625 Tubes sprayed at NSWC for the conditions shown. The overall sticking efficiencies (SE) required to achieve the match with the experimental shapes is also shown.

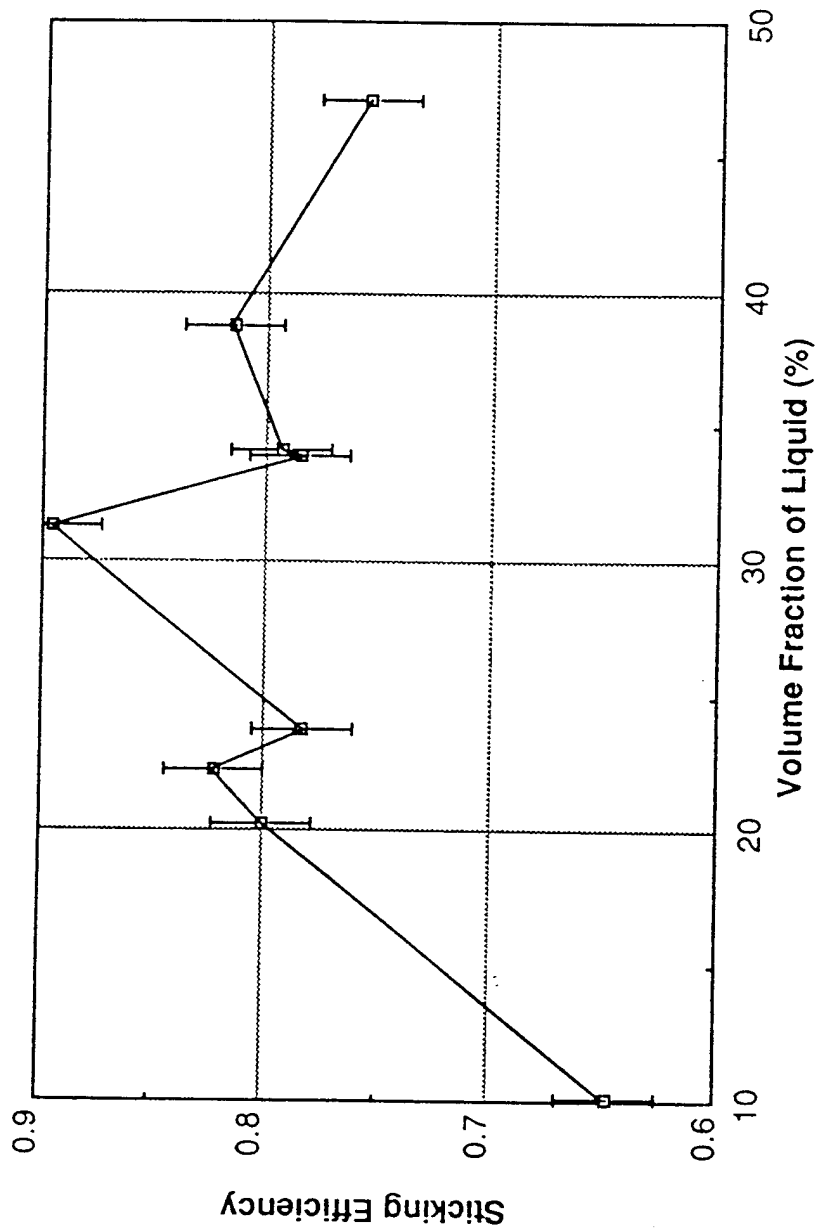


Fig.54 Variation of the sticking efficiency, measured from experimental runs in comparison to the prediction of the Shape Model with the designed Fraction Liquid (as %) in the spray as predicted by the Spray Model. Cu-6wt% Billets spray formed at the Osprey facility at Drexel University.

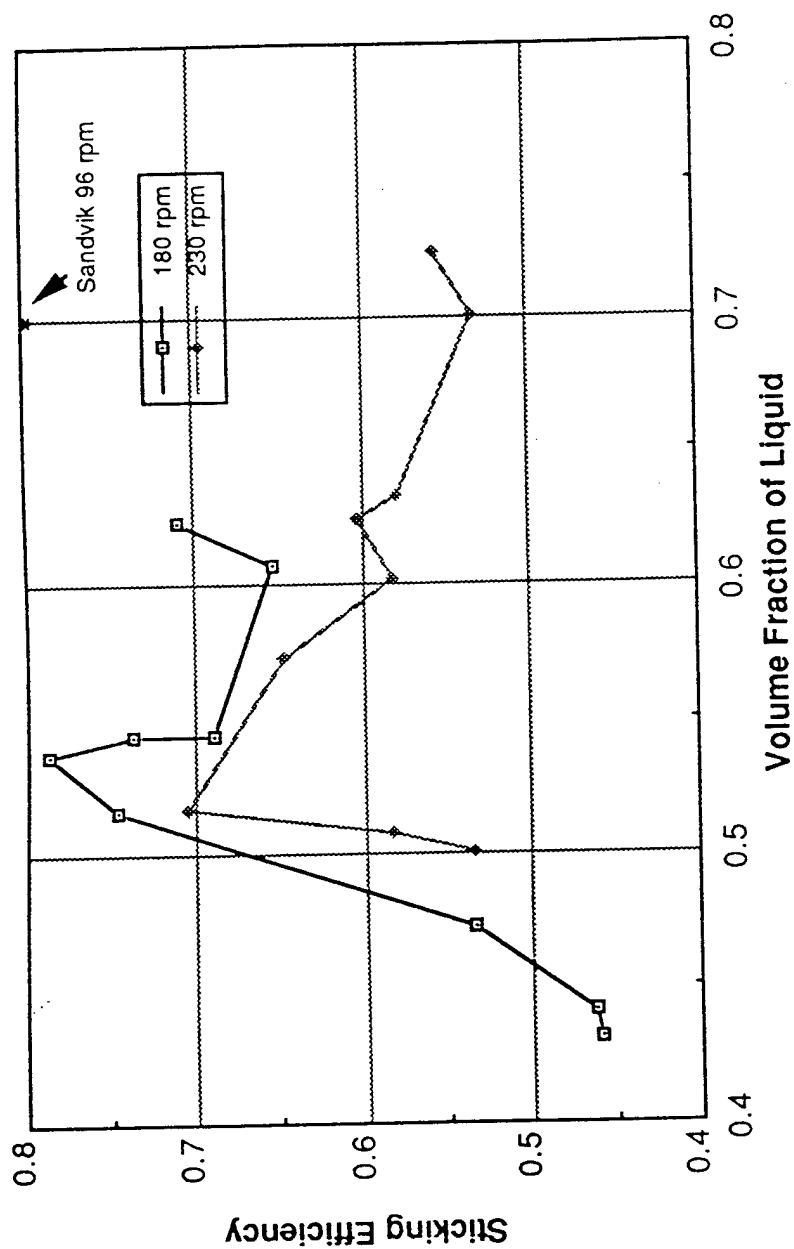


Fig.55 Variation of the sticking efficiency, measured from experimental runs in comparison to the prediction of the Shape Model with the Fraction Liquid in the spray as predicted by the Spray Model. Data for IN625 spray formed at NSW at two different madre/substrate rotation rates together with one data point determined from data supplied by Sandvik at the lowest rotation speed.

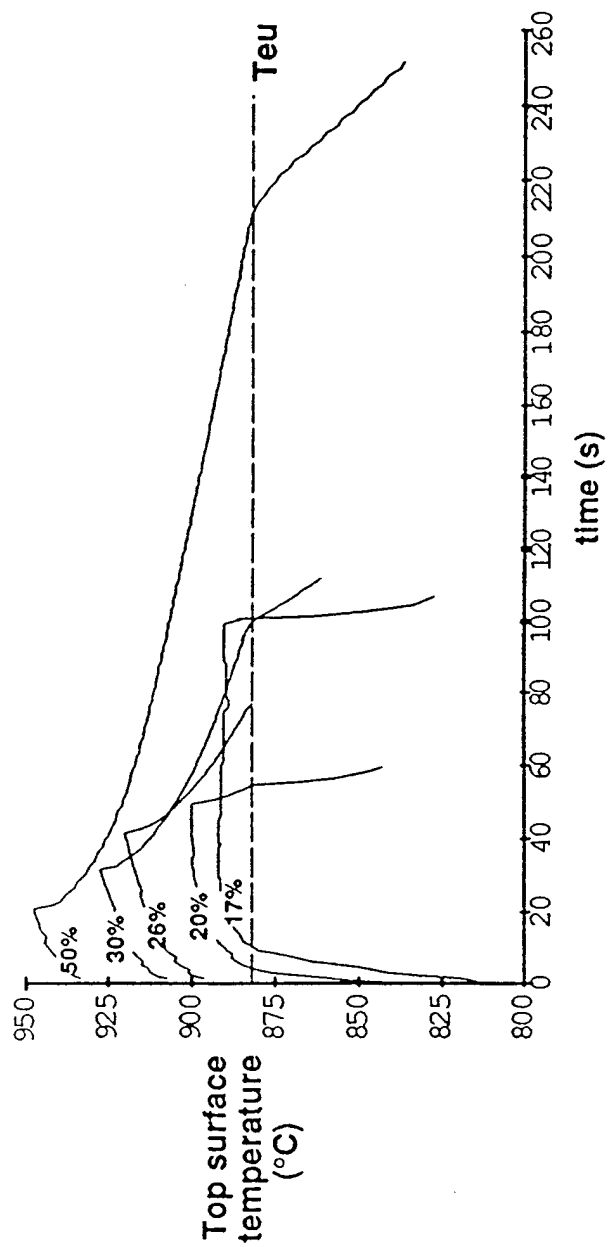


Fig.56 Billet temperatures at the top surface as predicted by the two dimensional thermal model for five of the Cu-Ti experiments at different liquid fractions in the spray.

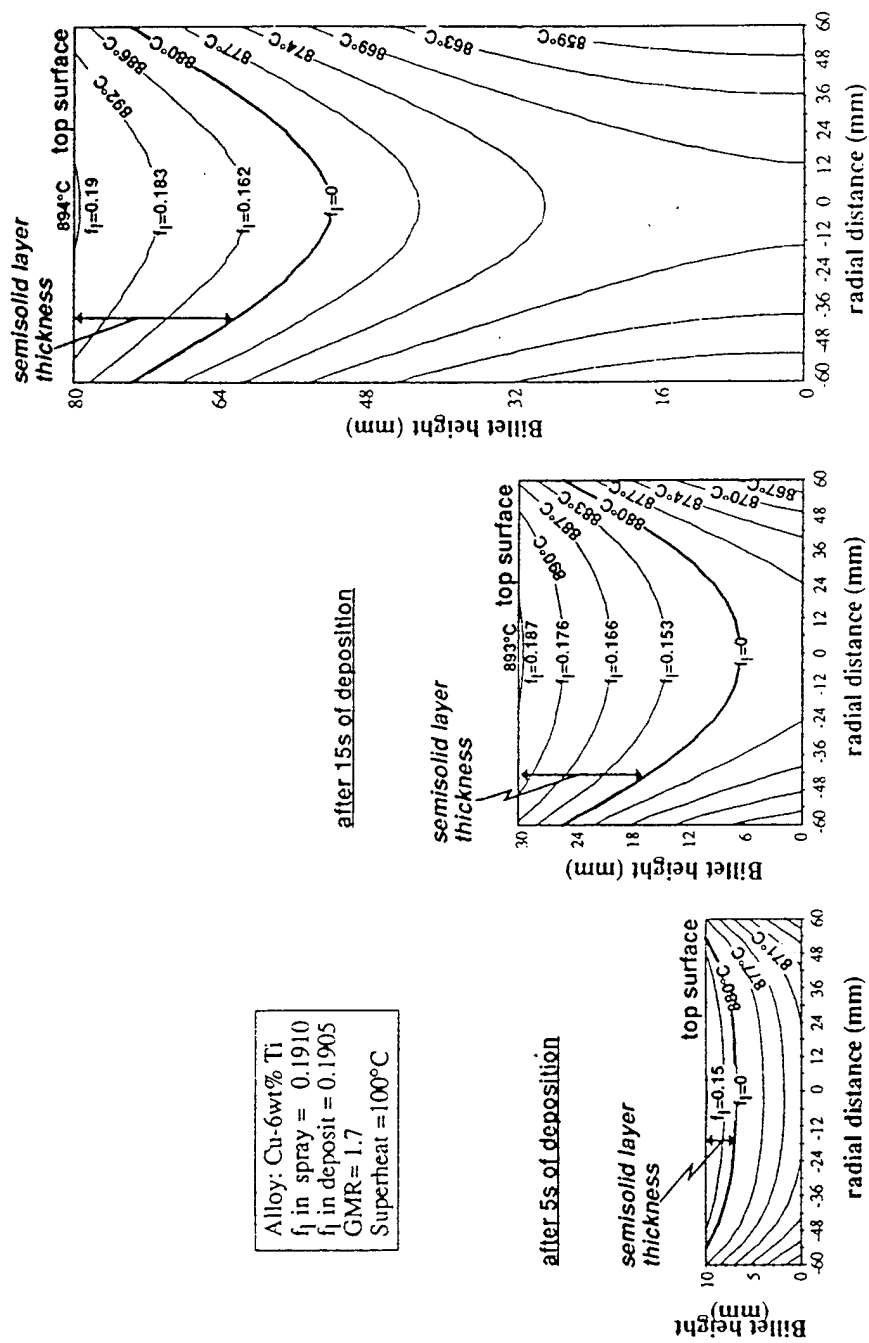


Fig 57 Predicted temperature contours after 5, 15 and 20s deposition of Cu-6wt%Ti at a fraction liquid in the spray of 0.19 (20% in Fig.56) showing the depth of the semi-solid region at the top of the ingot.

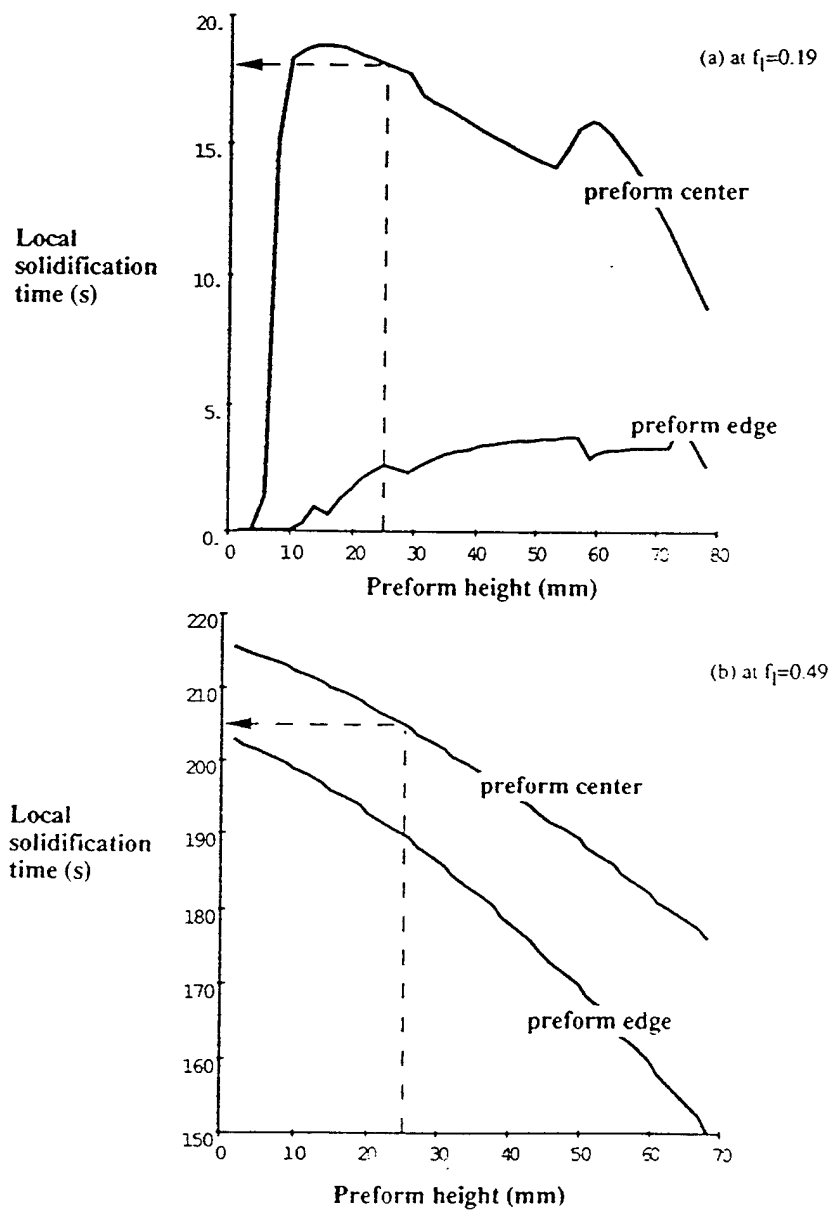


Fig.58 Predicted local solidification times for two Cu-6wt%Ti billets sprayed at two different liquid fractions (a) 0.19 and (b) 0.49.

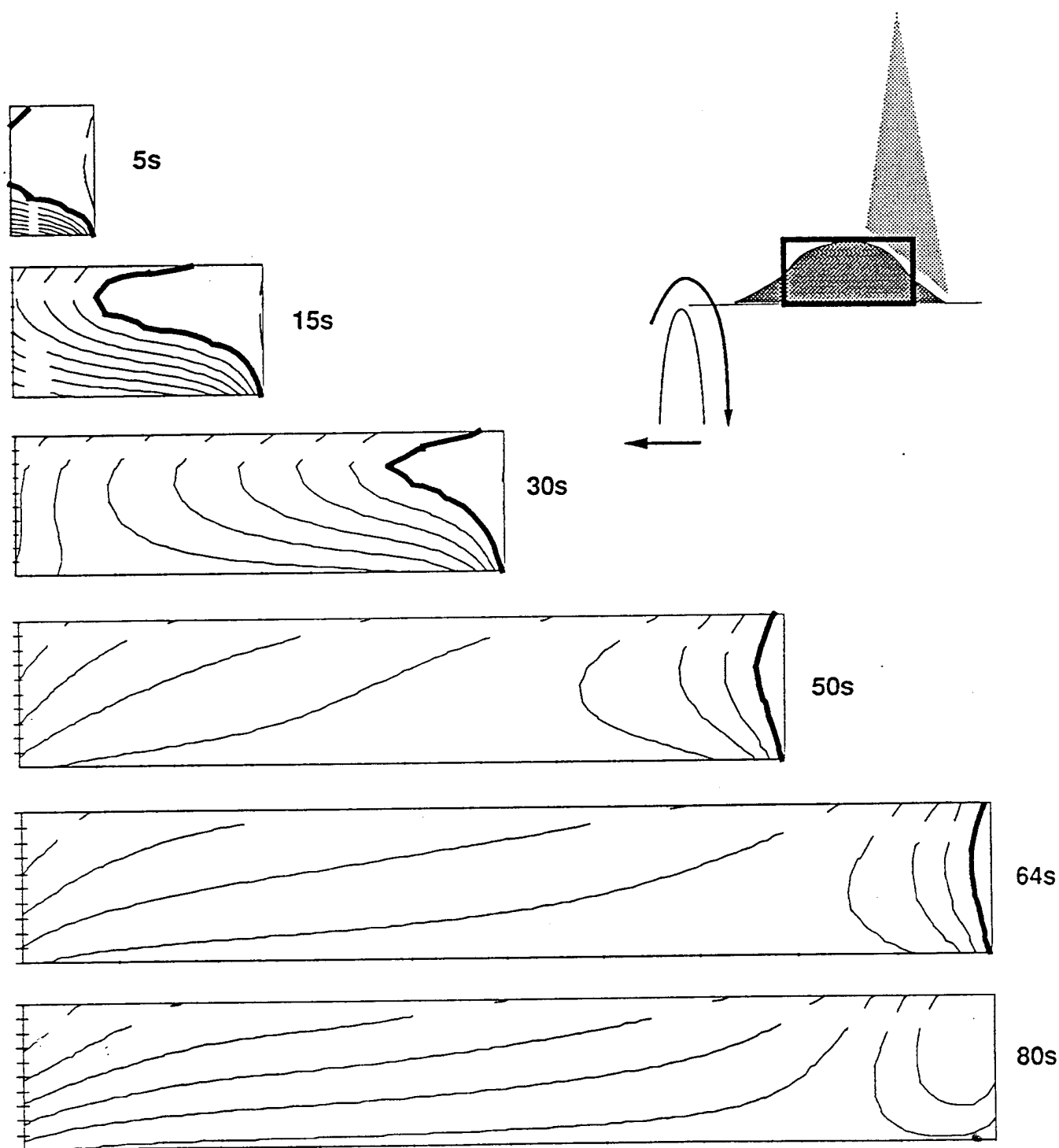


Fig.59 Computed isotherms for an IN 625 tube deposited at NSW at a fraction liquid, in the spray, of 0.46. The geometry is indicated in the cartoon. The solid line in the deposit makes the predicted solidus isotherm where the fraction liquid reaches zero.

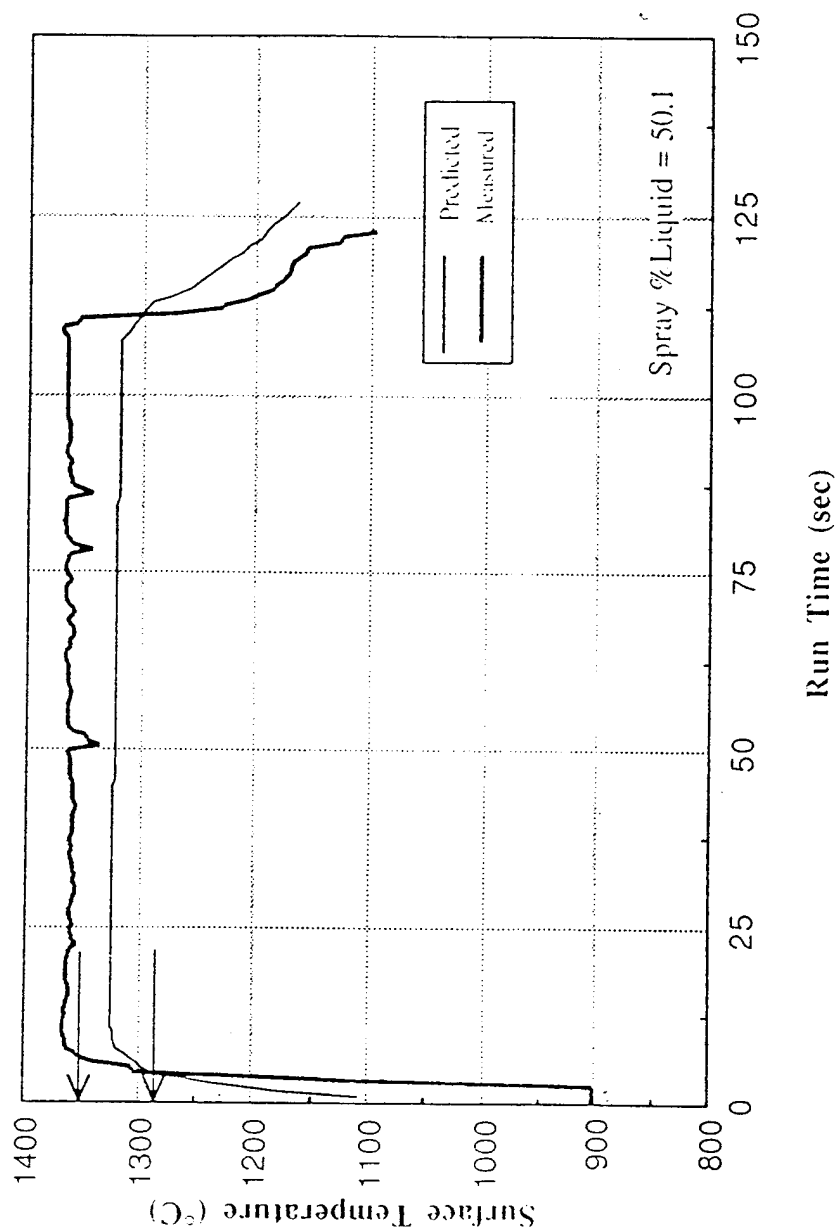


Fig.60 Comparison of the model predictions and pyrometer measurements of the surface temperature , under the spray, for IN625 deposited at NSWCC at a fraction liquid, in the spray, of 0.5. The alloy liquidus and solidus temperatures are indicated.

Model Prediction

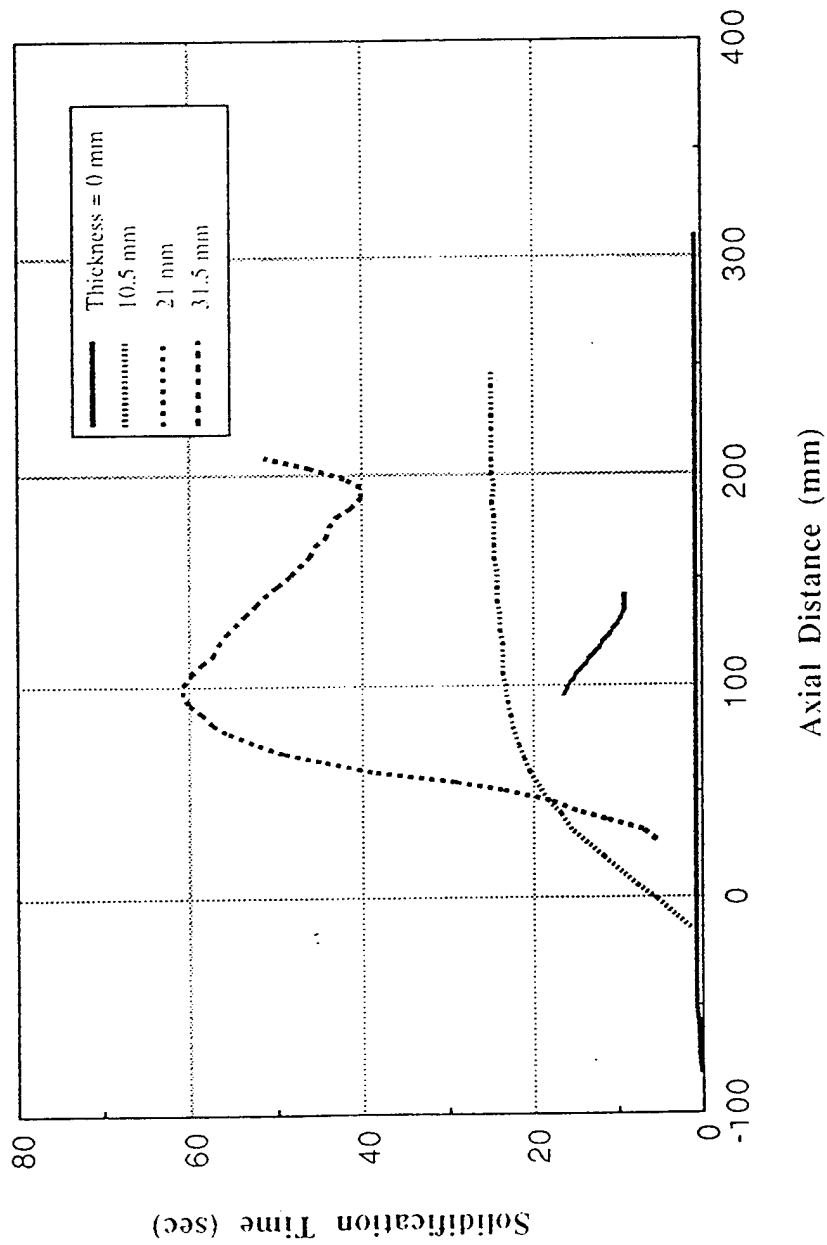


Fig.61 Predicted solidification times along the axial distance of the IN625 tube spray formed as shown in Fig.60. The axial distance of zero is the starting position of the center of the spray. The short curve from about 95 to 145mm is that at a radial distance of 31.5mm from the inner surface of the tube and is close to the outer surface. (The shape of the tube is similar to that at run #247 in Fig.53)

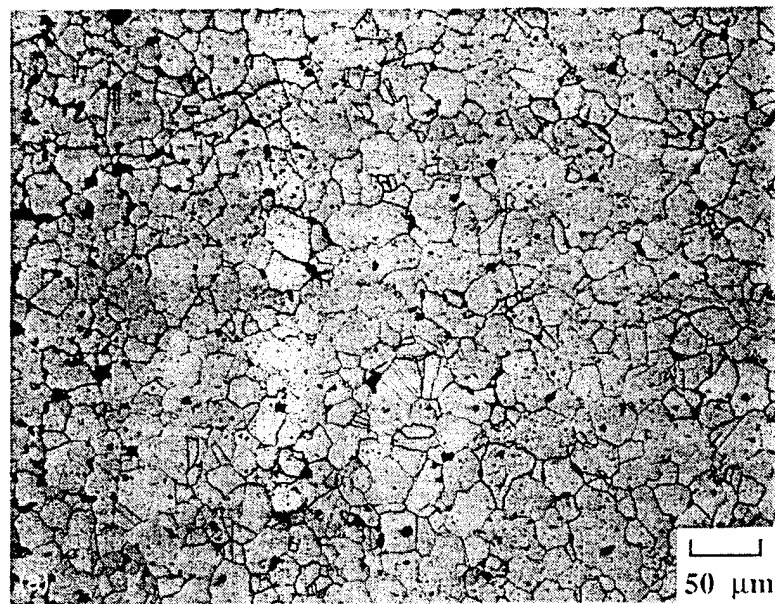


Fig.62 Microstructure produced in spray formed billets of Cu-6wt%Ti billets at heights of 25mm from the substrate in the center of the billets at two different fractions liquid in the spray. (a) f_l of 0.19 with a solidification time of 18s giving a grain size of $19\mu\text{m}$ and (b) f_l of 0.49 with a solidification time of 206s giving a grain size of $46\mu\text{m}$. The reduced fine scale porosity at the higher fraction liquid is also clearly visible (measured at 5% and 1%). The positions observed are those indicated in fig. 58, describing the thermal model.



Fig.63 Dendrite fragmentation of a Cobalt alloy, MP35N, during spray forming. From independent work by R.P. Singh at Drexel University.

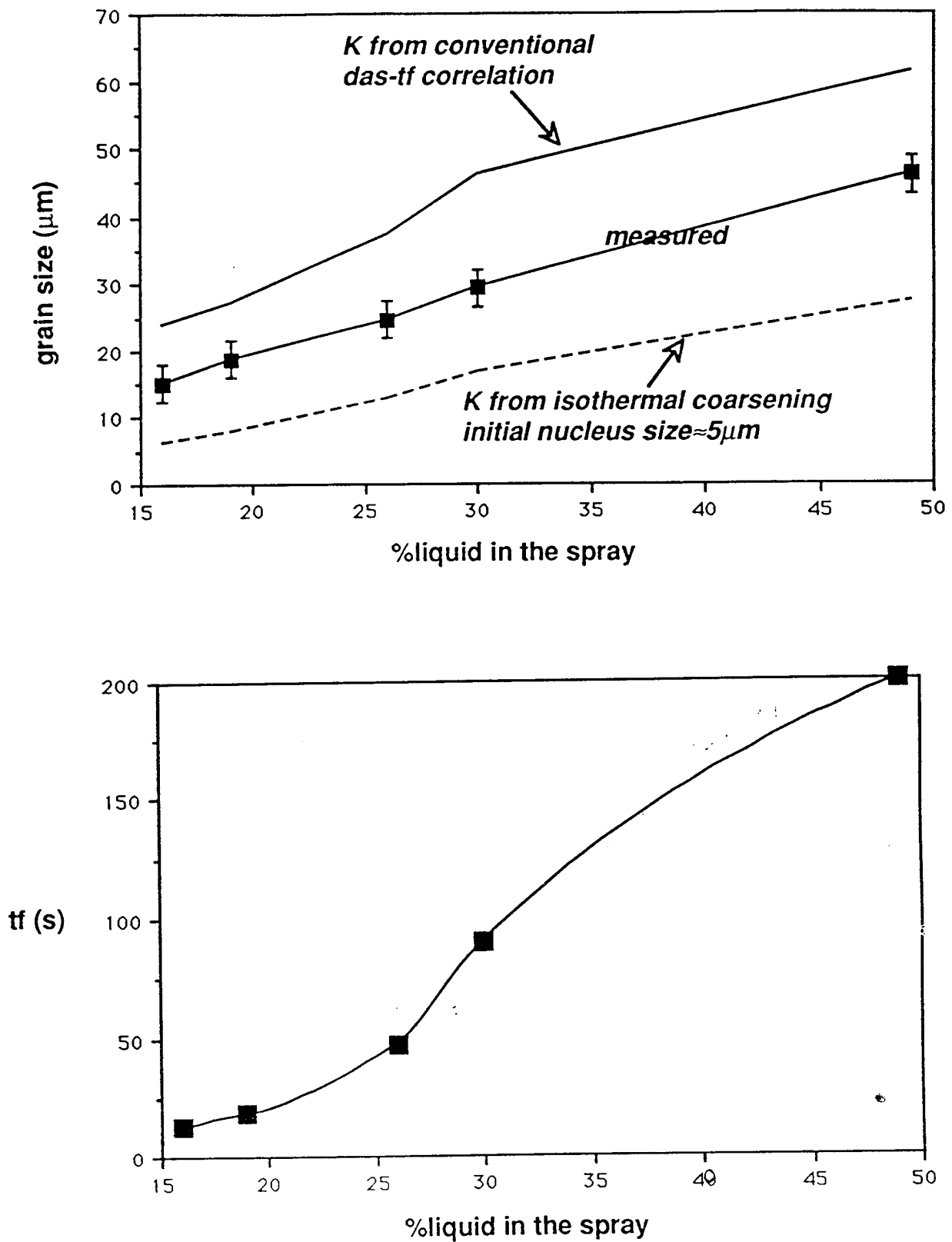


Fig.64 (a) The variation of grain size and (b) the variation of solidification time at an axial location in Cu-6wt%Ti billets 25 mm from the substrate both plotted against the fraction liquid in the spray. Two different attempts to model the change of grain size are also shown.

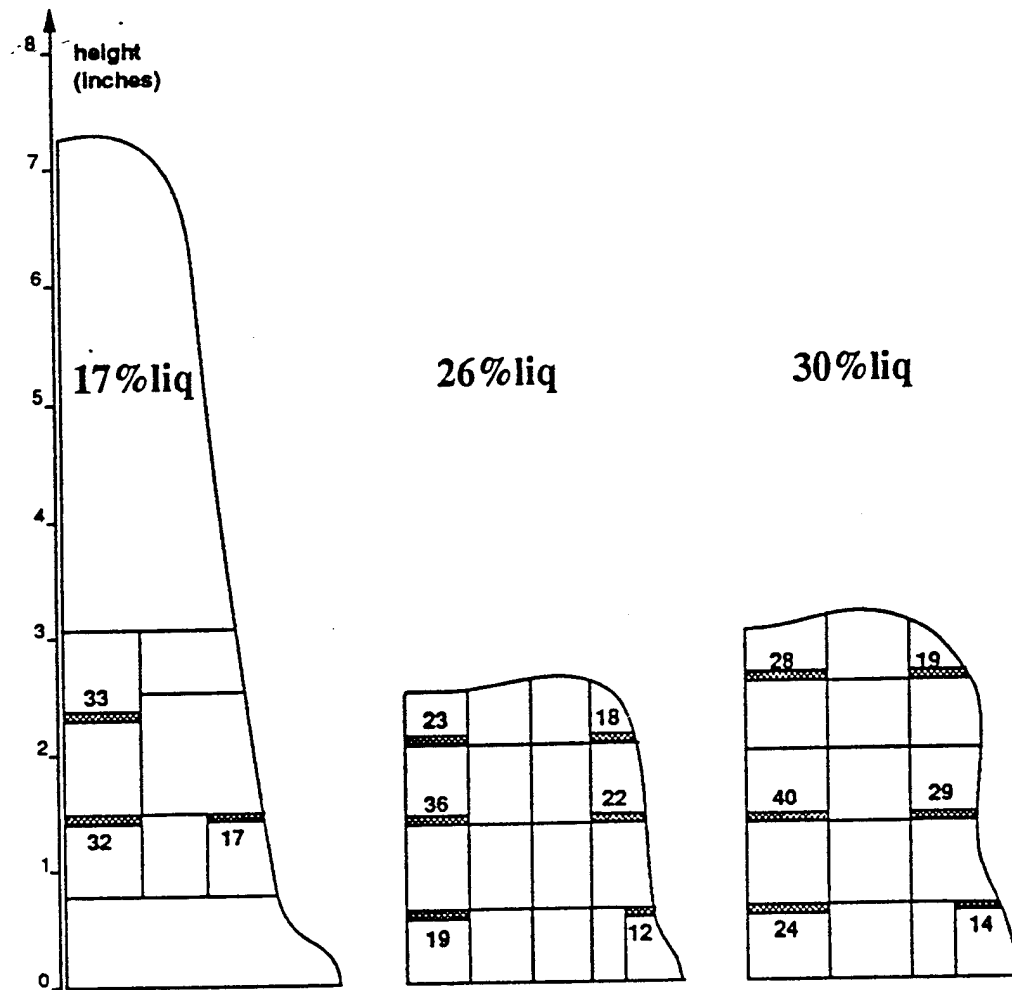


Fig. 65 Variation of grain size (in μm) with position in Cu-6wt%Ti billets formed with different liquid fractions in the spray

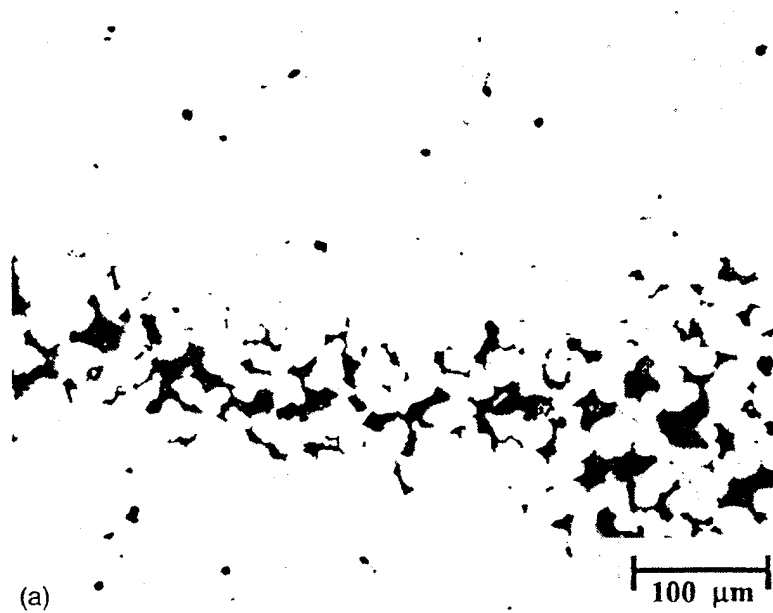


Fig. 66 Interconnected non spherical pores found here between subsequent layers in a Cu-6%Ti billet arising from enhanced gas cooling due here to incorrect substrate motion - the fraction liquid in the spray was 0.2.

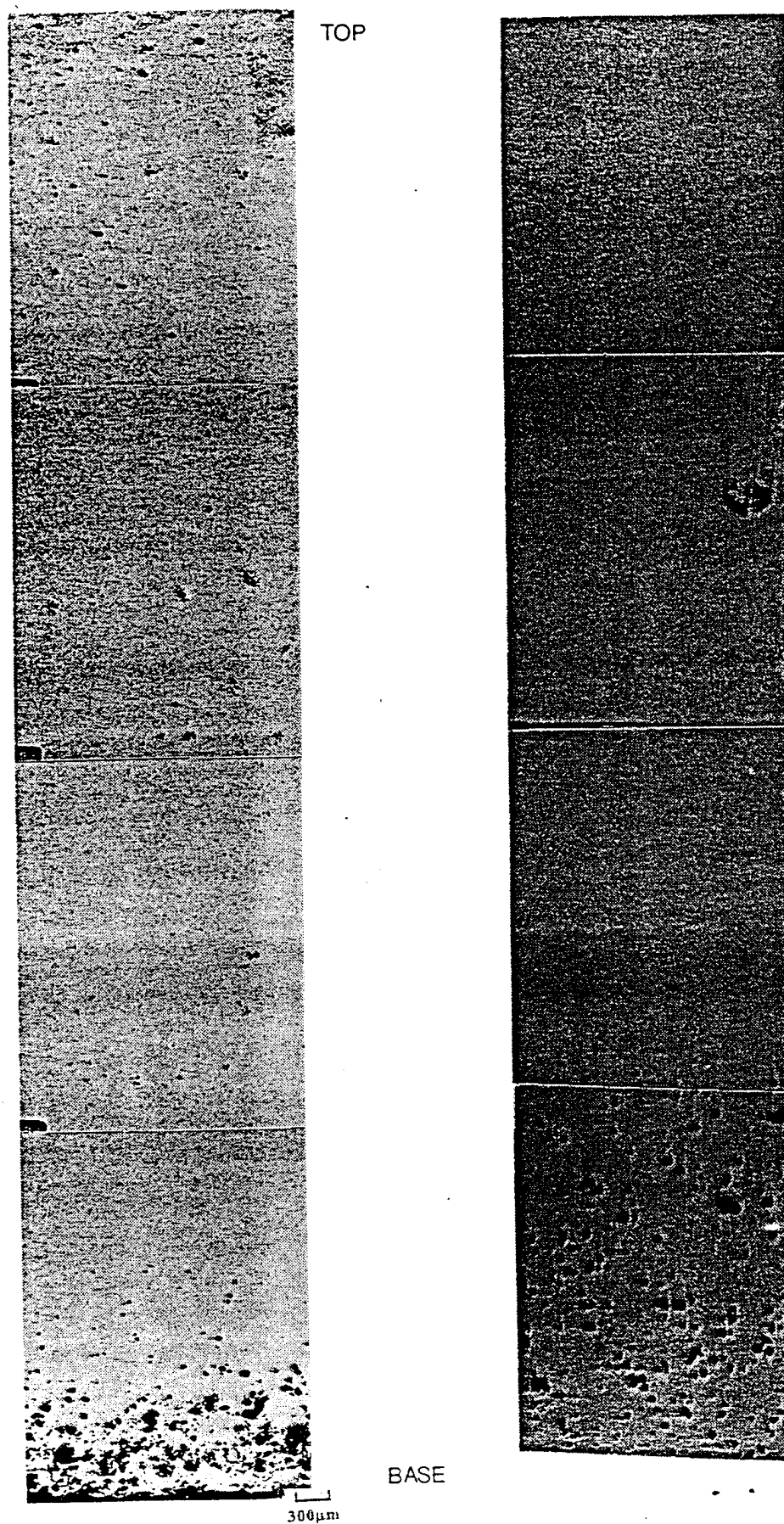


Fig. 67 High levels of porosity seen close to the substrate surfaces in a tube of In 625. The positions shown are described in fig.70.

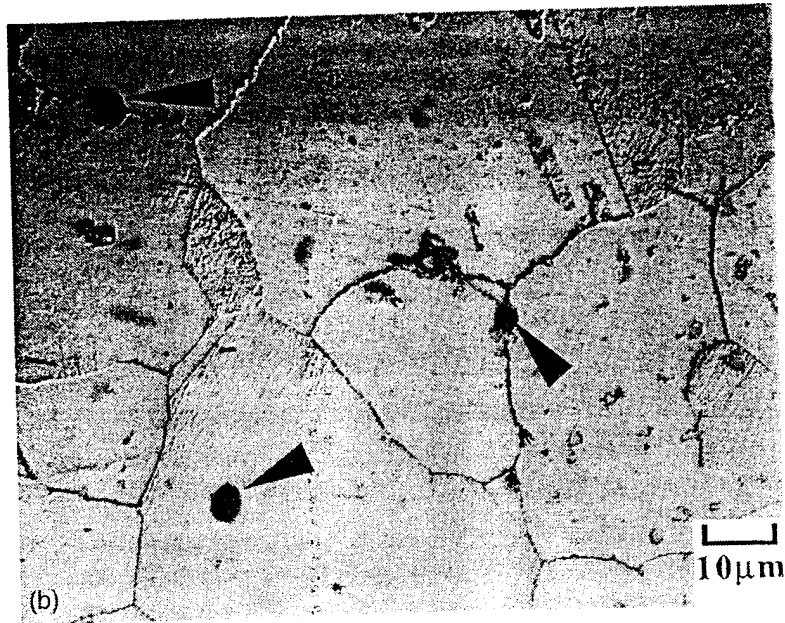


Fig. 68 Fine scale pores seen mainly but not universally at grain boundaries in the spray formed deposit. Cu-6wt%Ti billet sprayed at a fraction liquid of 0.26.

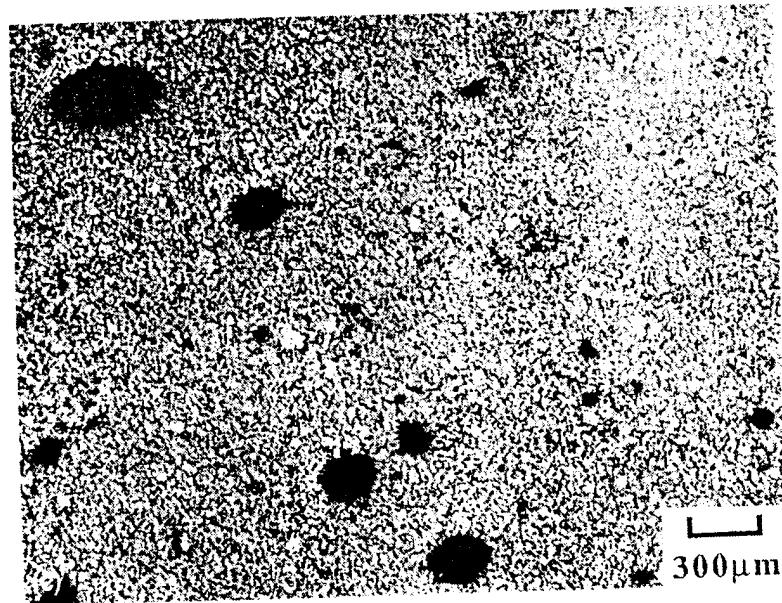


Fig. 69 Large spherical pores seen mainly in deposits formed at at very high liquid fractions. Cu-6wt%Ti billet sprayed at a fraction liquid of 0.6.

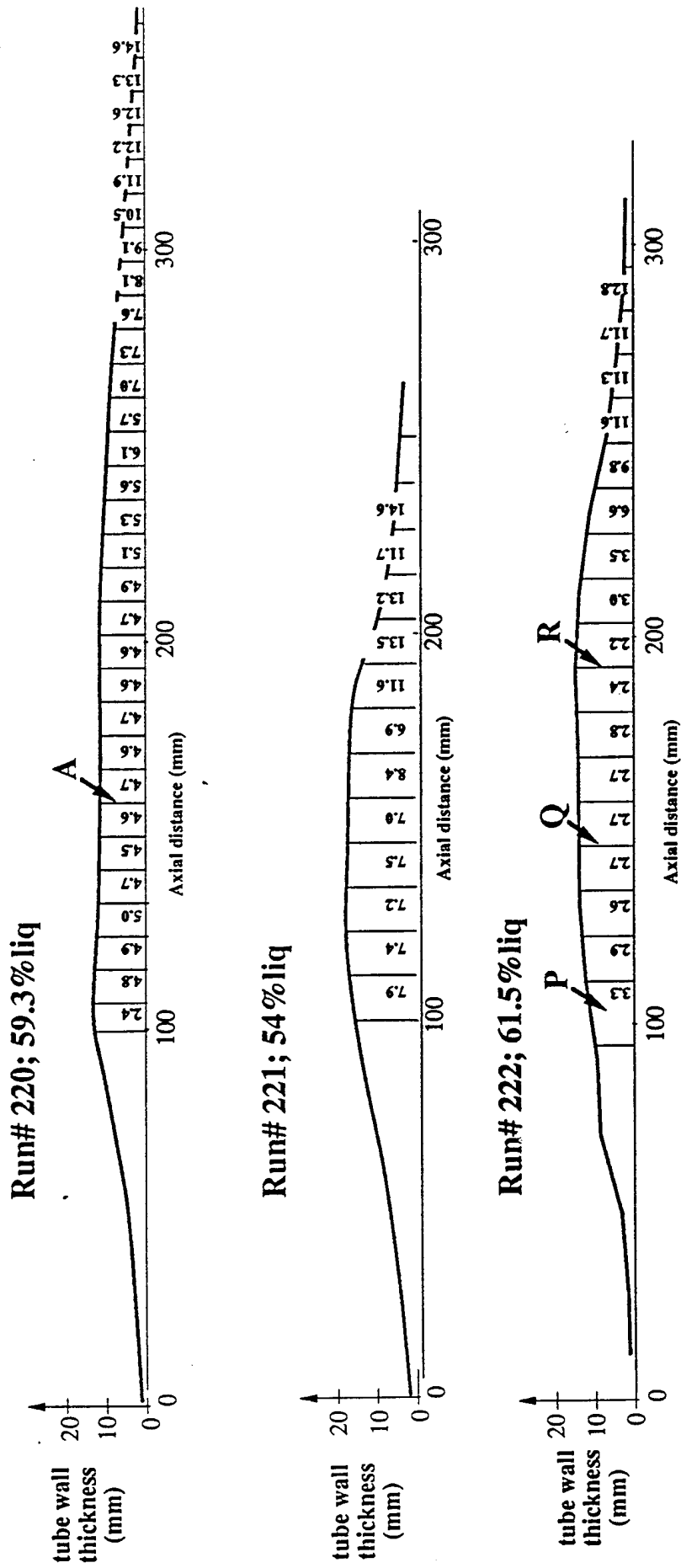


Fig. 70 Variation in porosity along the length of three IN626 tubes. The microstructures at positions Q and R in run 222 were previously shown in fig.67.

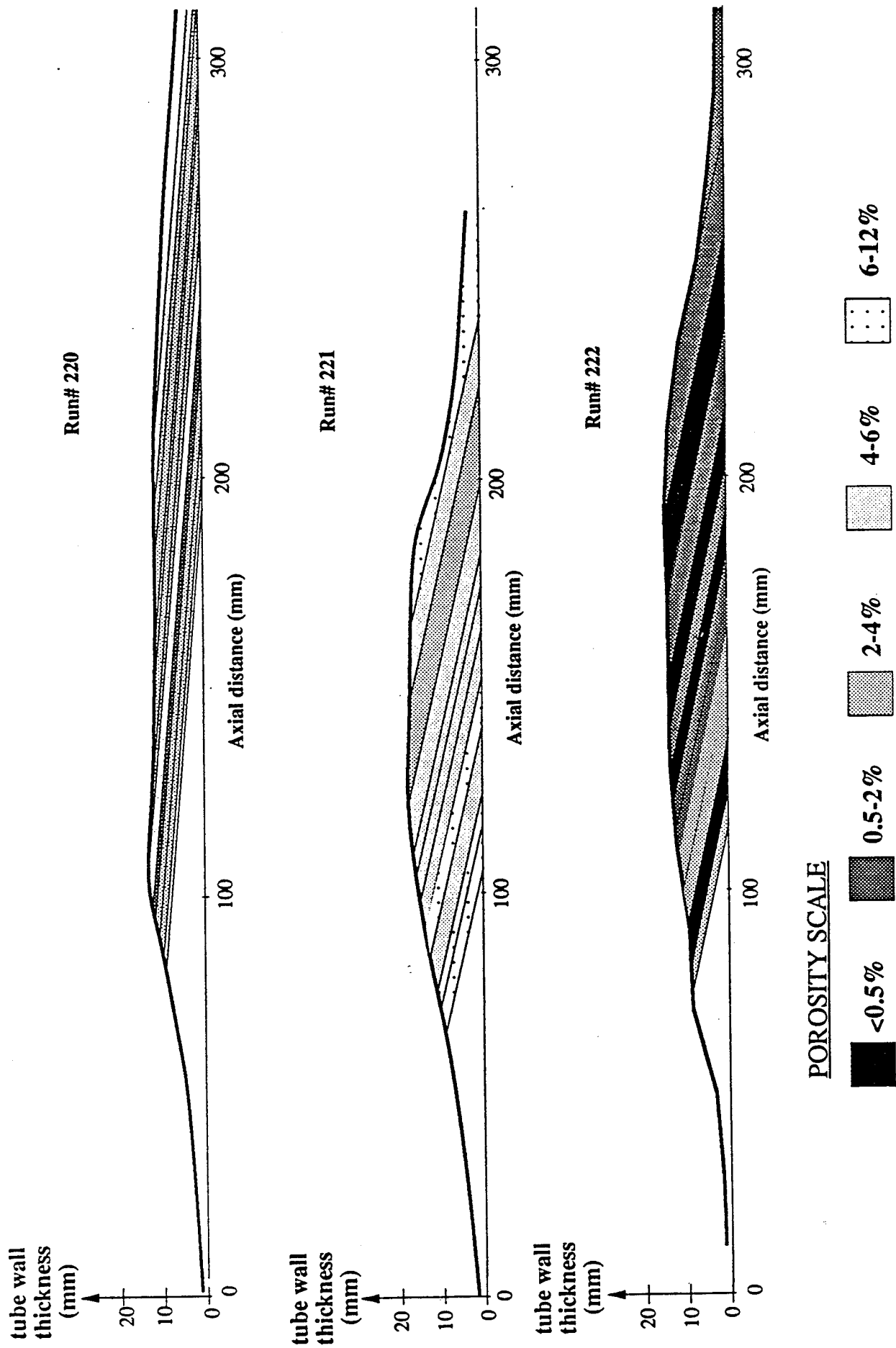


Fig. 71 Variation in porosity along the length of the three IN625 tubes seen in Fig.70 - but measured on slant samples to give for each position a full sampling of the different radial positions in the tube.

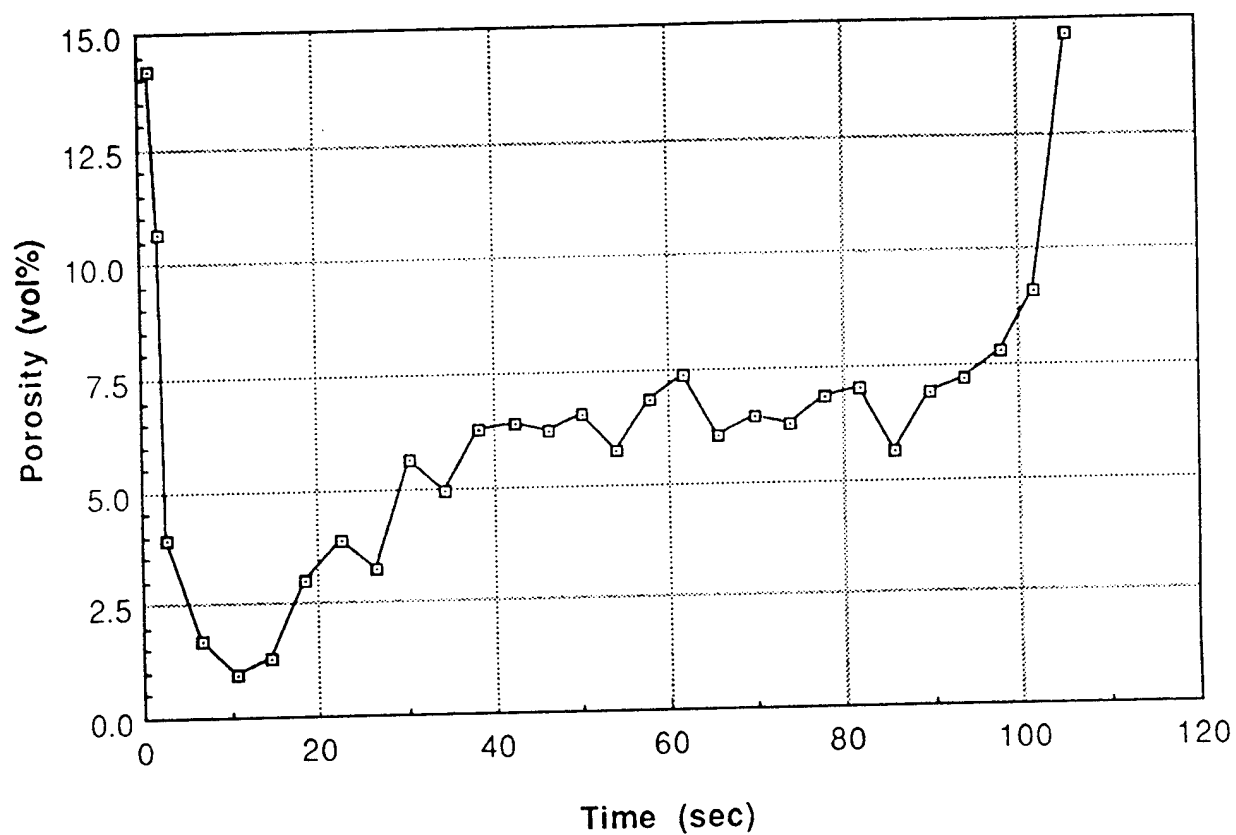


Fig. 72 Variation in porosity along a further IN 625 tube - the tube previously shown in figs. 50-52, with a fraction liquid of 0.50.

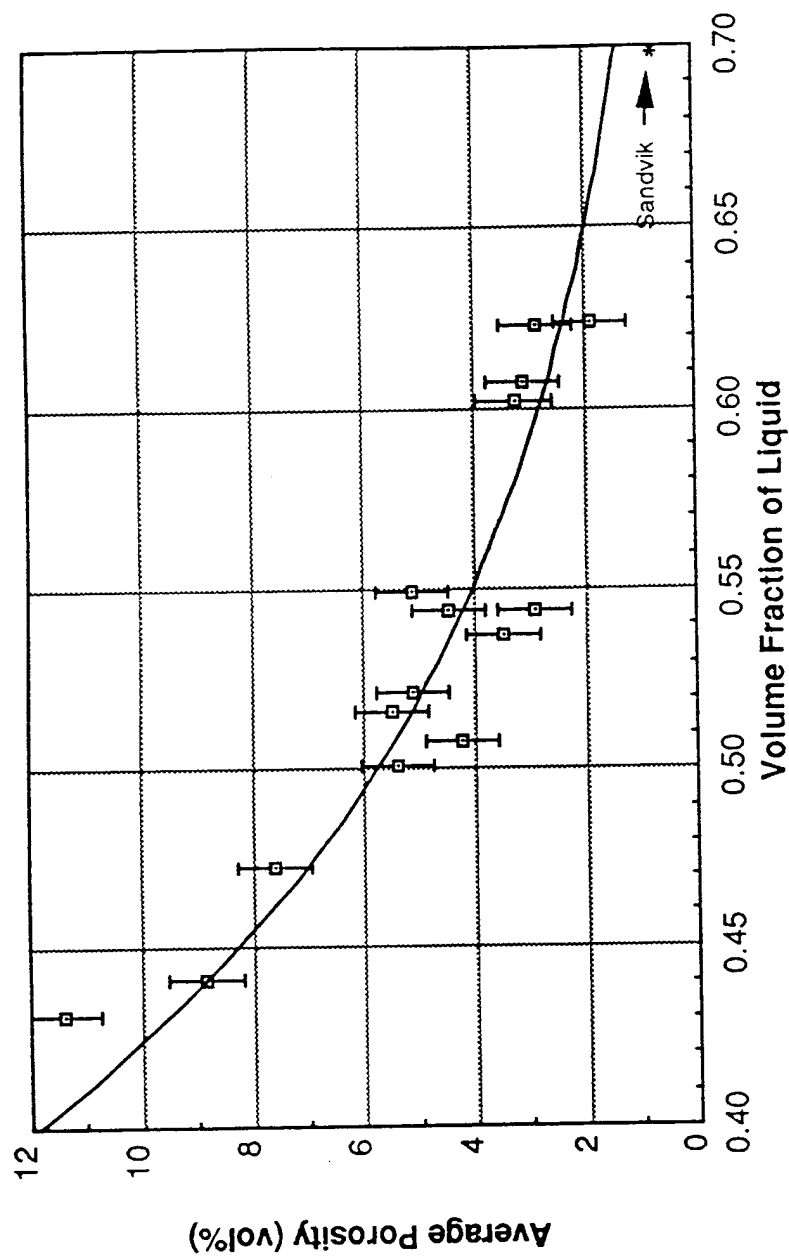


Fig. 73 Variation of average porosity for IN 625 tubes, avoiding the transient regions at start and end of the tube, as a function of fraction liquid *in the spray*.

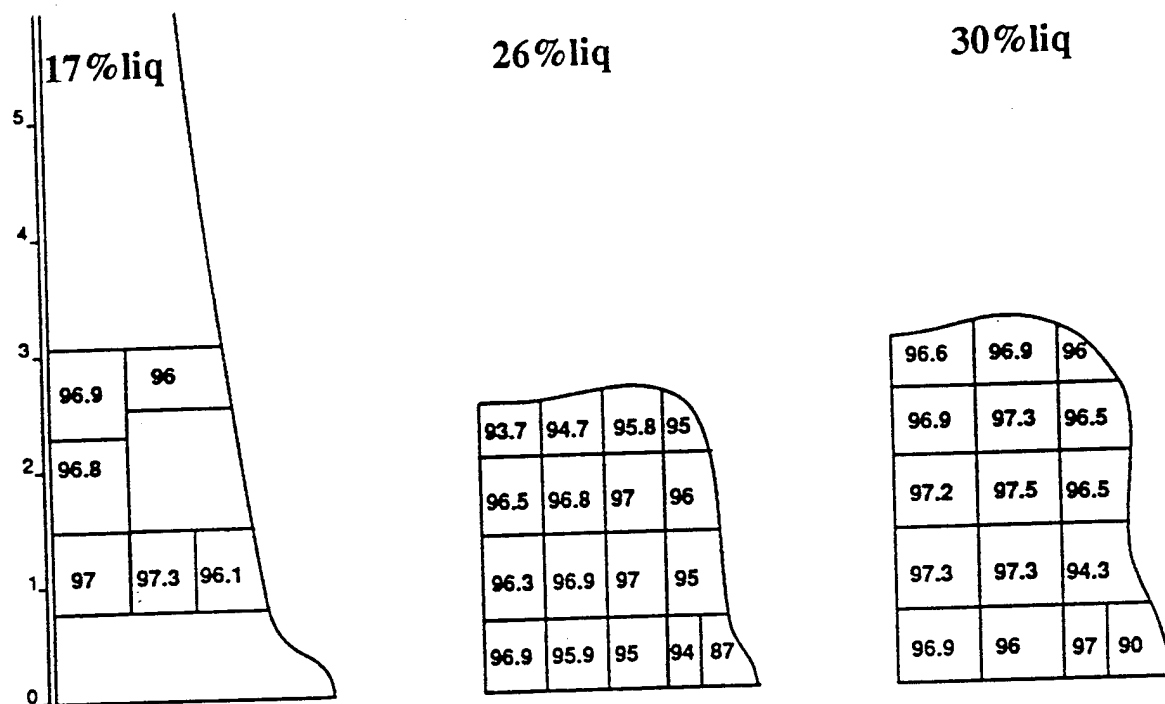


Fig.74 Density distribution in spray form billets of Cu-6wt5 Ti at different liquid fractions.

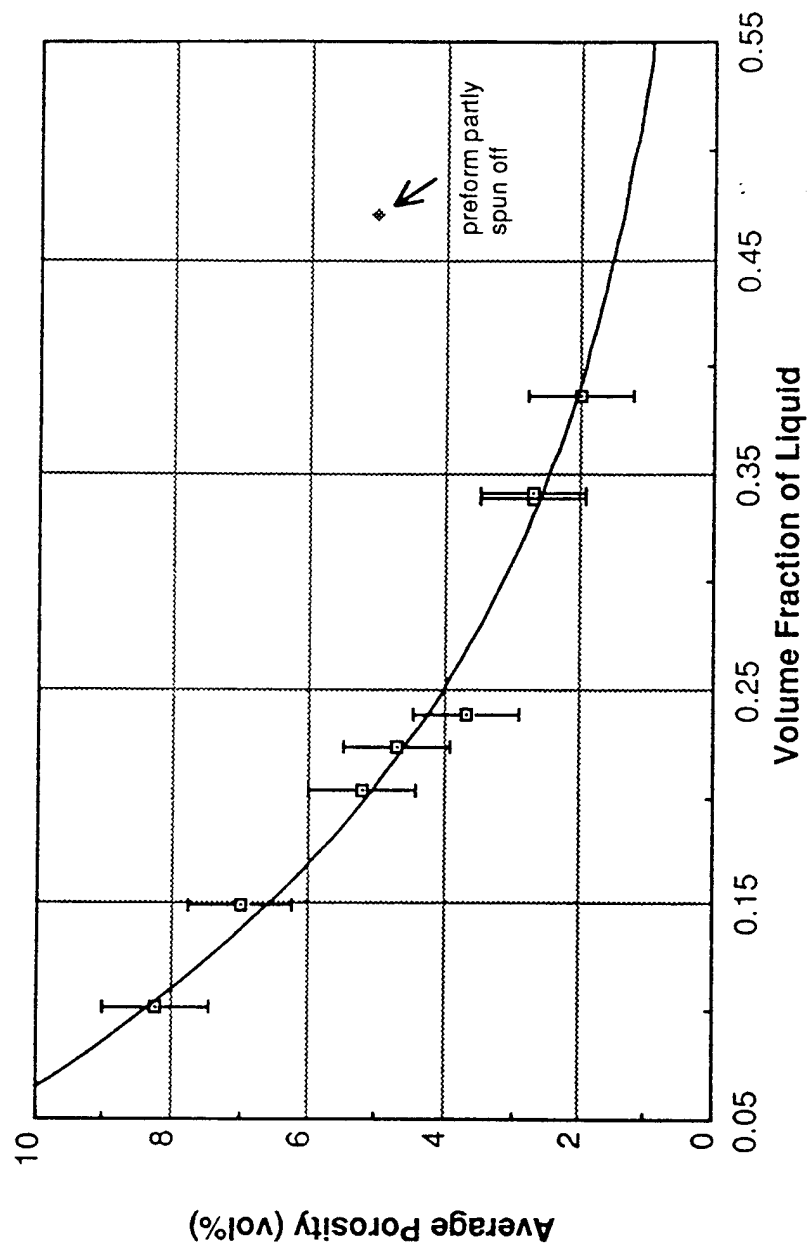


Fig. 75 Variation of average porosity for Cu-6wt%Ti billets as a function of fraction liquid in the spray.

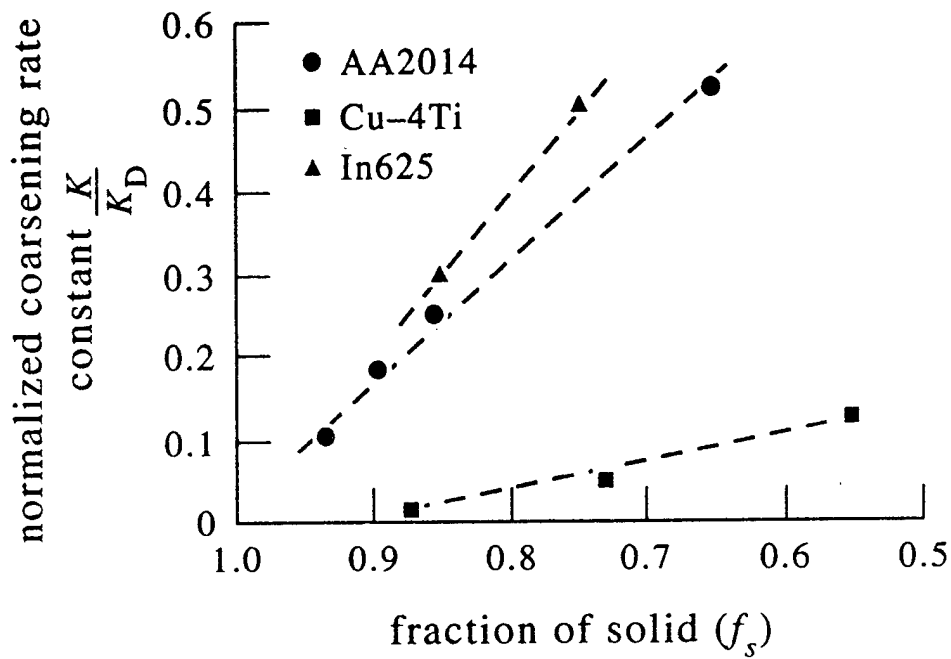
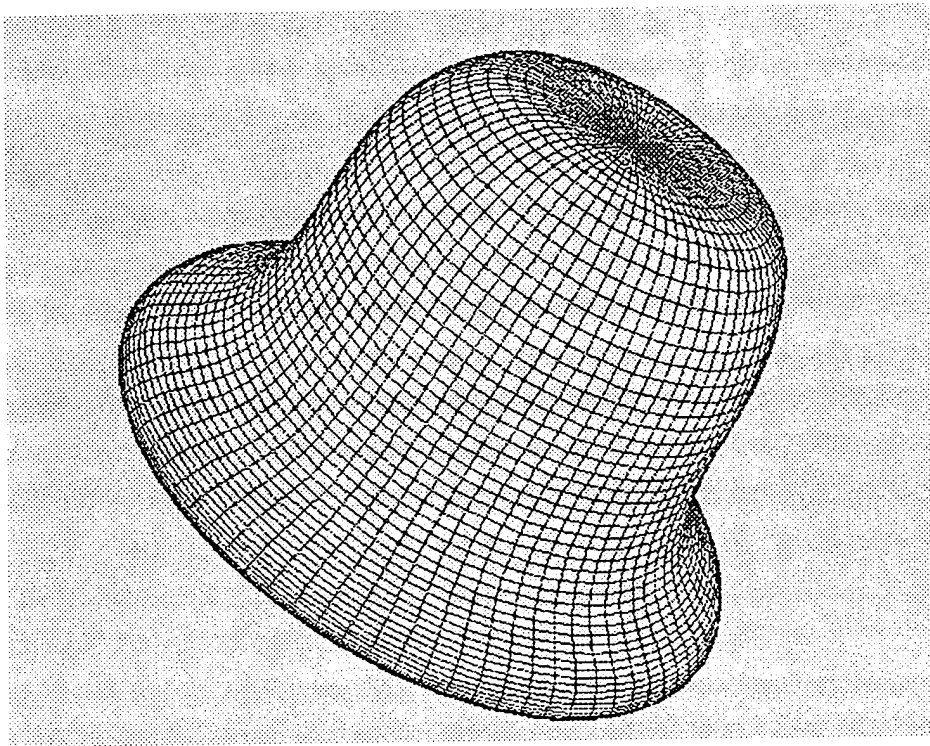


Fig. 76 Normalized coarsening rate constant, K_{exp}/K_d , as a function of fraction solid, f_s , for three spray formed alloys AA 2014, Cu-4%Ti and IN625.

DU SHAPE

3D Shape Modeling for Spray Forming



Software Notes
Version 1.2a

Contents

1 Overview.....	1
2 Disclaimer.....	1
3 Introduction.....	2
3.1 Background	2
3.2 Fundamentals of 3D Shape Modeling.....	2
3.3 Object-Oriented Approach	3
4 Installing the Software	4
4.1 System Requirements.....	4
4.2 Installation Instructions	4
5 Compiling Instructions	6
6 Running the Software	7
7 Preprocessor and Postprocessor.....	9
7.1 Preprocessor	9
7.2 Postprocessor	9
8 Comment	10
9 Bugs Report.....	10
10 Appendix.....	10
A Explanation of Aforementioned Abbreviations	10
B An Input Format for Prototyping a Step-Tube.....	10

1 Overview

This is the introductory document for exploring DU SHAPE. DU SHAPE is a shape modeling tool kit (abbreviated as "the TK" below) developed at the Drexel University for simulating three-dimensional preform shapes formed in the spray deposition process. It contains an object-oriented 3D class library implemented with C++, which was designed to provide an easy and powerful access to 3D shape modeling.

The DU SHAPE Version 1.2 is an example application constructed by using the TK to demonstrate the main features of the Drexel 3D shape model for predicting simple and complex shapes, including prototypes such as disk, straight tube, curved tube (elbow), tube of variable diameters (step-tube) and sheet.

The Drexel 3D shape model for spray deposition process, that underlies the TK and Version 1.2, is a generic computational method based on the knowledge of 3D surface modeling, spatio-temporal distribution of spray mass, sticking efficiency and motions of the spray jet and substrate manipulator. With the method established on fundamental theories, the TK can be easily extended to develop advanced application software dealing virtually any 3D geometries expectedly encountered in the spray forming process.

2 Disclaimer

Copyright (C) 1993 - 1995
Drexel University

PERMISSION TO USE, COPY, AND DISTRIBUTE THIS SOFTWARE AND ITS DOCUMENTATION FOR ANY NONCOMMERCIAL PURPOSE WITHOUT FEE IS HEREBY GRANTED, PROVIDED THAT THE ABOVE COPYRIGHT NOTICE APPEARS IN ALL COPIES AND THAT BOTH COPYRIGHT NOTICE AND THIS PERMISSION NOTICE APPEAR IN SUPPORTING DOCUMENTATION. PERMISSION TO MODIFY THE SOFTWARE IS ALSO GRANTED, BUT NOT THE RIGHT TO DISTRIBUTE THE MODIFIED CODE. MODIFICATIONS ARE TO BE DISTRIBUTED AS PATCHES TO RELEASED VERSION. THIS SOFTWARE IS PROVIDED "AS IS" WITHOUT EXPRESS OR IMPLIED WARRANTY.

AUTHOR

DU SHAPE Modeling Tool Kit: Cheng Cai.
DU SHAPE Version 1.2: Cheng Cai.

MAILING ADDRESS

Department of Materials Engineering
Drexel University
32nd and Chestnut St.
Philadelphia, PA 19104
Telephone: (215) 895-6610
Fax: (215) 895-6760
E-mail: *caic@duvm.ocs.drexel.edu*

3 Introduction

3.1 Background

The spray casting process (e.g., Osprey™) offers a Near Net-Shape Manufacturing (NNSM) route for complex shapes with a refined microstructure at high casting rates, a low-cost solution to traditional high-cost machining.

Over the past five years, Drexel and David Taylor Research Center (DTRC, now NSWC) have been collaborating, under the auspices of an Office of Naval Research Program, to apply process modeling for process optimization and control for spraying simple shapes such as tubes and complex shapes such as elbows, tapered tubes, and hemispheres. The modeling approach has been to improve and tailor the existing process to match industrial experience, in general and particularly the requirements of the NSWC spray casting group.

3.2 Fundamentals of 3D Shape Modeling

The newly developed 3D shape model for the process by Cheng Cai at Drexel is a generic computational method based on the knowledge of 3D surface modeling, spatio-temporal distribution of spray mass, sticking efficiency and motions of both spray and substrate. In the method, the geometry of a solid preform is represented by its bounding surface which is a function of x, y, z coordinates in three-dimensional space. The deposit surface is divided into small elements or patches. Each patch is composed of a segment of spline between at nodes thus maintaining smooth and connected edges. Any location \mathbf{p} on the surface, upon deposition over the time step dt , is displaced by $d\mathbf{p}$. This displacement $d\mathbf{p}$ is determined by the growth rate resolved along the direction of normal \mathbf{n} to the patch surface at \mathbf{p} :

$$d\mathbf{p} = [G_{\mathbf{n}}(\mathbf{p}) \cdot \mathbf{n}] dt$$

The normal growth rate $G_{\mathbf{n}}$ is governed by the mass flux distribution (MFD), sticking efficiency (SE) and shadowing factor g at the location \mathbf{p} :

$$G_{\mathbf{n}}(\mathbf{p}) = D(\mathbf{p}, A, B, C, \dots) \cdot SE(f_l(\mathbf{p}), f_{l_{spr}}(\mathbf{p})) \cdot g(\mathbf{p}, \mathbf{n}, \mathbf{v})$$

where A, B, C, \dots , etc., are coefficients from the MFD data. The SE is a function of the liquid fractions on the top surface of preform $f_l(\mathbf{p})$ and in the spray $f_{l_{spr}}(\mathbf{p})$. In the present version, constant SE values are assumed. The shadowing factor g accounts for the absence of deposition at locations which are in the shadow region of the deposit (i.e. out of the line-of-sight of the spray) and is a function of surface normal \mathbf{n} and velocity \mathbf{v} at the location \mathbf{p} . When a location \mathbf{p} is in the shadow of the preform, $g = 0$, ensuring zero growth and vice versa. However, g can be > 1 or < 1 , depending on the flight distance to \mathbf{p} (which is also a function of \mathbf{p}) and the velocity \mathbf{v} . All variables described above are, in turn, implied functions of time requiring numerical integration to obtain the solution.

3.3 Object-Oriented Approach

By using the fundamental method described above, a library of 3D object classes defined with C++ has been established and implemented by Cheng Cai. The C++ class library functions as a modeling tool kit by providing an undeletable base for further developing object-oriented applications in 3D shape modeling. The object-oriented approach makes the code extensible, reusable and robust.

The DU SHAPE Version 1.2 is just an example of applications constructed by using the TK to test the capabilities of the Drexel 3D shape model for predicting simple and

complex shapes. Common shape prototypes such as disk, straight tube, curved tube (elbow), tube of variable diameters (step-tube) and sheet are provided in the version. However, the TK itself can be used to construct an application software dealing virtually any 3D geometries expectedly encountered in the spray deposition process.

4 Installing the Software

4.1 System Requirements

The DU SHAPE TK and DU SHAPE Version 1.2 are supported on Unix, Windows 3.1 (with Win32s) or Windows NT systems.

For Unix

- 5 MB available hard disk space
- Any recent versions of GNU C++, i.e., g++ must be installed

For Windows 3.1 or NT

- 386 DX/25 or higher, minimum 4MB RAM and 20 MB available hard disk space
- Borland C++ 4.0
- For Windows 3.1 only, Win32s extension from Microsoft Corp must be installed

4.2 Installation Instructions

The installation of the software is easy:

Under Unix

- Just copy all files in the package into ONE working directory. That's it!

Under Windows

- Copy all files in the package into ONE working directory;
- PKUNZIP the win32s.zip

The following is a listing of files contained in the package:

The Unix version

FILENAME

DESCRIPTION

3dvector.h

Definitions and implementations of 3D vector classes

dushape1.cc

Source file for main program, including all definitions and implementations of 3D object classes

preform.lsp

AutoLisp source file for postprocessing

*.mp

MTS manipulator motion plan files

The Windows version

FILENAME

DESCRIPTION

3dvector.h

Definition of various 3D vector-related classes

3dvector.cpp

Implementation of the vector-related classes

node.h

Definition of a 3-D node class

node.cpp

Implementation of the node class

meshes.h

Definition of a 3-D mesh classes

meshes.cpp

Implementation of the mesh classes

sprayer.h

Definition of a spray design class

sprayer.cpp

Implementation of the spray design class

motions.h

Definition of a motion design classes

motions.cpp

Implementation of the motion design classes

mtsisfcs.h

Definition of common variables for MTS ISFCS

mtsplans.h

Definition of common variables for MTS spray and motion plans

mtsmanip.h

Definition of a MTS manipulator motion plan

mtsmanip.cpp

Implementation of the MTS motion plan

mtsspray.h

Definition of a MTS spray plan

mtsspray.cpp

Implementation of the MTS spray plan

duproc.h

Definition of various process-related classes

duproc.cpp

Implementation of the process-related classes

disk.h

Definition of a deposition class for disk preforms

disk.cpp

Implementation of the deposition class for disk preforms

tube.h

Definition of a deposition class for tubular preforms

tube.cpp

Implementation of the deposition class for tubular preforms

elbow.h	Definition of a deposition class for elbow preforms
elbow.cpp	Implementation of the deposition class for elbow preforms
funnel.h	Definition of a deposition class for multi-segment tubular preforms
funnel.cpp	Implementation of the deposition class for multi-segment tubular preforms
dshplapp.h	Header file for main program of the DU SHAPE Version 1.2 application
dshplapp.cpp	Main program of the application (Version 1.2)
globals.h	Definition of global variables
dshlmdi1.h	Definition of a MDI Child class
dshlmdi1.cpp	Implementation of the MDI Child class
dshlmdic.h	Definition of a MDI Client class
dshlmdic.cpp	Implementation of the MDI Client class
dshplabd.h	Definitions of an about-dialog class
dshplabd.cpp	Implementation of the about-dialog classes
apxprev.h	Definition of a print preview class
apxprev.cpp	Implementation of the print preview class
apxprint.h	Definition of a print class
apxprint.cpp	Implementation of the print class
dushape1.ide	Project file of vesion 1.2 for Borland C++ 4.0 IDE
dushape1.rh	Resource header file (1.2)
dushape1.rc	Resource script file (1.2)
dushape1.res	Resource file (1.2)
dushape1.def	Application definition file (1.2)
dushape1.mak	MAKE file for building the application (1.2)
win32s.zip	PKZIP Compressed file of Microsoft Win32s extension
*.bmp	BITMAP files used in the application
*.ico	ICON files used in the application
*.mp	Manipulator motion plan files
*.msp	Spray plan files
*.ssp	Substrate plan files

5 Compiling Instructions

Compiling the programs must follow the instructions provided by the compiler vendors mentioned above. Please refer to the GNU C++ manual or the Borland C++ 4.0 User's Guide for details. A MAKE file for compiling under Borland C++ 4.0 is provided if necessary.

Under Unix

- At system prompt, type "g++ dushapel.cc -lm";
- It produces an executable file with the name "a.out".

Under Windows 3.1 or NT

Option #One - using Borland C++ 4.0 IDE

- Run Borland C++ 4.0 IDE from Windows;
- Open project file "dushapel.ide";
- Choose "Build All";
- It produces an executable file "dushapel.exe".

Option #Two - using Borland C++ 4.0 command-line compiler

- Make sure your system is a clean boot;
- At DOS prompt, type "make -fdushapel.mak";
- It produces an executable file "dushapel.exe".

6 Running the Software

Under Unix

- At system prompt, type "a.out";
- It produces AutoCAD scriptable output files with the following names

*prf.scr

*sec.scr

*grw.scr

where prf, sec and grw briefly means "preform", "section" and "growth", respectively.

* stands for a three-letter abbreviation corresponding to different shape prototypes. For example:

dsk - disk

tub - tube

elb - elbow

fnl - funnel or multi-segment tube

stp - strip

plt - plate.

- You are ready for postprocessing.

Under Windows 3.1 or NT

- From Windows File menu, choose Run, at prompt, type "dushape1.exe", then click OK, or, from File Manager, go to the directory containing the executable file dushape1.exe, double click it;
- After the application appears, select a target shape from Shape menu;
- Choose Load Spray Plan ... to load a spray plan file from Plan menu;
- Choose Load Motion Plan ... to load a motion plan file from Plan menu;
- Choose Load Substrate Plan ... to load a substrate plan file from Plan menu;
- Choose Settings... from Control menu, the following dialog window appears:

Change Settings		
Simulation Options	View Options	<input type="button" value="OK"/>
<input checked="" type="radio"/> Deposition	<input checked="" type="radio"/> Auto Zoom	<input type="button" value="Cancel"/>
<input type="radio"/> Motion Only	<input type="radio"/> Manual Zoom <input type="text" value="1"/>	<input type="button" value="Default"/>
Time Setting (sec)	<input checked="" type="radio"/> Front <input type="radio"/> Top	<input type="button" value="Help"/>
Run Period: <input type="text" value="10.0"/>	<input type="radio"/> Right <input type="radio"/> Isometric	
Step Size: <input type="text" value="0.02"/>	Updating Rate (steps)	
	<input type="text" value="10"/>	
Initial Mesh Size	Sticking Efficiency	
Axial: <input type="text" value="50"/>	<input type="text" value="1.00"/>	
Annular: <input type="text" value="60"/>	<input type="text" value=""/>	

- Modify the settings in the windows and click OK.
- Click Run from Control menu;
- It produces output files with the following names

*prf.scr

*sec.scr

*grw.scr

where prf, sec and grw briefly means "preform", "section" and "growth", respectively. * stands for a three-letter abbreviation corresponding to different shape prototypes. For example:

dsk - disk

tub - tube

elb - elbow

fnl - funnel or multi-segment tube

stp - strip

plt - plate.

- You are ready for postprocessing.

7 Preprocessor and Postprocessor

7.1 Preprocessor

No preprocessor is provided in the current version. The next version will be expected (but not guaranteed) to include a flexible interface to import 2D and 3D meshes from other applications like AutoCAD or Excel.

7.2 Postprocessor

The current DU SHAPE Version 1.2 produces output files which are directly scriptable to AutoCAD release 12 - a new feature having improved performance over previous versions using AutoLisp. The shape and growth profiles of a preform are subjected to viewing and editing by users after being loaded into AutoCAD. 3DMESH and POLYLINE commands are used to draw surfaces and curves in AutoCAD.

View a Preform with AutoCAD

- Copy the "*prf.scr" file into your AutoCAD working directory;
- At AutoCAD command prompt, type "script";
- Locate the script file you want to view.

View a Section with AutoCAD

- Copy the "*sec.scr" file into your AutoCAD working directory;

- At AutoCAD command prompt, type "script";
- Locate the script file you want to view.

View Growth Profiles with AutoCAD

- Copy the "*grw.scr" file into your AutoCAD working directory;
- At AutoCAD command prompt, type "script";
- Locate the script file you want to view.

8 Comment

Comments are provided as many as possible to give a clear and understandable style and better readability.

9 Bugs Report

Any bugs reports are welcome. Please send your suggestions to the AUTHOR.

10 Appendix

A Explanation of Aforementioned Abbreviations

DU SHAPE - Drexel University SHAPE modeling tool kit for spray forming process

ISFCS - Intelligent Spray Forming Control System.

MTS - MTS Corporation.

B An Input Format for Prototyping a Step-Tube

A step-tube is combination of tubular segments of variable diameters. Usually, the inner diameter of each segment is constant or changing linearly along the axis of the tube. In other words, a step-tube consists of straight-side tubular segments and/or tapered-side tubular segments. Thus, a such shape can be defined by the following input format:

Line No.	Variable	Description
=====	=====	=====

1	NUM	number of segments
2	LENGTH[0]	the length of each segment with index i (i = NUM-1)
0, ...,		
...	...	
i+2	LENGTH[i]	
...	...	
NUM+1	LENGTH[NUM-1]	
NUM+2	RADIUS[0]	the radius of each segment with index j (j = NUM)
0, ...,		
...	...	
NUM+j+2	RADIUS[j]	
...	...	
2NUM+2	RADIUS[NUM]	



INHIBITED COARSENING OF SOLID-LIQUID MICROSTRUCTURES IN SPRAY CASTING AT HIGH VOLUME FRACTIONS OF SOLID

S. ANNAVARAPU† and R. D. DOHERTY

Department of Materials Engineering, Drexel University, Philadelphia, PA 19104, U.S.A.

(Received 1 August 1994)

Abstract—Experimental studies on coarsening in fine grained solid-liquid microstructures at high volume fractions of solid (f_s) have been carried out to determine if inhibited coarsening under these circumstances could account for the anomalous fine cell sizes observed in spray castings. The materials investigated included a chill-cast dendritic binary alloy of Al-Cu, two spray cast alloys—AA2014 and Cu-Ti, whose grain size was the segregate spacing, and a d.c.-cast alloy Al-4.5 wt% Cu-1.5 wt% Mg in both coarse-grain and grain-refined conditions. The observed segregate spacings after coarsening were smaller than that predicted by empirical correlations of dendrite arm spacing and freezing time. In all cases, the coarsening was found to become slower as the temperature was reduced and f_s increased. Conventional coarsening theories and experiments predict the opposite, i.e. faster coarsening at higher volume fractions of solid. Two additional coarsening models were developed for the grain growth at high volume fractions of solid by processes whose rates are limited by migration of liquid at grain boundaries as liquid films on 2-grain surfaces or liquid rods on 3-grain triple points. In both models, the conventional diffusion-limited $t^{1/3}$ coarsening law was reproduced, but the rate constant K contained the term $1/(1-f_s)$ and so also predicted accelerated coarsening as $f_s \rightarrow 1$. Three possible explanations for the observed lower K values at increasing f_s are proposed. The first is the effect of the increasing difference between the solute contents of solid and liquid as the temperature is reduced. This produces a $1/X_i$ dependence of the coarsening rate constant K . The second inhibiting effect, specific to dendritic structures, is in-grain coalescence of dendrite arms at high f_s which produces isolated liquid particles within the grains. The final possibility is particle-inhibition of grain boundary migration by minority (impurity) particles at the grain boundaries. Such particles were seen, however, for only two of the alloys, viz. the grain defined d.c. cast Al-4.5 wt% Cu-1.5 wt% Mg and the spray case AA2014, but they or gas-filled pores are proposed as strong possibilities to account for the fine grain sizes observed in all spray cast microstructures.

1. INTRODUCTION

The substructure size in a cast alloy is dependent on the amount of coarsening the dendrite arms undergo during solidification. It has been long recognized that dendrite arm coarsening is a surface tension driven process. Solid at highly curved surfaces is melted and preferentially redeposited at sites with less curvature by solute transport through the liquid. Several models have been proposed for this process in which the smaller dendrite arms melt back leading to an overall increase in the average dendrite arm spacing λ_i [1, 2]. Simple analytical treatment, assuming diffusion-control, of the coarsening process at low to medium solid fractions, yields a cubic dependence of λ_i on the local solidification time t_i ,

$$\lambda_i^3 = \lambda_0^3 + K_D t_i \quad (1)$$

where K_D is the dendritic coarsening rate constant and a function of several material properties [1-3].

Measurements of λ_i as a function of t_i have validated equation (1) [2-4] for various alloys, with the exponent being approx. 3 though varying between 2 and 4. The resulting λ_i - t_i correlation has been widely and successfully used to determine the cooling rate from measured final spacings (dendrite arm, cell or segregate) in alloys solidified with a single cooling rate. At high f_s , solid dendrite arms from within the same grain contact each other and coalesce ending the coarsening process and trapping solute rich liquid pools within the grain [1, 2, 5]. After coalescence, however, previously dendritic grains whose boundaries are wetted by liquid films should continue to coarsen via grain growth processes, i.e. liquid-wetted grain boundaries migrate, contact and collect the trapped liquid from within the grains. Similar observations of grain growth via migration of the liquid-wetted grain boundaries have been reported in reheating studies on fine-grained alloys containing solute-rich precipitates within the grains [6-8]. The fine-grained equiaxed structures in these studies were prepared by strain induced melt activation, viz. SIMA [9]. In an earlier unpublished study by Enright

†Present address: Materials Research Corporation, Orangeburg, NY 10962, U.S.A.

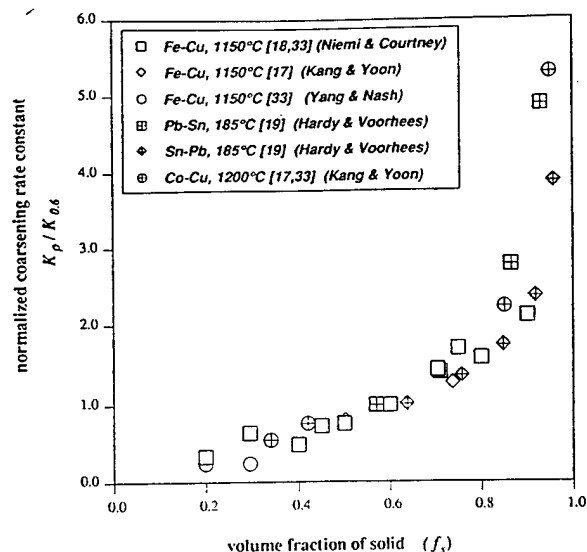


Fig. 1. Measured dependence of the coarsening rate constant K_p on volume fraction of solid during isothermal liquid phase sintering of various binary alloys [17–20, 33]. For ease of comparison the raw data was normalized to the measured K_p value for $f_s \approx 0.6$ (Fe–Cu data in Refs [17, 18, 33] normalized using Niemi and Courtney's $K_{0.6}$ value). In all of the data presented, volume fraction was varied by changing the composition. Intercept length (l) data converted using $\rho^3 = 0.239l^3$ as computed in Ref. [19]. S_v data in Ref. [18] converted using $\rho = 3f_s/S_v$.

and Doherty at Sussex University [10], retarded endrite arm coarsening was observed at high f_s in samples reheated to just above the eutectic temperature for extended times, though the reason was not determined.

Despite the general and successful use of the λ_t – t correlate, recent studies on spray casting [11–13] have found that the usual correlation appears to overestimate, by 100%, the value of the segregate/cell spacing λ_t . Spray casting [13] consists of atomization of bulk liquid metal into a spray of droplets which consolidate to yield a net-shaped preform with a refined microstructure (equiaxed grains $\leq 50 \mu\text{m}$). In most spray castings the segregate spacing is the grain size. Modeling work supported by measurements [11] suggests that the alloys solidify rapidly within a few milliseconds during droplet flight to an average f_s of 0.5–0.8 with a fine dendritic structure with an arm spacing of about $1 \mu\text{m}$. The remaining liquid solidifies after consolidation in the deposit much more slowly over times of 10–200 s, i.e. over 99% of the solidification time, t_f , is spent at high f_s in the deposit [13, 14]. Segregate spacings predicted from the applicable λ_t – t correlation for these local solidification times have been found to be 2–3 times those measured at the corresponding locations [11, 13, 15]. This mismatch indicates either a serious failure of the models for the spray casting process or some unexpected failure of equation (1) for this casting process in which alloys spend a prolonged period at high f_s towards the end of solidification. Limited thermal measurements of t_f within the deposit [13, 15] support the modeling results on solidification time

and are thus in conflict with the predictions of the standard coarsening theory. Given that one of the important advantages of spray forming is the fine grain size, this conflict needs to be resolved.

The failure of equation (1) may occur because the solidification conditions during spray casting differ from conventional casting processes in at least two ways: solid morphology and solid volume fraction. The dendritic structure of the rapidly but only partially frozen droplets arriving at the surface of the deposit is broken-up giving a spherical morphology to the solid. The small spheroidal solid particles derived from broken-up dendrites, as in stir casting [16], rapidly coarsen in the slowly cooled deposits—with each surviving solid particle having its own orientation so becoming a “grain”. Experimental studies, in stir-casting [6, 7, 16] and particle coarsening [17–20], and theoretical modeling by several researchers [21, 22], however, have shown that at high volume fractions of solid coarsening of spherical grains continues to obey equation (1). This result has also been found in a range of experimental and theoretical analysis in solid-state coarsening [23, 24]. Experimental studies in Refs [17–20] present unambiguous evidence that for spherical solid particles in a liquid matrix, the coarsening rate constant K increases sharply at volume fractions approaching unity, see Fig. 1. Boettinger *et al.* [25] confirmed this dependence by *in situ* observations of the coarsening of equiaxed grains in binary semisolids. Theoretical and computer modeling of particle coarsening in a liquid-matrix [22, 26, 27] appear to accurately predict the measured variation of K with f_s . The same does not hold for the solid-state case—many investigations, with the exception of Jayanth–Nash [28], have failed to discern a volume fraction effect in the much studied Ni–Ni₃Al system [29, 30]. A similar

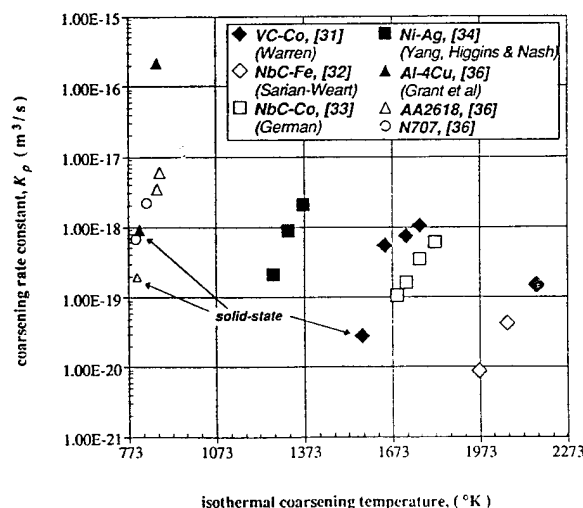


Fig. 2. Reported dependence on K_p on isothermal coarsening temperature during liquid-phase sintering (LPS) of various carbides [31–33]. Superimposed are data from Ref. [34] on Ni–Ag and from Ref. [36] on Al alloys. Eutectic or solidus temperature is 1233 K in the Ni–Ag system, 853 K for Al–4 wt% Cu and AA2618 and 1623 K in the VC–Co system.

absence of volume fraction effect with a liquid matrix, though at low volume fractions of 0.25–0.45, was noted in a recent paper by Bender and Ratke [31]. Early coarsening studies by Warren [32, 33] and Sarian-Weart [34] on liquid phase sintering of carbide particles in metallic liquids have clearly shown inhibited coarsening with decreasing temperature (or f_s), Fig. 2. Two recent isothermal coarsening studies—one by Yang *et al.* [35] on Ni–Ag and the other by Grant *et al.* [36] on *spray formed* Al alloys lend support to these observations of lower K values at lower temperatures, i.e. higher fractions of solid.

Given the apparently conflicting results from spray casting experiments where there might be some doubt on the actual coarsening times, the objective of the present paper was to study coarsening in isothermal studies. For this purpose various solid–liquid mixtures were observed at medium to high f_s , in order to establish the appropriate coarsening kinetics for use in modeling the spray casting process. A study of isothermal coarsening of both dendritic and spray cast microstructures at high f_s in the range 0.6–0.95 was conducted. Rapidly solidified material with a fine dendritic or equiaxed, spray cast, microstructure was reheated into the two-phase regime and isothermally annealed to coarsen the structure over periods of time comparable to, or larger than, those prevalent during solidification in spray castings. Comparison was made, in the same alloys, with the dendrite spacings measured in conventional castings using the observed solidification times. Initial work was conducted using chill-cast dendritic Al–6.7 wt% Cu alloy and lower coarsening rates than in the conventional castings were first reported in September 1989 at the *First International Conference on Spray Forming* at Swansea, Wales [37]. In the current paper, we describe and discuss this coarsening behavior, and attempt to find models that might account for the observations. The Al–Cu system was selected since it has been extensively studied and dendrite coarsening at low f_s is well characterized. Additional

studies were carried out on spray cast AA2014 (Al–4.5 wt% Cu–1.5 wt% Mg–0.4 wt% Fe) and spray cast Cu–4 wt% Ti and In–625 alloys to compare the coarsening results in spray cast microstructures with those for dendritic structure in the Al–Cu alloy. A second comparison of the coarsening behavior of equiaxed and dendritic structures was conducted using d.c.-cast high purity Al–4.5 wt% Cu–1.5 wt% Mg alloy prepared with and without the addition of a grain refiner.

2. EXPERIMENTAL METHODS AND RESULTS

2.1. Chill-Cast Al–Cu

A master alloy of Al–6.7 wt% Cu was remelted under an argon atmosphere and chill cast into a steel wedge mold. The solidification times at various sections was measured by means of thermocouples and a data acquisition system at a sampling interval of 0.1 s. A plot of the observed dendrite arm spacing, λ_i , as a function of t_f is shown in Fig. 3 for Al–6.7 wt% Cu. Previously reported data for alloys containing 2–10.2 wt% Cu are superimposed [1–4]. These results indicate that the alloy used in this study, Al–6.7 wt% Cu, follows the correlation developed in the earlier studies. Samples were cut from the thin end of the wedge; sample mass was 0.10–0.15 g. The starting material at the pre-marked section had a λ_i of about 7 μm as shown in Fig. 4, with an expected initial t_f of about 1 s from Fig. 3. The lowering of the coarsening rate with increased Cu content in the dendritic structure in this study should be noted.

The samples were then introduced into a preheated lead bath and isothermally aged at 550, 575, 600 and 625 \pm 2°C corresponding to f_s (the volume fraction of solid) of 0.97, 0.91, 0.81 and 0.58 respectively (Lever Rule values). The sample temperatures were monitored by the means of a K-type thermocouple inserted about 2 mm into the sample. Various aging times, up to 8.5 min, were applied after

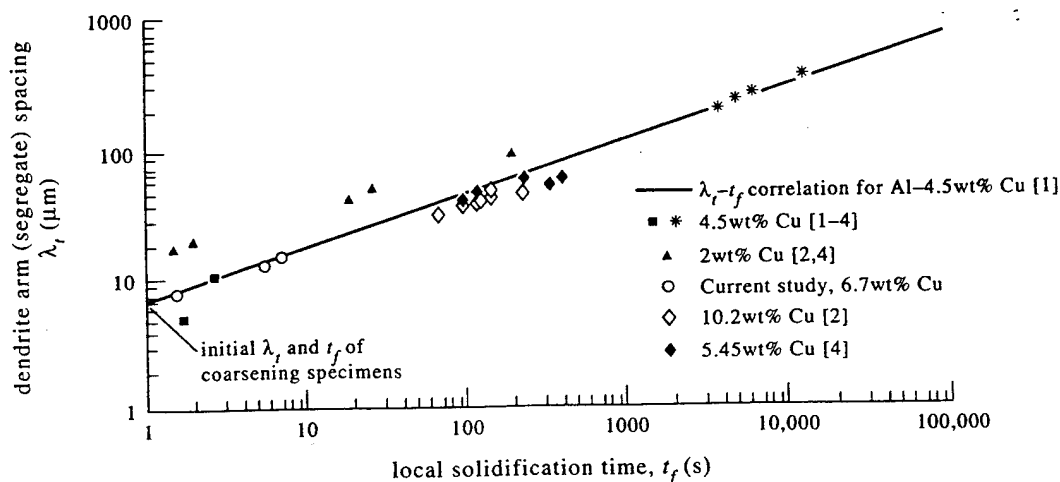


Fig. 3. Experimental correlation of secondary of secondary dendrite arm, i.e. segregate spacing (λ_i) with the local solidification time (t_f) for conventionally cast Al–Cu alloys [1–4]. Data from current study on Al–6.7 wt% Cu is superimposed.

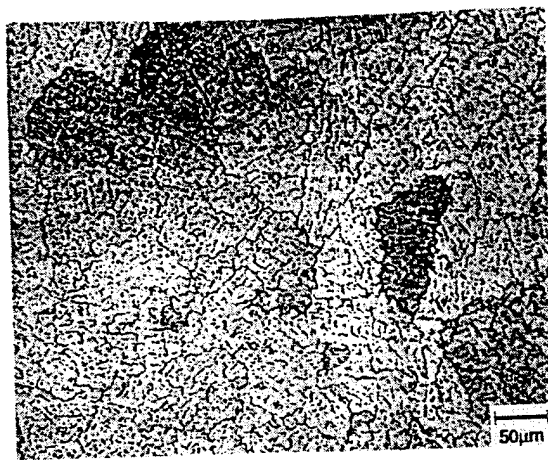


Fig. 4. The initial dendritic structure in the samples of chill-cast Al-6.7 wt% Cu prior to isothermal coarsening. Average secondary dendrite arm spacing (λ_2) $\approx 7 \mu\text{m}$.

which the samples were quenched in water. The samples required about 30 s to heat up from the eutectic temperature to the hold temperature and this time is included in the aging times. The aged samples were cut at a pre-marked section, polished and subjected to metallographic analysis after successive etches of picric acid and Keller's reagent.

Figures 5(a) and 5(b) show the observed structures of the quenched samples after hold times of 510 s at two different volume fractions of solid. Figure 5(a) depicts the structure after 510 s at the highest temperature of 625°C ($f_s = 0.58$). The structure has coarsened significantly and comprises of low curvature solid interfaces in contact with a matrix of seemingly interconnected (quenched) liquid. A few large but apparently isolated liquid droplets that have curvature similar to the interconnected liquid are seen. We assume that these arise from sectioning through matrix liquid. In addition, a distribution of fine and coarse liquid droplets is present. The density of the small ones arise from a real distribution of fine droplets and not from a sectioning effect as confirmed by serial sectioning. Figure 5(b), material held at 575°C ($f_s = 0.91$), typifies the observed structure for samples held at 550, 575 and 600°C , and shows that the interdendritic eutectic within the grains seen in Fig. 4 has largely spheroidized, on remelting. It is evident that dendrite arms within grains have fully coalesced trapping the liquid as isolated droplets. The eutectic at the grain boundaries has apparently formed a liquid film with occasional large droplets at triple points, and with a few droplets close to but detached from the boundary film. However, most of the in-grain quenched liquid droplets appear to have coarsened little from the as-cast structure, Fig. 4. In addition, there is some evidence of migration of some of the grain boundary films. The large grains marked A and B have grown larger than their neighbors and a region depleted of fine droplets can be seen, apparently swept by the movement of the grain boundaries from left to right (as indicated by the arrows). In

Fig. 6(a), material held for 150 s at 600°C ($f_s = 0.81$), a large droplet apparently about to detach itself from the boundary is seen above the arrow indicating the direction of apparent grain boundary movement. Other large droplets, both attached and unattached to adjacent grain boundaries can also be seen. In addition, there is also a region of small grains with several large droplets mostly detached from the grain boundaries. At high magnification, some of the grain boundary films and liquid drops revealed the presence of a few fine Fe-rich plates which did not appear to affect the grain boundary film migration. Figure 6(b) shows a larger area of the structure in the same sample at a lower magnification revealing an unusual grain structure in the samples after aging. A layer of coarse grains can be seen near, but not at the sample surface, and these bigger grains contain a distribution of fine droplets seen in more detail in Figs 5(b) and 6(a). We assume that the non-uniform grain structure arose from the solidification structure of the cast wedge.

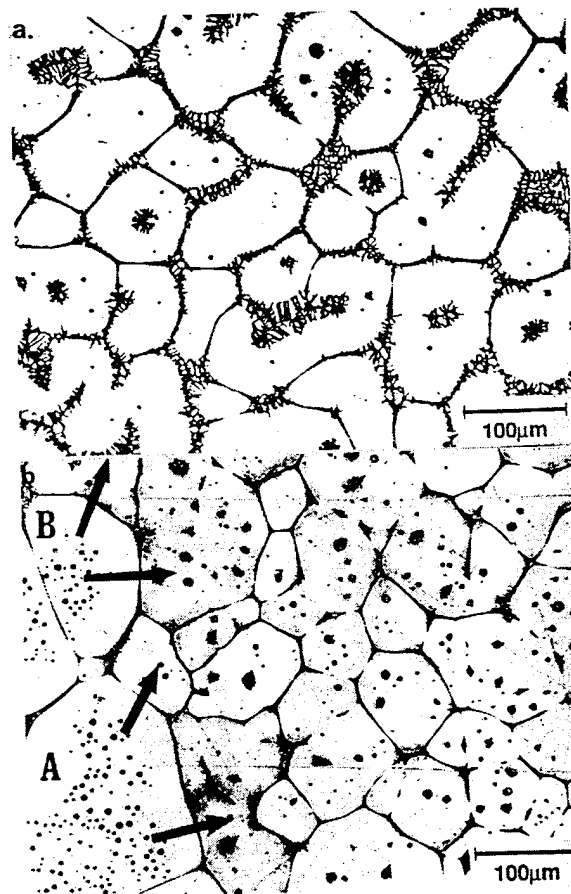


Fig. 5. Quenched-in microstructure of dendritic Al-6.7 wt% Cu after isothermal coarsening for 8.5 min at: (a) 625°C ($f_s = 0.57$) and (b) 575°C ($f_s = 0.92$). Note the thicker "frozen liquid" at grain/cell boundaries and pockets of liquid in cell interiors. The "frozen liquid" in the lower f_s sample, (a), appears as a fine "dendritic necklace" because of the quench was not rapid enough to prevent a breakdown of the solid-liquid interface. In (b), grains A and B contain isolated frozen droplets from pinched-off interdendritic liquid and a droplet-depleted zone marking the area swept by migrating grain boundary liquid film.

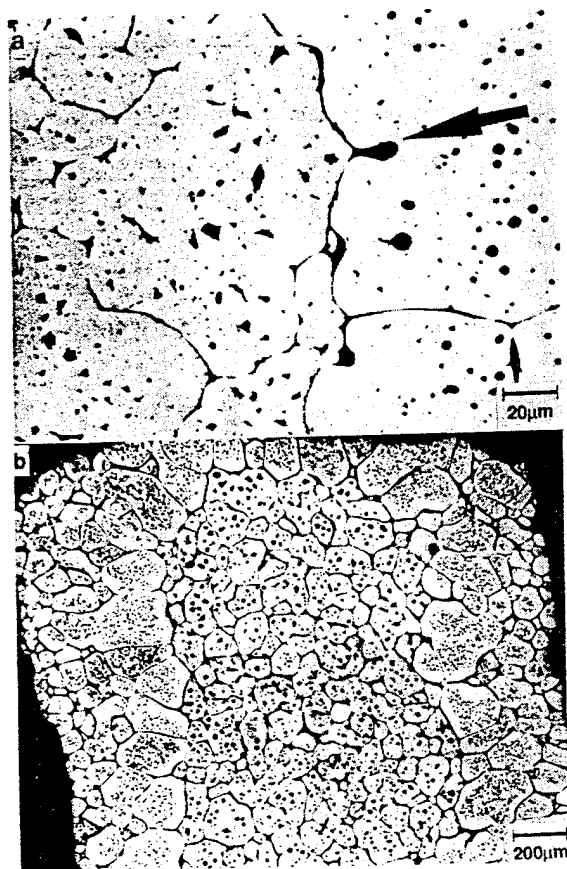


Fig. 6. Observed structures in dendritic Al-6.7 wt% Cu quenched after isothermal coarsening in solid + liquid regime. (a) Impending release of large droplet behind a migrating grain boundary liquid film; sample was aged for 2.5 min at 600°C ($f_s = 0.83$); (b) Duplex grain structure in samples evident at lower magnifications with fine grains at the surface and center, the coarse grains 100 μm away from the surface; sample was aged for 4.5 min at 600°C ($f_s = 0.83$).

Quantitative measurements of the segregate spacing (listed in Table 1) were made by counting the number of intercepts per unit length on an image analyzer, the same method used to determine the spacing in Fig. 4. The results are plotted as λ_i^3 vs t_f in Fig. 7 for a total solidification time of the initial 1 s (from Fig. 3) plus the hold time above the eutectic temperature. It is readily seen that the actual coarsening rates at 575°C ($f_s = 0.91$), 600°C ($f_s = 0.81$) and 625°C ($f_s = 0.58$) are below than those seen in the measured arm coarsening rates in conventional solidification, Fig. 3 plotted as the solid line in Fig. 7. The data at 550°C ($f_s = 0.97$) was not plotted since it showed a wide scatter between the coarse and fine grained regions, the data if plotted lay below that for 575°C ($f_s = 0.91$). Each line in Fig. 7 shows a cubic dependence on t_f but with a slope, i.e. a coarsening rate constant K significantly lower than corresponding to the λ_i - t_f correlation [viz. K_D in equation (1)] from Refs [1-4]. Experimentally measured values of K (subsequently referred to as K_{exp}) decrease by about 2 orders of magnitude as f_s increases from 0.58 to 0.91.

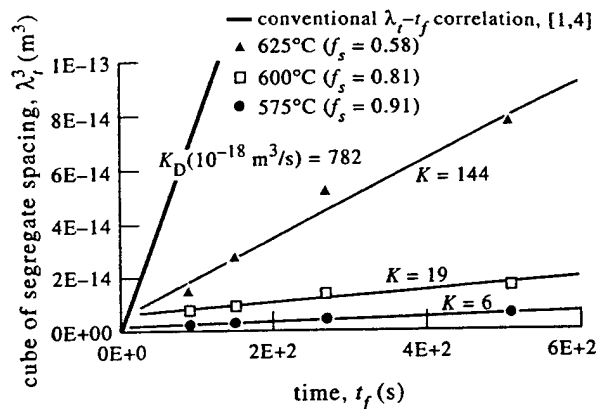


Fig. 7. The dependence of segregate spacing (λ_i) on isothermal coarsening time (t_f) for chill cast Al-6.7 wt% Cu showing a reduction in the coarsening rate at lower temperatures, i.e. higher fractions of solid (f_s). Also shown is the conventional correlation of segregate spacing, λ_i , on solidification time, t_f . Values of K are marked for each isothermal data-set. Samples initially had a dendritic microstructure with an average spacing of 7 μm (Fig. 4).

2.2. Spray Cast AA2014

The starting material was an AA2014 spray-deposited preform kindly supplied to us by Osprey Metals Inc. Although Drexel University has a pilot Osprey plant, it is not equipped to deal with the safety problems of fine aluminum powders. Samples were cut from the top 5 mm of the preform, and weighed 0.10-0.15 g. The starting material exhibited a homogeneous microstructure of equiaxed grains with precipitates of CuAl_2 (θ phase) and $(\text{Fe, Mn})_3\text{SiAl}_{12}$ (α phase) at the grain boundaries, as shown in Fig. 8. The interior of the grains was covered with solid-state precipitates of Si and $\text{Al}_4\text{CuMg}_5\text{Si}_4$ (Q phase), and

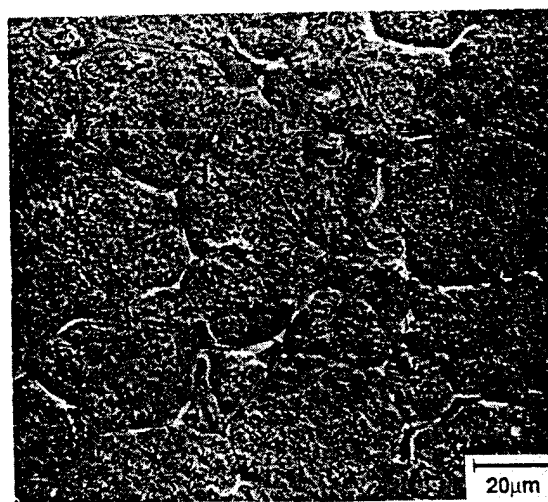


Fig. 8. The starting microstructure in spray cast AA2014 aluminum alloy samples, before isothermal coarsening in solid + liquid regime, showing fine equiaxed grains with an average grain size or segregate spacing (λ_i) of about 17 μm . Grain boundary precipitates are θ (CuAl_2) and α ($(\text{Fe, Mn})_3\text{SiAl}_{12}$) phases, and the dispersoid in the grain interiors are Si and Q ($\text{Al}_4\text{CuMg}_5\text{Si}_4$) particles produced by a solid-state reaction.

Table 1. Summary of measurements on various alloys reported in the current study

Alloy (processing)	Time, t_f (s)		Segregate spacing, λ —secondary dendrite arm or grain diameter (μm)				
	solidification + coarsening	as-cast	after isothermal aging in solid-liquid regime				
			575°C	600°C	625°C		
Al-6.7Cu (chill cast)	1.0	7†					
	1.6	8					
	5.5	13					
	7.2	15					
	90		13	20	24		
	150		14	21	30		
	270		15	24	37		
	510		17	25	42		
AA2014 (spray cast)			525°C	550°C	575°C	660°C	625°C
	15†	17‡					
	60		25	26	28	28	29
	90		26	29	31	31	34
	150		30	32	35	37	39
	990		34	45	53	58	73
Cu-4Ti (chill cast)	2	5					
	6	20					
	32	33					
	48	38					
	375	69					
	885	98					
Cu-4Ti (spray cast)			975°C	1000°C	1015°C		
	14†	13§					
	49		18				
	124		21				
	624		24				
	924		27	32	38		
	1824			40	55		
	3624			59			
In-625 (spray cast)	14,424		44	83			
			1304°C	1314°C			
	10†	15§					
	1800		60	75			
Al-4.5 Cu-1.5 Mg (d.c.- cast w/o grain refiner)	3600			90			
			515°C				
	160	75‡	103§				
	2860		104				
Al-4.5 Cu-1.5 Mg (d.c.- cast w. grain refiner)	14,560		112				
			515°C				
	160	75‡	233§				
	2860		313				
	14,560		363				

λ measurements for all Al-6.7 Cu data, for as-cast Cu-4Ti and for as-cast Al-4.5 Cu-1.5 Mg correspond to secondary dendrite arm spacing. Rest of λ data is for grain diameter.

†Computed using preform solidification model by Mathur [11, 13].

‡Initial secondary dendrite arm spacing size of samples subjected to isothermal coarsening runs.

§Initial equiaxed grain size of samples (spray cast and grain refined d.c. cast) subjected to isothermal coarsening runs.

the average grain size was 17 μm . The t_f was estimated to be ≈ 15 s using Mathur's preform solidification model [13] for Al-4.5 wt% Cu sprayed at typical process conditions—gas pressure of 0.8 MPa and gas:metal ratio (GMR) of 2.0.

The samples were isothermally aged at 525, 550, 575, 600 and 625 $\pm 2^\circ\text{C}$ corresponding to f_s of 0.97, 0.93, 0.89, 0.85 and 0.65 respectively. Aging times, from 1/2 to 16 min, were applied after which the samples were quenched in water and subjected to metallographic analysis.

Figures 9(a-c) show the observed structures of the quenched samples after hold times of 16 min at various volume fractions of solid. Figure 9(a) is the structure after 16 min at 550°C ($f_s = 0.93$) and has a

structure that is representative of 525 and 575°C. The precipitates have dissolved on reheating and the eutectic θ phase at the grain boundaries has melted and is concentrated at the triple points. Fine particles ($< 2 \mu\text{m}$) of insoluble α are located on the grain boundaries and in the grain interior close to the boundaries. As the hold temperature increased from 525 to 575°C, the fraction of liquid increased yielding similar structures with larger triple points. Figure 9(b) shows the structure after 16 min at 600°C ($f_s = 0.85$) where it seems that the liquid has penetrated into many of the grain boundaries. The α particles are often near the triple points and have coarsened to $\approx 5 \mu\text{m}$. The grain boundary α particles appear to have undergone coupled-phase coarsening

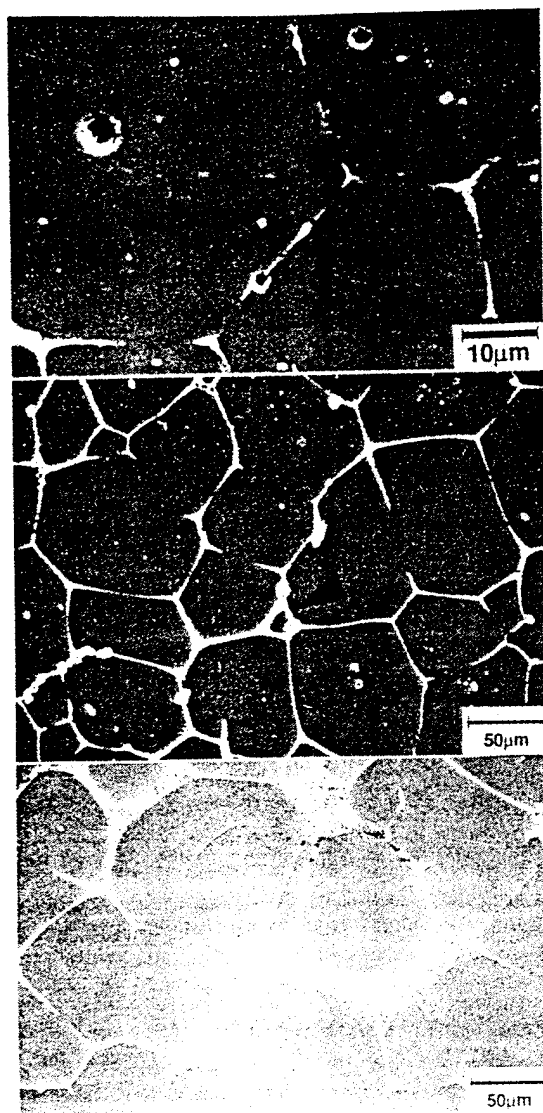


Fig. 9. Observed microstructures in an equiaxed spray cast AA2014 aluminum alloy that was quenched after isothermal coarsening for 16 min at: (a) 550°C ($f_s = 0.93$), (b) 600°C ($f_s = 0.85$), and (c) 625°C ($f_s = 0.65$). The micrographs illustrate different morphological regimes at different fractions of solid. Note in (a) and (b) the presence of coarse Fe-rich particles and pores on the grain boundary liquid films—faces, edges and triple points. Also note decrease in film thickness and grain boundary curvature with decreasing f_s .

as proposed by Higgins *et al.* [38], i.e. α particles on grain boundaries were dragged by moving grain boundaries and coalesced with other α particles at triple points formed by shrinking small grains [as shown by the arrow in Fig. 9(b)]. A dispersion of fine ($< 2 \mu\text{m}$) θ and medium-sized ($2\text{--}5 \mu\text{m}$) α particles is observed in the interior of the grains. These dispersions within the interior of the grains are believed to have evolved by the same mechanism of release of liquid droplets, possibly containing α particles, by unstable sections of the moving grain boundary liquid films. Finally, at the highest temperature of 625°C ($f_s = 0.65$) the structure after 16 min is shown in Fig. 9(c). The structure has coarsened significantly and is similar to that observed for the cast Al-Cu

alloy at 625°C, i.e. low curvature solid interfaces in contact with a matrix of seemingly interconnected (quenched) liquid. Most of the second phase particles lying on grain boundaries have dissolved into the liquid but a few small isolated particles of α and θ remain dispersed within the grains. These are likely to have solidified during cooling and were not expected to have been present during the 625°C hold; 625°C appears to be the above the α eutectic temperature in AA2014. In all the cases, the grains and the liquid pockets at triple points coarsened with increasing aging time, while the grain boundary films became thinner and straighter. The same coarsening behavior held true for the grain boundary α particles at all temperatures except 625°C.

Quantitative measurements of the segregate spacing (listed in Table 1) are plotted as λ_1^3 vs t_f , i.e. the total solidification time in Fig. 10. The total solidification time comprised the initial solidification time of 17 s and the time the samples were held above the eutectic temperature. The results again clearly show slower coarsening at the higher fractions of solid. The expected rate from conventional casting is plotted as the thick line. The data, within the experimental scatter, can be fitted to a cubic dependence on t_f . This is questionable at the higher f_s values where the lines do not intersect the origin. However, for cubic kinetics the measured rate constant K_{exp} decreases by an order of magnitude as f_s increases from 0.65 to 0.93.

2.3. Spray Cast Cu-4 wt% Ti

In this case, the samples were taken from the base of a Cu-4 wt% Ti spray deposit made at Drexel in our Osprey facility [12]. The conventional λ_1 - t_f correlation was established from wedge castings

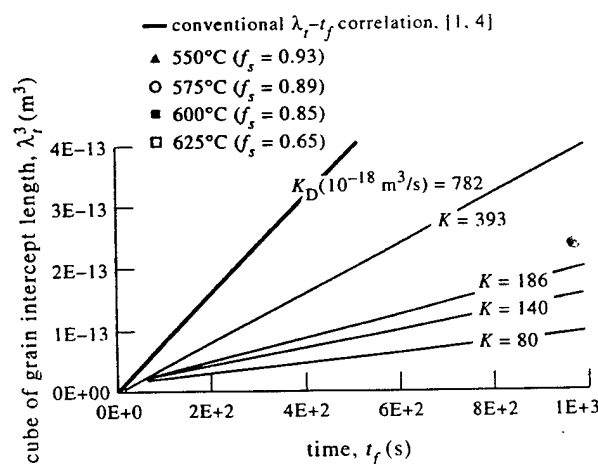


Fig. 10. The dependence of segregate spacing (λ_1) on isothermal coarsening time (t_f) for spray cast AA2014 alloy showing a reduction in the coarsening rate at lower temperatures, i.e. higher fractions of solid (f_s). Also shown is the conventional correlation of segregate spacing, λ_1 , on solidification time, t_f . Values of K are marked for each isothermal data-set. Samples initially had an equiaxed microstructure with an average grain size $17 \mu\text{m}$ (Fig. 8).

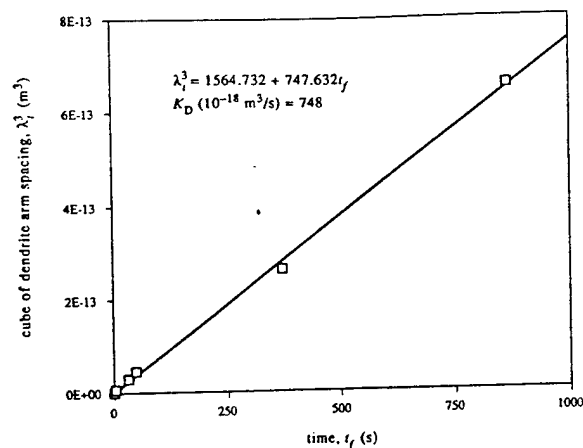


Fig. 11. Measured dependence of the dendrite arm spacing (λ_1) on local solidification time (t_f) in conventionally cast Cu-5 wt% Ti.

with embedded thermocouples to measure the local solidification time; this data is plotted vs λ in Fig. 11. The starting material from the spray deposit exhibited a structure composed of Widmanstatten plates and precipitates of Cu_4Ti and Cu_3Ti , Fig. 12(a). The solidification structure was recovered by heating the material to 900°C into the single phase field and quenching. The solidification structure is composed of equiaxed grains and a number of twins which may have arisen from the heat treatment. Intercepts on twin boundaries were not counted during image analysis to determine the grain size. The average grain size, excluding twins, of the starting material was $13\text{ }\mu\text{m}$, as shown in Fig. 12(b); t_f was calculated to be 14 s using the Drexel model for spray casting [13]. Use of the experimental data for dendrite arm coarsening in Cu-Ti, Fig. 11, predicts that after 14 s of coarsening the dendrite cell size should be $22\text{ }\mu\text{m}$ which is significantly larger than the $13\text{ }\mu\text{m}$ observed in the spray cast structure. Similar observations of

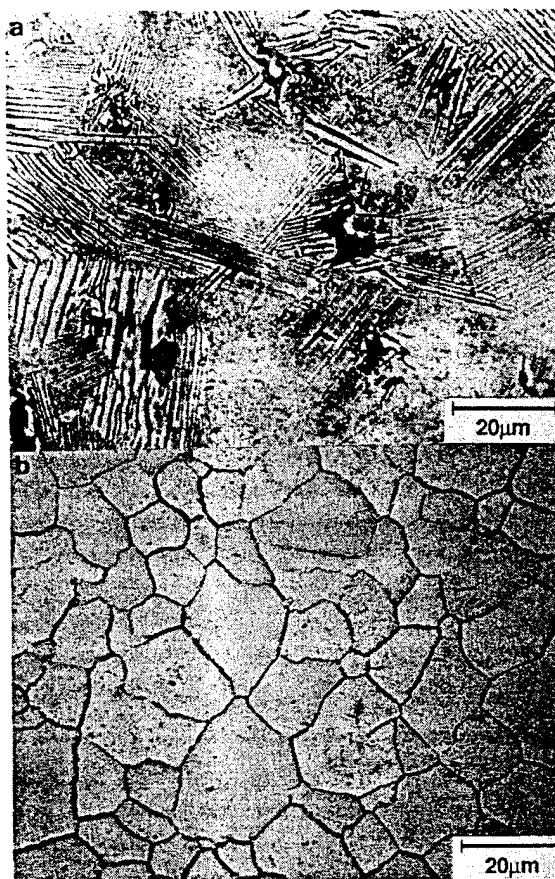


Fig. 12. Microstructure of Cu-4 wt% Ti (a) in spray cast condition showing coarse Widmanstatten plates which obscure the grain structure, and (b) after solution treatment at 900°C for 10 min revealing the spray cast grain structure; average grain size (λ_1) was about $13\text{ }\mu\text{m}$.

inhibited coarsening in spray cast Cu-Ti have been previously reported [37].

The samples were inserted in stainless steel envelopes and isothermally aged in a lead bath at 950 , 975 and $1000 \pm 4^\circ\text{C}$ corresponding to volume

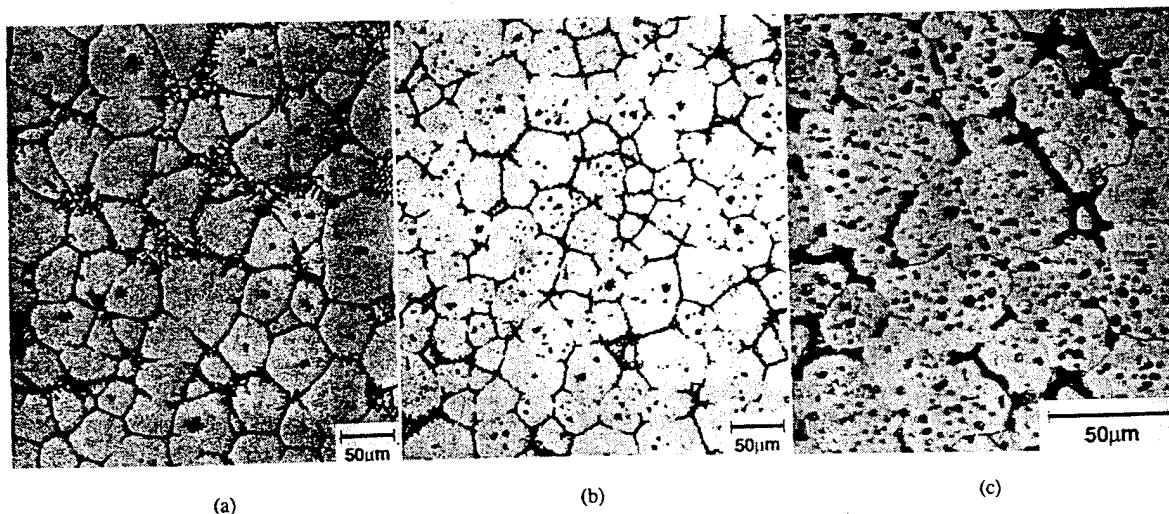


Fig. 13. Observed microstructures in an equiaxed spray cast Cu-4 wt% Ti alloy that was quenched after isothermal coarsening for 15 min at: (a) 1015°C ($f_s = 0.62$), (b) 1000°C ($f_s = 0.73$), and (c) 975°C ($f_s = 0.87$). Note the corrugated grain boundaries on coarsening at 975°C and appearance of low wettability of the solid by the Ti-rich liquid. The "frozen liquid" shows the typical dendritic necklace at low f_s .

fractions of solid of 0.86, 0.73 and 0.62 respectively (as calculated from Lever Rule using the phase diagram due to Shunk [39]). Aging times up to 4 h were applied after which the samples were quenched in water and subjected to metallographic analysis.

Figures 13(a-c) show the observed structures of the quenched samples after hold times of 15 min at various volume fractions of solid. Figures 13(a, b), the structure after 15 min at 1015°C ($f_s = 0.62$) and 1000°C ($f_s = 0.73$), show that the eutectic at the grain boundaries has melted and the liquid was concentrated at triple points yielding boundaries of relatively low curvature. A small number of Cu_4Ti precipitates and liquid droplets can be observed inside the grains which appear to coarsen marginally as the temperature increased. After 15 min at 975°C (i.e. $f_s = 0.86$), an interesting structure, shown in Fig. 13(c), developed. The liquid was restricted to grain boundary triple points but grain boundaries between these triple points appeared to be highly curved and irregular. In addition, a large number of droplets and precipitates are dispersed inside the grains.

Quantitative measurements of the grain size intercepts (listed in Table 1) are plotted as λ_i^3 vs t_i in Fig. 14; t_i comprised the initial solidification time of 30 s and the hold time above the eutectic temperature. Again, the results show retarded coarsening at high fractions of solid. The expected rate from the measured chill castings is plotted as the thick line with the slope corresponding to K_D ; K_{exp} decreases by as much as two orders of magnitude as f_s increases from 0.62 to 0.86.

2.4. Spray Cast In-625

Through thickness samples were taken from a In-625 tubular (12 mm thick, 150 mm i.d.) spray cast

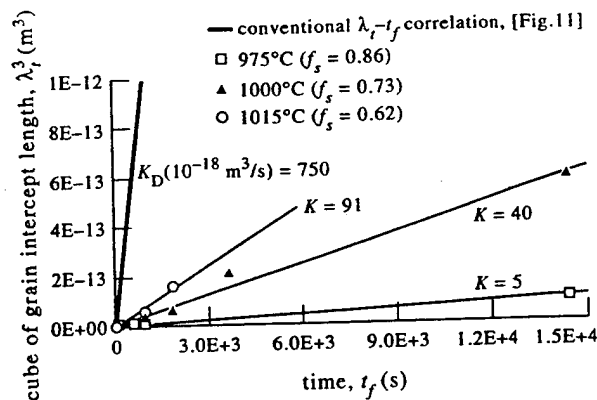


Fig. 14. The dependence of segregate spacing (λ_i) on isothermal coarsening time (t_i) for spray cast Cu-4 wt% Ti showing a reduction in the coarsening rate at lower temperatures, i.e. higher fractions of solid (f_s). Also shown is the conventional correlation of segregate spacing, λ_i , on solidification time, t_f . Values of K for each isothermal data-set are noted. Samples initially had an equiaxed microstructure with an average grain size of 13 μm (Fig. 12).

at the Osprey facility at the Navy's David Taylor Research Center (Annapolis, Md) and kindly provided to Drexel for analysis. The spray cast λ - t_f correlation was established by isothermal coarsening of spray cast samples under argon atmosphere in a glow-bar furnace from 5 min to 1 h at 1304 and 1314°C. The solidus temperature for the alloy is 1288°C and the liquidus 1349°C.

The starting material from the spray deposit exhibited a structure composed of equiaxed grains (average size = 15 μm) shown in Fig. 15. Figures 16(a, b) show the observed structures of the quenched samples after hold times of 1/2 h at volume fractions of solid of 0.75 and 0.85. The structure after 30 min at 1304°C ($f_s = 0.85$) and 1314°C ($f_s = 0.75$), show that the eutectic at the grain boundaries has melted and the

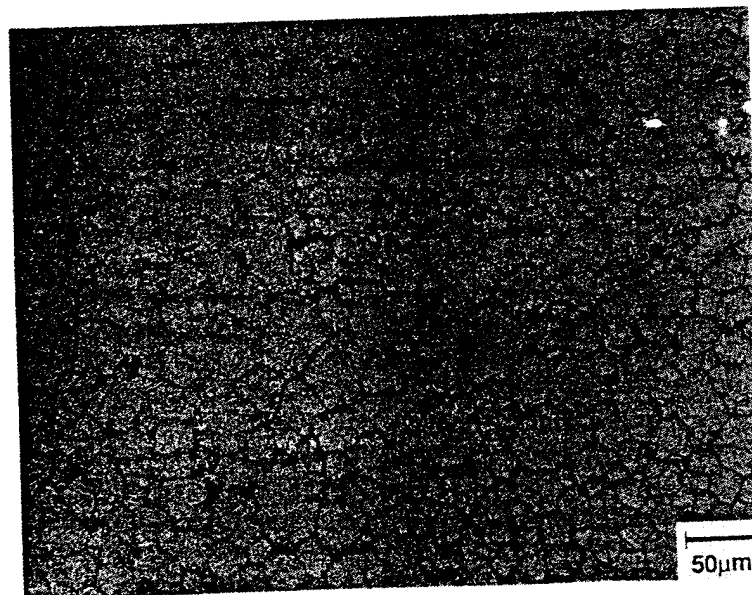


Fig. 15. The starting microstructure in spray cast In-625 samples before isothermal coarsening in solid + liquid regime showing fine equiaxed grains with an average grain size, i.e. segregate spacing (λ_i) of about 15 μm .

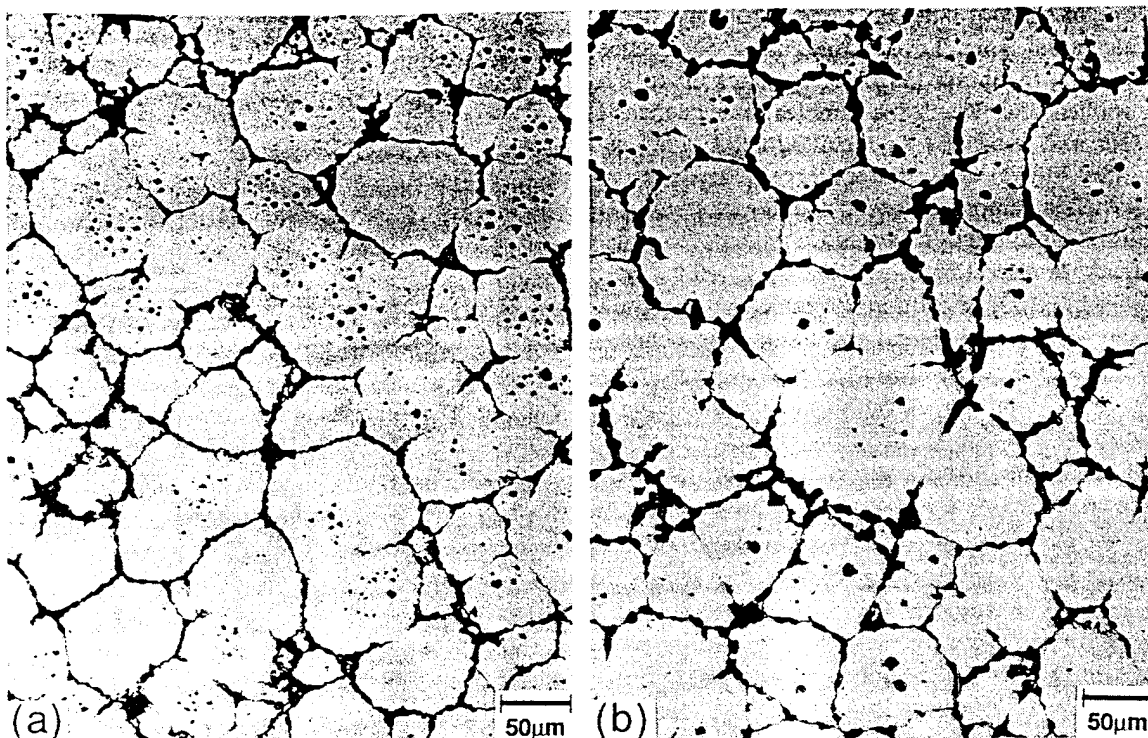


Fig. 16. Observed microstructures in an equiaxed spray cast In-625 alloy that was quenched after isothermal coarsening for 30 min at: (a) 1304°C ($f_s = 0.85$) and (b) 1314°C ($f_s = 0.75$) reproducing features seen in the other alloys.

liquid was concentrated at grain boundary edges and triple points. Note, however, that in many instances the solid-liquid interface is irregular and unlike the curvature-free boundaries seen in the Al-Cu alloy.

Quantitative measurements of the grain size intercepts (data listed in Table 1) on isothermally aged spray cast samples are plotted as λ_i^3 vs t_i in Fig. 17; t_i comprised the initial solidification time of approx.

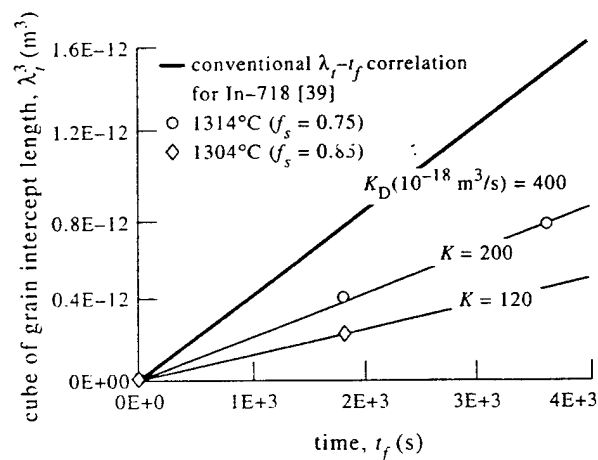


Fig. 17. The dependence of segregate spacing (λ_i) on isothermal coarsening time (t_i) for spray cast In-625 showing a reduction in the coarsening rate at lower temperatures, i.e. higher fractions of solid (f_s). Also shown is the measured [39] correlation of segregate spacing, λ_i , on solidification time, t_i for In-718. Values of K are marked for each isothermal data-set. Samples initially had an equiaxed microstructure with an average spacing of 15 μm (Fig. 15).

10 s and the hold time above the eutectic temperature. As previously the results show retarded coarsening at high fractions of solid. The expected rate for In-718 castings [40] is plotted as the thick line with its slope corresponding to K_D in equation (1); K_{exp} decreases by an order of magnitude as f_s increases from 0.75 to 0.85. The measured $\lambda_i^3-t_i$ correlation for In-718 was used because the same was unavailable for In-625. In-718 has a composition close to that of In-625 and therefore, its solidification response can be assumed representative of In-625.

2.5. Direct Chill Cast Al-4.5 wt% Cu-1.5 wt% Mg

Samples of dendritic and equiaxed d.c.-cast Al-4.5 wt% Cu-1.5 wt% Mg alloys were obtained from a separate research study on hydrogen porosity in Al-Cu-Mg alloys involving Drexel University and Alcoa Technical Center. Samples of both microstructures were isothermally annealed at 515°C ($f_s \approx 0.95$) for times of 45 min and 4 h.

The two grain morphologies had been produced by casting with and without grain-refining additions of Ti and B. Measured values of t_i , as-cast dendrite arm spacing and as-cast grain size for the two cases were provided by Dr Jie Zou of Drexel University. Both the as-cast samples had the same t_i and hence the same average secondary arm spacing ($\lambda \approx 75 \mu\text{m}$). The grain refined sample was composed of equiaxed grains, average size $\approx 103 \mu\text{m}$, whereas the unrefined sample consisted of larger dendritic grains, average size $\approx 253 \mu\text{m}$ [41]. The hydrogen content of the grain refined sample (0.27 cm³/100 g

or 0.24 ppm) was higher than that of the unrefined sample (0.06 cm³/100g or 0.05 ppm) yielding a significantly higher porosity in the former (7% as opposed to 0.13%).

Figures 18(a) and (b) show the observed structures of the samples after hold times of 45 min at 515°C ($f_s \approx 0.95$) for the two morphologies. Figure 18(a) of the unrefined sample, showed a structure consistent with previous observations by Chien and Kattamis [5], and in the other aluminum alloys of this study viz. trapped solute-rich liquid droplets within non-equiaxed grains whose boundaries are wetted by liquid films. On the other hand, in the grain-refined sample [Fig. 18(b)], all the liquid was concentrated at the grain boundary triple points yielding boundaries of relatively low curvature. Thus, the grain refined sample after coarsening in semisolid state developed an equiaxed grain structure like that of spray castings. The grain refined samples exhibited coarse pore clusters of $\approx 20 \mu\text{m}$ at a few grain corners but these were spaced so much further apart than the grain size that they did not appear to have affected the grain coarsening.

Quantitative measurements of the grain size intercepts (data listed in Table 1) are plotted as λ_i^3 vs t_f in Fig. 19. Again t_f comprised the initial solidification time of 156 s plus the hold time above the eutectic temperature. Note that at short times grain size

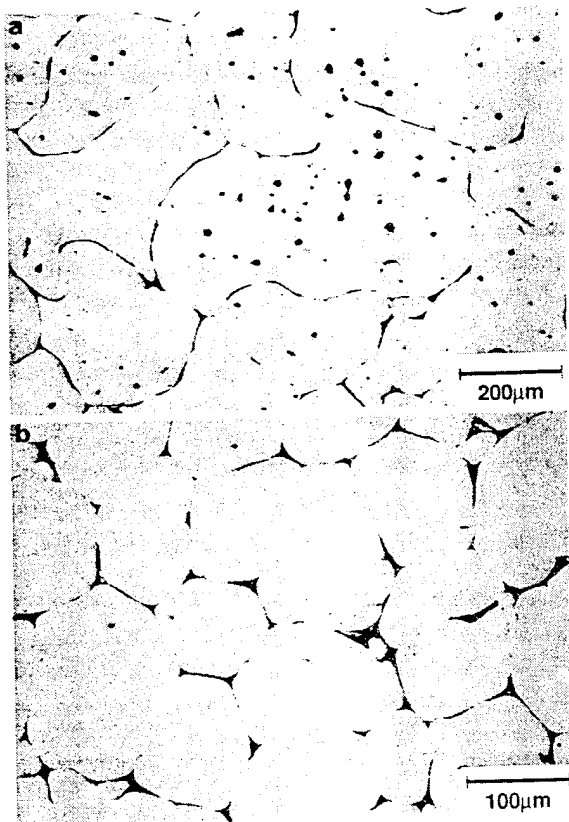


Fig. 18. Observed microstructures in a d.c.-cast [39], high purity Al-4.5 wt% Cu-1.5 wt% Mg alloy after coarsening for 45 min at 515°C ($f_s \approx 0.95$) showing: (a) coarse grain structure in the un-grain refined (i.e. dendritic) sample and (b) a finer equiaxed structure in the grain refined sample.

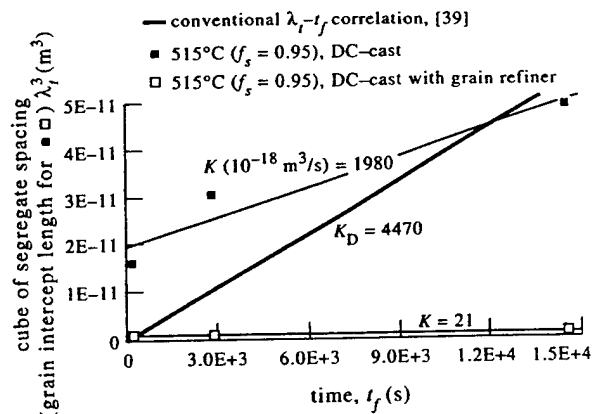


Fig. 19. The dependence of segregate spacing (λ_i) on isothermal coarsening time (t_f) for d.c.-cast Al-4.5 wt% Cu-1.5 wt% Mg showing a reduction in the coarsening rate constant K at high f_s . Note that the inhibition is significantly stronger in the grain refined samples. The initial segregate spacing was $75 \mu\text{m}$ in both cases. Initial grain size was $253 \mu\text{m}$ in the untreated sample and $104 \mu\text{m}$ in the grain refined sample [39].

exceeds the secondary dendrite arm spacing, but slower coarsening over time results in smaller grain sizes than secondary arm spacing predicted by the thick line. The thick line corresponds to the λ_i - t_f equation for conventional casting processes [41]. Once again, the results show retarded coarsening for both morphologies at high f_s compared to the conventional dendrite coarsening equation. It should be noted that the rate constant for the grain refined sample decreased by two orders of magnitude while that for the unrefined sample decreased only marginally.

3. DISCUSSION

The results of the entire set of isothermal coarsening experiments described in this paper are summarized in Fig. 20 by plotting the measured coarsening rate constant K_{exp} , normalized by the measured dendritic coarsening rate constant K_D , vs f_s . It is clear from Fig. 20 that as $f_s \rightarrow 1$ in all these alloys, K_{exp} decreased monotonically but at differing rates. Based on the micrographs presented earlier in this paper, we can identify in these experiments four different

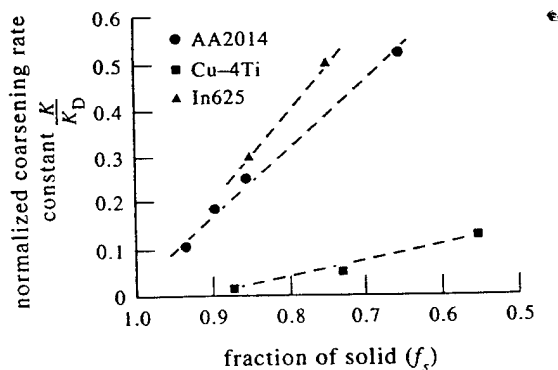


Fig. 20. Plot summarizing the dependence of the normalized coarsening rate constant (K/K_D) on the fraction of solid (f_s) observed in this study.

structural regimes for the coarsening in the mushy zone:

- (i) dendrites surrounded by liquid,
- (ii) spherical grains dispersed in liquid,
- (iii) impinged grains/spheroids with liquid films at the grain boundaries, i.e. liquid concentrated at grain boundaries, grain edges and triple points, and
- (iv) isolated liquid droplets within dendritic grains following in-grain coalescence.

These different morphologies appear to each require a separate analysis. A large part of the morphology differences arises from the increase of volume fraction of solid for a given alloy composition as the temperature falls. There is, however, a second important variable in the kinetics of coarsening, viz. the composition difference between solid and liquid. This difference usually increases as the temperature falls and its effect must be included in any discussion on the effect of fraction solid for a given alloy, as studied here experimentally. The effect on coarsening of these two aspects derived from the solid-liquid structure are considered below.

3.1. Composition of Solid and Liquid

This effect is much better understood than the morphology effects. It is well established and applies to all coarsening processes, and will, therefore, be briefly discussed first. As is well known, the atomic fraction of solute in liquid changes from the equilibrium (phase diagram) value under a flat interface, X_1 , to that under a radius of curvature ρ , $X_1(\rho)$, which is given by the Gibbs-Thomson (G-T) equation [42]:

$$X_1(\rho) = X_1 \left(1 - \frac{2\gamma V(1 - X_1)}{\rho \epsilon RT (X_1 - X_s)} \right) \quad (2)$$

where ρ is considered positive for a solid sphere surrounded by liquid. X_s is the atomic fraction of solute in the solid (with $k = X_s/X_1$), V is the molar volume of the liquid, γ is the solid-liquid interfacial energy, ϵ is the Darken coefficient [21-24, 35, 42] which accounts for the non-ideality of the solution and equals $(1 + \partial \ln g / \partial \ln X_s)$. The G-T relation, when applied to the process of Ostwald ripening of spherical solid particles in a liquid matrix, yields the equation derived by the standard LSW analysis [42, 43] for the mean radius after time t of coarsening, ρ_t , of a dispersed phase which is not a pure element but a solution content X_s .

$$\rho_t^3 = \rho_0^3 + \left(\frac{8D_l \gamma V}{9RT} \right) \left(\frac{1 - X_1}{X_1 - X_s} \right) \left(\frac{X_1}{X_1 - X_s} \right) t_f \quad (3)$$

where D_l is the solute diffusion coefficient in the liquid, V is the molar volume of the solid and $X_s < X_1$ (i.e. $k < 1$). Note that ϵ is absent from equation (3) since for a liquid with variable activity coefficient, g ,

(i.e. $\epsilon \neq 1$), the actual diffusion coefficient, D , is a product of a coefficient determined by atomic mobility and the Darken parameter ϵ .

Equation (3) shows an acceleration of the coarsening rate with decreasing temperature over the classical LSW rate by two terms which arise from two different sources. The first term given by $X_1(1 - X_1)/X_1 - X_s$, is derived directly from equation (2) and enhances the G-T change of solubility. The second term given by $1/(X_1 - X_s)$, is a coefficient that reflects the reduction of the amount of solute to be transported from a melting to a growing interface as temperature is reduced. This differs from the factor derived by Chaix *et al.* [44] which equals $1/(1 - X_s)$ because they considered the Fe-Cu system as the model where $X_1 \rightarrow 1$. The solute that must be transported for coarsening decreases from all atoms in the solid for a pure solid to the difference between the two phases (a smaller value) when the solid and/or liquid phases are solutions. This second effect has clearly been illustrated in previous work by Kang-Yoon [17] and Ferrante [45]. However, the data on coarsening from various studies such as Niemi-Courtney [18] and others [17, 19] are for various volume fractions of solid at constant temperatures where the composition of the solid and liquid phases remained unchanged. In the absence of the complicating effect of changing composition as the fraction solid changes, these well-characterized isothermal coarsening experiments clearly showed a significantly enhanced coarsening rate (by about 8 times over the range studied) at larger solid fractions in the range 0.2-0.95. Yang *et al.* [35] show that the inclusion of these two accelerating terms into existing models—LSEM, i.e. Lifshitz-Wagner Encounter Modified [46], BWEM, i.e. Brailsford-Wynblatt Encounter Modified [35] and GV, i.e. Glicksman-Voorhees [26] appears to yield a better match with experimental results in Refs [17-20].

When $X_s > X_1$ (i.e. $k > 1$), equation (3) takes the following form

$$\rho_t^3 = \rho_0^3 + \left(\frac{8D_l \gamma V}{9RT} \right) \left(\frac{1 - X_1}{X_s - X_1} \right) \times \left(\frac{X_1}{X_s - X_1} \right) t_f \quad (3a)$$

When $X_1 \ll 1$, then $(1 - X_1) \rightarrow 1$, $X_s \rightarrow 1$ so that $(X_1 - X_s)^2 \rightarrow 1$ and equation (3) reduces to the usually quoted relationship given below

$$\rho_t^3 = \rho_0^3 + \left(\frac{8D_l \gamma V X_1}{9RT} \right) t_f \quad (3b)$$

For solidification coarsening in alloys where the partition coefficient k is a constant, a more useful version of equation (3) is

$$\rho_{at}^3 = \rho_0^3 + \left(\frac{8D_l \gamma V}{9RT} \right) \left(\frac{1 - X_1}{X_1(1 - k)^2} \right) t_f \quad \text{for } k < 1 \quad (3c)$$

$$\rho_t^3 = \rho_0^3 + \left(\frac{8D_l \gamma V}{9RT} \right) \left(\frac{1 - X_1}{X_1(k - 1)^2} \right) t_f \quad \text{for } k > 1. \quad (3d)$$

For very dilute alloys where $(1 - X_1) \rightarrow 1$, equations (3e), (3f) or (3g) are applicable.

$$\rho_i^3 = \rho_0^3 + \left(\frac{8D_1\gamma V}{9RT} \right) \left(\frac{1}{X_1(1-k)^2} \right) t_f \quad \text{for } k < 1 \quad (3e)$$

$$\rho_i^3 = \rho_0^3 + \left(\frac{8D_1\gamma V}{9RT} \right) \left(\frac{1}{X_1(k-1)^2} \right) t_f \quad \text{for } k > 1 \quad (3f)$$

$$\rho_i^3 = \rho_0^3 + K_p t_f \quad (3g)$$

where

$$K_p = \left(\frac{8D_1\gamma V}{9RT} \right) \left(\frac{1}{X_1(1-k)^2} \right) \quad \text{for } k < 1$$

and

$$= \left(\frac{8D_1\gamma V}{9RT} \right) \left(\frac{1}{X_1(k-1)^2} \right) \quad \text{for } k > 1.$$

The reciprocal dependence of coarsening rate on the alloy content, in equations 3(c, e, g), is well established experimentally for alloy systems where $k < 1$, e.g. the data on conventional dendrite coarsening in Al-Cu shown in Fig. 3 in Refs [1-4]. This rate dependence on $1/X_1$ will clearly lead to a steady fall in the expected coarsening rate for a given alloy composition as the temperature falls and the fraction solid, f_s , rises. It may be noted that for alloys in which the partition coefficient $k > 1$, the contribution from $(k-1)^2$ term will compensate the decrease in X_1 as the temperature falls and f_s rises. However, there are no experimental reports, known to the present authors, of data that would allow this prediction to be tested.

In addition, any impurities in the alloy that can lower the equilibrium partition coefficient k will increase the amount of solute that must be transported across the liquid film for grain growth. Applying this to equation (3c), it is clear that the $(1-k)^2$ term in the denominator will increase and thus decrease K . There is some evidence such behavior in the liquid phase sintering of carbide particles. Warren reported 3- and 2-fold reductions in K upon addition of 5 wt% WC and 3.75 wt% NbB₂ to NbC-Co during LPS at 1420°C; WC is known to reduce the solubility of NbC in liquid Co [47]. He had previously observed similar trends in LPS of WC-Co with additions of NbC, TaC and C [48]. Additional support is available from Lassner and Schreiner [49] who observed a refinement in WC grain size upon LPS in Co with VC impurity of 200 ppm. The same material, however, upon milling prior to sintering, yielded a coarse grain size. Lassner [49] suggested that the impurity concentration in the un-milled sample was sufficient to cover all grain boundaries and inhibited coarsening by reducing surface wettability and interfacial solute transport. The milled

sample, on the other hand, contained fractured and thus fresh, impurity-free surfaces which permitted wetting by Co liquid and did not inhibit interfacial solute transport. Fukuhara and Mitani's study [50] of TiC-TiN sintering in 30% liquid Ni showed a similar suppression of K with increasing N content; K decreased 5-fold from pure TiC to TiC_{0.8}N_{0.2}. There are two issues that must be answered: (i) What is the cause/mechanism for this reduction of the partition coefficient k in the presence of a second solute species? and (ii) To what extent can k be reduced? Since a solid-liquid interface is not atomically smooth, it appears *unlikely* that the removal of solute atoms from the solid can be hindered due to the presence of other species even if present as a stable mono-atomic layer, from Sarian-Weart [34], on the solid-side of the solid-liquid interface analogous to a passivating oxide film. Besides, such a suppression cannot be to the extent of zero solid solubility. Consequently, this does not appear a viable reason for the observed dramatic decrease in K as $f_s \rightarrow 1$.

One other term in equation (3) that can vary with temperature is solute diffusivity in liquid D_1 since $D = D_0 \exp(-Q_D/RT)$; the magnitude of this decrease in D_1 will be determined by the value of Q_D . As a rule, Q_D (in cal/mol) is approx. 10 times the melting temperature (in K) of the solute element). Comparison of estimated values shows that D_1 increases by a factor of 1.5 as the temperature increases from (that corresponding to) $f_s = 0.9$ to $f_s = 0.5$ in Al-Cu, Cu-Ti, In-625 or Fe-Cu. This retardation of coarsening accruing from this decrease in D_1 is much less than an order of magnitude and cannot account for the observations in this study. On the other hand, this effect may contribute significantly to the observed increase in K with coarsening temperature by Kang-Yoon in Fe-Cu and Co-Cu [17]. The retardation of coarsening due to the chemical terms in equation (3), as the temperature falls and the fraction solid rises in the alloys studied here, applies to the diffusion-limited coarsening kinetics for all the morphologies discussed in the following section.

3.2. Coarsening in the Different Microstructural Morphologies

3.2.1. Dendrite to sphere comparison

The simplest morphology for modeling coarsening should be the case of spherical solid grains in a medium fraction solid, $f_s \leq 0.5$. Here the simple results of equation (3) should apply, though expressed in terms of the inter-particle spacing, λ , using $\lambda^3 = \alpha \rho^3 / f_s$ where α is a numerical constant of order 1, from Mortensen [51]. This substitution yields

$$\lambda_i^3 = \lambda_0^3 + \left(\frac{\alpha K_p}{f_s} \right) t_f. \quad (3h)$$

By comparison with equation (1) we see that the coarsening rate determined by particle spacing, K_D will be given by:

$$K_D = \left(\frac{\alpha K_p}{f_s} \right). \quad (4)$$

This is an interesting result that arises from the significant difference between the study of coarsening by measurement of the average particle radius and that by measurement of the inter-particle spacing. The former method is usually adopted for precipitate coarsening [42] while the latter method is the conventional method in most solidification studies. It should be noted that the simple analysis, leading to equation (4), ignores at least two important effects. One, the more complex geometry of a dendritic structure where the mean curvature varies continuously between the dendrite tip and other locations. Two, the much discussed reduction of the diffusion distances by an increase in the volume fraction of the coarsening phase. In the simple case of spherical particles, this effect leads to a predicted increase of K_p as f_s increases; For example, Voorhees and Glicksman [26] found that K_p rises by a factor of 2 as f_s increased for 0.2 to 0.4 and by a factor 10 as f_s increased from 0.2 to 0.95 (Fig. 1), the regime of interest here. As noted previously, this expectation of accelerated coarsening with increasing fraction solid has been clearly demonstrated experimentally for coarsening at constant phase composition on a range of Fe-Cu, Sn-Pb and Co-Cu alloys by Refs [17-20] (see Fig. 1). However, the only partial success of this prediction for the solid-state coarsening of Ni_3Al in Ni [28-30] should be noted. Examples of

the reduction of diffusion distances as f_s increases are discussed below for different morphologies.

3.2.2. Free spheres to compacted spheres

As f_s increases beyond about 0.74 (the packing factor for close-packed structures of spheres of equal size), the individual solid particles can no longer exist as spheres but they must be compacted into a conventional polycrystalline grain structure subject to normal grain growth. Microstructural examples of this are given in Figs 9, 13, 16 and 18(b). The subject of grain boundary migration and grain growth with liquid film wetted boundaries is outlined here although it was previously discussed in a recent conference on grain growth [8, 37].

Liquid film migration limited grain growth—one-dimensional analysis

The simplest case is that of a liquid film on a grain boundary surface for a spherically curved surface of radius r , Fig. 21. There will be a composition difference ΔC , in atoms of solute per unit volume across the film, from the negatively to positively curved solid-liquid interface given by:

$$\Delta C = \frac{\Delta X}{V_l} = \frac{2(X_l(\rho) - X_l)}{V_l} \\ = \frac{4\gamma V_l}{\rho RT V_l} \frac{X_l(1 - X_l)}{(X_l - X_s)} \quad \text{for } k < 1 \quad (5)$$

where V_l is the atomic volume in the liquid. For a liquid film thickness, δ , and a liquid diffusion

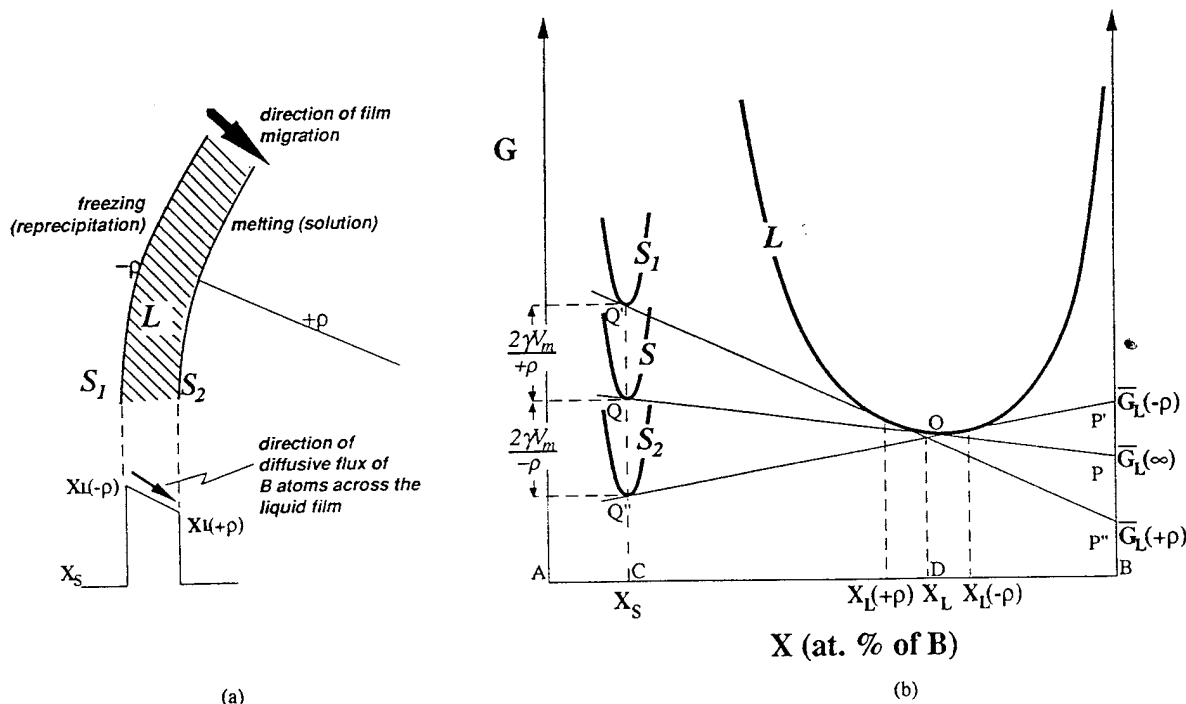


Fig. 21. (a) Schematic of a grain boundary liquid film on a grain edge or face with one-dimensional diffusive flow, and (b) free energy of the solid and liquid phases corresponding to (a).

coefficient, D_1 , the flux of solute J down this gradient is given by equation (6):

$$J = \frac{D_1 \Delta X}{\delta V_1} \quad (6)$$

The velocity of the liquid film wetted grain boundary, v_b , towards its center of curvature is given in turn by equation (7):

$$v_b = \frac{JV_1}{(X_1 - X_s)} \quad (7)$$

so that

$$v_b = \frac{D_1 4\gamma V X_1(1 - X_1)}{\delta \rho RT (X_1 - X_s)^2} \quad (7a)$$

$$= \mu_b \frac{2\gamma}{\rho} \quad (7b)$$

where

$$\mu_b = \frac{D_1 2V X_1(1 - X_1)}{\delta RT (X_1 - X_s)^2} \quad (7c)$$

and is the mobility of the liquid-wetted grain boundary film under a capillarity pressure of $2\gamma/\rho$. This result is the same as that for curvature-driven liquid film migration in DIGM [52-54]. Using the simplest model for normal grain growth (e.g. [42]) equation (7b) can be used to obtain a model for grain growth, equation (8), yielding a square dependence of grain size or segregate spacing on time. The simple model has:

$$\alpha \frac{d\lambda}{dt} = v_b = \mu_b \frac{2\gamma}{\beta\lambda} \quad (8)$$

where α and β are constants that, for a steady-state grain size or segregate spacing distribution [55], relate the change of the mean grain size or spacing to the mean velocity which, in turn, is determined from the mean grain size or spacing. This, on integration, yields equation (9)

$$\lambda_i^2 = \lambda_0^2 + K_{GBF} t \quad (9)$$

where

$$K_{GBF} = \left(\frac{8D_1\gamma V}{\alpha\beta\delta RT} \right) \left(\frac{X_1(1 - X_1)}{(X_1 - X_s)^2} \right) \text{ for } k < 1 \quad (9a)$$

K_{GBF} is the coarsening rate constant for the migration of a grain boundary liquid film. The λ_i^2-t relationship in equation (9) will, however, only be valid if the

grain boundary film thickness δ remained constant. It is important to note that δ must be a function of λ , since δ multiplied by grain boundary area per unit volume corresponds to the volume fraction of liquid f_l , i.e. $\delta \cdot \lambda^2/\lambda^3 \approx f_l$ or $\delta = \lambda(1 - f_s)$. Since the volume fraction of solid essentially remains constant for isothermal coarsening (apart from the small increase due to the G-T equation), we can substitute for δ by $\lambda(1 - f_s)$, in equation (8) thus recovering in equation (10) the cubic dependence of λ on time t , seen in Figs 3, 7, 10, 14, 17 and 19.

$$\lambda_i^3 = \lambda_0^3 + K'_{GBF} t \quad (10)$$

where

$$K'_{GBF} = \left(\frac{12D_1\gamma V}{\alpha\beta RT} \right) \left(\frac{1}{1 - f_s} \right) \left(\frac{X_1(1 - X_1)}{(X_1 - X_s)^2} \right) \text{ for } k < 1. \quad (10a)$$

For dilute solutions, with a constant partition coefficient, k , this becomes:

$$K'_{GBF} = \left(\frac{12D_1\gamma V}{\alpha\beta RT} \right) \left(\frac{1}{1 - f_s} \right) \left(\frac{1}{X_1(1 - k)^2} \right) \text{ for } k < 1. \quad (10b)$$

Equation (10) nicely illustrates the two effects of coarsening at different temperatures in a given alloy system. As the temperature falls the solute content of the liquid, X_1 , rises causing the fall of coarsening rates observed in this study. On the other hand, the fraction solid, f_s , rises towards 1 giving a very rapid increase in coarsening rate, similar to that predicted by Voorhees-Glicksman [26] and Yang-Nash [20], but this type of increase was not seen in the present studies. The predicted acceleration in K'_{GBF} with increasing f_s from the term in $1/1 - f_s$ arises, as in the detailed Glicksman-Voorhees coarsening model [26], from the reduction in diffusion distance which, in this case, is the grain boundary film thickness, δ .

One aspect of the reciprocal relationship between film velocity, v_b , the local boundary thickness, δ , derived in equation (7) was commonly seen in this study. This is the tendency of a migrating grain boundary liquid film to release, as a liquid inclusion, any region with a locally enhanced thickness. A schematic of this feature that has been previously* observed in liquid phase sintering [18, 56, 57] is given in Fig. 22. A large liquid inclusion captured and

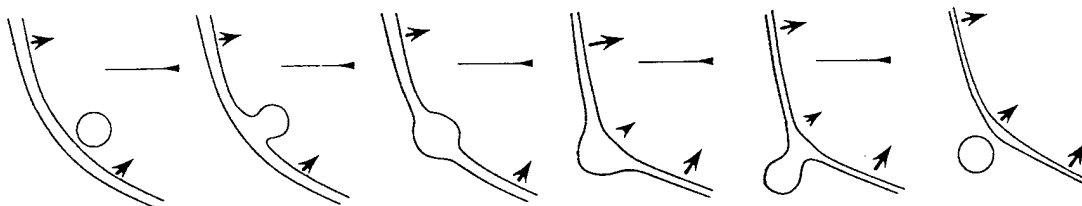


Fig. 22. Schematic illustrating capture and release of isolated liquid particles by a migrating grain boundary liquid film.

wetted by a moving grain boundary may not have sufficient time to redistribute the liquid along the boundary as the boundary moves through. Consequently, if the boundary is migrating fast enough the inclusion can be released, i.e. left behind if criteria for closure of the neck are satisfied. From Kang *et al.* [58], criterion for closure of the neck connecting the liquid droplet to the migrating boundary can be written as

$$\Delta\mu = \gamma V \left(\frac{1}{r_1} - \frac{1}{r_2} - \frac{2}{\rho_1} \right) < 0 \quad (11)$$

where r_1 and r_2 correspond to the internal and external radii of curvatures of the neck, and ρ_1 is the average radius of curvature of the grain boundary (i.e. one of the two principal radii). Experimental observations, Fig. 6(a), clearly show this process, thus resolving the problem of persistent isolated liquid inclusions, despite extensive grain growth, in regions swept by grain boundaries. As the grain size rises, the average radii of curvature of the boundaries, ρ in equation (7), and the velocity of boundary migration will both fall. At sufficiently slow rates of boundary migration, this process of releasing liquid inclusions into the growing grains should end since the captured droplet will have time to spread itself along the boundary. Detailed studies of the grain morphology in two phase (solid + liquid) systems [8] have shown that as the grain size increases the frequency of liquid droplets trapped in the grains does fall; this effect is also seen in regions with small grains in Fig. 6(b). Similar observations have been reported in liquid phase sintering of Fe-Cu powder compacts by Kang-Azou [56] and Hwang *et al.* [57] who attribute this feature solely to rapid grain growth of strained material during reheating. In the present study, the liquid film was also made thicker in places by the presence of coarse Fe-rich plates and thus destabilized resulting in the release of the observed droplets.

A further important microstructure effect seen in the present work and recognized in previous studies

[8, 17, 52, 53] is curvature driven transport of liquid along the grain boundaries in the two-phase solid plus liquid microstructure at high volume of fractions solid. This is illustrated in Fig. 23 showing that even for the usual condition of complete wetting of the grain boundaries by liquid, $2\gamma_{sl} \leq \gamma_{gb}$, typical in metals [59], at high f_s the local curvature at the 3-grain triple points will be much larger than that arising from grain size differences. The higher curvature, i.e. the smaller radii ρ , results in solute transport from the liquid films at the boundaries between 2 grains to 3-grain triple lines or edges. A further application of this effect will, at small enough values of the fraction liquid (relative to the grain size), continue the transfer of solute and thus liquid from the 3-grain edges to 4-grain corners. This is universally observed during liquid phase sintering in the various studies cited earlier in this paper, viz. Refs [17-20, 52, 53]. This concentration of liquid at triple points is exacerbated if the hold temperature is below the wetting transition temperature which, according to Straumal *et al.* [60], is an inverse function of the grain boundary energy, γ_{gb} . This is illustrated by the structure in Fig. 13(c) corresponding to isothermally coarsened Cu-6 wt% Ti at 975°C for 15 min. The liquid morphology indicates that in Cu-6 wt% Ti below 975°C $2\gamma_{sl} > \gamma_{gb}$ even for high angle boundaries, so that liquid no longer penetrates along the grain boundaries. As a consequence, the liquid prisms at triple points are larger than expected for good wetting, thus increasing diffusion distance across the liquid film and reducing K . A second consequence of poor wetting is that the liquid film thickness δ can decrease below a critical value creating a solid-solid grain interface which would, intrinsically, be very mobile since migration of such a boundary only requires atom transport across a disordered interface. In the condition of high grain boundary mobility with liquid pockets at the triple points, grain boundary curvatures will be eliminated (see Figs 5 and 9) [38]. However, the observation of corrugated grain boundaries in Fig. 13(c) suggests some local inhibition of

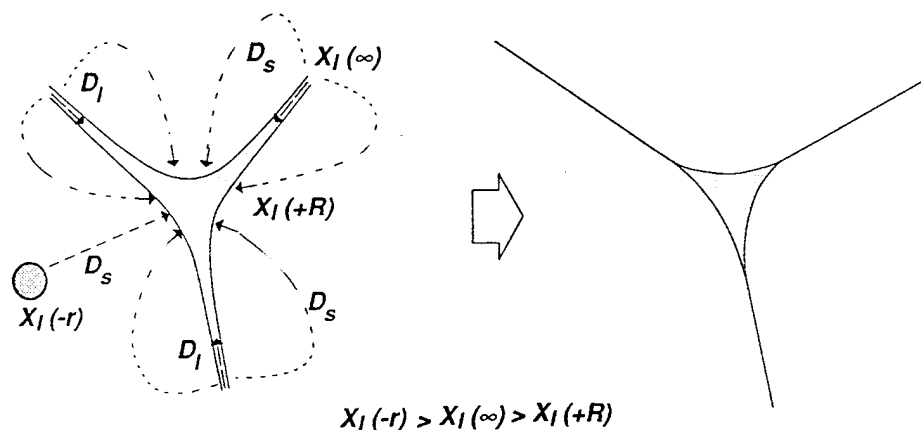


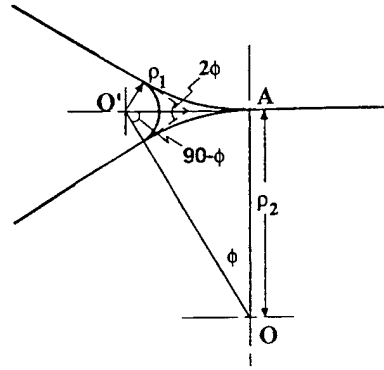
Fig. 23. Flow of solute to the triple point at high f_s via solid and liquid diffusion causing the removal of grain boundary curvature and imposition of curvature on the solid-liquid interface at the triple point.

grain boundary motion due to pinning, for example, by particles.

Liquid film migration limited grain growth—two-dimensional analysis

Higgins *et al.* [38] have proposed an analysis for coupled coarsening of a two-phase structure which had all of the minority phases at grain corners. The process of coarsening of the grains and grain corner particles was analyzed as curvature-driven migration of second phase inclusions at grain corners. The principle of this analysis is that in a situation such as that shown in Figs 24(a–c), 3-grain boundaries meeting at an edge or 4-grain edges meeting at a corner, can for a mobile grain boundary meet at angles different from the required values of 120° (for edges) or 109° (for corners). For non-equilibrium angles, local force balance will impose a differential curvature on the sides of the inclusion (which, in the present case, is a liquid droplet). The difference in curvature of different faces of such an inclusion then leads to a solute flux across the droplet resulting in migration or drag of the liquid droplet under the influence of unbalanced grain boundary tension. This methodology is instantly applicable to the present situation of tubes or prisms of liquid at 3-grain edges or tetrahedrons of liquid at 4-grain corners, Figs 24(d, e).

The equilibrium angle of 120° for a 3-sided grain in two dimensions can be reduced to $2\phi = 60^\circ$ by the presence of wetting liquid tubes/prisms at the triple



In triangle OAO', $\cos \phi = \frac{\rho_2}{\rho_2 + \rho_1}$

Fig. 25. Construction to derive the dependence of the dihedral angle ϕ on the radii of curvature of the growing and receding solid-liquid interfaces at a triple point in a 3-sided grain depicted in Fig. 24.

points if all grain boundary curvature is concentrated at the solid-liquid interface, Fig. 25. There will be two radii of curvature at the triple points, ρ_1 and ρ_2 . In the triangle OAO' the angle $O'OA$ is ϕ , so we obtain:

$$\frac{\rho_2}{\rho_1} = \frac{\cos \phi}{1 - \cos \phi} \quad (12)$$

When $2\phi = 60^\circ$, ρ_2 is $7.5\rho_1$. When $2\phi = 120^\circ$, the ratio of the radii has the expected value of 1, while

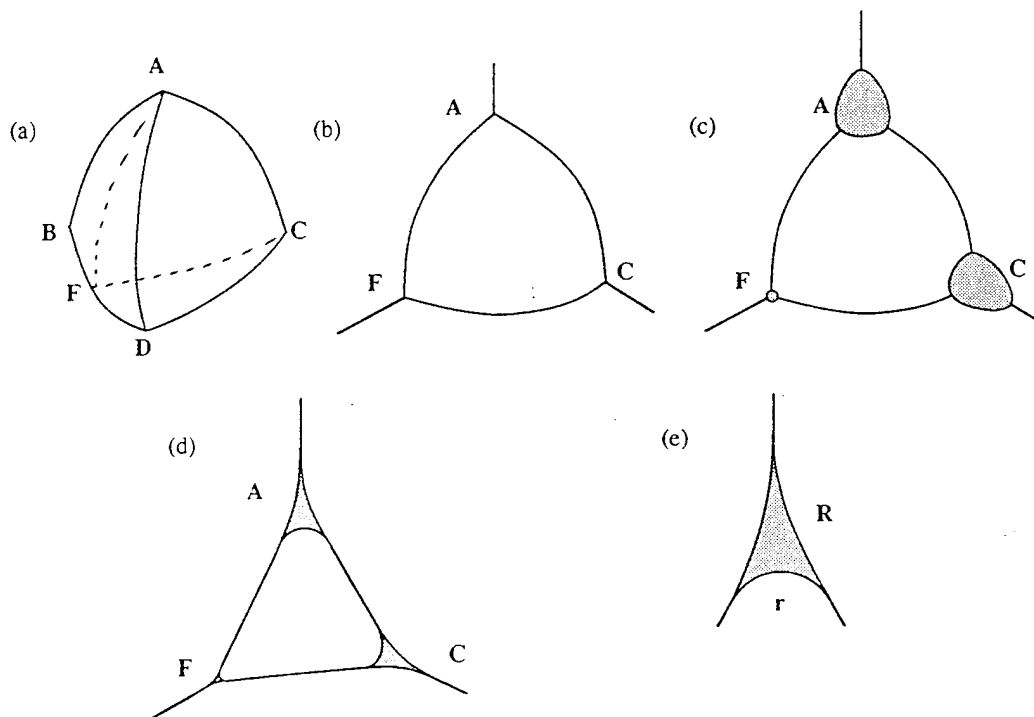


Fig. 24. The removal of grain boundary curvature by particles (solid/liquid) at the grain boundary triple points in a tetrahedral grain ABCD. (b) section ACF through (a), (c) section ACF through the tetrahedral grain with solid particles at all four corners after Higgins *et al.* [36], (d) representation of (c) for liquid particles at the triple points, and (e) enlarged view of the liquid film wetting the grain boundary triple point in (d).

the ratio of the radii rises rapidly as 2ϕ falls to smaller angles. Under this difference in radii there will be a concentration gradient across the liquid droplet determined from the concentration difference obtained from equation (2) across a distance of order a , where $a^3/8$ is the volume of the liquid triple point. Taking λ as the diameter as of an average 14-sided grain and noting that each such grain shares 6 triple points, the fraction liquid can be written as:

$$f_l = \psi \left(\frac{a^3}{\lambda^3} \right) \quad (13)$$

where ψ is a numerical constant approximately equal to 1. A first order model for the migration velocity, v_d , of a triple point droplet is obtained by taking ρ_1 as a and ρ_2 as much larger than ρ_1 , assuming liquid diffusion control yields equation (14).

$$v_d = \frac{2D_l \gamma V}{a^2 RT} \left(\frac{X_l(1 - X_l)}{(X_l - X_s)^2} \right) \quad (14)$$

This droplet velocity gives a very approximate value for the rate of grain growth, $d\lambda/dt$. The argument is that it will take a time τ , where $\tau = \lambda/v_d$, to cross an average grain diameter λ . During this time interval the mean grain size will approximately double since about 50% of the grains will have vanished. This gives equation (15) which integrates to equation (16).

$$\frac{d\lambda}{dt} = \frac{2D_l \gamma V}{\lambda^2 f_l^{2/3} RT} \times \left(\frac{X_l(1 - X_l)}{(X_l - X_s)^2} \right) \quad (15)$$

$$\lambda_t^3 = \lambda_0^3 + K'_{TPG} t \quad (16)$$

$$K'_{TPG} = \frac{6D_l \gamma V}{RT} \left(\frac{X_l(1 - X_l)}{(X_l - X_s)^2} \right) \times \left(\frac{1}{1 - f_s} \right)^{2/3} \text{ for } k < 1. \quad (16a)$$

For dilute solutions, with a constant partition coefficient, k , this becomes:

$$K'_{TPG} = \frac{6D_l \gamma V}{RT} \left(\frac{1}{X_l(1 - k)^2} \right) \left(\frac{1}{1 - f_s} \right)^{2/3} \text{ for } k < 1 \quad (16b)$$

Table 2. Comparison of K_{th} predicted by equation (16a) with K_{exp} for various alloys in previous and current studies illustrating the effect of temperature on contributions of different terms to K

Alloy (wt%)	Temperature (°C)	Diffusion term $\frac{6D_l \gamma V_m}{RT}$ ($\times 10^{18} \text{ m}^3/\text{s}$)	Composition term $\frac{X_l(1 - X_l)}{(X_l - X_s)^2}$	Volume fraction term $\frac{1}{(1 - f_s)^{2/3}}$	K_{th} [equation (16a)] ($\times 10^{18} \text{ m}^3/\text{s}$)	K_{exp} [17, 20] ($\times 10^{18} \text{ m}^3/\text{s}$)	$\frac{K_{th}}{K_{th1}}$	$\frac{K_{exp}}{K_{exp1}}$
Fe-20Cu	1150	7.13	0.05	3.40	1.21	0.76	1.00	1.00
Fe-20Cu	1200	7.73	0.07	3.47	1.91	1.32	1.58	1.74
Fe-20Cu	1250	8.33	0.09	3.55	2.67	1.88	2.21	2.47
Fe-20Cu	1300	8.93	0.12	3.67	3.91	3.20	3.24	4.21
Fe-30Cu	1150	7.13	0.05	2.33	0.83	0.41	1.00	1.00
Fe-30Cu	1200	7.73	0.07	2.34	1.29	0.71	1.55	1.73
Fe-30Cu	1250	8.33	0.09	2.35	1.77	1.12	2.14	2.73
Fe-30Cu	1300	9.93	0.12	2.37	2.52	1.15	3.05	2.80
Fe-50Cu	1150	7.12	0.05	1.56	0.55	0.25	1.00	1.00
Fe-50Cu	1200	7.73	0.07	1.55	0.85	0.44	1.54	1.76
Fe-50Cu	1250	8.33	0.09	1.54	1.16	0.74	2.09	2.96
Fe-50Cu	1300	8.92	0.12	1.53	1.63	1.10	2.94	4.40
Co-20Cu	1150	3.94	0.10	4.76	1.87	1.21	1.00	1.00
Co-20Cu	1200	4.27	0.15	5.84	3.87	2.75	2.07	2.27
Co-20Cu	1250	4.60	0.22	7.11	7.30	5.20	3.91	4.30
Co-20Cu	1300	4.93	0.33	8.47	13.62	11.40	7.29	9.42
Co-30Cu	1150	3.97	0.10	2.66	1.05	0.51	1.00	1.00
Co-30Cu	1200	4.30	0.15	2.79	1.86	1.18	1.77	2.31
Co-30Cu	1250	4.64	0.22	2.87	2.97	1.95	2.83	3.82
Co-30Cu	1300	4.97	0.33	2.88	4.66	4.00	4.44	7.84
Co-50Cu	1150	4.02	0.10	1.61	0.64	0.24	1.00	1.00
Co-50Cu	1200	4.36	0.15	1.61	1.09	0.52	1.68	2.17
Co-50Cu	1250	4.70	0.22	1.59	1.67	0.90	2.59	3.75
Co-50Cu	1300	5.04	0.33	1.55	2.54	2.16	3.94	9.00
Ni-20Ag	1000	4.62	0.008	3.35	0.12	0.02	1.00	1.00
Ni-20Ag	1050	4.99	0.013	3.36	0.22	0.09	1.81	4.23
Ni-20Ag	1100	5.35	0.014	3.39	0.25	0.20	2.11	9.74
Al-6.7Cu	550	17.95	6.56	9.15	1078		1.34	
Al-6.7Cu	575	19.26	8.32	5.01	802	6†	1.00	1.00
Al-6.7Cu	600	20.56	11.76	3.02	731	19†	0.91	3.17
Al-6.7Cu	625	21.86	20.45	1.79	799	144†	1.00	24.00
Cu-4Ti	950	24.51	7.28	5.54	988		1.16	
Cu-4Ti	975	26.03	8.74	3.65	851	5†	1.00	1.00
Cu-4Ti	1000	29.75	10.46	2.40	730	40†	0.85	8.00
Cu-4Ti	1015	30.48	12.46	1.90	732	91†	0.86	18.20

$D_l(\text{m}^2/\text{s}) = D_l(\text{Cu in liquid Cu}) = 1.5 \times 10^{-7} \exp(-4855/T)$ [60]
 $= D_l(\text{Ag in liquid Ag}) = 4.6 \times 10^{-8} \exp(-3890/T)$ [60]
 $= D_l(\text{Cu in liquid Al}) \approx 3.8 \times 10^{-7} \exp(-2799/T)$ (est.)
 $= D_l(\text{Ti in liquid Cu}) \approx 4.0 \times 10^{-6} \exp(-6541/T)$ (est.)

†Current study

$\gamma_{(s) - \eta_{Fe} Cu} = 0.04 \text{ J/m}^2$ [17]
 $\gamma_{(s) - \eta_{Co} Cu} = 0.234 \text{ J/m}^2$ [17]
 $\gamma_{(s) - \eta_{Ag} Ni} = 0.57 \text{ J/m}^2$ [20]
 $\gamma_{(s) - \eta_{Cu} Ti} = 0.3 \text{ J/m}^2$ (est.)
 $\gamma_{(s) - \eta_{Al} Cu} = 0.163 \text{ J/m}^2$ [58].

Although this is an approximate model, it yields very similar kinetics to those expected for grain boundary film limited migration, equation (10). This indicates that the expected kinetics of grain boundary film limited coarsening should not change when the two-phase material attains the characteristic microstructure for a high fraction of solid. The expected decrease in coarsening kinetics due to the increase in liquid concentration X_1 will, in the case considered here, be more than offset by the rapid acceleration due to the increase in the volume fraction of solid as $f_s \rightarrow 1$. Application of equation (16a) reproduces the observed increase of K with increasing temperature in Co-Cu, Fe-Cu and Ni-Ag. Table 2 compares the contributions of diffusion, composition and solid fraction terms for various alloys and gives a computed K_{th} to be compared with measured K_{exp} . For the Fe-Cu, Co-Cu and Ni-Ag systems, the simple model for coarsening at high fraction solid at rates limited by the migration of liquid at triple points gives a surprisingly close agreement with the experimental values even at 50% Cu, i.e. $f_s = 0.5$. The agreement in Ni-Ag though good at the highest temperature, 1100°C, fails at lower temperatures when the experimental coarsening occurs at much slower rates than expected. In the present samples when data were available for testing Al-Cu and Cu-Ti systems, the model fails completely. The experimental results are again much slower than expected, particularly as the temperature falls and the fraction of solid rises—in the condition where the grain boundary/triple line model should be most applicable. A full comparison between the simple theory developed, as equation (16a), for binary alloys cannot be made for the multicomponent AA2014, the Al-Cu-Mg ternary or for the nickel-based In-625. However, a comparison of normalized K (i.e. K_{exp} divided by K_D , the K for dendritic coarsening) for these alloys with that for Al-Cu and Cu-Ti where data are available (Table 2), indicates that other systems will also exhibit a strong inhibition of coarsening, though in a less extreme form than that seen for the binary Al-Cu and Cu-Ti systems. Given that the model works for the non-spray cast high purity Fe-Cu and Co-Cu systems (to within a factor of less than 2), the failure in the other systems indicates that at low temperatures there is some other factor involved in Ni-Ag and the systems studied here. As discussed in the following section 3.2.3, the failure for the dendritic Al-Cu and non-grain refined Al-Cu-Mg is readily understood within the current theories of solidification, but for the other systems at least one additional factor is required. As discussed in Section 3.3, we propose that the additional factor appears to be the drag exerted on migrating grain boundaries by a minority second phase of solid particles or (in other spray cast systems) gas pores.

3.2.3. Coarsening of dispersed liquid droplets within solid grains

In the case of a dendritic structure where the dendrite arm spacing is significantly smaller than the grain size yields the one case where strongly inhibited coarsening is actually predicted by theory. This is the situation for the dendritic Al-6.7 wt% Cu and non-grain refined Al-4.5 wt% Cu-1.5 wt% Mg cast samples reheated to temperatures just above the eutectic temperature, see Figs 6(a-c) and 18(a). During the last stages of solidification there will be large scale coalescence of adjacent dendrite arms with the same orientation. As the solid regions come in contact, no grain boundary forms. This type of coalescence has long been recognized [5, 61, 62] as leading to the formation of trapped liquid pockets within the grains, thus terminating the rapid coarsening of the segregate spacing, seen in Figs 5(a, b). The liquid droplets are dispersed in a solid matrix and the situation is analogous to that of particle coarsening in solid-state. As a consequence, the operative radius of curvature has a sign reverse of that applicable for liquid droplets at grain boundaries/corners. This results in the melting at the surface of the largest droplets and freezing at the surface of the smallest with solute transport occurring by solid-state diffusion. Since D_s in face-centered-cubic solids close to the melting point is typically four orders of magnitude lower than D_l , negligible coarsening of the liquid inclusions within the grains is expected. This was seen experimentally and provided an explanation for this effect previously noted by Enright and Doherty [10]. The only significant changes to be expected for in-grain droplets will be the following two processes: (i) capture of in-grain droplets by migrating grain boundaries and (ii) occasional release of such captured droplets when the boundary velocity is faster than the processes redistributing the captured liquid along the grain boundaries towards 3-grain triple points [58]. Segregate spacing measurements in the Al-Cu binary samples included intercepts by in-grain droplets. Macroscopic non-uniformity of the initial grain structure from the wedge casting further complicated these measurements. Therefore, the coarsening data from the remelted dendritic structures of the binary Al-Cu samples was assumed to be irrelevant to the problem of slow grain-scale coarsening observed in the spray cast alloys. This indicates that only the results on AA2014, Cu-Ti and In-625, and the grain-refined d.c. cast Al-4.5 wt% Cu-1.5 wt% Mg systems are of real significance in establishing a much lower than expected coarsening rate at high f_s for spray cast (equiaxed) microstructures.

3.3. Role of a Minority Second Solid Phase

In the spray case AA2014 sample, after remelting, small amounts of a second solid phase were observed in the grain boundary liquid films, Figs 9(a, b). This

type of iron-rich "constituent phase" is a common feature of all commercial aluminum structural alloys. In the present case, the solid particles appear, like the matrix grains, to be fully wetted by the liquid. Similar coarse iron-rich second-phase particles were observed in the triple points of grain-refined Al-4.5 wt% Cu-1.5 wt% Mg sample after being remelted, Fig. 26(a). In addition, very fine, possibly Ti-rich, particles derived from grain-refining additions of Ti and B are clearly seen causing corrugations on apparently mobile grain boundaries in Fig. 26(b). During grain coarsening by the migration of liquid-wetted grain boundaries, these second-phase particles present on grain boundaries would be dragged along by the liquid-wetted grain boundaries analogous to the solid-state case. In the early stages of coarsening, the particles would be small and distributed equally between grain corners and grain edges. At later stages in the coarsening, as a consequence of couple-phase coarsening [35, 38], most of the particles would be coarse and located predominantly at the 4-grain corners. This trend was evident in the case of the spray cast AA2014 [Figs 9(a-c)] and in grain-refined d.c.-cast Al-4.5 wt% Cu-1.5 wt% Mg [Figs 26(a, b)]. The potential influence of such second-phase particles, forming late in solidification, on the coarsening of fine-grained structures (such as those of spray casting) must be considered in any analysis of grain- or segregation-scale coarsening.

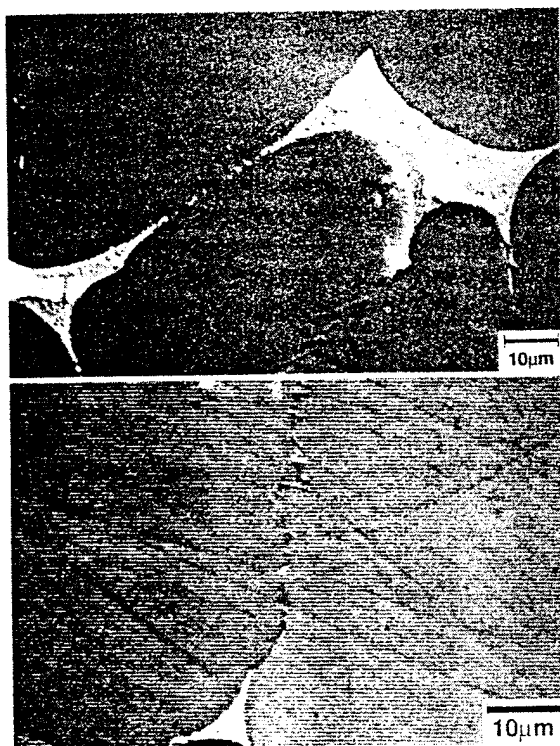


Fig. 26. Ti-rich particles observed on grain boundaries in the grain-refined Al-4.5 wt% Cu-1.5 wt% Mg sample [refer to Fig. 18(b)] after isothermal coarsening at 515 C ($f_s \approx 0.95$). (a) Coarse particles at grain boundary triple points that were wetted by liquid, and (b) fine particles that appear to be pinning a grain face or edge producing corrugations as shown.

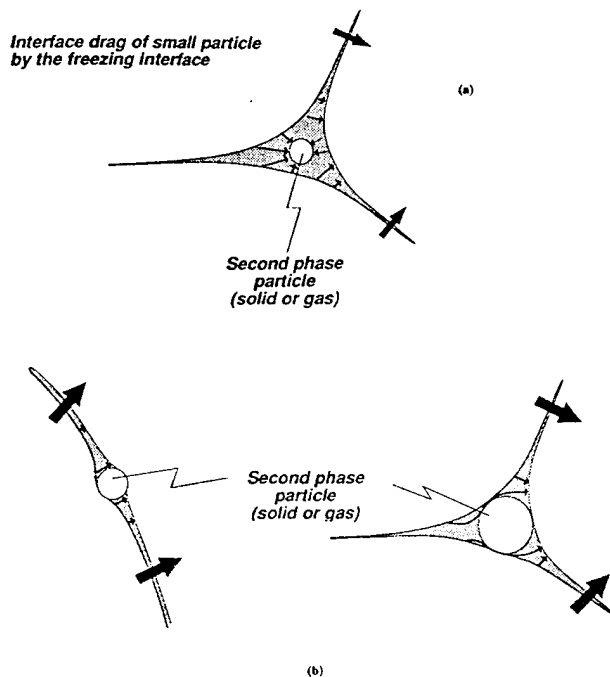


Fig. 27. Possible mechanisms of impedance of solute diffusion in the grain boundary liquid films by second phase particles: (a) drag by the freezing interface of a particle of diameter $<$ liquid film thickness, δ , located at a triple point wetted by liquid; (b) barrier to diffusion in the liquid film between the melting and freezing interfaces by particle of diameter $>$ δ located either on a grain edge or at a triple point wetted by liquid.

We propose that particles lying on the grain boundary liquid films inhibit the grain growth process. These particles can achieve this inhibition by different mechanisms on their propensity to wet the liquid and their size. Particles that wet the liquid will be dragged along but will thicken the liquid film, i.e. increase the diffusion distance [δ in equation (6) or a in equation (12)] over which solute must be transported during coarsening. From this, we can visualize the manner in which the particle size may affect the coarsening process. In one case, particles much smaller than the thickness of the liquid film should provide little barrier to solute transport around them, Fig. 27(a). Their only effect should be to create a small region of negative curvature (center of curvature on the liquid side of the solid-liquid interface) on the freezing interface. This negative curvature will generate a low pressure region in the liquid stimulating liquid flow to relieve the pressure and to displace the second-phase solid particle. This type of interface drag of small particles by freezing interfaces was originally identified by Van Vlack [63]. In the second case, particles of sizes comparable to the thickness of the liquid film, Fig. 27(b), are likely to strongly inhibit the free migration of the liquid by becoming a barrier to solute diffusion and fluid flow around them. This would apply to large particles located at triple point liquid droplets seen in Fig. 27(a) and to almost any size particle at the negligibly thin residual grain boundary liquid films seen in Fig. 27(b). On the other hand, previous liquid phase sintering studies

by Kang *et al.* [58] on Mo-Ni with 0.6 and 1 wt% Al_2O_3 (mean particle size $\approx 30 \mu\text{m}$) have shown that upon coarsening to a certain grain size the migrating liquid films shed these particles even for wettable particles. However, the authors reported a small (10%) decrease in K upon addition of 3 vol.% of Al_2O_3 which was proposed to accrue from localized inhibition of grain coarsening by the Al_2O_3 particles.

This possibility for inhibition of coarsening, which appears to be an important one, is easily identified in the AA2014 spray cast alloy and the Al-4.5 wt% Cu-1.5 wt% Mg d.c.-cast alloy. However, no particles have been identified so far in the Cu-Ti spray cast alloy which also showed inhibited coarsening as $f_s \rightarrow 1$. The presence of fine-scale impurity particles such as oxides/nitrides or even gas-filled voids from the gas atomization step remains a distinct possibility for all spray cast structures. There is some indirect evidence in the present and previous work supporting this position. First, the sample held at 975°C , Fig. 13(c), did exhibit corrugated and irregular grain boundaries despite the presence of liquid at triple points. Since, liquid at triple points should ideally absorb all the curvature and apply sufficient tension on the grain boundaries to flatten them, these corrugations would imply that there are obstacles to grain boundary movement which we hypothesize to be fine titanium nitride particles pinning the grain boundaries. These particles can form when the highly reactive Ti species in Cu-Ti reacts with trapped nitrogen. Nitrogen pick-up ranging from 200 to 1000 ppm has been reported for alloys spray cast using nitrogen [64-66]. In addition, results of gas absorption analysis of spray cast copper-based alloys by Ashok *et al.* [64] point to the presence of compound/s of nitrogen. Pure copper in spray cast condition released nitrogen just above the melting temperature of copper whereas spray cast copper alloys of Zr and Cr released nitrogen at temperatures well above 1084°C (Cu melting point). No direct TEM observations of such sub-micron particles have so far been reported to validate this inference. The hypothesis would suggest that typical grain refinement of spray cast alloys should not be observed when spraying with a gas that is inert and does not produce any particles, e.g. nickel-based superalloys spray cast in argon. But results reported by Benz *et al.* and Dalal [65-67] on In-718 are to the contrary. This is explained by the fact that In-718 melts containing > 5 ppm of nitrogen contain a dispersion of fine TiN particles which act as nuclei for NbC precipitation during the final stages of solidification [65, 68, 69] (therefore termed "carbonitride" particles). Alternately, pores or voids formed by trapped, insoluble gas may be equally effective in pinning grain boundaries and inhibiting coarsening at high volume fractions of solid. The presence of trapped gas in the form of voids/pores (up to 3 wt%) on grain boundaries when spray casting with gases inert to the alloys

has clearly been identified by several groups involved in spray casting work [64-68]. However, there was no opportunity to evaluate this possibility in the current study and is not considered significant. Additional support for particle-inhibition is provided by Grant *et al.*'s [36] observation of inhibited semisolid coarsening in reheated spray casting of aluminum alloys. The alloys used in that study, i.e. Al-4 wt% Cu, Al-10 wt% Zn-2 wt% Mg-1 wt% Cu-0.2 wt% Zr and AA2618 (Al-2.5 wt% Cu-1.5 wt% Mg-1.1 wt% Ni-1.1 wt% Fe) manifest the following insoluble particles respectively—Fe-rich constituents, ZrAl_3 and Al_3FeNi . We believe that such particles, present from the early stages of solidification, inhibit coarsening by pinning liquid-wetted grain boundaries (edges or triple points). The hypothesis put forward here needs to be experimentally confirmed by additional investigations, currently being attempted by the authors. It would be of value if similar tests were to be attempted by other groups studying spray casting on different alloys and using different facilities. This phenomenon which yields a fine equiaxed grain structure appears to be a universal effect in spray casting.

Particles that do not wet the liquid can also produce inhibition until they are released from the liquid film by the same mechanism outlined for the release of liquid droplets in Al-6 wt% Cu chill-cast alloy. On the other hand, the Fe-rich particles in the Al-6 wt% Cu, the Ti-rich particles in Al-4.5 wt% Cu-1.5 wt% Mg samples and the TiN particles in Cu-6 wt% Ti [70] are known to be wetted by the parent liquid phase. Therefore, the observed retarded coarsening in the present study cannot be attributed to inhibition by non-wetting particles.

3.4. General Considerations in Coarsening at High Fractions of Solid

The experimental results in all five systems investigated, chill cast Al-Cu, d.c. cast Al-4.5 wt% Cu-1.5 wt% Mg, and spray cast AA2014, Cu-Ti and In-625 showed considerably lower coarsening rates than expected from standard dendrite arm coarsening or Ostwald ripening results, see Figs 1 and 20. This experimental discrepancy in samples subjected to isothermally coarsening over controlled periods of time indicates that the reduced coarsening detected in spray cast deposits is a real result and not caused by errors in thermal modeling of the process. This result is of significance to the utilization of spray casting since it shows that finer grain structures and reduced segregation spacings will be produced in samples made by this process. Spray casting is not a true rapid solidification processing route [8, 11-15, 35, 70] in comparison, for example, with plasma spraying or conventional P/M compaction of rapidly solidified powders since solidification in the deposit occurs over extended periods of time (1-100 s). However, as a result of slow coarsening

during solidification and cooling, spray cast deposits yield significantly finer microstructures than expected from conventional wisdom. Incorrect or incomplete solidification theory should not, therefore, be an argument against experimental consideration of this processing route.

However, the reduction of coarsening rates found in the present study remains a considerable theoretical challenge. Standard coarsening theory for spherical particles in a solid or liquid matrix [21–24, 26, 42–46] clearly predicts an acceleration of coarsening as the fraction solid increases and there are clear experimental confirmations of this effect [17–20]. The opposite result, found in the present study and in those reported in Refs [32–35, 47, 48] is thus a problem. Additional, but approximate, theoretical models for coarsening developed here for the particular grain microstructures seen at high fraction solids confirm the trend observed previously [17–20, 33] in that the rates should vary as $1/(1 - f_s)$. These models based on grain growth at rates limited by grain boundary liquid film migration are similar to previous models for DIGM [52–54] and particle coarsening [37]. The increase in the coarsening rate with increasing fraction of solid, in all the theories, arises from a reduction in the required diffusion distance for an individual coarsening event, as previously noted by Yoon-Huppmann [72] and Kang-Yoon [17].

Only two well-understood mechanisms were found that could produce the opposite effect, i.e. the retardation of coarsening at higher fractions of solids. The first of these is the larger amount of solute that must be transported across the solid-liquid interface at lower temperatures (i.e. higher f_s) thus reducing the coarsening rate as shown by equation (3) for LSW coarsening. This effect is well known and is derived from the larger difference between the solute content of the liquid and solid ($X_l - X_s$) at lower temperatures in binary eutectic systems with $k < 1$. However, this effect, as discussed earlier, is more than compensated for by the decrease in diffusion distance, i.e. the liquid film thickness δ , as temperature and f_s are lowered. The second mechanism applies for a dendritic solid, when the dendrite arm spacing is significantly smaller than the grain size. Under such circumstances, at a high volume fraction of solid dendrite arm coalescence occurs leading to isolated liquid droplets inside grains, and thus an early termination of rapid coarsening at liquid diffusion controlled rates. Such a phenomenon was seen in the chill cast Al-Cu binary alloy and has been reported by Ashok and Ogilvy [64, 73] in isolated instances in spray castings where a single grain surrounded the skeleton of a pre-solidified droplet. But this is not applicable to this study's results on the equiaxed structures.

A comprehensive review of literature reveals six other mechanisms that could generate the opposite

effect, viz. the retardation of coarsening at high fractions of solid by reducing the driving force of for liquid film migration due to:

- (i) Coherency strain ahead of the solid-liquid interface, as in DIGM, caused by rapid volume diffusion, Song-Yoon [52–54, 68, 74].
- (ii) Artificially narrow or skewed particle size and thus curvature distribution [75].
- (iii) Interface-diffusion limited grain growth caused by the presence of a solute impurity reaction layer at the solid-liquid interface [32–35].
- (iv) Decrease in wettability (i.e. large dihedral angle) due to solute impurities in liquid, [63, 76, 77].
- (v) Decrease in D_s with decreasing temperature or fraction of solid, Glicksman *et al.* [26].
- (vi) Suppression of solubility of solute in solid and liquid due to the presence of a third component, e.g. NbC in WC-Co, [47–50].

A detailed discussion of each of the above reported mechanisms will not be attempted in this paper due to space limitations. It is sufficient to note, however, that none of the listed possibilities can generate the magnitude of inhibition in binary metallic systems reported in this paper. Consequently, the inhibited coarsening observed in previous and present studies is hypothesized to accrue from drag on liquid film migration at high fractions of solid by minority second phase particles—solid or gas. In the Yang *et al.* study [35], the authors sintered the Ni-Ag powder blend in a vacuum-sealed container which was not at a sufficiently low vacuum level ($p_{O_2} = 10^{-10}$ atm) to prevent formation of NiO. These oxide inclusions may have caused the retarded coarsening observed in that paper. Micrographs of the Ni-Ag study, kindly made available by the authors, do exhibit corrugated boundaries similar to those seen in Al-Cu-Mg and Cu-Ti. On the other hand, no such corrugations were observed in the studies by Warren [32, 47, 48] and Kang and Yoon [17].

Further study is required to verify this hypothesis by conducting new isothermal coarsening studies at high solid fractions on equiaxed microstructures with and without particles. This can be achieved by the following experiments, currently being attempted by the authors. One, repetition of Yang *et al.*'s Ni-Ag liquid phase sintering [35], however, under reducing atmosphere to prevent oxidation. Two, reproduction of Kang-Yoon's or Niemi-Courtney's liquid phase sintering of Fe-Cu alloys [18, 19] in the presence of oxides introduced either by sintering at $<10^{-6}$ atm vacuum or by blending in fine Al_2O_3 powders (0.06 and 1 μm). Comparison of coarsening rate constants in the proposed experiments with data in Refs [17–19, 34] should provide a rigorous test of the present hypothesis. Three, isothermal coarsening studies using equiaxed microstructures, without inclusions,

prepared by SIMA, i.e. strain-induced-melt-activation [9] of an ingot cast under an argon atmosphere. We expect that the SIMA material will be devoid of impurity oxide/nitride particles or gas-filled voids. A comparison of the results with those for spray cast samples should show if particle-inhibited grain coarsening is a dominant mechanism. Four, additional isothermal coarsening studies on spray cast samples where variation of the volume fraction of solid in the liquid matrix is set by the alloy composition and not by the temperature so as to eliminate the $(X_1 - X_s)$ inhibition.

CONCLUSIONS

- i. Isothermal coarsening at high f_s in equiaxed structures, both spray cast and grain refined d.c.-cast, occurs by the migration of liquid-wetted grain boundary films via solution and reprecipitation mechanism, Kang-Yoon [17].
- ii. Dendritic structures, at high f_s , reproduce this grain growth-type behavior after in-grain coalescence of solid dendrite arms. Consequently, conventional dendrite arm coarsening theory and correlations may not be valid at high f_s .
- iii. During coarsening in the semi-solid regime, isolated pockets/droplets of liquid ($1-5\ \mu\text{m}$) were observed in the grain interiors. In the dendritic case, these arise primarily from trapped interdendritic liquid. A second source, proposed for all microstructures, is the occasional release of large liquid droplets behind fast-moving boundaries.
- iv. The isothermal coarsening rate in equiaxed—both cast and spray cast structures—is reduced at temperatures where the fraction of solid exceeds 0.5.
- v. Models, derived for this grain growth by migration of films determined by solution-precipitation at grain edge and grain corner solid-liquid interfaces, reproduce the classic Ostwald ripening cubic kinetics and predict a rapid increase in the coarsening rate constant K with increasing f_s or decreasing temperature.
- vi. in non-dilute alloy systems, K is an inverse square function of the amount of solute that must be transported across the liquid film, i.e. $(X_1 - X_s)$. Therefore, in a simple binary eutectic system with partition coefficient $k < 1$, as the isothermal aging temperature is decreased the coarsening rate constant K will decrease. This decrease, however, is more than compensated for by the exponential decrease in the distance over which the solute must be transported, essentially given by $1/1 - f_s$.
- vii. Observations reveal the presence of minority insoluble second phase particles in nearly all

the samples analyzed. In the absence of any other possibility, we hypothesize that these inclusions are inhibiting the coarsening process in the spray cast structures and in other systems studied in this work.

Acknowledgements—The authors are grateful for donations of materials used in this research from Alcoa Technical Center, Osprey Ltd and from the U.S. Navy (NSWC) and for valuable discussions from many people but in particular from Dr John Liu, Dr Pravin Mathur, Dr Jie Zou and Dr Cheng Cai. The research was funded by The Office of Naval Research (code 332). Dr A. K. Vasudevan, the contract monitor for this part of the project, is gratefully acknowledged for his helpful scientific guidance and advice

REFERENCES

1. A. Mortensen, *Metall. Trans.* **20A**, 247 (1989).
2. K. P. Young and D. H. Kirkwood, *Metall. Trans.* **6A**, 197 (1975).
3. T. Z. Kattamis, J. C. Coughlin and M. C. Flemings, *Trans. Metall. Soc. AIME* **239**, 1504 (1967).
4. M. C. Flemings, *Solidification Processing*, p. 150. McGraw-Hill, New York (1974).
5. K. H. Chien and T. Z. Kattamis, *Z. Metallk.* **61**, 475 (1970).
6. A. Vogel, D. Phil. thesis, Univ. of Sussex, Brighton, England (1977).
7. J. Liu and R. D. Doherty, unpublished research. Drexel University, Philadelphia, Pa (1989).
8. S. Annavarapu, J. Liu and R. D. Doherty, in *Materials Science Forum* (edited by G. Abbruzzese and P. Brozzo), Vols 94-96, p. 649. TransTech Publications, Amsterdam (1991).
9. M. C. Flemings, *Metall. Trans.* **22A**, 957 (1991).
10. P. G. Enright and R. D. Doherty, unpublished research. Univ. of Sussex, Brighton, England (1970).
11. P. Mathur, D. Apelian and A. Lawley, *Acta metall.* **37**, 429 (1989).
12. E. Gutierrez-Miravete, E. J. Lavernia, G. M. Trapaga, J. Szekely and N. J. Grant, *Metall. Trans.* **20A**, 71 (1989).
13. P. Mathur, S. Annavarapu, D. Apelian and A. Lawley, *Mater. Sci. Engng A* **142**, 261 (1991).
14. W. G. Watson, *Proc. First Int. Conf. Spray Forming*, Paper No. 23. Osprey Metals Ltd, Swansea, Wales (1990).
15. S. Annavarapu, D. Apelian and A. Lawley, *Metall. Trans.* **21A**, 3237 (1990).
16. A. Vogel, *Metal Sci.* **12**, 576 (1978).
17. S. S. Kang and D. N. Yoon, *Metall. Trans.* **13A**, 1405 (1982).
18. A. N. Niemi and T. H. Courtney, *J. Mater. Sci.* **16**, 226 (1981).
19. S. C. Hardy and P. W. Voorhees, *Metall. Trans.* **19A**, 2713 (1988).
20. S. C. Yang and P. Nash, *Mater. Sci. Technol.* **4**, 860 (1988).
21. P. W. Voorhees, *J. Stat. Phys.* **38**, 231 (1985).
22. C. S. Jayanth and P. Nash, *J. Mater. Sci.* **24**, 3041 (1989).
23. A. D. Brailsford and P. Wynblatt, *Acta metall.* **27**, 489 (1979).
24. A. J. Ardell, *Acta metall.* **20**, 61 (1972).
25. W. J. Boettinger, P. W. Voorhees, R. C. Dobbryn and H. E. Burdette, *Metall. Trans.* **18A**, 487 (1987).
26. P. W. Voorhees and M. E. Glicksman, *Metall. Trans.* **15A**, 1081 (1984).

27. M. E. Glicksman, R. N. Smith, S. P. Marsh and R. Kuklinski, *Metall. Trans.* **23A**, 659 (1992).
28. C. S. Jayanth and P. Nash, *Mater. Sci. Technol.* **6**, 405 (1990).
29. A. J. Ardell, in *Phase Transformations '87* (edited by G. W. Lorimer), p. 485. The Institute of Metals, London, England (1988).
30. A. J. Ardell, *Scripta metall. mater.* **24**, 343 (1990).
31. W. Bender and L. Ratke, *Scripta metall. mater.* **28**, 737 (1993).
32. R. Warren, *J. Mater. Sci.* **7**, 1434 (1972).
33. R. M. German, *Liquid Phase Sintering*, p. 140. Plenum Press, New York (1985).
34. S. Sarian and H. W. Weart, *J. appl. Phys.* **37**, 1657 (1966).
35. S. C. Yang, G. T. Higgins and P. Nash, *Mater. Sci. Technol.* **8**, 10 (1992).
36. P. S. Grant, R. P. Underhill, W. T. Kim, K. P. Mingard and B. Cantor, in *Spray Forming 2* (edited by John V. Wood), p. 45. Woodhead, Cambridge, England (1993).
37. S. Annavarapu, P. Mathur, D. Apelian and R. Doherty, *ibid.* Ref. [14], Paper No. 31.
38. G. T. Higgins, S. Wiryolukito and P. Nash, *ibid.* Ref. [8], p. 671.
39. F. A. Shunk, *Constitution of Binary Alloys, Second Supplement*. McGraw-Hill, New York (1969).
40. G. K. Bouse and J. R. Mihalisin, in *Superalloys, Supercomposites, and Superceramics* (edited by J. K. Tien and T. Caulfield), p. 122. Academic Press, Boston, Mass. (1989).
41. J. Zou and R. D. Doherty, Alcoa Technical Report, p. 3 (1990).
42. J. W. Martin and R. D. Doherty, *Stability of Microstructure in Metallic Systems*, p. 179. Cambridge Univ. Press, Cambridge, England (1976).
43. G. R. Purdy, *Metal Sci. J.* **5**, 81 (1971).
44. J. M. Chaix and N. Eustathopoulos and C. H. Allibert, *Acta metall.* **34**, 1589 (1986).
45. M. Ferrante and R. D. Doherty, *Acta metall.* **27**, 1603 (1979).
46. C. K. L. Davies, P. Nash and R. N. Stevens, *Acta metall.* **28**, 179 (1980).
47. R. Warren, *J. Mater. Sci.* **3**, 471 (1968).
48. R. Warren, *Plansee. Pulvermetall.* **20**, 299 (1972).
49. E. Lassner and M. Schreiner, *Refractory Hard Mater.* **9**, 97 (1982).
50. M. Fukuhara and H. Mitani, *Powder Metallurgy* **25**, 62 (1982).
51. A. Mortensen, *Metall. Trans.* **22A**, 569 (1991).
52. Y. Song, S. Ahn and D. N. Yoon, *Acta metall.* **33**, 1907 (1985).
53. S. S. Kim and D. N. Yoon, *ibid.* **33**, 281 (1985).
54. J. C. M. Li and B. B. Rath, *Scripta metall.* **19**, 689 (1985).
55. W. W. Mullins and J. Vinals, *Acta metall.* **37**, 991 (1989).
56. S. L. Kang and P. Azou, *Powder Metallurgy* **28**, 90 (1985).
57. H. Hwang, S. L. Kang and D. N. Yoon, *Metall. Trans.* **17A**, 1429 (1986).
58. S. L. Kang, W. A. Kaysser, G. Petzow and D. N. Yoon, *Acta metall.* **33**, 1919 (1985).
59. M. Gunduz and J. D. Hunt, *Acta metall.* **33**, 1651 (1985).
60. B. Straumal, T. Muschik, W. Gust and B. Predel, *Acta metall. mater.* **40**, 939 (1992).
61. P. C. Dann, L. M. Hogan and J. D. Eady, *Metals Forum* **2**, 212 (1979).
62. R. D. Doherty, E. A. Feest and K. Holm, *Metall. Trans.* **4**, 115 (1973).
63. L. H. Van Vlack and G. I. Madden, *Trans. Metall. Soc. AIME* **230**, 1200 (1964).
64. S. Ashok, private communication. Metals Research Labs, Olin Corp., New Haven, Conn. (1991).
65. R. Dalal, private communication. Howmet Tech. Center, Howmet Corp., Whitehall, Miss. (1992).
66. M. G. Benz, T. F. Sawyer, W. T. Carter, R. J. Zabala and P. L. Dupree, *ibid.* Ref. [36], p. 171.
67. M. G. Benz, T. F. Sawyer, F. W. Clark and P. L. Dupree, *ibid.* Ref. No. 14, Paper No. 20.
68. M. G. Benz, R. J. Zabala, P. L. Dupree, B. A. Knudsen, W. T. Carter and T. F. Sawyer, in *Superalloys 718, 625, 706 and Various Derivatives* (edited by E. A. Loria), p. 99. T.M.S.-AIME, Warrendale, Pa (1994).
69. A. Mitchell, A. J. Schmalz, C. Schvezov and S. L. Cockcroft, *ibid.* Ref. [68], p. 65.
70. D. H. Kim, S. H. Hwang and S. S. Chun, *J. Mater. Sci.* **26**, 3223 (1991).
71. S. Ashok, *Int. J. Rapid Solid.* **7**, 283 (1992).
72. D. N. Yoon and W. J. Huppmann, *Acta metall.* **27**, 973 (1979).
73. A. J. W. Ogilvy, in *Spray Forming: Science, Technology and Applications* (edited by A. Lawley and A. Leatham), p. 33. A.P.M.I., Princeton, N.J. (1992).
74. Y. Song and D. N. Yoon, *Metall. Trans.* **15A**, 1503 (1984).
75. Z. Fang, B. R. Patterson and M. E. Turner, *Acta metall. mater.* **40**, 713 (1992).
76. J. White, in *Sintering and Related Phenomena* (edited by G. C. Kuczynski), p. 81. Plenum Press, New York (1973).
77. O. K. Riegger, G. I. Madden and L. H. Van Vlack, *Trans. Metall. Soc. AIME* **227**, 971 (1963).